Imperial College London
Department of Bioengineering

The mechanobiology of the inner wall endothelium of Schlemm's canal

Alice SPENLEHAUER

Supervisors : Prof Darryl R. OVERBY and Dr Chiu Fan LEE

Thesis submitted for the degree of Doctor of Philosophy and the Diploma of Imperial College

August 2019

Abstract

Glaucoma is the leading cause of irreversible blindness worldwide. The main risk factor for glaucoma is elevated intraocular pressure caused by increased resistance to aqueous humour (AH) flow in the region near the inner wall endothelium of SC. In the healthy eye, AH flow across the SC endothelium generates a basal-to-apical transendothelial pressure drop, which tends to push the cells off their basement membrane and inflates dome-shaped structures known as giant vacuoles (GVs). GV formation leads to substantial cell thinning associated with formation of transendothelial pores that provide a flow pathway across the SC endothelium. **Our overarching hypothesis is that the coupled interaction between transendothelial basal-to-apical pressure drop, and GV and pore formation, is centrally involved the regulation of flow resistance and IOP.**

We examined this hypothesis across four studies carried out using an *in vitro* model of SC endothelium that mimicked the *in vivo* basal-to-apical transendothelial pressure drop. A first study demonstrated that GV-like structures (GVLs) form in perfused SC endothelial (SCE) cells and that they can retract against a load likely through an actomyosin-dependent process. A second study demonstrated that a proportion of GVLs are surrounded by an F-actin band that presumably contracts during GVL retraction. Together these findings suggest that SCE cells can modulate GV dynamics, which may be important for outflow resistance regulation. The third study showed that the hydraulic resistivity of SCE cell layers exhibits both pressure and time-dependent characteristics that likely reflect changes in the cell layer morphology. The study also highlighted that the existence of non-physiological intercellular gaps limits the interpretation of resistivity measurements. The final study established that culturing SCE cells under a long-term transendothelial pressure drop may overcome this limitation as it leads SCE cell layers to better reproduce key cytoskeletal, cellular and multicellular morphological characteristics of the SC endothelial barrier.

“Il faut voir toute la vie comme lorsqu’on était enfant.”

Henri Matisse, 1953

To my parents for their unwavering support,

To my siblings for their cheerful encouragements,

To my grandparents for the example of kindness that they set out.

Acknowledgements

I would like to express my sincere gratitude to my supervisor Prof. Darryl R. Overby for having granted me the opportunity to work on a truly stimulating and challenging research project, and for having provided me with a breadth of expert knowledge throughout my doctoral research. I am also deeply indebted to my co-supervisor Dr. Chiu Fan Lee for his continued commitment to improving my research and for his support in my development as a researcher.

Beyond my supervisors, I would like to thank: Kristin Perkumas and Prof. W. Daniel Stamer from Duke University for providing the cells used throughout my research; Dr. Steve Rothery and Dr. David Garboriau from the FILM facility at Imperial College for their consulting and technical support in microscopy; Dr. A. Thomas Read and Prof. C. Ross Ethier from Georgia Tech for a fruitful collaboration on different parts of my project; Dr. Neil Poloso and Dr. Ying Yu from Allergan Plc. for having offered me the invaluable opportunity to work as an intern at Allergan for a few months during a hiatus in my PhD.; Dr. Andrea Cairoli from the Lee group for an engaging interdisciplinary collaboration; former members of the Overby group – Dr. Sietse Braakman, Dr. Cristoforo Silvestri and Dr. Joseph Sherwood – for their assistance in the early stages of my PhD. A sincere thank you also goes to Britta Ross from the Bioengineering Department student office for all her dedicated assistance.

I am grateful for having worked with a group of people who wore the two hats of colleagues and friends, and who supported me both scientifically and morally through the bumpy road of scientific research: Jacques Bertrand, for making sure that the lab was spotless and running smoothly, and for reminding me that going out for drinks on Friday is a tradition worth keeping up with; (soon-to-be Dr.) Anabela Cepa Areais, for being a truly dedicated and caring friend both inside and outside of the lab, and for taking the time to help me think through problems; Dr. Ester Reina Torres, for the aura of peace that accompanies her presence, and for always reminding me to stay positive; Dr. Michael Madekurozwa, for being kind and thoughtful, and for always going the extra mile to help out; and Dr. Kathy (Pei-Jung) Wu, for being cheerful no matter what, and for often providing a different perspective on situations.

I would like to acknowledge my friends who have all greatly enriched my life far beyond my academic studies, and who have always been both fun and caring. A special mention goes to my past and current flatmates – Juan, Mary and Simon; my friends at Imperial – Jean-David, Anna, and Mehrdad; my childhood friends – Celia and Shona; and my friends back in California, Judy, Tiffany and Andrei.

Last but not least, I am truly grateful to my parents and to my siblings – Margaux and Pierre-Louis – who have given me a vast amount of moral and sentimental support throughout my PhD and who have always encouraged me to pursue the way of curiosity.

Declaration of Originality

I hereby declare that the work presented in this thesis is my own and that it was performed under the supervision of Prof. Darryl Overby and Dr Chiu Fan Lee. My PhD studies were funded by a BBSRC DTP scholarship and an NIH-funded BRP grant obtained by Prof. Darryl Overby. My four and a half months industrial placement at Allergan Plc in Irvine, USA was funded by Allergan Plc.

I further certify that this thesis complies with copyright laws and does not contain any instance of plagiarism. The work of others is duly referenced where necessary throughout the thesis and a complete list of references is included in the Bibliography at the end of this thesis. Contributions by other researchers is listed in the Contribution Statement. All permissions to reprint figures from published work are included at the end of this thesis.

Copyright Declaration

The copyright of this thesis rests with the author. Unless otherwise indicated, its contents are licensed under a Creative Commons Attribution-Non Commercial 4.0 International Licence (CC BY-NC). Under this licence, you may copy and redistribute the material in any medium or format. You may also create and distribute modified versions of the work. This is on the condition that: you credit the author and do not use it, or any derivative works, for a commercial purpose. When reusing or sharing this work, ensure you make the licence terms clear to others by naming the licence and linking to the licence text. Where a work has been adapted, you should indicate that the work has been changed and describe those changes. Please seek permission from the copyright holder for uses of this work that are not included in this licence or permitted under UK Copyright Law.

Contributions

Several researchers have contributed to the work presented in this thesis.

All chapters. All human Schlemm's canal endothelial (SCE) cells used in this thesis were isolated by Ms. Kristin Perkumas in Prof. W. Daniel Stamer's laboratory at Duke University, USA. The perfusion system used throughout this thesis was adapted from an existing system with guidance from Dr. Joseph M. Sherwood and Dr. Michael Madekurozwa.

Chapter 2 to 4. All experimental procedures and analysis were carried out by Alice Spenlehauer.

Chapter 3. Dr David Gaboriau and Dr Stephen Rothery from the FILM facility at Imperial College consulted on the acquisition of confocal images and deconvolution.

Chapter 5. All experimental procedures and analysis were carried out by Alice Spenlehauer, except the sectioning and imaging of semi-thin sections of SCE cells on filter membranes which were carried out by Dr A. Thomas Read in Prof. C. Ross Ethier's laboratory at Georgia Tech, USA.

Publications and conferences

Publications in preparation:

- **Spenlehauer A**, Cairoli A, Lee CF, Overby DR. The role of actomyosin contractility in the life cycle of giant vacuole-like structures in Schlemm's canal endothelial cells. In preparation., to be submitted to *Experimental eye research.*
- **Spenlehauer A**, Read AT, Ethier CR, Lee CF, Overby DR. Cytoskeletal organisation around giant vacuole-like structures in Schlemm's canal endothelial cells. In preparation., to be submitted to *Experimental eye research.*
- **Cairoli A**, Spenlehauer A, Overby DR, Lee CF. A model of inverse bleb growth to describe giant vacuole dynamics. In preparation., to be submitted to *Proceedings of the National Academy of Sciences.*
- **Spenlehauer A**, Read AT, Ethier CR, Lee CF, Overby DR. Effects of long-term transendothelial pressure conditioning in Schlemm's canal endothelial cells. In preparation., to be submitted to *Investigative Opthalmology & Visual Science.*

Conference presentations:

- *Summer Biomechanics, Bioengineering and Biotransport Conference (SB3C)*, June 2015: Time and pressure-dependent hydraulic resistance across Schlemm's canal endothelial cell layers. **Spenlehauer A**, Sherwood JM, Overby DR. Podium presentation.
- *ARVO*, May 2017: Stretch-Dependent Pore Formation in Glaucomatous Schlemm's Canal Cells. Overby DR, Braakman ST, **Spenlehauer A**, Rodrigues JR, Teal C, Read AT, Stamer WD Ethier CR. Podium presentation.
- *Physical biology circle meeting*, April 2018: A biophysical model of inverse blebbing. Cairoli A, **Spenlehauer A**, Overby DR, Lee CF. Podium presentation.
- *World Congress of Biomechanics (WCB)*, July 2018: The role of actomyosin contractility on giant vacuole biomechanics in cultured Schlemm's canal endothelial cells. **Spenlehauer A**, Stamer WD, Sherwood JM, Lee CF, Overby DR. Podium presentation.
- *Association for Research in Vision and Opthalmology (ARVO)*, May 2019: Actomyosin contractility and the vimentin cytoskeleton influence giant vacuole life-cycle in Schlemm's canal endothelial cells. Overby DR, **Spenlehauer A**, Cairoli A, Sherwood JM, Vahabikashi A, Stamer WD, Lee CF. Poster presentation.

- *BiomedEng 2019*, September 2019: Model of inverse bleb growth explains giant vacuole dynamics during cell mechanoadaptation. Cairoli A, **Spenlehauer A**, Overby DR, Lee CF. Poster presentation.

Contents

List of Figures **23**

List of Tables **27**

List of Abbreviations and Symbols **29**

1 Introduction **31**

1.1 Morphology of the conventional outflow pathway 33

1.2 Functional morphology of SC endothelium 36

1.2.1 Morphology of GVs 37

1.2.2 Morphology of pores 41

1.2.3 Aqueous humour transport across the inner wall endothelium of SC 43

1.2.4 Outflow resistance generation 44

1.3 Mechanobiology of the inner wall endothelium 46

1.3.1 Biomechanical environment of SC endothelium 46

1.3.2 Influence of pressure drop on GVs and strain in SCE cells 47

1.3.3 Mechanically supporting cellular structures 49

1.3.4 Influence of cellular strain on pore formation 50

1.3.5 Influence of SCE cell mechanical properties on outflow resistance 51

1.3.6 Mechanisms of GV and pore formation 52

1.4 Specific aims of doctoral research 54

2 The role of actomyosin contractility in the life cycle of GVLs in cultured SCE cells **57**

2.1 Introduction 58

2.2 Materials and Methods 59

2.2.1 Cell isolation and culture 59

2.2.2 Cell seeding on porous membranes 59

2.2.3 Sample preparation for perfusion 60

2.2.4 Drug treatment 61

2.2.5 Pressure-controlled perfusion system 61

2.2.6 Perfusion and image acquisition protocol 62

2.2.7 GVL identification and contour tracking . . . 64
2.3 Results . . . 65
2.3.1 SCE cell morphology and transendothelial perfusion . . . 65
2.3.2 Characteristics of the life cycle of GVLs . . . 66
2.3.3 Effects of Y-27632 on the life cycle of GVLs . . . 72
2.4 Discussion . . . 75
2.4.1 Pressure-dependence of GVL formation and survival . . . 76
2.4.2 Effects of Y-27632 on the life cycle of GVLs . . . 77
2.4.3 Limitations of GVL contour tracking method . . . 79
2.5 Conclusion . . . 79
2.6 Supplementary Material: Movie Captions . . . 80

3 The F-actin and vimentin structures organised around GVLs in cultured SCE cells 83
3.1 Introduction . . . 84
3.2 Materials and methods . . . 85
3.2.1 Experimental design . . . 85
3.2.2 Sample preparation for perfusion . . . 85
3.2.3 Pressure-controlled perfusion system . . . 86
3.2.4 Perfusion protocol and fixation method . . . 88
3.2.5 Drug treatment . . . 88
3.2.6 Immunocytochemistry and fluorescent labelling . . . 89
3.2.7 Confocal imaging . . . 89
3.2.8 Cytoskeletal structure quantification . . . 90
3.3 Results . . . 90
3.3.1 Effects of transendothelial pressure drop on F-actin and vimentin architecture . . . 90
3.3.2 F-actin and vimentin organisation around GVLs . . . 97
3.3.3 Effects of Y-27632 on F-actin and vimentin architecture . . . 102
3.3.4 Effects of Y-27632 on F-actin and vimentin organisation around GVLs . . . 103
3.4 Discussion . . . 107
3.4.1 Effects of transendothelial perfusion on F-actin architecture . . . 107
3.4.2 Effects of Y-27632 on F-actin architecture . . . 107
3.4.3 Effects of transendothelial perfusion and Y-27632 on vimentin architecture . . . 108
3.4.4 F-actin and vimentin structures surrounding GVLs . . . 108
3.4.5 Conclusion . . . 110

4 Characteristics and limitations of hydraulic resistivity measurements in cultured SCE cell layers **111**

4.1 Introduction . . . 112

4.2 Materials and methods . . . 113

4.2.1 Experimental design . . . 113

4.2.2 Pressure-controlled perfusion system . . . 113

4.2.3 Perfusion protocol . . . 114

4.2.4 Hydraulic resistivity measurement . . . 114

4.3 Results . . . 115

4.4 Discussion . . . 118

4.4.1 Time and pressure-dependent characteristics of *in vitro* R_p . . . 119

4.4.2 Comparison with *in situ* R_p and other reported *in vitro* R_p . . . 121

4.5 Conclusion . . . 123

4.6 Appendix A: Parallel Resistances Model . . . 123

4.6.1 Introduction . . . 123

4.6.2 Parallel resistances model . . . 124

4.6.3 Effects of different filter resistances on R_{p_s} . . . 125

4.6.4 Contributions of changes in ϕ to the measured time-dependent changes in R_{p_s} . . . 127

5 Effects of long-term transendothelial pressure conditioning on cultured SCE cells **129**

5.1 Introduction . . . 130

5.2 Materials and Methods . . . 131

5.2.1 Experimental design . . . 131

5.2.2 Cell isolation, culture and seeding on porous membranes . . . 133

5.2.3 Experimental set-up for long-term conditioning . . . 133

5.2.4 Hydraulic resistivity measurements . . . 136

5.2.5 Fluorescent labelling . . . 137

5.2.6 Fluorescence imaging . . . 137

5.2.7 Image analysis and quantification . . . 139

5.3 Results . . . 142

5.3.1 Effects of conditioning on R_p . . . 142

5.3.2 Effects of conditioning on cell distribution, cell confluence and nuclei density . . . 142

5.3.3 Effects of conditioning on cell morphology and F-actin organisation . . . 144

5.3.4 Effects of conditioning on multicellular organisation . . . 147

5.4 Discussion . . . 149

5.4.1 Effect of conditioning on SCE cell morphology, multicellular arrangement and F-actin architecture . . . 150
5.4.2 Effect of conditioning on $\mathbf{R_p}$ . . . 153
5.4.3 Strengths and limitations of the experimental set-up . . . 154
5.5 Conclusion . . . 155
5.6 Supplementary Figures . . . 156

6 Conclusions **161**
6.1 Future work . . . 164

A Permissions to reprint **167**

Bibliography **185**

List of Figures

1.1 General anatomy of the human eye. . . . 34
1.2 Aqueous humour flow pathway in the human eye. . . . 34
1.3 Light micrograph of a cross-section of the conventional outflow pathway. . . . 35
1.4 Transmission electron micrograph of a cross-section through SC endothelium in the human eye. . . . 37
1.5 Three-dimensional confocal reconstruction of a GV-like structure (GVL) formed. . . . 38
1.6 Transmission electron micrograph of the the fine structure of a GV (part 1). . . . 39
1.7 Transmission electron micrograph of the the fine structure of a GV (part 2). . . . 40
1.8 Scanning electron micrograph of the morphology of the inner wall endothelium of SC as seen from the canal lumen. . . . 41
1.9 Scanning electron micrographs of transendothelial pores in SC endothelium. . . . 42
1.10 Transmission electron serial section micrographs of a transendothelial channel formed by a GV and a pore. . . . 45
1.11 Schematic representation of the aqueous flow patterns through the JCT and SC endothelium in the funnelling model. . . . 46
1.12 The influence of pressure drop on the morphology of the conventional outflow pathway. 48
1.13 Hypothetical model of GV and pore formation. . . . 53

2.1 Method for SCE cell seeding onto porous membranes. . . . 60
2.2 Set-up and protocol for live-imaging during cell perfusion. . . . 63
2.3 Comparison of the aspect of GVLs using different modes of visualisation and imaging. . 65
2.4 Cells before and after acclimatisation to basal-to-apical directed perfusion. . . . 66
2.5 Time-lapse image series of SCE cells during basal-to-apical perfusion at a series of pressure drops. . . . 68
2.6 Representative GVL tracked over time. . . . 69
2.7 Characteristics of the GVL life cycle. . . . 71
2.8 Effects of Y-27632 on GVL formation and disappearance over time and pressure. . . . 73
2.9 Effects of Y-27632 on GVL formation. . . . 74
2.10 Effects of Y-27632 on GVL disappearance. . . . 75

2.11 Effects of Y-27632 on GVL maximum size and GVL growth time. 75
2.12 Hypothetical GVL life cycle model. 78

3.1 Experimental set-up used for the basal-to-apical perfusion and perfusion-fixation of cultured SCE cell layers. 87
3.2 Effects transendothelial perfusion on SCE cell morphology, F-actin and vimentin architecture. 92
3.3 Comparison of cross-section and thickness in unperfused and perfused cell layers. 93
3.4 Confocal scanning Z-series through an individual perfused SCE cell. 94
3.5 Longitudinal cross-section through an individual perfused SCE cell. 95
3.6 Negative control for vimentin IF staining. 97
3.7 F-actin and vimentin organisation around GVLs. 98
3.8 F-actin and vimentin organisation at different Z-sections through a GVL (Part 1). 99
3.9 Transversal section through a GVL surrounded by an F-actin band. 100
3.10 F-actin and vimentin organisation at different Z-sections through a GVL (Part 2). 101
3.11 Transversal section through a GVL with F-actin band and a vimentin cage. 102
3.12 Effects Y-27632 on cell morphology, F-actin and vimentin architecture in unperfused and perfused cell layers. 104
3.13 Comparison of cross-section and thickness in unperfused and perfused cell layers treated with Y-27632. 105
3.14 Effects of Y-27632 treatment on the number of GVLs per nucleus, and on the proportion of GVLs with an F-actin band, a vimentin cage and both structures together. 106

4.1 Representative plot of measured ΔP and Q through the cells and filter, and of the corresponding R_p. 116
4.2 Representative ΔP and Q trace through the filter membrane alone, and corresponding R_F trace. 116
4.3 Time and pressure-dependent changes in R_p for all cell layers. 117
4.4 Comparison of R_{p_f} at 2 mmHg and at 6 mmHg. 118
4.5 Hypothetical scenarios of cell morphological changes accounting for time and pressure-dependent changes in R_p. 121
4.6 Model of parallel resistances for subconfluent cell layers cultured on a filter membrane. . 124
4.7 Predicted R_{p_S} for different filter resistances. 126

5.1 Timeline of conditioning experiment. 133
5.2 Long-term transendothelial pressure conditioning system. 134

5.3 Set-up and protocol for hydraulic resistivity measurements. 138
5.4 Method for cell thickness measurement. 141
5.5 R_p measurements at 4 mmHg in the basal-to-apical (B $\rightarrow$ A) and apical-to-basal (A $\rightarrow$ B) direction in SC68 and SC60. 143
5.6 Comparison of cell confluence, morphology and nuclei density. 145
5.7 F-actin distribution in static control SC60 cell layers. 146
5.8 F-actin distribution in conditioned SC60 cell layers. 147
5.9 Cell layer thickness and multicellular arrangement of static control and conditioned SC60 samples. 148
5.10 Hypothetical model comparing the existing flow pathways through conditioned and static control cell layers perfused in the basal-to-apical and apical-to-basal direction. 154
5.11 Filter clogging due to the presence of serum in the cell culture medium. 156
5.12 Representative plot of the change over time in the pressure drop across the conditioned samples. 156
5.13 Morphology and arrangement of SC68 cells in the static control and conditioned group. . 157
5.14 F-actin organisation in static control SC68 cell layers. 158
5.15 F-actin organisation in conditioned SC68 cell layers. 159
5.16 Brightfield images of semi-thin sections (0.5 μm) through conditioned and static control SC68 cell layers. 160

List of Tables

2.1 Summary of the number of cell layers perfused for each cell line and treatment group, and of the total number of identified GVLs and trackable GVLs. 70

3.1 Summary of nuclear counts, GVL counts, GVLs per nucleus and proportion of GVLs with an actin band, a vimentin cage or both features in each cell layer imaged. 106

4.1 Summary of time and pressure-dependent change in R_p across all samples perfused. . . . 117

4.2 Comparison of measured R_p with other published values. 122

4.3 Parameters used to estimate the effects of the filter resistance R_F on the computed R_{pS} . 126

4.4 Predicted change in cell confluence needed to account for the measured time-dependent change in R_p. 127

List of Abbreviations and Symbols

ϕ	Cell confluence
$\mathbf{R_F}$	Filter resistance
$\mathbf{R_p}$	hydraulic resistivity of the cell layer
ANOVA	Analysis of variance
DPBS	Dulbecco's phosphate buffered saline
ECM	Extracellular matrix
FBS	Foetal bovine serum
GV	Giant vacuole
GVL	Giant vacuole-like structure (formed in cultured SCE cells)
IF	Intermediate filaments
IOP	Intraocular pressure
JCT	Juxtacanalicular tissue
MIP	Maximum intensity projection
POAG	Primary open-angle glaucoma
ROCK	Rho-kinase
ROI	Region of interest
SC	Schlemm's canal
SCE	Schlemm's canal endothelial
SD	Standard deviation
TM	Trabecular meshwork

1

Introduction

> "Blindness is enveloping. It's beyond belief to step outside and see so little, just a milky haze. Indoors, a smothering dark. It means that you can't shed a mood of loneliness with a brisk walk down the street because you might trip, fall and break something. Nor will you see a passing friend, the sight of whom could be as cheery as an actual conversation. Sights, like sounds, randomly evoke a surge of memories ordinarily inaccessible that lighten and brighten the day."
>
> *Extract from essay 'Feeling my way through blindness' written by Edward Hoagland for the New York Times [1].*

According to a study carried out in 2016, a majority of people regard visual impairment and blindness as the worst ailment that could happen to them [2]. Out of the 2044 people surveyed, a majority of respondents expressed their concern about the impact that vision-related conditions would have on their quality of life and independence.

The leading pathological cause of irreversible blindness worldwide is primary open-angle glaucoma (POAG) [3]. POAG is chronic and incurable eye disease that currently affects around 3% of the world population [4]. Due to population growth and ageing, the number of individuals with POAG is predicted to increase by over 70% in the next couple of decades [4]. POAG causes progressive damage to the optic nerve, and an associated loss of visual field. While POAG is a multifactorial disease, elevated intra-ocular pressure (IOP) is the main risk factor for disease development and progression. Importantly, IOP reduction is the only proven method to slow down the progression of the disease [5, 6] *.

IOP is controlled by the turnover of aqueous humour, a clear fluid that bathes and nourishes the avascular tissues of the anterior segment of the eye (Figure 1.1 and Figure 1.2). Aqueous humour is secreted into the posterior chamber by the ciliary processes, flows towards the front of the eye into the anterior chamber through the pupil, and mainly drains back into the vasculature through the conventional outflow pathway found at the angle formed between the iris root and the cornea. The conventional outflow pathway includes a series of mesh-like tissues adjoined to a fluid-collecting canal, known as Schlemm's canal (SC), and downstream branches of smaller collecting vessels that lead to the venous system.

The flow of aqueous humour through the resistive tissues that comprise the conventional outflow pathway is what maintains IOP. In the human eye, the resistance generated along the conventional pathway results in a pressure drop of nearly 5 mmHg [8] between the anterior chamber and the venous system. In POAG, the outflow resistance generated along the conventional outflow pathway becomes

* including in normo-tensive glaucoma, in which IOP is within normal ranges [7].

elevated and leads to increased IOP [9].

The bulk of outflow resistance is generated in the vicinity of the continuous endothelial-lining of SC and its underlying matrix [8–10]. Of significance, the source of elevated outflow resistance in POAG is also attributed to the same tissues [11]. The mechanisms by which outflow resistance is generated in the healthy eye, and why it becomes elevated in glaucoma are however not known [12, 13]. The lack of a mechanistic understanding of outflow resistance elevation in POAG has stymied the development of effective sight-preserving glaucoma therapies with long-lasting IOP reduction effects.

Regardless of the exact mechanism of outflow resistance generation, it is key to recognise that almost all of aqueous humour must somehow cross SC endothelium to enter the canal lumen. It is now generally accepted that aqueous humour crosses SC endothelium through transendothelial micron-sized pores (Figure 1.2, right panel). Transendothelial pores are often associated with large cellular outpouchings known as giant vacuoles (GVs) and together GVs and pores form channels providing direct openings into the lumen of SC through which aqueous humour can flow. Because these pores are essential for the transport of aqueous humour across an otherwise continuous layer of cells, they are likely important modulators of outflow resistance. Importantly, in POAG the number of pores opening into the lumen of SC is reduced [14, 15], and it has been hypothesised that decreased pore density may be a major contributing factor to the pathological increase in outflow resistance.

While the exact mechanisms involved in GV and pore formation are not known, these structures appear to be largely influenced by the biomechanical environment of SC endothelium. The interaction between SC endothelium and its mechanical environment is therefore likely important for outflow resistance generation and IOP regulation. The overarching goal of this thesis is to better understand the relationship between the transport function of SC endothelium and its biomechanical environment.

In the remainder of this chapter we will review the current literature and background regarding the morphology of the SC endothelium and how it relates to its biomechanical environment and transport function.

1.1 Morphology of the conventional outflow pathway

Aqueous humour drains out of the anterior chamber of the eye through one of two pathways located at the angle formed by the iris root and the cornea and extending circumferentially around the iris (Figure 1.2). The conventional outflow pathway carries the majority of aqueous humour outflow, and consists of the trabecular meshwork (TM), SC and the collector vessels leading to the episcleral veins. The unconventional or uveoscleral outflow pathway only accounts for less than 35% of total outflow in the human eye [18], and likely contributes little to IOP regulation in the normal human eye. The unconventional outflow pathway is nonetheless important for glaucoma drug therapies involving prostaglandin analogues,

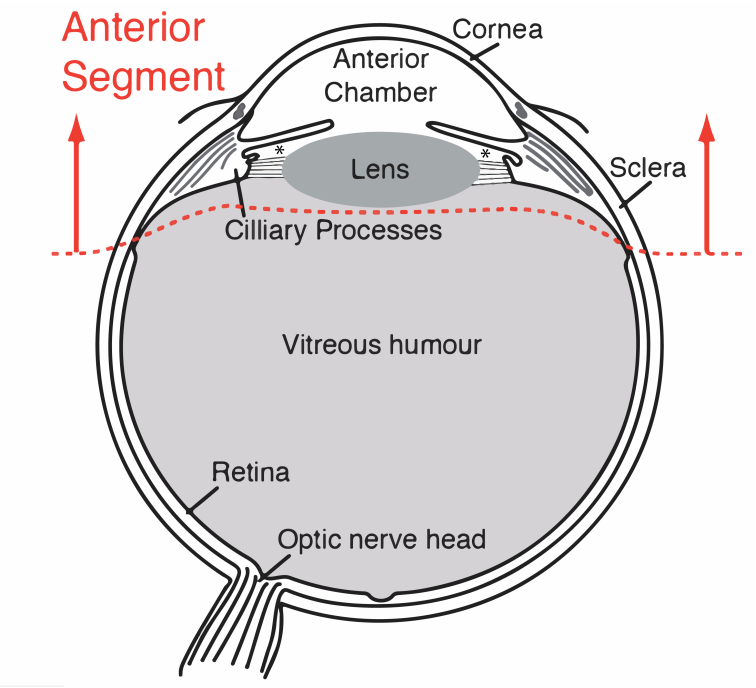


Figure 1.1: **Schematic of general anatomy of the human eye.** The asterisks indicate the posterior chamber. The white region, consisting of the anterior and posterior chamber, is filled with aqueous humour. Adapted from [16].

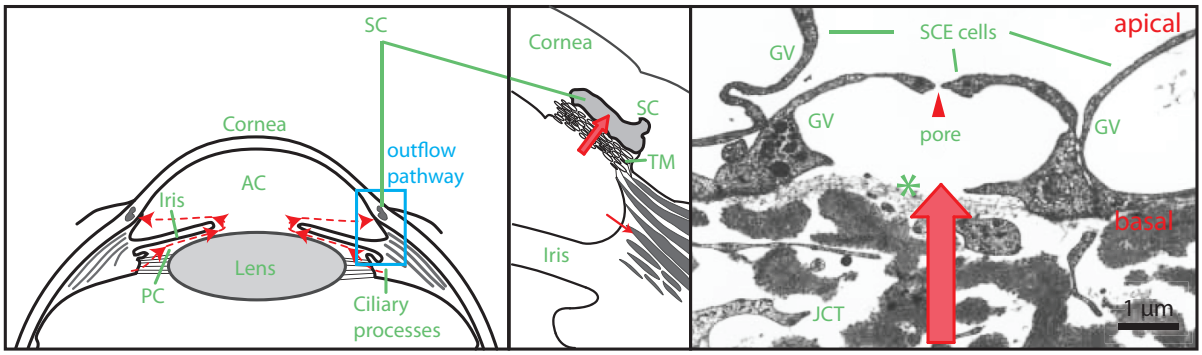


Figure 1.2: **Aqueous humour flow pathway in the human eye.** *(Left)*: Schematic of the anterior segment of the eye and of the flow pathway of aqueous humour (red arrows). AC: anterior chamber; PC: posterior chamber; SC: Schlemm's canal. *(Middle)*: Schematic of the irido-corneal angle, and of the conventional outflow pathway (large red arrow) and uveoscleral outflow pathway (thin red arrow). TM: trabecular meshwork. *(Right)*: Transmission electron microscopy of section through endothelial cells in SC endothelium. Aqueous humour enters the lumen of SC by crossing the SC endothelium in the basal-to-apical direction (red arrow) flowing through transendothelial channels composed of GVs and pores. The asterisk points to the mouth or "meshwork" pore of the GV, which corresponds to the area where the cell has detached from its basement membrane likely during the initiation of GV formation. JCT: Juxtacanalicular tissue. Figure modified from [17] with permission.

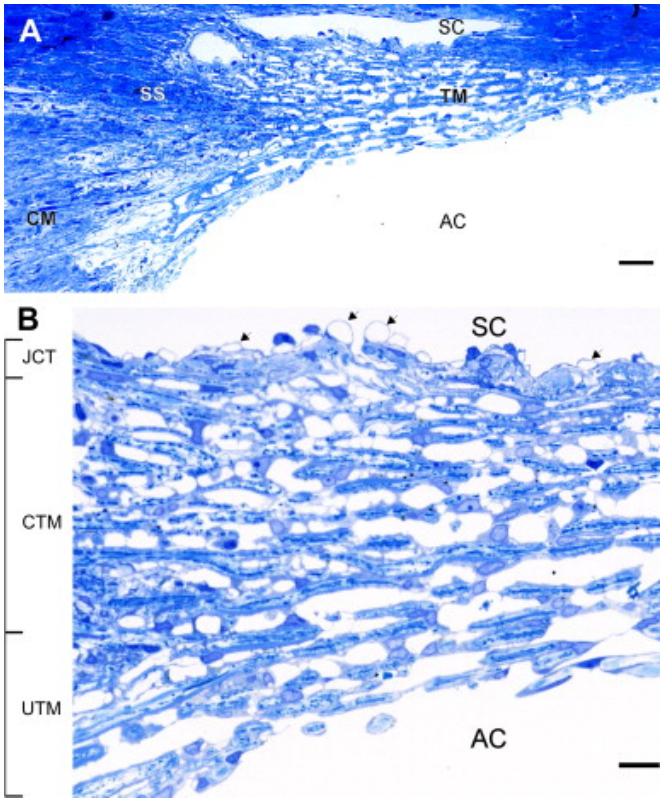


Figure 1.3: **Light micrograph of a cross-section of the conventional outflow pathway.** AC: Anterior chamber; CM: Ciliary muscle; SS: Scleral spur; TM: Trabecular meshwork; SC: Schlemm's canal; UVM: Uveoscleral meshwork; CTM: Corneoscleral meshwork; JCT: Juxtacanalicular tissue. The SC endothelium is easily recognisable because of the presence of cellular outpouchings known as GVs (black arrows in panel B). Figure reproduced from [21] with permission.

as these drugs are thought to lower IOP by increasing outflow along the unconventional pathway [19].

Along the conventional outflow pathway aqueous humour first flows through the TM (Figure 1.3), which includes the superficial uveal meshwork, the deeper corneoscleral meshwork, and the juxtacanalicular connective tissue (JCT) adjacent to the endothelium of SC. The openings in the TM are large, and decrease progressively in size as the deeper aspects of the tissue are reached, with a structure resembling that of a well-designed filter [20]. After flowing through the TM, aqueous humour enters SC by crossing the inner wall endothelium of SC in the "backwards" basal-to-apical direction flowing through transendothelial pores (Figure 1.2, right panel). Once in Schlemm's canal, aqueous humour flows circumferentially through the canal lumen until it reaches one of the 30 collector channels, leading to the collector vessels and finally to the downstream episcleral veins.

The flow of aqueous humour through the conventional pathway occurs at a rate of approximately 2 μl/min [8]. The pressure drop occurring across the entire conventional outflow pathway is nearly 5 mmHg [8] and is largely maintained by the hydraulic resistance generated in the vicinity of the inner wall endothelium of Schlemm's canal, its basement membrane and the JCT [10]. Current knowledge considers that outflow resistance is generated by the interaction between the SC endothelium and the

JCT [12, 13, 22]. Because transendothelial pores influence the rate and the pattern of flow through the underlying JCT, it is currently thought that they serve as important modulators of outflow resistance generation [12, 13].

1.2 Functional morphology of SC endothelium

SC is an endothelial-lined vessel that encircles the root of the iris, and that has the appearance of a highly elongated ellipse (Figure 1.3, panel A). Aqueous humour enters the lumen of SC by crossing the inner wall endothelium of Schlemm's canal in the "backwards" basal-to-apical direction. The endothelial cells of the inner wall of Schlemm's canal form a continuous monolayer joined to one another by tight junctions [23], and the monolayer lies on a discontinuous basement membrane which contacts the JCT. Overall, the total surface area of the inner wall endothelium is approximately 11 mm^2 [19]. En face images acquired by scanning electron microscopy were used to estimate that approximately 23,000 endothelial cells make up the inner wall of SC [20]. The endothelium cells are long and spindle-shaped, with a length of 100-150 μm and a width of 4-8 μm [20], with a projected area between 408 μm^2 [24] and 480 μm^2 [20], and they are generally oriented with their length along the axis of the canal [20].

The endothelium of SC exhibits similarities with both the blood endothelial cells and the lymphatic endothelial cells [25]. Schlemm's canal endothelial (SCE) cells express markers that are also found in blood endothelial cells such as PECAM-1, VE-Cadherin [26] and von Willebrand factor [27]. From a structural perspective, on the one hand the cells of the inner wall endothelium of SC form a continuous monolayer and are joined to one another by tight junctions [23] as observed in the endothelia of blood vessel. On the other hand, the inner wall endothelium lies on a discontinuous basement membrane [28–30] as characteristically observed in lymphatic endothelia. The discontinuity of the basement of SC endothelium and lymphatic vessel endothelia may be associated to the basal-to-apical transendothelial flow experienced by both endothelia.

When visualised by light-microscopy, the inner wall endothelium of Schlemm's canal is easily recognisable because it exhibits large cellular outpouchings that bulge into the lumen of SC (black arrows in Figure 1.3, panel B) known as GVs. Another peculiarity of the inner wall endothelium is the presence of micron-sized transendothelial pores [31]. Due to their micron-scale size, pores are not visible by light-microscopy and were first imaged by Holmberg in 1959 [31] in the advent of electron microscopy (Figure 1.2, right panel). Pores are often associated to GVs, and pore formation is thought to be linked to cell thinning caused by GV formation [32]. It is generally accepted that aqueous humour crosses the inner wall endothelium through transendothelial pores. Importantly, in glaucoma, pore density is significantly reduced [14, 15] and this may be linked to outflow resistance increase.

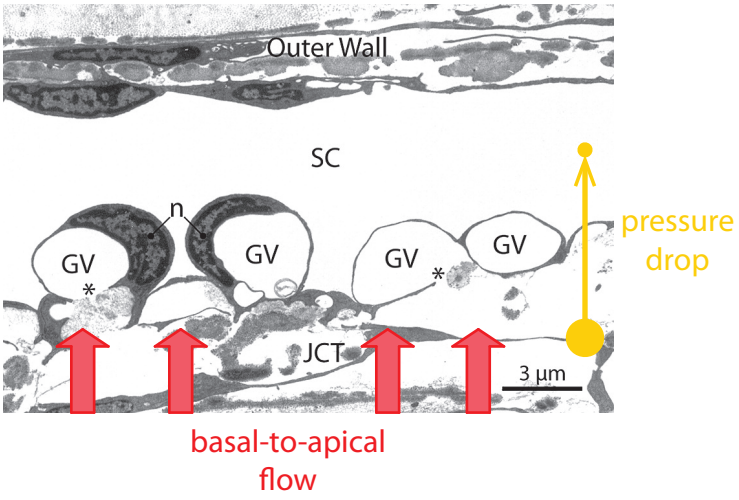


Figure 1.4: **Transmission electron micrograph of a cross-section through SC endothelium in the human eye.** Aqueous humour crosses the inner wall endothelium in the basal-to-apical direction. The pressure drop across the inner wall endothelium drives the formation of cellular outpouchings known as GVs. GVs tend to have a signet ring appearance as they deform and push the nucleus to the side (n: nucleus). The asterisks point to the mouth or meshwork pore of two GVs, which corresponds to the area where the cell has detached from its basement membrane likely during the initiation of GV formation. Note that on a single section the mouth of only two GVs are seen. Image modified from [33] with permision.

1.2.1 Morphology of GVs

The structure of GVs was first described by Garron in 1958 using transmission electron microscopy [28]. Given the appearance of GVs in single tissue sections, Garron compared the structure of GVs to that of a signet ring: the entire perimeter of the GV cavity is surrounded by a continuous cellular lining and the nucleus usually bulges to one side (Figure 1.4). While to Garron the GV cavity appeared to be fully surrounded by a cellular lining, later serial sectioning studies of the inner wall endothelium revealed that the GV cavity is in fact entirely extracellular as most, if not all, GVs have a basal opening, known as meshwork pore or GV mouth, to the JCT (asterisk Figure 1.2, right panel and Figure 1.4).

Given their structure, GVs are characterised as enlarged invaginations of the basal SCE cell surface that bulge into the lumen of SC, leaving an aqueous-filled cavity between the basal cell membrane and the underlying JCT (Figure 1.5). The structure of GVs relate to their origin: GVs result from the basal-to-apical directed pressure drop across the inner wall endothelium of SC, which drives aqueous humour flow and tends to push cells off their basement membrane. GVs are not seen in enucleated eyes fixed at zero pressure [34, 35], and GVs tend to be more numerous near the collector channels of SC, where the pressure drop is largest [36].

The geometry of GVs can be simplified to that of dome-like structure stretched out along the long axis of the cell, comparable to a prolate spheroid. In non-human primates at physiological IOP (around 15 mmHg), the width and length of GVs have been reported to be 2-8 μm and 5-15 μm

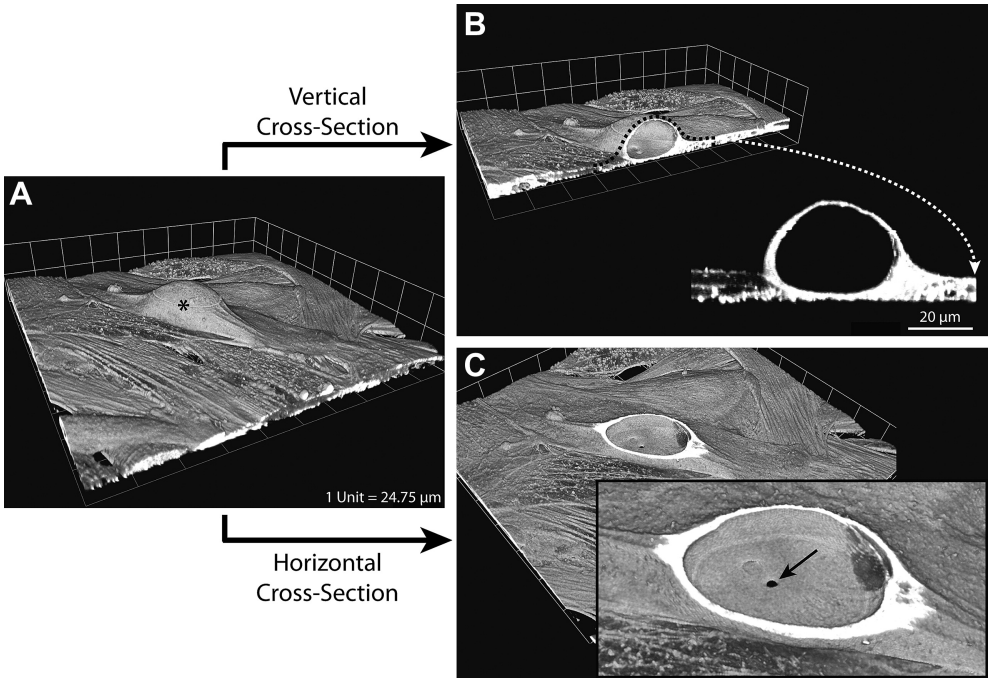


Figure 1.5: **Three-dimensional confocal reconstruction of a GV-like structure (GVL) formed.** The GVL was formed in response of the basal-to-apical directed perfusion of cultured SCE cells. The SCE cells were perfusion fixed with gluteraldehyde and fluorescently labelled for F-actin. The arrow points to the meshwork pore or mouth of the GV. Figure reproduced from [33] with permission.

respectively [30, 37]. Using these dimensions and approximating the GV cavity to a prolate spheroid [†], one can estimate that the volume of the GV cavity is approximately 16 μm^3. Using three-dimensional reconstruction of serial-block face electron microscopy images of human tissue, Lai et al. [38] more recently reported that GV volume is approximately 145 μm^3 at physiological IOP. As pointed out by Lai et al., the GV volume based on previously published serial section images is likely an underestimation of their true size as using serial sections it is difficult to measure GVs at the exact location where they are largest.

While GVs are large enough to be visible by light microscopy, the finer details of their structure can only be appreciated using transmission electron microscopy (Figure 1.6 and Figure 1.7). Importantly, the cellular lining surrounding the cavity of GVs can be very thin around parts of the GV such that the cytoplasm in these cells is very attenuated and the basal and apical surface of the cell are only a few tens of nanometres away from one another [29, 30, 39]. GVs are often formed in the perinuclear region resulting in significant nuclear deformation and indentations [30]. Multiple GVs can occur in the same cell; neighbouring GV cavities are separated by a thin cellular lining, and sometimes the cavities intercommunicate via openings [30, 37, 40].

Grierson and Lee [37] used serial sectioning light microscopy imaging to quantify GV density in rhesus monkey, and reported an average of 2284 GVs per canal length (GVs/mm^{-1}). Assuming that

[†]The volume of a prolate spheroid is given by $V = \frac{4}{3}R_e^2 R_p$ where R_e and R_p are the equatorial and polar radii respectively.

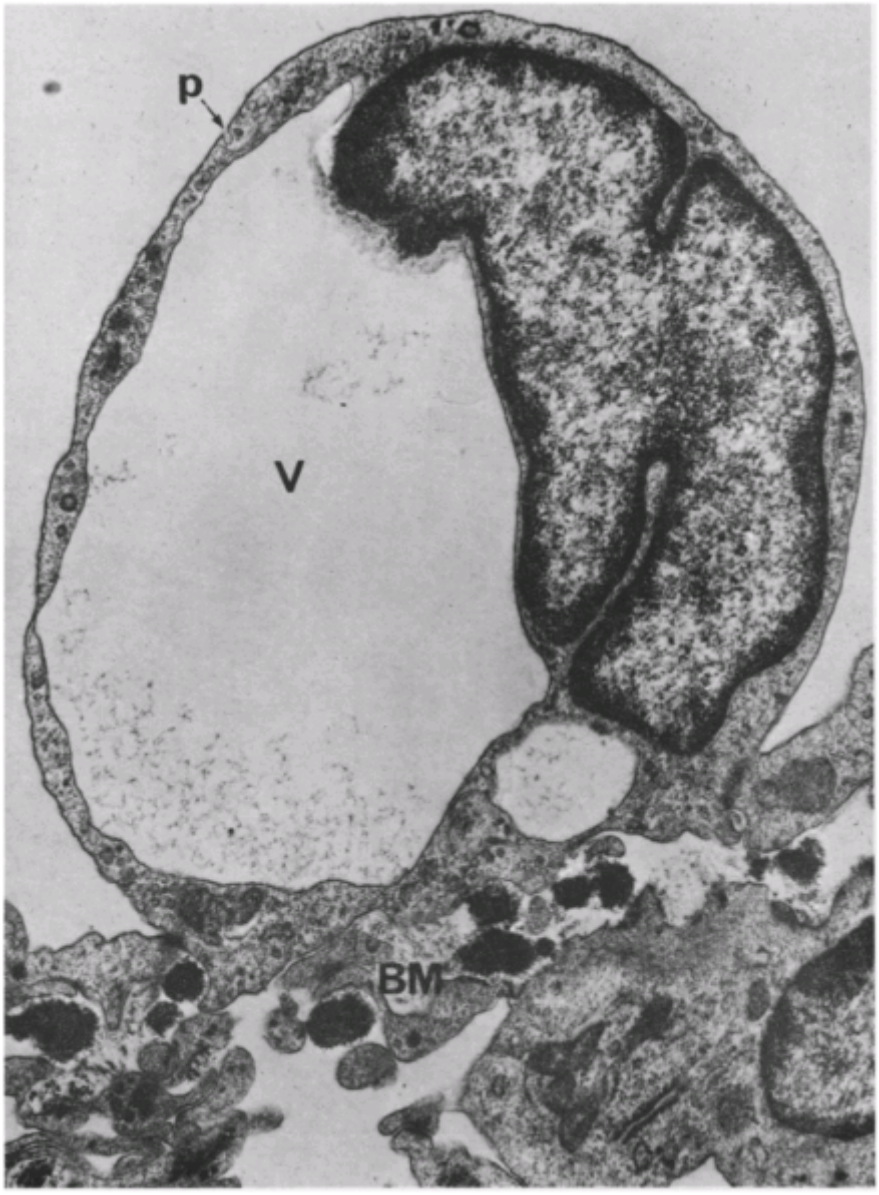


Figure 1.6: **Transmission electron micrograph of the the fine structure of a GV (part 1).** In this section, the GV (V) appears to be entirely lined by the cell. The cell body lining the GV cavity is highly attenuated, and in some areas the basal and apical membrane are in close apposition (less than 100 nm separation). Note the existence of caveolae, also known as pinocytotic vesicles (p), which may act as membrane storage for further GV growth, or may facilitate membrane fusion between the basal and apical side of the cell. The nucleus is pushed to one side of the cell, and is highly deformed. (Magnification: ×27,456) Figure reproduced from [39] with permission.

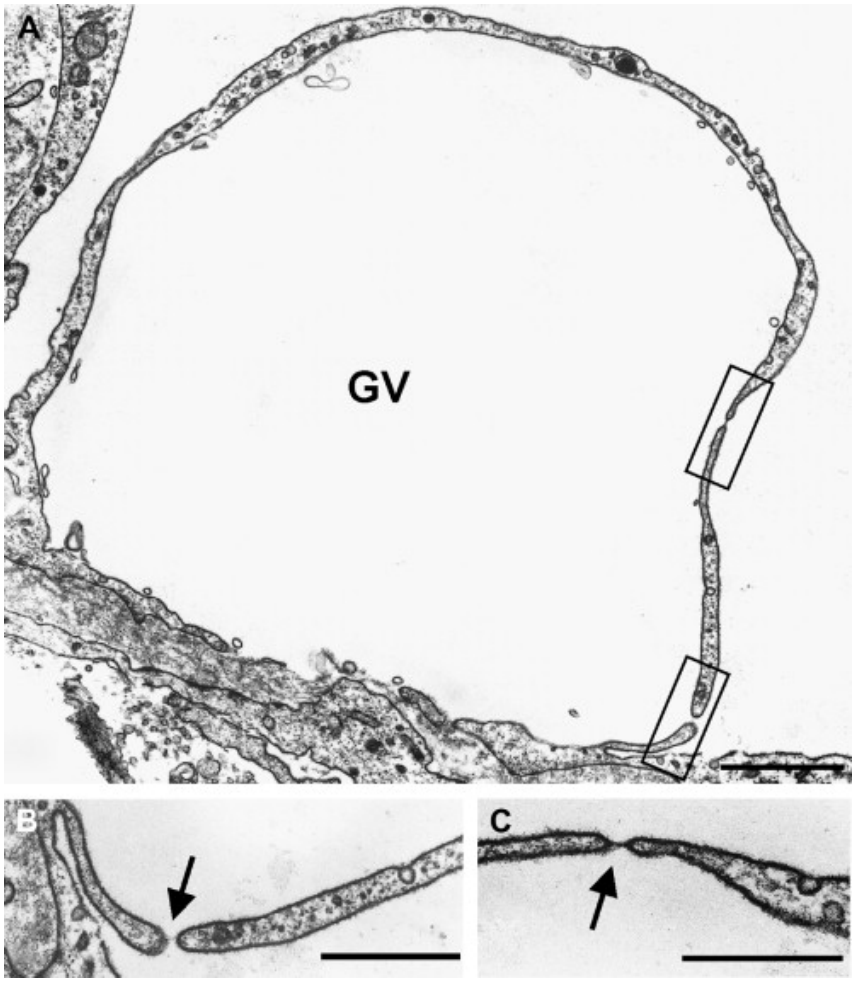


Figure 1.7: **Transmission electron micrograph of the the fine structure of a GV (part 2).** The cell lining surrounding the GV cavity is highly attenuated. Note the presence of numerous vesicles in the cell cytoplasm and caveolae-like structure on the apical membrane of the cell. *(Left inset)* The basal and apical membrane of the cell have fused forming a transendothelial pore on the side of the GV. *(Right inset)* A fenestrae-like opening with a diaphragm known as a minipore is also observed in the wall of the GV. Figure reproduced from [21] with permission.

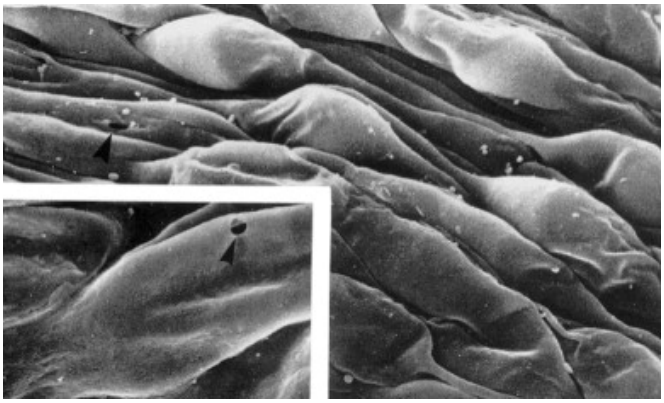


Figure 1.8: **Scanning electron micrograph of the morphology of the inner wall endothelium of SC as seen from the canal lumen.** A cell in the endothelium exhibits a transendothelial pore (arrowhead). *(Inset)* high magnification image of transendothelial pore. Image reproduced from [14] and figure arrangement reproduced from [13], both with permission.

the GV density in human is similar to that in monkey, and assuming an average cell area of 450 μm^2 [20, 24], predicts that there are around 1.5 GV per cell in the human inner wall endothelium at physiological pressure [41].

Some, but not all, GVs have a transendothelial pores on their apical surface, creating an opening into the lumen of SC (Figure 1.7). Together, GVs and associated transendothelial pores are thought to provide a route for aqueous humour outflow across the inner wall endothelium. Interestingly, these pores are often found in areas where the cell wall is thinnest around the GV cavity; this may be related to the formation mechanism of pores, which requires the fusion of the basal and apical membranes of the cells.

1.2.2 Morphology of pores

Pores in the inner wall endothelium of SC are elliptically shaped openings that are 1 μm in diameter on average [14, 20, 42, 43] that pass from the basal side to the apical side of the cell side (Figure 1.8). Transendothelial pores are not rips or tears in the SCE cells as they are lined by a continuous cell membrane. Pores are generally associated to GVs, however a proportion of pores is also found along flat, non-vacuolated regions of the inner wall endothelium [30].

There are two types of pores: intra-cellular pores (I-pores) and border pores (B-pores) [42] (Figure 1.9). I-pores are thought to result from the fusion the membrane on the basal and apical surface of the cell, and B-pores are thought to result from the local disassembly of cell-cell junctions. It is generally thought that there are between 1.4 to 4 times more B-pores than I-pores [42, 44] in the inner wall endothelium. Size-wise, B-pores are on average larger than 1 μm whereas I-pores are on average just below 1 μm [42, 45].

Pore density has been reported to approximately range between 1000-2000 pores/mm^2 [20, 42–44, 46]. However, the exact pore density is not known with certainty as studies have shown that

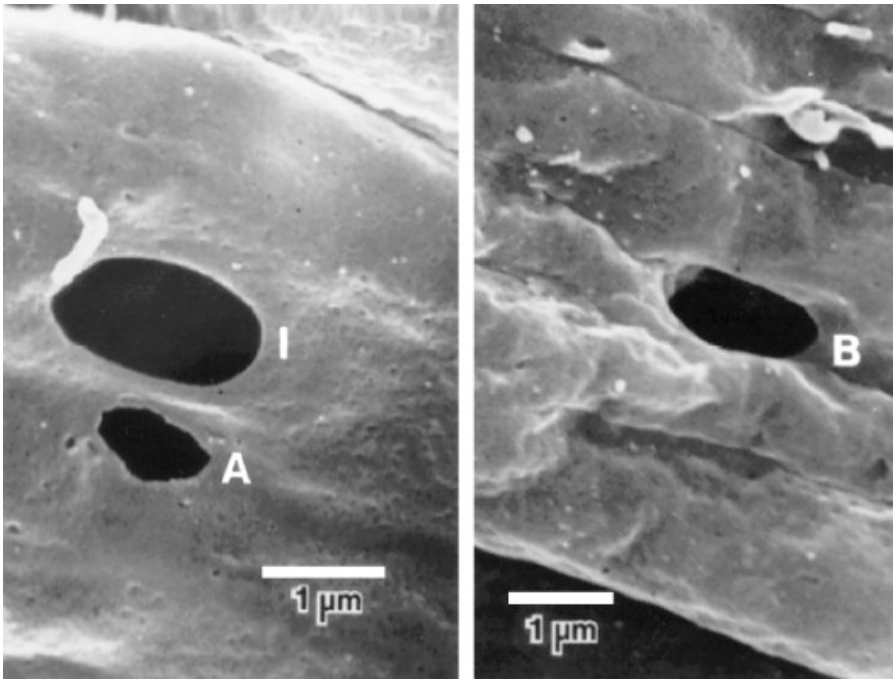


Figure 1.9: **Scanning electron micrographs of transendothelial pores in SC endothelium.** *(Left)* Intracellular pore (I) and artefactual pore caused by a tear in cell (A). *(Right)* Border pore (B). Figure reproduced from [42] with permission.

the process of tissue fixation leads to an artefactual increase in pore density [15, 42, 46]. Based on the correlation found between the volume of fixative perfused and pore density, Johnson et al. extrapolated a zero-fixative pore density of 835 pores/mm^2 [15]. More recently, to avoid artefactual pore formation Braakman et al. [44] used a two-step method zero-temperature cooling followed by immersion in ice cold fixative, and found an average pore density of 2181 pores/mm^2. It is likely that the true pore density lies somewhere in between these two values.

Assuming that the pore density is 1500 pores/mm^2 (taken as a midpoint between the two pore densities from Johnson [15] and Braakman [44] discussed in the previous paragraph), and assuming a cell area of 450 μm^2 (taken as the midpoint between the two published values mentioned above [20, 24]), one can estimate that there is close to 1 pore per cell of the inner wall endothelium of SC.

While accounting for the artefactual increase of pores during perfusion-fixation, Johnson et al. [15] showed that there is a five-fold reduction in pore density in POAG eyes compared to in healthy eyes, confirming an earlier report [14]. This finding suggests that inner wall cells may have an impaired ability to forming pores, and this may contribute to outflow resistance increase in POAG.

1.2.3 Aqueous humour transport across the inner wall endothelium of SC

While the pore density in the inner wall endothelium is still not exactly known, there is strong evidence that aqueous humour crosses the endothelium through these pores. First, microspheres of 200-500 nm in diameter can flow freely through the conventional outflow pathway, and microspheres of up to 1 μm are able to cross the inner wall endothelium [30, 47]. Second, the inner wall endothelium of Schlemm's canal appears to have the lowest hydraulic resistivity of any endothelium in the body. Johnson and Erickson [19] estimated that the hydraulic resistivity of the inner wall endothelium would be around 0.3 mmHg.min.cm^2.μl^{-1} assuming that all of the outflow resistance was attributable to the inner wall endothelium (which is almost definitely an overestimation) and assuming an inner wall filtration area of 11 mm^2. Note that this is an upper bound estimate of hydraulic resistivity of the inner wall endothelium because if the pressure drop across the inner wall is lower, then this value would be even smaller. Furthermore, the upper bound of the hydraulic resistivity of the inner wall endothelium is at least 10-fold smaller than the hydraulic resistivity of fenestrated vascular endothelia; this strongly suggests that fluid crosses the inner wall endothelium through specialised channels, namely transendothelial pores, that are not present in other endothelia.

As pointed out by Johnson [12], the combined arguments presented above rule out the possibility that aqueous humour pass through gaps between the tight junction strands of the cells of the inner wall. Gaps between tight junctions strands are only nanometres wide [23, 48, 49], and Raviola and Raviola [48] estimated that only negligible flow could occur through these gaps. In addition, in vascular vessels with tight junctions it is well known that macromolecules larger than a couple tens of nanometres are largely precluded from passing through intact tight junctions [12].

Part of aqueous humour must cross the inner wall endothelium through the channels composed of the GV mouth, the GV cavity and the luminal transendothelial pore that opens the GV cavity to the lumen of SC [29, 31, 50–52] (Figure 1.10). This is corroborated by the fact that microspheres are observed within the cavities of GVs, which also confirms that GV cavities are extracellular [30, 53]. The proportion of GVs considered to be true channels, with both a basal and an apical opening, is not known with certainty. This is likely due both to the technical difficulty to image the combination of pores and GVs over a large area of the inner wall endothelium, and to the uncertainty around artefactual pores (and perhaps even GVs) formed during perfusion-fixation [15, 46]. Earlier studies by Kayes [51] and Tripathi [29] using serial sectioning transmission electron microscopy reported that only 1 to 2% of GVs were true transendothelial channels; but both of these studies reported that many GVs did not have a basal opening to the JCT, which was challenged by a later study by Inomata et al. [30] that found that all GVs

had a basal opening. Using similar techniques to those of Kayes [51] and Tripathi [29], a later study by Grierson and Lee [54] found that between 8 to 14% of GVs were true transendothelial channels.

For comparison with these experimental quantification, an estimation of the expected number of true transendothelial channels based on the pore density (1500 pores/mm^2), cell area (450 μm^2), and the estimated number of GVs per cell (1.5 GV per cell), predicts that there are 0.5 pores per GV. The discrepancy between this theoretical estimation and the experimental findings by Grierson and Lee suggest that the number of GVs that constitute true transendothelial channels may be underestimated because of sampling errors, and that true number of channels is likely somewhere between the theoretical and experimental estimates. We note here that the images of fixed tissue only offer a snapshot in time of the number of open GVs and pores, and as we will discuss further in Section 1.3.6, it is possible that GVs and pores may in fact be dynamic structures that open and close, such that their true density may not be well captured during tissue fixation.

1.2.4 Outflow resistance generation

The flow resistance generated by the pores of the inner wall endothelium was first considered by Bill and Svedbergh [20]. They found that given the pore density and pore size distribution, the inner wall endothelium could only account for at most 10% of total outflow resistance. Their conclusion was confirmed by later studies [55–57].

The outcome of these studies [20, 55–57] appear to rule out the functional importance of the inner wall endothelium in the generation of outflow resistance. However, this conclusion conflicts with a number of other experimental findings. Specifically, treatment with pharmacologic agents that caused disruption the continuity of the inner wall endothelium (e.g. the chelating agent EDTA [58] and the proteolytic enzyme α-chymotrypsin [59]) was associated with a decrease in outflow resistance that was greater than the resistance of the inner wall endothelium estimated by Bill and Svedbergh [20]. Similar outflow resistance results were observed with pharmacologic treatment associated with the detachment of the JCT and the inner wall endothelium [60], and of increased paracellular pore density [43].

Johnson et al. [61] proposed a model, known as the funnelling effect, that accounts for the hydrodynamic interaction between the JCT and the pores in the inner wall endothelium, presumably reconciling the findings of Bill and Svedbergh [20] and Hamanaka and Bill [58] (Figure 1.11). In this scenario, while the pores contribute a negligible amount to flow resistance, they force the aqueous humour to funnel through the regions of the JCT closest to the pores, reducing the effective filtration area within the JCT and thus increasing the resistance generated within this tissue. The funnelling model therefore predicts that pore density acts as a modulator of outflow resistance. The presumable funnelling effect could have important implications in glaucomatous eyes, where pore density is known to be

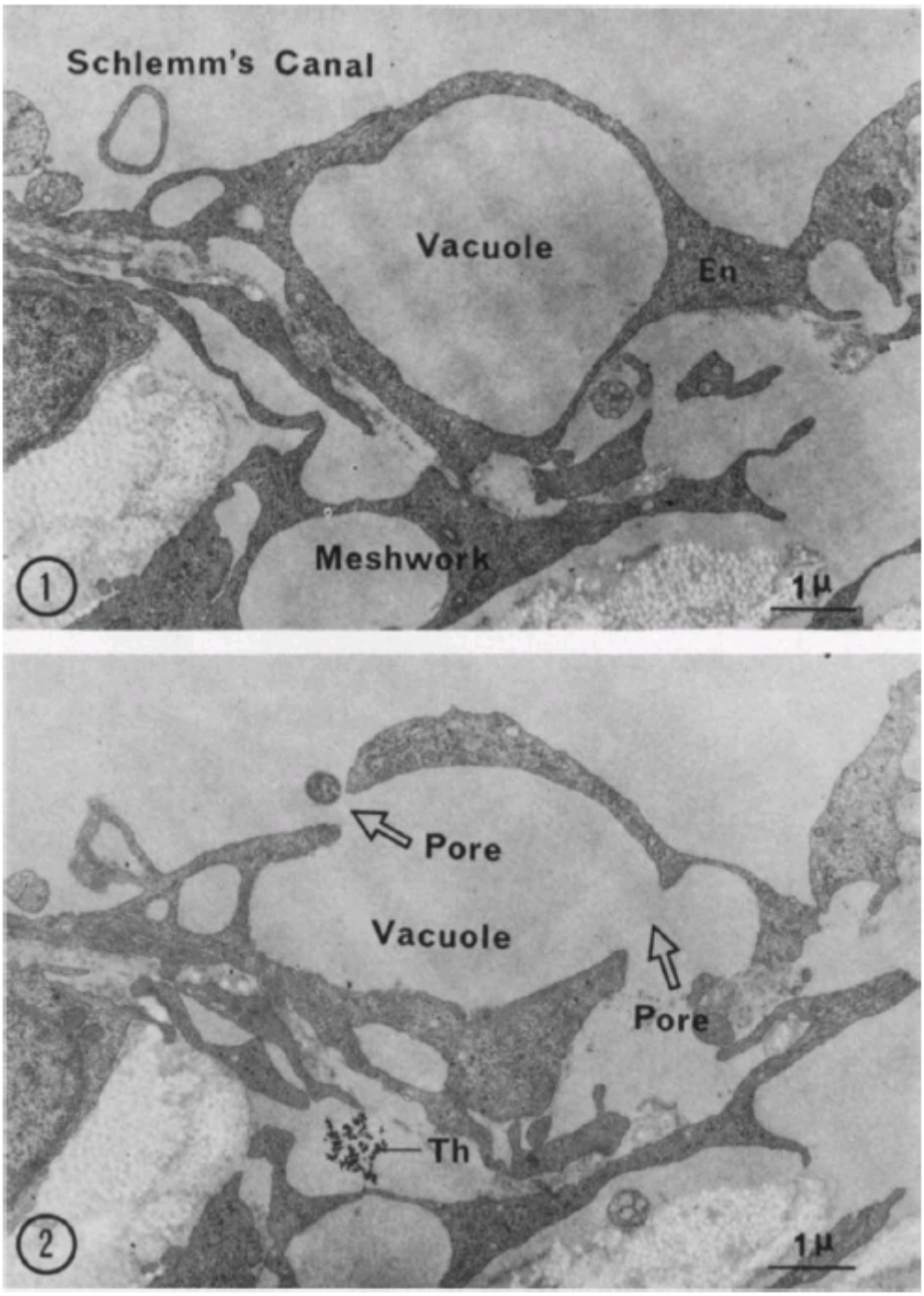


Figure 1.10: **Transmission electron serial section micrographs of a transendothelial channel formed by a GV and a pore.** *(Top)* In an individual section, the GV appears to be entirely intracytoplasmic, however in a neighbouring section *(Bottom)*, the GV exhibits both a meshwork pore and a apical pore opening into the lumen of SC. This illustrates that GVs serve as a transendothelial flow channels (arrows). Figure reproduced from [30] with permission.

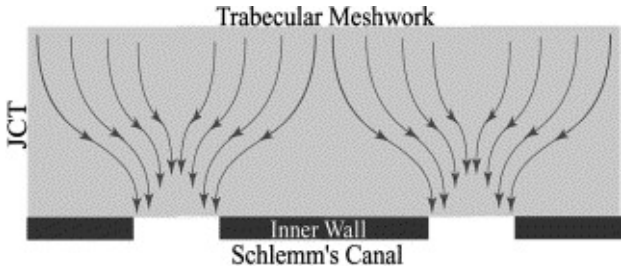


Figure 1.11: **Schematic representation of the aqueous flow patterns through the JCT and SC endothelium in the funnelling model.** The pores in the inner wall endothelium are sparse enough that they force the aqueous humour to funnel through the regions of the JCT closest to the pores, reducing the effective filtration area within the JCT and thus increasing the resistance generated within this tissue. Figure reproduced from [62] with permission.

reduced. Although several studies are consistent with the funnelling model [62, 63], it has not yet been proven, and the contribution of pores to outflow resistance generation is still not definitively known.

Regardless of the exact mechanism of outflow resistance generation, all of the aqueous humour outflow must go cross the inner wall endothelium of SC. This endothelium is subjected to a particular biomechanical environment due to the basal-to-apical direction of aqueous humour flow and of transendothelial pressure drop, and the resulting biomechanical stresses likely influences its barrier properties.

1.3 Mechanobiology of the inner wall endothelium

1.3.1 Biomechanical environment of SC endothelium

Unlike endothelial cells in the blood vasculature, SCE cells are subjected to a "backwards" directed flow driven by a basal-to-apical directed pressure drop. The pressure drop that occurs across the inner wall endothelium exerts forces on the endothelial cells. Due to the direction of the pressure drop, the resulting forces tend to push the SCE cells off their basement membrane, driving GV formation [34, 35] and causing large strains in the cells [41].

The exact magnitude of the pressure drop that occurs across the inner wall endothelium depends on the contribution of the endothelium to total outflow resistance, which is unknown. Previous investigators have nonetheless estimated that the pressure drop across the inner wall endothelium is at least close to 1 mmHg in the normal eye, if one assumes that the inner wall endothelium only accounts for 10% of the total outflow resistance [64]. Taking the cell area to be 450 μm^2, Overby [41] estimated that at normal IOP each endothelial cell of the inner wall is at least exposed to a transversal force of approximately 60 nN, with higher forces expected at elevated IOP. These forces are significant on the scale of cells; by analogy, forces exerted at focal adhesions during cell contraction are typically on the order of 10 nN [65, 66].

Regardless of the exact magnitude of the transendothelial pressure drop and force applied to the endothelial cells, it is well-documented that changes in the total pressure drop across the entire conventional outflow pathway significantly affects the morphology of the inner wall endothelium, and particularly on GVs.

1.3.2 Influence of pressure drop on GVs and strain in SCE cells

Johnstone and Grant [34] were the first to describe the effects of changes in IOP on the morphology of the conventional outflow pathway. When IOP is increased above episcleral venous pressure, the inner wall endothelium progressively becomes distended and distorted, with larger and more numerous GVs, the underlying JCT expands, and the SC progressively collapses as the inner wall displaces towards the outer wall (Figure 1.12). Johnstone and Grant [34] made two other interesting observations: (i) When IOP is lowered down to episcleral pressure (corresponding to a zero pressure drop across the conventional outflow pathway), the inner wall endothelium is flat with very few vacuoles and the underlying JCT is more densely packed, (ii) No "reverse" GVs are observed when IOP is lowered below episcleral pressure (corresponding to a reverse apical-to-basal pressure drop across the outflow pathway). Later studies confirmed their observations [37, 40, 52, 67, 68]. Based on these findings, it was hypothesised that the inner wall endothelium functions as a pressure-sensitive one-way valve that serves as a blood-aqueous barrier ([34]): the valve opens when IOP is higher than venous pressure to allow for the flow of aqueous humour and particulates (e.g. blood cells and pigments) into the SC, and the valve closes when IOP falls below venous pressure preventing blood coming from the downstream veins from entering the anterior segment of the eye.

Another important conclusion that can be drawn from Johnstone and Grant's original study [34] is that GV size and GV density are pressure-dependent. Grierson and Lee [37] further quantified the changes in GV dimension and numbers as a function of IOP in rhesus monkey eyes fixed *in vivo* and imaged using serial sectioning light microscopy. They found that when IOP was increased from 15 to 30 mmHg the GV width increased by 100% and GV length increased by 40%, and that GV density increased by 2.5-fold [37].

Using the GV dimensions and densities at different IOP levels reported by Grierson and Lee [37], Overby [41] estimated the strain experienced by SCE cells during GV formation. In this estimation, the GV were considered as either a complete or a half a prolate spheroid (i.e. a spheroid elongated along its polar axis), and the possible existence of multiple GVs within the same cell was accounted for. At physiological changes in IOP between 15 and 22 mmHg, Overby [41] reported that the estimated strains experienced by SCE cells are between 6 to 84%. These estimates are consistent with other previously published values [69]. Such cellular strains are significant given that a similar magnitude of cellular strain

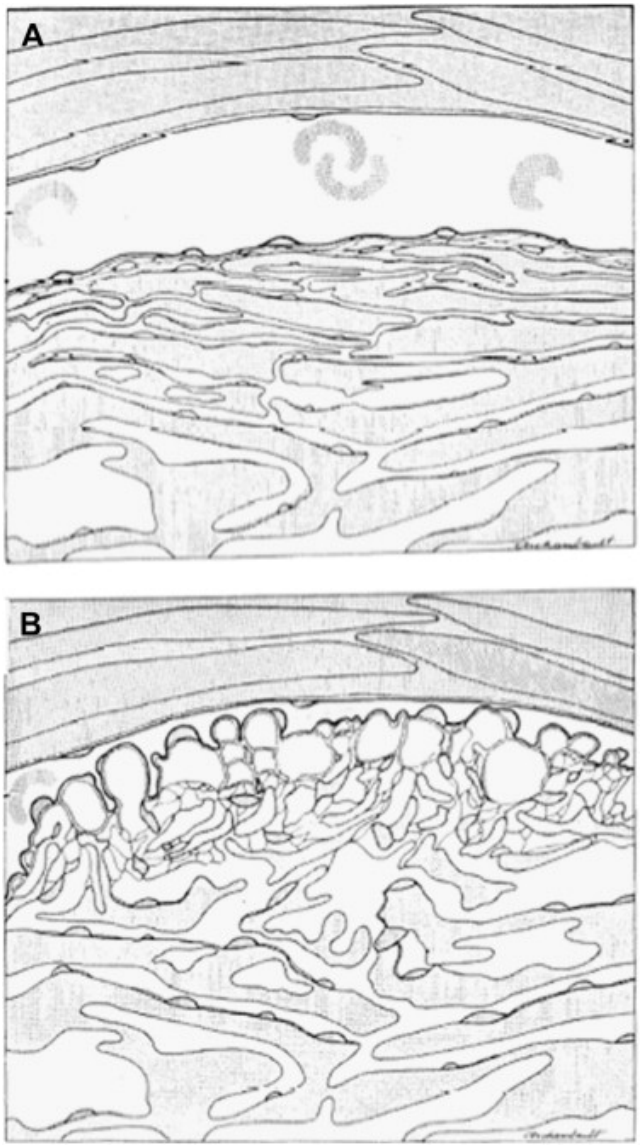


Figure 1.12: **The influence of pressure drop on the morphology of the conventional outflow pathway.** *(Top)*: IOP is equal to episcleral venous pressure, such that there is no pressure drop across the outflow pathway. No GVs are seen at this pressure drop. *(Bottom)*: IOP is higher than episcleral venous pressure, such that there is a positive pressure drop across the conventional outflow pathway. The inner wall is largely distended and vacuolated at this pressure drop. Figure reproduced from [34] with permission.

leads to cell damage and death in lung epithelial cells, a cell type that is known to undergo significant deformation under physiological conditions [70].

1.3.3 Mechanically supporting cellular structures

The endothelial cells of the inner wall endothelium must support the biomechanical stresses they are subjected to, namely the basal-to-apical pressure drop and resulting GV formation. Cytoskeletal elements in the SCE cells are bound to be involved in maintaining the integrity of these cells during biomechanical loading. In fact, electron microscopy studies revealed that the inner wall cells are enriched with actin microfilaments [35, 64, 71–73], as well as vimentin intermediate filaments (IFs) [71, 72, 74].

IFs have been observed in abundance throughout the cytoplasm of SCE cells [71, 72], organised in densely packed networks [72]. The major IF in the inner wall endothelial cells is vimentin [72, 74]. While the role of vimentin IFs in SCE cells is not know, it has been hypothesised that these filaments may be important to help SCE cells withstand the strain imposed by GV formation [72].

Studies in human tissue using single section transmission electron microscopy [35, 71, 72] reported that while some actin filaments are observed throughout the endothelial cells of the inner wall [35, 71], F-actin is predominantly associated with the membrane region of junctional complexes [71, 72]. A study of human tissue using whole-mount fluorescence confocal microscopy [64, 73] further confirmed these findings, reporting that in SCE cells F-actin is organised in a prominent peripheral band. The presence of F-actin near cell-cell junctions is presumably involved in maintaining the integrity of tight junctions and distributing biomechanical stresses across the monolayer [64, 71, 72].

Two groups of investigators [30, 35] reported that F-actin is also prominently observed in cell tethers that project downwards through the basement membrane of the endothelium, contacting either JCT cells or JCT cell processes. SCE cell tethering to the underlying JCT cells and extracellular matrix (ECM), as well as to their basement membrane are likely important to maintaining the integrity of the inner wall endothelium as discussed in a review paper [13].

The biomechanical environment of the inner wall SCE cells likely affects the cytoskeletal architecture in these cells. This hypothesis is supported by a study by Ethier et al. [64] that compared the F-actin organisation between the inner and outer wall SCE cells. Unlike the inner wall, the outer wall endothelium is not subjected to a basal-to-apical pressure drop, does not exhibit any GVs, and does not allow for any significant aqueous humour filtration. Overall, the inner wall cells experience much higher biomechanical stresses than outer wall cells. Interestingly, in most regions of the outer wall endothelium of SC, the F-actin is distributed in fairly prominent fibres throughout the cell rather than in a peripheral band associated with cell-cell junctions as observed in the inner wall SCE cells. These findings suggest that re-enforcement of cell-cell junctions may be important to help SCE cells in the inner

wall endothelium support the transendothelial pressure drop applied across them.

The architecture of both F-actin and vimentin IFs around GVs has not been studied in detail. Only one study using transmission electron microscopy [71] reported that IFs were found associated to the wall of GVs, while F-actin was mainly absent. A better characterisation of the cytoskeletal organisations in GVs may help understand how the SCE cells are mechanically able to withstand the large strains they are subjected to.

1.3.4 Influence of cellular strain on pore formation

Johnstone and Grant [34] were the first to suggest that the inner wall endothelium may act as a pressure-sensing and pressure-regulatory one-way valve that facilitates the flow of aqueous humour with increasing IOP. While the studies examining the relationship between IOP and transendothelial pores are largely inconclusive (see reviews by Ethier [69] and Johnson [12]), there is nonetheless evidence that pore formation may be influenced by the strain imposed by GVs. First, the majority of transendothelial pores are associated with GVs, and are usually found in areas where the cell wall around the GV has significantly thinned, presumably because cell thinning facilitates fusion between the basal and apical cell membrane [20, 30]. Second, Braakman et al. [32] have shown that equibiaxial stretching of SCE cells leads to pore formation in cultured human SCE cells, and that increasing strain increases pore density but not pore size.

The hypothesis that strain may induce pore formation suggests that the inner wall endothelium may act as a "smart" one-way valve that adjusts its local porosity to accommodate local and punctual demands in filtration [32, 44]. Increases in IOP leading to increases in GV number and size may increase the strain experienced by cells, resulting in pore formation. Pore formation may modulate outflow resistance and feedback to influence GV formation by affecting the transendothelial pressure drop across the endothelium.

While the strain caused by GV formation is likely a key determinant of pore formation, GV formation does not seem to be an absolute requirement as pores have been found in flat portions of the endothelium, where there are no GVs [30]. We note that these pores found in the flat regions of the inner wall may however have been associated to GVs that then shrunk and disappeared or these pores may have formed due to the distension of the inner wall due to its collapse into the lumen of SC [34]. While pore formation may be facilitated by thinning of the cell, other factors such as fusogenic proteins, vesicle and caveolae fusion may also be necessary for pore formation to occur (this was reviewed in detail by Overby [41]).

1.3.5 Influence of SCE cell mechanical properties on outflow resistance

A number of studies carried out in the late 1990s and early 2000s examined the effects of cytoskeletal active agents on outflow resistance. In the human eye, agents that directly or indirectly disrupt F-actin, such as H-7 [75], Latrunculin-B [43], and cytochalasin-D [22] decrease outflow resistance. Together these studies suggested that the mechanical properties of the cells along the conventional outflow pathway may be an important modulator of outflow resistance.

Zhou et al. later conducted a study specifically examining the mechanical responsiveness of cultured SCE cells to pharmacological agents known to alter outflow resistance [76]. All drugs known to increase outflow resistance caused an increase in SCE cell contractility and stiffness, while all drugs known to decrease outflow resistance caused a decrease in SCE cell contractility and stiffness [76]. Zhou et al. also considered whether the effects of these drugs could be mediated by changes in cell junctional permeability. Remarkably, there wasn't a direct relationship between junctional permeability and outflow resistance as some drugs associated with increased junctional permeability act to increase outflow resistance. The outcome of the study by Zhou et al. thus seems to support the idea that outflow resistance is modulated by SCE cell stiffness and contractility.

The mechanism by which SCE cell stiffness may modulate outflow resistance is not exactly known. However, the coupled interaction between the biomechanical stresses acting on the inner wall endothelium and the formation of GVs and pores predicts that the biomechanical properties of SCE cells is one of the main determinants of aqueous humour transport across the endothelium. Less stiff cells deform more at a given pressure drop, leading to increased strain presumably then resulting in increased pore formation. Increased pore density may decrease outflow resistance by decreasing the funnelling effect. This hypothesis is supported by a study examining the effects of latrunculin-B in human eyes [43]. Decreased outflow resistance in response to latrunculin B results in a significant increase in the number and size of B-pores, without affecting the integrity of the inner wall endothelium [43]. Other studies examining the effects of H7 [75] and cytochalasin-D [22] in human eyes are less conclusive: these reported that treatment with these agents disrupted the integrity of the inner wall endothelium, but they did not quantify pore density.

In further support for the hypothesis that SCE cell stiffness may affect the ability for these cells to form pores, Overby et al. [17] recently reported altered biomechanical behaviour in glaucomatous SCE cells compared to healthy SCE cells in culture. Glaucomatous SCE cells have an elevated sub-cortical stiffness compared to healthy SCE cells [17]. Increased subcortical stiffness in glaucomatous SCE cells is correlated with decreased pore density in response to basal-to-apical directed perfusion[17]. Together

these data suggest that impaired pore formation in glaucomatous SCE cells may be attributable to an increased subcortical stiffness. Such a conclusion implies that the glaucomatous SCE cells deform less at any given load; the effect of SCE cell stiffness on GV formation is however not known.

1.3.6 Mechanisms of GV and pore formation

The mechanisms underlying GV and pore formation are unknown. In the literature, two hypothetical models have so far been proposed. In 1971, Tripathi [39, 53] proposed a cyclic model of GV and pore formation in the inner wall endothelium of SC (Figure 1.13). In this model, Tripathi considered that GV formation is initiated by an infolding on the basal aspect of the cell surface, likely driven by the pressure drop across the inner wall endothelium. The infolding then progressively grows forming a GV, and eventually opens on the luminal aspect of the cell surface allowing aqueous humour outflow through the transcellular channel. Tripathi proposed that after a certain time interval, the basal mouth of the GV is occluded and that the cell returns to its initial non-vacuolated stage. Tripathi argued that transendothelial channels formed of GVs and pores are transient structures that would only be opened for a short period of time, and that this could explain why he only observed around 2% of GVs with a transcellular pore in his studies using serial section transmission electron microscopy [29].

There are at least two disadvantages of Tripathi's model. First, as explained earlier, the 2% expected opened transendothelial channels reported by Tripathi appears to be inconsistent with the estimated number of pores per GVs based on pore and GV counts [20, 30, 77]. Second, despite noting that the fluid pressure gradient across the inner wall endothelium may be an important factor for the initiation of GV formation, Tripathi did not provide a detailed mechanism for the formation and closure of GVs and pores and the relationship of these events with pressure drop.

In 1972, Inomata, Bill and Smelser [30] proposed an alternative and more detailed model of GV and pore formation. In this model, the authors proposed that GV formation is initiated by an invagination near the nucleus in an area where the attachment of the SCE cell to the subjacent tissue is poor. The invagination enlarges, forming a GV, and the cell wall surrounding the GV progressively becomes thinner. The severe thinning of the cell together with the presence of numerous caveolae in the apical membrane of the cell facilitates the fusion of the basal and apical side of the cell membrane (see Figure 1.6 and Figure 1.7 for examples of caveolae in the GV wall). As the caveolae present in the inner wall cells are covered by diaphragms [21], membrane fusion produces fenestrae-like structures known as diaphragmed minipores[‡](see Figure 1.7 for an example of a minipore in the GV wall). These structures allow water flow but excludes higher molecular weight substances. Eventually, the pressure difference between the inside of the GV and the lumen of SC becomes great enough to break the diaphragm of the minipore, and a transcellular channel is formed allowing aqueous humour to pass freely into SC. At this

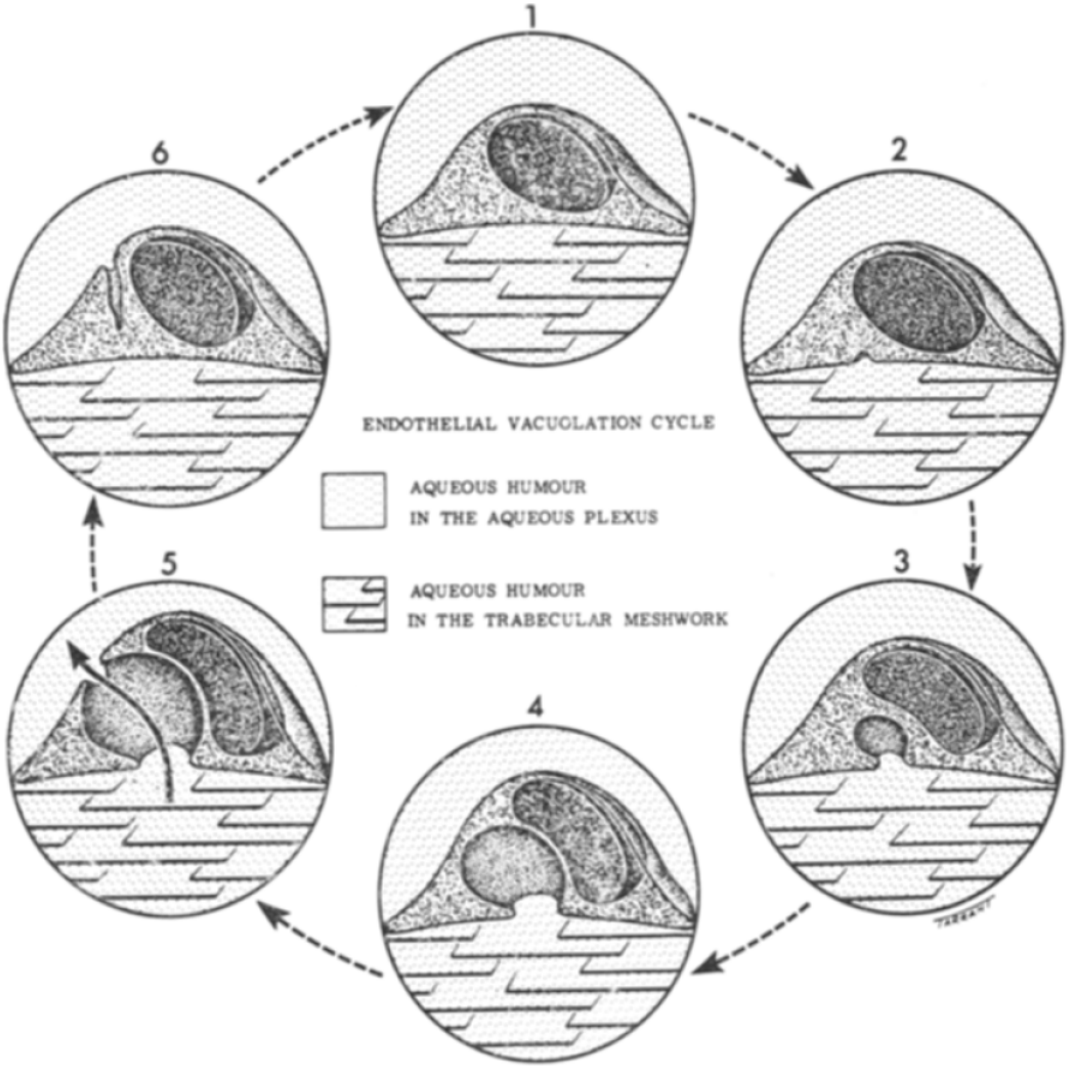


Figure 1.13: **Hypothetical model of GV and pore formation.** Figure reproduced from [39] with permission. See text for description of the figure.

stage, the authors noted that several new GVs may have formed within a single cell, and these GVs tend to open into each other.

A key advantage of the Inomata model is that at any given time, a higher percentage of GVs can exist in a transendothelial channel state (30% [30]) compared to the Tripathi model, which is quantitatively consistent with predictions based on pore counting. The model implies that transendothelial channels, once formed, stay opened for a longer time compared to the Tripathi model. However, a disadvantage of the Inomata model is that despite mentioning that pores may be dynamic structures that open and close frequently, the model does not propose any mechanism for the closure of the transendothelial channels, and does not discuss whether GVs eventually close or stay patent once formed.

Since the formulation of the Tripathi and the Inomata models, little more has been uncovered about the mechanisms of GV and pore formation and about the dynamics of these structures. Following the studies by Johnstone and Grant [34] and Grierson and Lee [37] on the effects of pressure drop on the morphology of the inner wall endothelium, GV formation has been considered to be a largely passive response of the cell to the transendothelial pressure occurring across the endothelium. This hypothesis is supported by a study by Brilakis and Johnson [78] showing that GVs respond rapidly to changes in IOP, largely disappearing in less than 3 mins after IOP is reduced to zero in enucleated eyes.

1.4 Specific aims of doctoral research

While there is strong evidence supporting the functional importance of GVs and associated transendothelial pores to the regulation of outflow resistance and of IOP, little is known of the biomechanical cell processes and cytoskeletal structures linked to their formation and dynamics.

Our central hypothesis is that the biomechanical stresses acting on the inner wall endothelium of SC, namely the basal-to-apical directed pressure drop and resulting cell deformation, are key determinants of the barrier morphology and properties of the endothelium and of aqueous humour outflow resistance.

We propose that the basal-to-apical pressure drop across the endothelium drives the formation of GVs in the SCE cells, and that the large cellular strains imposed by GVs lead to pore formation, thereby allowing for the flow of aqueous humour across the endothelium. In this context, pore formation may modulate outflow resistance and may act as a feedback mechanism to influence cell deformation by regulating the pressure drop across the endothelium. This hypothesis predicts that the biomechanical properties of SCE cells affect the aqueous humour transport mechanism and may modulate outflow

[‡]Minipores are small openings found in the inner wall endothelium of SC that are 60-65 nm in diameter and are typically bridged by a diaphragm [21, 30]. Minipores are similar in size and structure to the diaphragmed fenestrae of fenestrated capillaries. However, minipores observed in SC endothelium are rare and isolated structures unlike fenestrae observed fenestrated endothelia which are numerous and usually organise into sieve plates [21].

resistance. Furthermore, the biomechanical stresses acting on the endothelium likely also regulate the cytoskeletal organisation and cell-cell junction assembly in the SC endothelium, and may thereby influence the barrier morphology of the inner wall endothelial monolayer.

In line with our hypothesis, the main goal of this thesis was to investigate the role of basal-to-apical directed transendothelial pressure drop on the cellular processes governing GV dynamics on the one hand, and on the barrier morphology and properties of SCE cell layers on the other hand. The proposed investigation is of significance as it should provide us with a better understanding of the mechanisms by which the cells of the inner wall endothelium modulate outflow resistance and regulate IOP. This is particularly relevant in the context of glaucoma, in which the pathological outflow resistance increase and associated elevated IOP may be caused by alterations in the biomechanical function of SCE cells.

The research goals of this PhD were explored across four studies:

Specific Aim 1: To investigate the role of actomyosin contractility in GV-like structure (GVL) dynamics in cultured SCE cells. GVs form in response to the basal-to-apical pressure drop that exists across the inner wall endothelium of SC [33–35]. Little is known about the effects of pressure drop on GV dynamics, and about the role of cellular contractility, which likely affects GV dynamics under load. In Chapter 2, we characterise the dynamics of GVLs formed *in vitro* in perfused SCE cells, specifically looking at the the effects of actomyosin contractility perturbation. We track the dynamics of GVLs using time-lapse fluorescence imaging during basal-to-apical perfusion of human SCE cells, and compare groups either treated with an actomyosin contractility reducing agent or with a vehicle.

Specific Aim 2: To examine the cytoskeletal structures that support GVLs in cultured SCE cells. As a result of GV formation, cells in the inner wall endothelium of SC undergo large strains that may exceed 50% [41, 69]. The ability of SCE cells to mechanically support the large strains imposed by GV formation and the associated biomechanical stresses suggests that the cytoskeletal elements in the inner wall cells are important. While it has been reported that inner wall cells are enriched in F-actin and vimentin IFs [72], the organisation of these cytoskeletal filaments around GVs has not been previously described. In Chapter 3, we use fluorescence confocal microscopy to examine the cytoskeletal structures involving F-actin and vimentin IF around GVLs in basal-to-apical perfusion-fixed human SCE cells.

Specific Aim 3: To investigate the short-term pressure and time-dependent characteristics of the hydraulic resistivity of cultured SCE cells. *In vitro* studies have shown that GV size and pore density both increase with pressure drop [17, 33], while the hydraulic resistivity of cultured SCE cells

decrease with pressure drop [33]. The time-dependent changes in the hydraulic resistivity of SCE cells in response to step changes in pressure drop have however not been studied. In Chapter 4, we measure the hydraulic resistivity of cultured SCE cell layers in response to a series of short-term basal-to-apical directed transendothelial pressure drops.

Specific Aim 4: To investigate the effects of long-term transendothelial pressure drop on the barrier organisation and function of cultured SCE cell layers. SCE cell culture models largely fail to replicate the barrier properties and morphology observed *in situ* in the inner wall endothelium of SC, and cultured SCE cells lose expression of key junctional and endothelial differentiation markers [12, 69, 79, 80]. We hypothesise that the native biomechanical environment of the SCE cells, namely the basal-to-apical pressure drop, is key to maintaining the native barrier morphology and function of SCE cell layers. To test this hypothesis, in Chapter 5 we study the effects of culturing human SCE cells under a long-term basal-to-apical transendothelial pressure drop.

2

The role of actomyosin contractility in the life cycle of GVLs in cultured SCE cells

2.1 Introduction

Aqueous humour flows across the inner wall endothelium of SC and generates a transendothelial pressure drop in the basal-to-apical direction. This basal-to-apical directed transendothelial pressure drop causes a local detachment of SCE cells from their supporting basement membrane and inflates dome-shaped outpouchings known as GVs that generate cellular strains exceeding 50% [41, 69]. GV formation causes severe thinning of the SCE cells and facilitates the formation of transendothelial pores that provide an outflow pathway across the SC endothelium [12, 19]. In glaucoma, increased outflow resistance leads to elevated IOP [11] and it is thought to be associated with a dysfunction in pore formation and possibly in GV formation [14, 15, 17]. Little is known, however, about the mechanics governing GV and pore formation or the factors that influence these processes.

The size and density of GVs increase with increasing transendothelial pressure drop [34, 37, 40, 67], and GVs are largely absent when the pressure drop is 0 mmHg or when it is reversed [34, 40]. These observations demonstrate that GVs are pressure-dependent structures. The mechanical properties of SCE cells likely determine the relationship between pressure drop and GV formation, and these properties may by extension affect pore formation and outflow resistance [17, 41, 76]. In particular, reduction of cell contractility using rho kinase (ROCK) inhibitors leads to decreased SCE cell stiffness and to decreased outflow resistance [76, 81]. These observations, together with the likely importance of GVs in outflow resistance regulation, motivates the investigation of the effects of ROCK inhibition and associated cell contractility reduction on GV biomechanics.

Our group has previously developed an *in vitro* model system for the visualisation of GV-like structure (GVL) dynamics [33]. This model system reproduces some of the key aspects of the morphology and pressure-dependent behaviour of true GVs observed *in situ* [33]. In this study, we extended the use of this model system and we aimed to characterise GVL dynamics and to evaluate the effects of ROCK inhibition. GVL dynamics were visualised using time-lapse fluorescence imaging of SCE cell layers during basal-to-apical perfusion at controlled pressure drops. GVLs were identified and their contour was semi-automatically tracked to characterise GVL dynamics. The effects of ROCK inhibition on GVL dynamics were assessed by treating the cells with the Y-27632 compound. Y-27632 is a cell permeant ROCK inhibitor that is highly selective for both ROCK1 and ROCK2 [82–84]. ROCK regulates the phosphorylation of the regulatory myosin light chain (MLC) to promote actomyosin-driven cell contractility. Inhibiting ROCK with Y-27632 inhibits MLC phosphorylation by promoting MLC-phosphatase activity [85]. This leads to the disassembly of stress fibres and of focal adhesions and to a reduction in cell contractility and cell stiffness without any cytotoxic effects in many cells, including in cultured SCE cells [76, 86]. Importantly, Y-27632 has also been shown to decrease outflow resistance

in different species [86–89].

2.2 Materials and Methods

2.2.1 Cell isolation and culture

The human SCE cells used in this thesis were isolated from eye tissue from human donors without a history of ocular disease. The isolation was carried out by Kristin Perkumas in Prof. WD Stamer's lab at Duke University (USA) using previously validated methods [79, 80].

Briefly, after separating the anterior segment of the eye from the rest of the eye globe, SC was cannulated with a sterile nylon suture coated with gelatin. The anterior segment with the cannulated SC was placed in Dulbecco's Modified Eagle's Medium (DMEM) containing 5mM L-glutamine (Gibco 12320, Thermo Fisher Scientific, USA), and supplemented with 10% highly defined foetal bovine serum (FBS; Hyclone, SH30070.03, GE healthcare, USA) and 1% penicillin-streptomycin-glutamine (Gibco, 10378016, Thermo Fisher Scientific, USA). This medium formulation will hereafter be referred to as culture medium. The eye segments were maintained in a cell culture incubator at 37 °C, 100% humidity and 5% CO_2 for at least 3 weeks allowing for the SCE cells to migrate onto the surface of the suture. After this time, the suture was removed from the lumen of SC and was placed inside gelatin-coated 6-well plate containing culture medium. The cells were removed from the suture by trypsin-EDTA digestion, and were then left to adhere to the culture plate. The SCE cells were then cultured in culture medium, and maintained in a tissue culture incubator. SCE cells were passaged once they reached 80% to 90% confluence.

SCE cells were characterised based on three criteria that are unique to SCE cells and have been consistently validated to differentiate them from the neighbouring TM cells [80]. These criteria include: the absence of myocilin production in response to dexamethasone treatment, the expression of VE-cadherin and fibulin-2 at protein level, and the formation of a cell barrier with a trans-endothelial electrical resistance of 10 $\Omega.cm^2$ or more after the first cell passage. Each successful isolation from each donor tissue established a different cell line.

This current study examined two human SCE cell lines isolated from non-glaucomatous donor eyes (SC60, donor aged 58 and SC68, donor aged 30). All SCE cells were cultured and used for experiments up to and including passage 6.

2.2.2 Cell seeding on porous membranes

SCE cells were seeded at 20,000 cells/cm^2 onto the bottom-facing surface of a filter membrane held by a culture insert (Milicell 24 well-plate, hanging culture inserts, MCHT24H48, Merck Millipore, USA;

polyethylene terepthtalate (PET) membrane with 1 µm diameter track-etch pores, 6.5 mm diameter membrane, 11 µm thick membrane and 2x10^6 pores/cm^2). The seeding procedure was similar to that previously described by Pedrigi et al. [33] and is schematically represented in Figure 2.1. First, the inside of the culture insert was filled with culture medium. A silicone stopper (10D Versilic Silicone Stopper, DX1069806, Saint-Gobain, France) was subsequently fitted inside of the insert to create a leak-proof seal and to introduce a small chamber between the apical surface of the membrane and the silicone stopper. The culture insert was then inverted such that the bottom side of the membrane faced upwards. Next, a hollowed silicone folding skirt stopper (Versilic, DX467007-100, Saint-Gobain, France) was adjusted around the outer surface of the culture insert to create a well above the membrane. A well-mixed cell suspension was pipetted inside of the well, and the well was covered with a silicone folding skirt stopper the to prevent contamination. The cells were then left to adhere overnight in this upright configuration in an incubator. The folding skirt was then delicately removed, and the insert was re-inverted and placed bottom-face down into a 24 well-plate filled with culture medium. Finally, the silicone stopper was removed from inside the insert. Prior to removing the silicone stopper, a 21G needle was threaded through the stopper to shunt any pressure spikes which would otherwise cause the cells SCE cells to detach from the membrane. SCE cells were cultured on the filter membranes for 2 to 3 additional days until the cells homogeneously covered the entire filter.

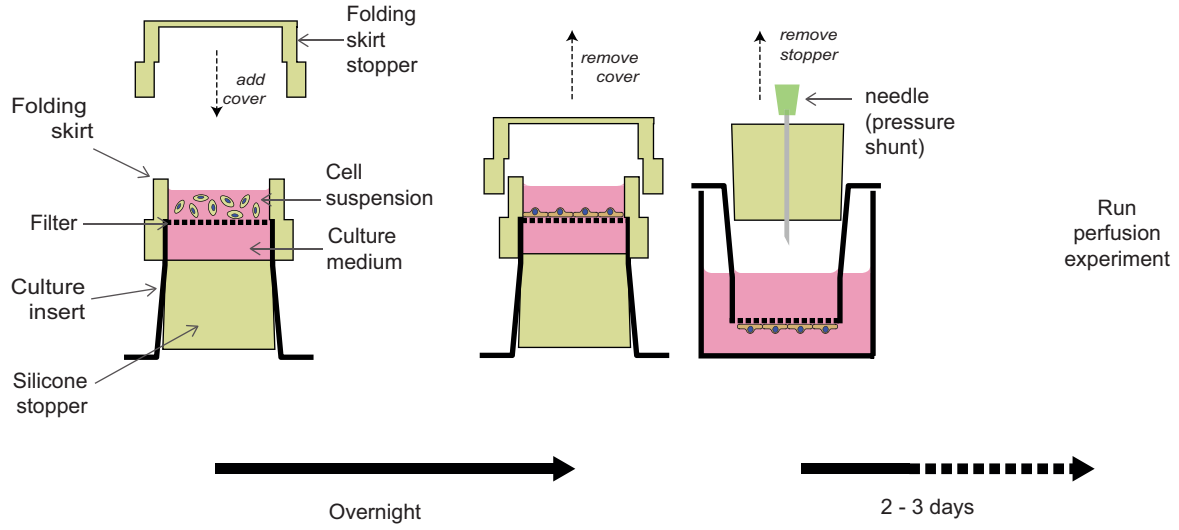


Figure 2.1: **Method for SCE cell seeding onto porous membranes.** See text for further details.

2.2.3 Sample preparation for perfusion

In preparation for time-lapse imaging, the SCE cell cytoplasm and nucleus were stained with 2 μM calcein-AM live-cell labelling dye (Invitrogen, Life Technologies Co., USA; calcein-AM in DMSO, with final DMSO concentration in the medium < 0.1%) for half an hour up to an hour.

In preparation for the perfusion experiment, the inside of the culture inserts were rinsed to

remove FBS and then filled with filtered DMEM with 1% PSG. A silicone stopper was subsequently fitted inside of the insert to create a leak-proof seal and to introduce a small chamber between the apical surface of the membrane and the silicone stopper. Prior to fitting the stopper inside of the insert, first a thin piece of tubing (length: $\sim$ 50 mm ; OD: 1.98 mm , ID: 1.02 mm , Portex 800/100/300, Smiths Medical, USA) was inserted through a punched 1.5 mm hole in the stopper, and a 19G needle was then threaded elsewhere through the stopper. During the fitting of the stopper inside of the stopper, both the tubing and the needle served to shunt any pressure spikes that would otherwise damage the cells. Once the stopper was placed inside of the insert, a larger piece of tubing (OD: 3.2 mm ; ID: 1.6 mm , C-Flex, 06422-02, Saint Gobain, France) filled with filtered DMEM was fitted onto the thin tube in the stopper. DMEM was then pushed through the tubing, into the chamber inside of the insert and out of the needle to flush out any bubbles. The tubing was then closed off and the needle was delicately threaded out of the stopper.

Immediately prior to perfusion, the culture insert and tubing assembly was placed in a insert adaptor (Artificial Membrane Adapter, 0420011301, Bioptech, USA) with the cells facing downwards, and the adaptor was placed in a 35 mm glass bottom dish (81218-200, Ibidi, Germany) that was filled with culture medium (DMEM with FBS). A custom-made 3D printed holder was adjusted over the insert and adaptor to hold the insert down and to keep the the tubing above the stopper in an upright position to avoid pulling the stopper out of the insert or moving the insert out of the focus plane of the microscope.

The samples were then checked under a tissue culture brightfield microscope to confirm that the cell layers were not damaged, and any damaged cell layers were discarded. Once assembled, the sample and tubing were placed in a tissue culture incubator until just prior to the start of the perfusion experiment.

2.2.4 Drug treatment

During each perfusion, the cells were treated with either 25 μM Y-27632 or an equivalent volume of the vehicle (diH_2O). The compound was added to both the DMEM with which the cells were perfused, and to the culture medium (DMEM + 10% FBS) which was in contact with the apical surface of the cells. In this way, there was no dilution of the compound concentration during the perfusion experiment. Treatment was started only a few minutes before the start of the perfusion experiment. For each treatment condition, at least three different cell layers were perfused separately.

2.2.5 Pressure-controlled perfusion system

We used a custom-made perfusion system to control the pressure drop applied across the filter and cells. The perfusion system was adapted from a previously described system (*iPerfusion* [90]). In this system,

the pressure drop applied across the filter and cells (ΔP) is controlled using a reservoir filled with water coupled to a vertically mounted linear actuator (L35, Nanotech, Germany, resolution of 1.25 μm per step). The pressure applied across the filter and cells is monitored throughout the perfusion by a wet-wet differential pressure transducer (PX409, Omega Engineering, USA; measurement range: 0 to 50 mmHg , uncertainty: 0.04 mmHg). Flow through the filter and cells (Q) is also measured using an in-line thermal flow meter (SLI430, Sensirion, Switzerland; measurement range: -120 μl/min to 120 μl/min, uncertainty: 5% of measured value). A custom-written LabView (National Instruments, USA) program controls the whole system and is used to record the pressure and flow measurements. Together, this perfusion system allows for an accurate control of the pressure drop applied, for almost immediate changes in the applied pressure, and for a precise measurement of pressure drop and flow rate.

2.2.6 Perfusion and image acquisition protocol

Just prior to the beginning of the perfusion experiment, the culture insert assembly was installed on the stage of an inverted fluorescence widefield microscope (Zeiss A1 Axiovert, Carl Zeiss, Germany) contained in a temperature-controlled box set at 37 °C. The SCE cells were imaged at 0 mmHg in multiple areas across the membrane to confirm uniform covering the filter, and the absence of cell detachment due to sample preparation.

Before the beginning of the perfusion experiment, the perfusion system was calibrated and tested following the methods described by Sherwood et al. [90]. First, the pressure sensor was calibrated by using an automated 8-point calibration with the automated linear actuator. Subsequently, the resistance of a glass capillary of a known-resistance comparable to the filter and cells was measured to confirm that the system was functioning properly. The system was always checked for bubbles and leaks before starting an experiment.

Once the system had been calibrated and tested, the tubing leading to the culture insert was connected to the perfusion system while the culture insert was still maintained in the microscope chamber. The pressure drop initially applied across the filter and cells was set to 0 mmHg. Immediately prior to the start of the perfusion recordings, the pressure and flow measurements were both checked to confirm that they were very close to 0 mmHg and 0 μl/min respectively.

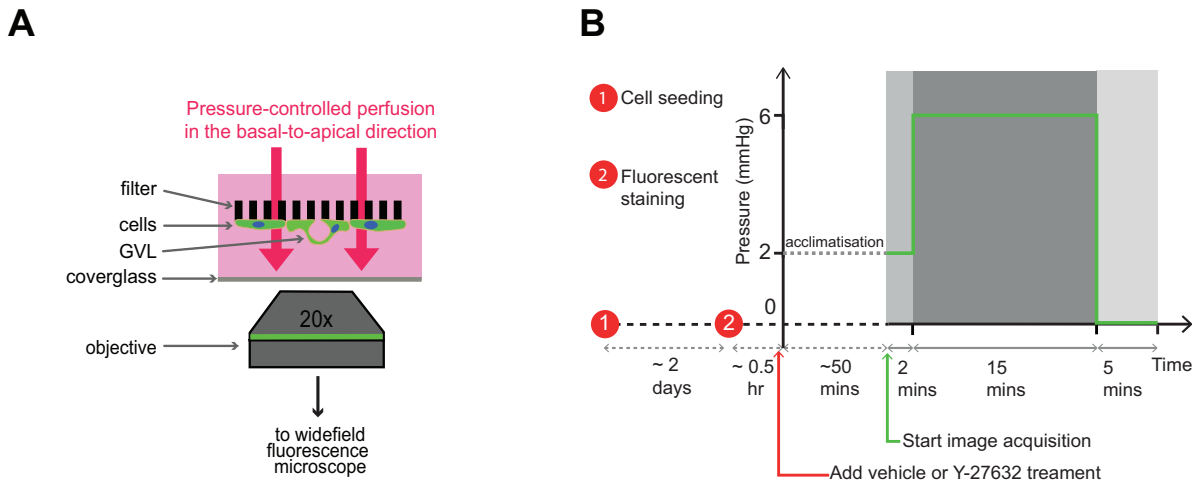


Figure 2.2: **Set-up and protocol for live-imaging during cell perfusion. (A)** Experimental set-up. The cells were cultured on the bottom face of a filter membrane and were perfused in the basal-to-apical direction, mimicking the *in situ* mechanical environment of the cells. The cells were stained with a fluorescent vital dye (calcein-AM AM) and were imaged using an fluorescence widefield microscope during perfusion. **(B)** Preparation procedure for the perfusion experiment, and pressure and image acquisition protocol. The cells were seeded approximately two days before the perfusion experiment. Just before the experiment, the cells were stained with a fluorescence dye and were then placed in a dish with 25 μM Y-27632 or with an equivalent volume of diH_2O (vehicle) in complete culture medium. The cells were also perfused with filtered DMEM containing the same concentration of Y-27632 or of the vehicle respectively. The cells were first acclimatised to a 2 mmHg pressure drop for approximately 50 mins (the rationale for this acclimatisation step is detailed in the text). After acclimatisation, time-lapse fluorescence image acquisition was started whilst the pressure drop across the cells was maintained at 2 mmHg for an additional 2 mins. Images were acquired every 11 s, during the rest of the pressure protocol (22 mins in total).

After 5 to 10 mins at 0 mmHg, the pressure drop applied across the filter and cells was increased to 2 mmHg. As the SCE cells were seeded on the bottom-side of the filter membrane, a positive pressure drop drove perfusion medium to flow in the basal-to-apical direction across the cells. The pressure drop was maintained at 2 mmHg for approximately 50 mins to acclimatise the cells to pressure and flow. After initial acclimatisation, time-lapse imaging was initiated whilst the pressure drop was maintained at 2 mmHg for an additional 2 mins. The pressure drop was then increased to 6 mmHg and held at this pressure drop for 15 mins. Finally, the pressure drop was lowered back down to 0 mmHg for a remaining 5 mins, after which imaging was stopped and the system was closed off. The cells across the whole area of the porous membrane were then checked for viability by checking that the live-cell labelling dye had not leaked out significantly and that the cells had not peeled off the filter.

Image acquisition was controlled by a custom-written LabView program to record the pressure drop applied across the cell at each image acquisition time-point. Time-lapse images were acquired with a 20x objective (Zeiss LD A-Plan 20x/0.30 Ph1) every 11 s at a single position in the cell layer. The dimensions of the imaged region of interest (ROI) was 640 μm x 640 μm spanned by 1024x1024 pixels

and acquired with a 8-bit pixel-depth camera (Orca 03G, C8484-03G02, Hamamatsu Photonics K.K., Japan). In total, the ROI was imaged for 22 mins.

2.2.7 GVL identification and contour tracking

Time-lapse image sequences were pre-processed using ImageJ (NIH, USA) and Icy Bioimage (Institut Pasteur, France) [91]. The sequences were first corrected for time-dependent fluorescence bleaching using the debleaching plugin in ImageJ. Second, image contrast was enhanced using the Contrast Limited Adaptive Histogram Equalisation (CLAHE) plugin in Icy. Finally, to correct for any movements of the culture insert during time-lapse image acquisition, the images in the sequence were registered to the first image acquired using the Virtual Stack Registration plugin in ImageJ.

GVLs were manually identified in the image sequence by looking for elliptical voids fully contained within the body of a single fluorescently labelled cell. Other investigators previously used a comparable *in vitro* SCE cell perfusion model and visualised the morphology of these void regions by creating 3-dimensional reconstructions of confocal Z-stack images of cells that were perfusion-fixed [33] (Figure 2.3). They reported that these void regions corresponded to sites where the cell had been displaced, forming dome-like structures that enclosed an extracellular ellipsoidal cavity, and further determined that these structures were morphologically analogous to GVs found *in situ* (compare with Figure 1.4 in Introduction). The void regions visualised in this current study using widefield imaging can be interpreted as a 2-dimensional projections of the 3-dimensional GVLs (Figure 2.3).

Identified GVLs were then selected for tracking based on the following morphological selection criteria: (1) Size: The GVL had to be larger than 10 μm^2; (2) Shape: The GVL shape had to be close to elliptical, and could not include any lobular-like extrusions indicative of a multi-chamber GVL structure; (3) Clear contrast: There had to be a clear contrast between the inside of the void region of the GVL and the fluorescent cell body; (4) Clear contour: The GVL always had to be surrounded by a continuous fluorescent contour such that the inside of the void region of the GVL and intercellular space could always be easily distinguished from one another by eye. This was particularly important when the GVL was very close to the cell edge or to another GVL. Any absence of fluorescence between two cells was considered to be an enlarged intercellular space and was not included in the analysis; (5)Focus: The GVL had to be in clear focus throughout the entire time-lapse image sequence.

Each GVL of interest that met these set of morphological criteria were then cropped into individual rectangular ROIs using Matlab. The selected GVLs were semi-automatically tracked over time using the active contour algorithm implemented by in Icy Bioimage Analysis [91, 92]. The algorithm was initialised with a user-drawn polygon around the GVL contour on the first frame where it appeared and with a set of user-inputted fitting parameters. The contour outputted by the algorithm was assessed

by eye looking at how closely it followed the GVL perimeter and captured its dynamics. The GVL was discarded if no set of parameters were found to output a satisfactory contour. The area contained inside the contour at each time point for each GVL tracked was then outputted into Matlab for quantitative and statistical analysis.

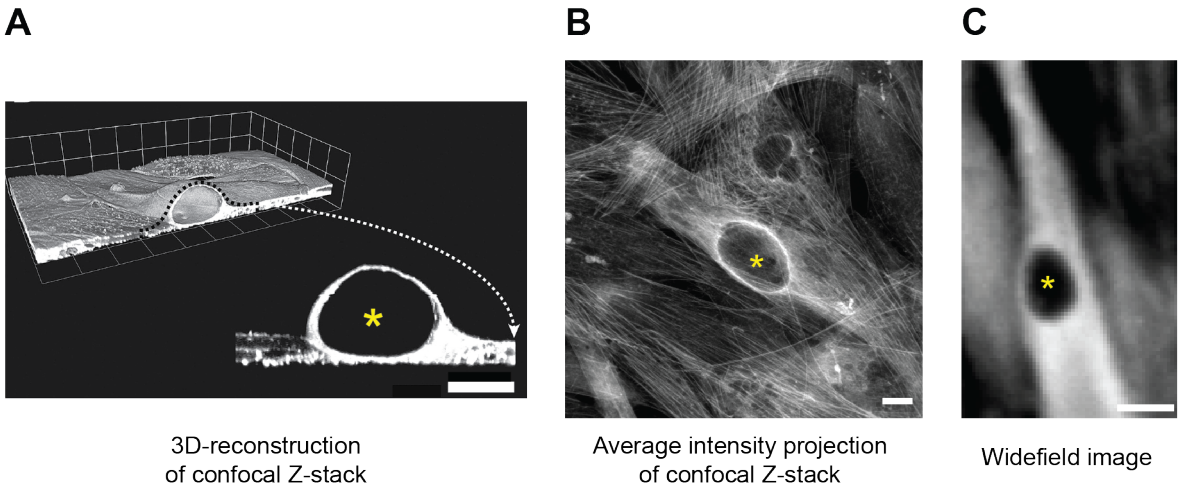


Figure 2.3: **Comparison of the aspect of GVLs using different modes of visualisation and imaging. (A)** A 3-dimensional reconstruction of a fluorescent confocal Z-series of GVL in perfusion-fixed SCE cells reproduced from Pedrigi et al. [33] with permission. The entire cell bodies are auto-fluorescent due to gluteraldehyde fixation and F-actin is also fluorescently labelled. This reconstruction demonstrates that GVLs are thin dome-like structures that enclose an extracellular ellipsoidal cavity. Scale bar: 20 μm. **(B)** An average intensity projection through the same Z-stack as that used to generate the 3-dimensional reconstruction of the GVL presented in panel A. In this mode of visualisation, the GVL appears as an elliptical void region surrounded by a fluorescent cell contour. The top and bottom walls of the GVL are thin and only dimly fluorescent. Scale bar: 20 μm. **(C)** A widefield image of a GVL acquired using our current set-up. The entire cell bodies are fluorescently labelled with calcein-AM, and the GVL appears as an elliptical void surrounded by an otherwise uniformly stained cell body as in panel B. In the modes of visualisation presented in panel B and C, the void region observed can be interpreted as a 2-dimensional projection of the 3-dimensional GVL cavity. Scale bar: 10 μm.

2.3 Results

2.3.1 SCE cell morphology and transendothelial perfusion

To visualise the dynamics of GVLs, fluorescence time-lapse images of SCE cell layers were acquired during basal-to-apical perfusion at controlled transendothelial pressure drops (Figure 2.2). Before the start of the perfusion, the fluorescently labelled SCE cells were examined for confluency and morphology. The SCE cells were elongated and appeared to cover the filter uniformly, although intercellular gaps and overlapping cells were often observed across the cell layers (Figure 2.4A).

Preliminary experiments revealed that in response to a step increase in pressure drop from 0 mmHg to 2 mmHg, SCE cells appeared to narrow, and new intercellular gaps opened while most ex-

isting gaps widened (compare Figure 2.4A and B). Importantly, this occurred without any obvious cell layer detachment or leakage of calcein-AM from the cells, indicating that transendothelial perfusion did not result in a loss of cell layer integrity nor in cell rupture. Along with these observed morphological changes, the flow rate measured through the SCE cell layers transiently increased for several tens of minutes while the transendothelial pressure drop was maintained at 2 mmHg*. Once the flow rate transient had reached stability, a further increase in pressure drop to 6 mmHg resulted in a shorter transient of a few minutes. As the flow rate transient through the SCE cell layers appeared to be related to changes in cell morphology, which could affect GVL formation, the SCE cells were acclimatised at 2 mmHg before the beginning of time-lapse image acquisition (Figure 2.2).

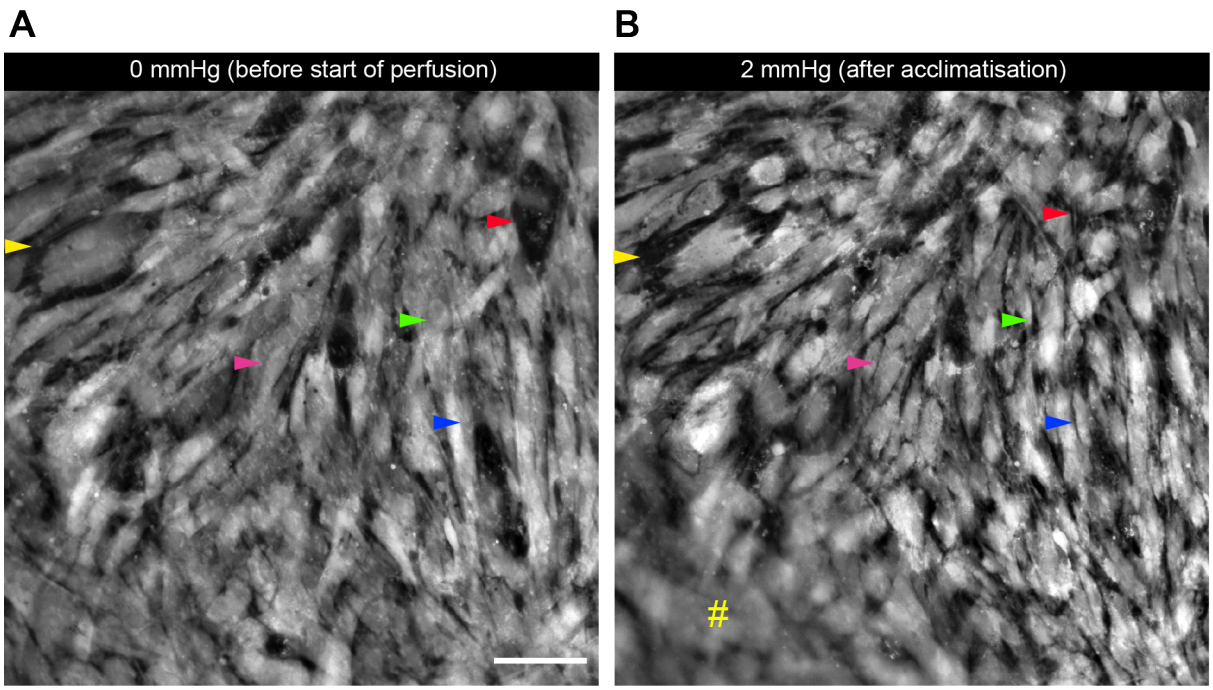


Figure 2.4: **Cells before and after acclimatisation to basal-to-apical directed perfusion. (A)** Before the start of the perfusion, the cells are fluorescently labelled with calcein-AM, and appear to be elongated and to cover the filter uniformly. Intercellular gaps (yellow and red arrowheads) and regions cell-cell overlap (magenta, green and blue arrowheads) are commonly seen across the cell layer. **(B)** After acclimatisation at a pressure drop of 2 mmHg (refer to Figure 2.2), the cells still appear to cover the filter uniformly and there are no obvious signs of cell detachment or cell death. There however appears to be an overall widening of intercellular gaps (compare coloured arrowheads between the two panels). The # symbol indicates an area of the cell layer that has come out of optical focus during perfusion. Scale bar: 100 µm.

2.3.2 Characteristics of the life cycle of GVLs

After the acclimatisation of the SCE cells to the basal-to-apical pressure drop, time-lapse image acquisition was started while the transendothelial pressure drop was maintained at 2 mmHg (Movie 1 in Digital

*The flow rate transient measured through SCE cells will be presented in Chapter 4.

Supplementary Material and Figure 2.5). At this pressure drop, elliptical-like void regions of different sizes were visible within the otherwise uniformly stained cytoplasm of the cells present in the field of view. These void regions have been previously characterised by others [33], and correspond to GVLs (refer to Methods Section 2.2.7 and Figure 2.3). A further step increase in pressure drop from 2 mmHg to 6 mmHg drove the formation of many new GVLs. Conversely, lowering the pressure drop down to 0 mmHg resulted in the retraction and eventual disappearance of most existing GVLs within a few minutes.

A closer examination of the time-lapse images acquired while the pressure drop was maintained at 6 mmHg revealed that GVLs could be categorised into two broad classes. The first class comprised smaller GVLs (less than 10 μm^2). These often tended to cluster on cells and often appeared to cyclically form and disappear within a few tens of seconds, giving the impression that these structures were bubbling underneath the cell (magenta arrows in Movie 1 and in Figure 2.5). The second class of GVLs observed comprised larger and more long-lasting GVLs (orange asterisks in Movie 1 and in Figure 2.5).

We sought out to evaluate dynamics of the larger and longer-lived class of GVLs. First, we manually identified GVLs in two different SCE cell lines, SC60 and SC68 (Table 2.1). The identified GVLs were then selected for tracking if they met a set of morphological criteria including a size larger than 10 μm^2, an elliptical-like shape, the presence of a continuous and distinguishable fluorescent contour surrounding the void region of the GVL, and a clear contrast between the inside of the void region of the GVL and the surrounding fluorescent body (refer to Methods Section 2.2.7). The contour of these selected GVLs were semi-automatically tracked using an active contour algorithm implemented in the open-source image analysis software Icy Bioimage [91, 92] (Movie 2, see Digital Supplementary Material, and Figure 2.6). We successfully tracked a total of 60 and 56 GVLs in SC60 and SC68 cells, respectively. The trackable GVLs will henceforth simply be referred to as GVLs, while acknowledging that the trackable GVLs only represent a subset of all identified GVLs in the perfused cell layers.

We focused on the dynamics of GVLs that formed at 6 mmHg (n = 41 for SC60 and n = 44 for SC68), and found that most GVLs followed a similar life cycle that occurred over a few minutes. First, the GVLs formed, starting at a size in the range of 10 μm^2 and 176 μm^2 (aggregate values for all GVLs formed at 6 mmHg in both SC68 and SC60, n = 85). After forming, the GVLs grew reaching a maximum area in the range of 16 μm^2 and 777 μm^2. Strikingly, after reaching a maximum size, most GVLs that had formed at 6 mmHg were seen shrinking and eventually disappearing despite the applied pressure load (80% in SC60, and 66% in SC68).

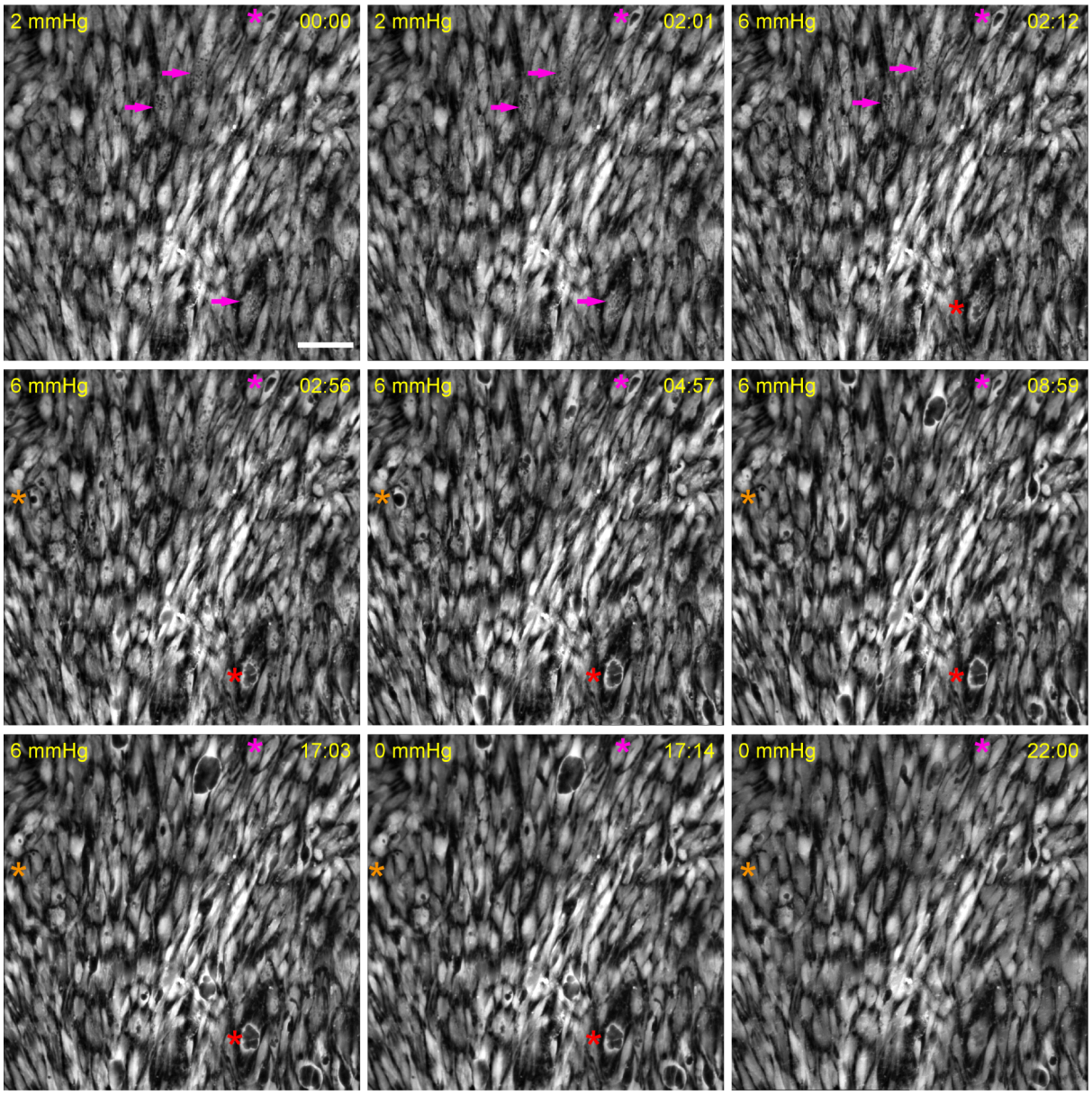


Figure 2.5: **Time-lapse image series of SCE cells during basal-to-apical perfusion at a series of pressure drops.** The pressure drop is increased from 2 mmHg to 6 mmHg and then is lowered down to 0 mmHg while time-lapse images are acquired every 11s (refer to Figure 2.2). GVLs are identified as elliptical void regions within the otherwise uniformly stained cytoplasm of the cells. At 2 mmHg, small and short-lived clusters of GVLs cyclically appear and disappear (magenta arrows), and there are only a few larger GVLs (magenta asterisk). The increasing step in pressure drop from 2 mmHg to 6 mmHg results in the appearance of many new GVLs (example indicated by orange asterisk; the red asterisk indicates a GVL with a complex morphology). Lowering the pressure drop down to 0 mmHg leads to the retraction and disappearance of most existing GVLs, although some GVLs persist even 5 mins after the removal of pressure drop. Scale bar: 100 μm.

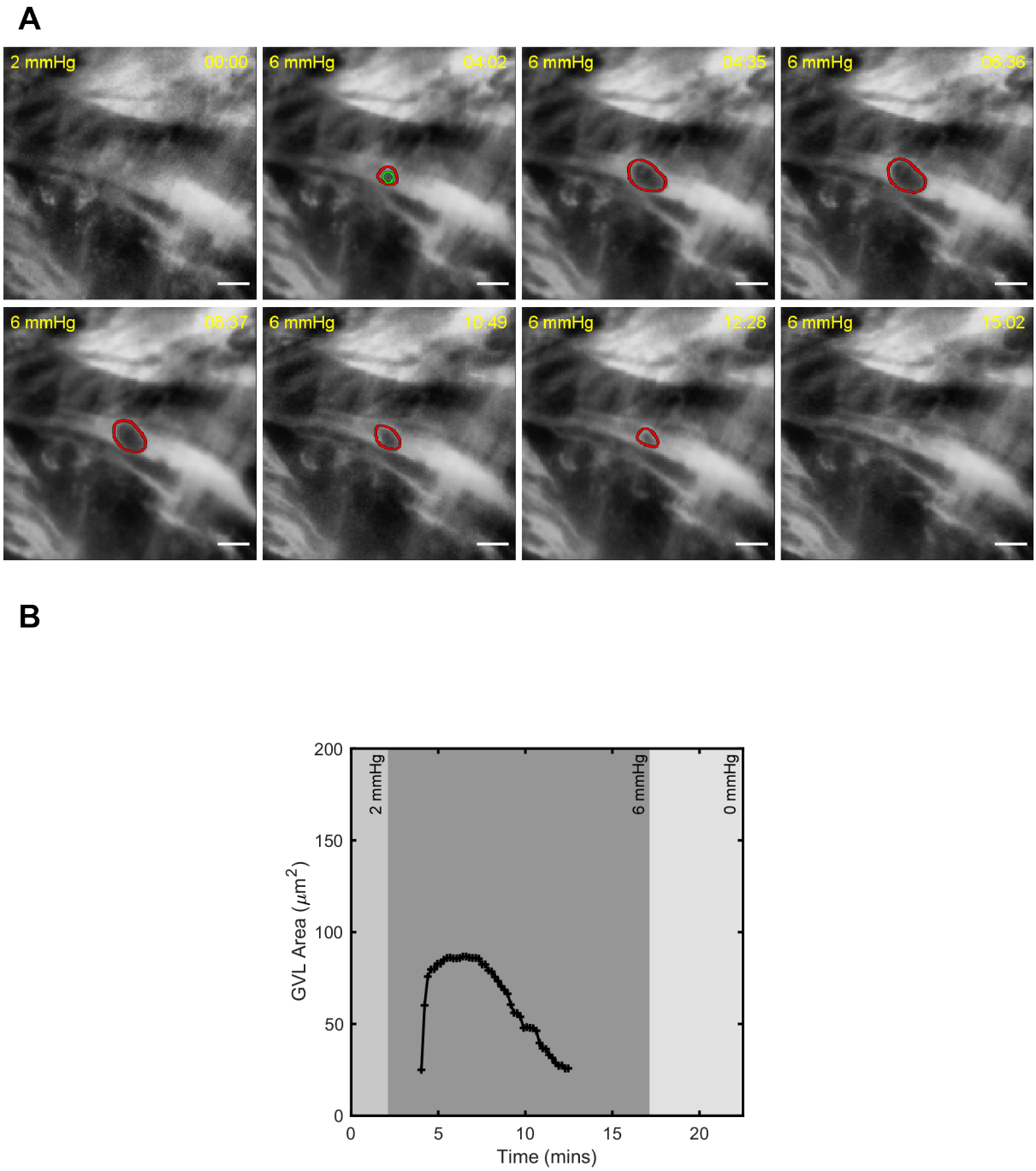


Figure 2.6: **Representative GVL tracked over time. (A)** Time-lapse images of a representative GVL tracked over time using the active contour algorithm plugin in Icy. To track the GVL, the frame at which the GVL first appears is identified and a polygonal ROI is manually drawn around the GVL (green contour in second top image from the left). Next, the active contour algorithm uses the user-inputted ROI and parameters to iteratively modify the contour until it converges (red contour). Finally, the algorithm uses the contour it converged to in the first image as a starting contour for the following image in the time-lapse series and runs again. This process continues until either the end of the image series is reached or the contour has shrunk and disappeared (which is what occurs in this particular example). Scale bar: 10 µm. **(B)** Representative area tracing of the GVL presented in panel A. The area of the GVL is extracted from the tracked contour of the GVL and can be interpreted as a projected area of the 3-dimensional GVL (refer to Figure 2.3).

Cell line	Donor age	Treatment	No. of cell layers	No. identified GVLs	No. trackable GVLs
SC60	58	Vehicle	3	128	60
		Y-27632	4	141	39
SC68	30	Vehicle	5	150	56
		Y-27632	4	112	42

Table 2.1: **Summary of the number of cell layers perfused for each cell line and treatment group, and of the total number of identified GVLs and trackable GVLs.** For each cell layer perfused, a single ROI was imaged during time-lapse acquisition (refer to Methods Section 2.2.6). For each individual cell line, the counts of identified and trackable GVLs of all the cell layers perfused were pooled altogether for analysis.

To characterise the life cycle of GVLs, we next compared the time for growth (time interval between GVL formation and maximum GVL size) and the time for retraction (time interval between maximum GVL size and GVL disappearance) (Figure 2.7A and B). For this analysis, only GVLs that both formed and disappeared at 6 mmHg were considered (n = 33 for SC60 and n = 29 for SC68). While there was a large variability in growth time and retraction time across all GVLs, we found that GVL retraction time was significantly longer than the GVL growth time (Mann-Whitney U-test, $p < 10^{-5}$ for both cell lines). To verify that this difference was consistent across all GVLs, no matter their size, we looked at the ratio of retraction time over growth time for each individual GVL (Figure 2.7C). Again, while there was a large variability in ratio of retraction to growth time between GVLs, we found that retraction time was longer than growth time in almost all GVLs and that retraction time was at least three times longer than growth time in the majority of GVLs in both cell lines studied.

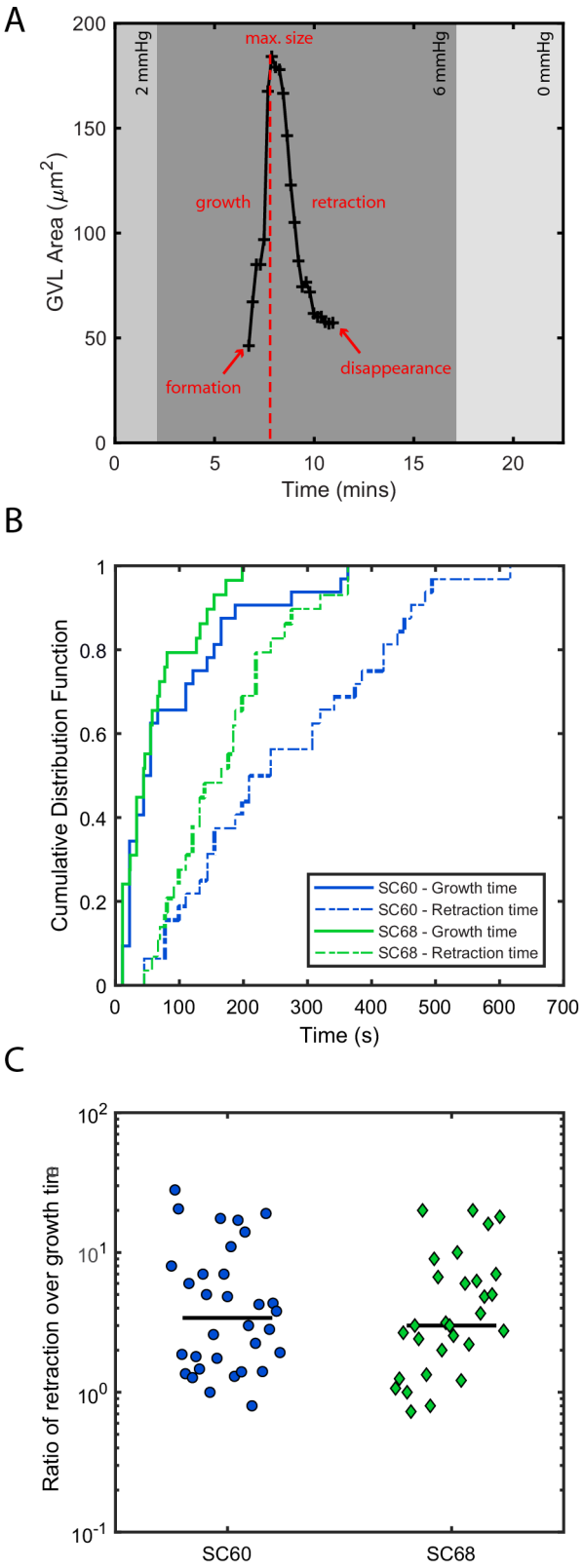


Figure 2.7: **Characteristics of the GVL life cycle. (A)** Representative tracing of GVL area over time, with annotations describing the different stages of the GVL life cycle. (Figure caption continues in the next page.)

Figure 2.7: (Continued from previous page.) At fixed pressure many GVLs exhibit a similar life cycle: first they appear, then they grow and reach a maximum size, and finally they retract and eventually disappear. **(B)** The cumulative distribution function comparing GVL growth time and GVL retraction time in SC60 and SC68. Note that only GVLs that both formed and disappeared at 6 mmHg were included in this analysis (n = 33 for SC60 and n = 29 for SC68). **(C)** The ratio of retraction time over growth time for each GVL that formed and disappeared at 6 mmHg in SC60 and SC68. The black lines indicate the median of each group.

2.3.3 Effects of Y-27632 on the life cycle of GVLs

To examine the effects of decreased actomyosin contractility on the life cycle of GVLs, we treated the SCE cells with the ROCK inhibitor, Y-27632 and applied the same perfusion protocol as used for the vehicle treated cells (Movie 3, Digital Supplementary Material). Y-27632 treated SCE cells exhibited an irregular morphology and were narrower than vehicle-treated cells. Basal-to-apical directed perfusion of Y-27632 treated cells led to the formation of GVLs similar to those observed in vehicle-treated cells.

In both the Y-27632 treated and vehicle treated cell layers, there were GVLs present at the start of the time-lapse imaging while the pressure drop was maintained at 2 mmHg. These GVLs had presumably formed during the acclimatisation of the cells at 2 mmHg before the start of time-lapse imaging. In the Y-27632 treated SC68 cell layers, there were close to 3 times as many GVLs per imaged ROI present at 2 mmHg than in the vehicle treated cell layers (Figure 2.8C and D, and Figure 2.9A). In the SC60 cell layers, there was less than a 10% difference in the GVLs per ROI present at 2 mmHg in the Y-27632 and vehicle treated cell layers (Figure 2.8C and Figure 2.9A).

We compared the number of GVLs formed per ROI within 1-minute time intervals in Y-27632 treated cell layers and in vehicle treated cell layers in response to a step increase in pressure drop from 2 mmHg to 6 mmHg (Figure 2.8). In the vehicle treated cells, there was a peak in GVL formation in the first minute interval following the step increase in pressure drop. Y-27632 treatment led to a two-fold reduction in the number of GVLs formed per ROI within the first minute after the increase in pressure drop in SC68 (Figure 2.8B and D), and a near complete arrest of GVL formation in the same time frame in the SC60 (Figure 2.8A and C). While the pressure drop was maintained at 6 mmHg, Y-27632 treatment reduced the average number of GVLs formed per minute interval compared to the vehicle treated cell layers by 50% in SC68 and by 40% in SC60 (Figure 2.8). Overall, Y-27632 treatment reduced the total GVLs formed at 6 mmHg by 70% in SC60 and by 50% in SC68 (Figure 2.9B). In addition, in Y-27632 treated cell layers there were fewer GVLs formed at 6 mmHg than GVLs present at 2 mmHg, while in the vehicle treated cell layers there were more GVLs formed at 6 mmHg than GVLs present at 2 mmHg (compare Figure 2.9A and B).

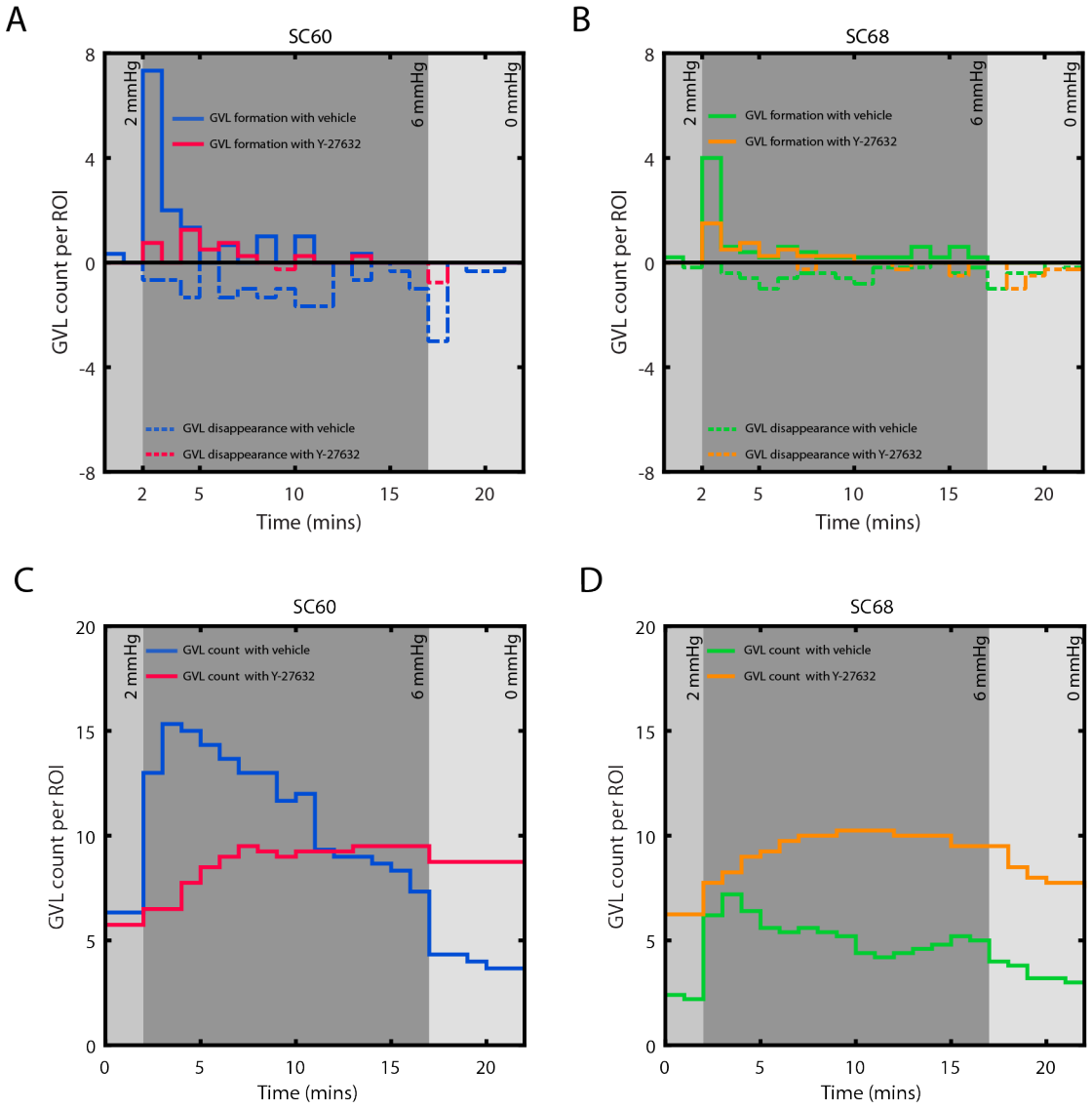


Figure 2.8: **Effects of Y-27632 on GVL formation and disappearance over time and pressure. (A)** and **(B)** Counts per imaged ROI of GVLs that formed (solid lines) and GVLs that disappeared (dashed lines) within each 1-minute time intervals during time-lapse imaging, in SC60 (panel A) and in SC68 (panel B) for each treatment group. GVL disappearance counts are represented as negative numbers while GVL formation counts are represented as positive numbers. Note that each cell layer was only imaged at one ROI. **(C)** and **(D)** GVL counts per ROI in SC60 (panel A) and in SC68 (panel B) for each treatment group within each 1-minute time intervals during time-lapse imaging. Note that the GVL counts per ROI in the first minute interval includes the GVLs that were already present at the start of time-lapse imaging at 2 mmHg.

In vehicle-treated cell layers, GVL retraction and disappearance appeared to be ongoing while the pressure drop was maintained at 6 mmHg. In these cell layers, GVL disappearance was occurring at a higher rate than GVL formation (Figure 2.8A and B), and as a result total number of GVLs present in the cell layers decreased over time (Figure 2.8C and D). Y-27632 treatment almost entirely arrested GVL disappearance while the pressure drop was maintained at 6 mmHg (Figure 2.8A and B). The total number of GVLs present in the cell layers first increased due to GVL formation, and then remained approximately

stable over time as there were very few events of GVL formation and of GVL retraction (Figure 2.8C and D). Overall, in the vehicle-treated cell layers over 50% of all GVLs retracted and disappeared while the pressure drop was maintained at 6 mmHg (Figure 2.10A). Y-27632 treatment significantly reduced the proportion of GVLs that retracted and collapsed while the pressure drop was maintained at 6 mmHg to below 10% (Figure 2.10A, $p < 10^{-5}$ in both cell lines, Chi-squared test on categorical data).

No GVLs formed in either treatment groups and cell lines once the pressure drop was lowered down to 0 mmHg. In the vehicle treated cell layers, close to half of the remaining GVLs retracted and disappeared within five minutes after the decrease in pressure drop (Figure 2.10B). These remaining GVLs corresponded to GVLs that were still present within the 1-minute interval before the pressure drop was reduced from 6 mmHg to 0 mmHg. Strikingly, Y-27632 treatment appeared to arrest GVL disappearance at 0 mmHg as less than 25% of the remaining GVLs present had disappeared within five minutes after the decrease in pressure drop.

Y-27632 treatment tended to increase the maximum size reached by GVLs formed at 6 mmHg, although this difference was only significant for one cell line (SC60, $p < 0.02$ and SC68, $p = 0.33$, Mann-Whitney U test) (Figure 2.11A). We wondered whether the dynamics of GVL growth was also affected by Y-27632 treatment. We looked at the time for growth of GVLs that formed at 6 mmHg including both GVLs that eventually disappeared and those that didn't. We found that GVL growth time was significantly larger in Y-27632 treated cells compared to the vehicle ($p < 10^{-5}$ for both cell lines, Mann-Whitney U-test) (Figure 2.11B).

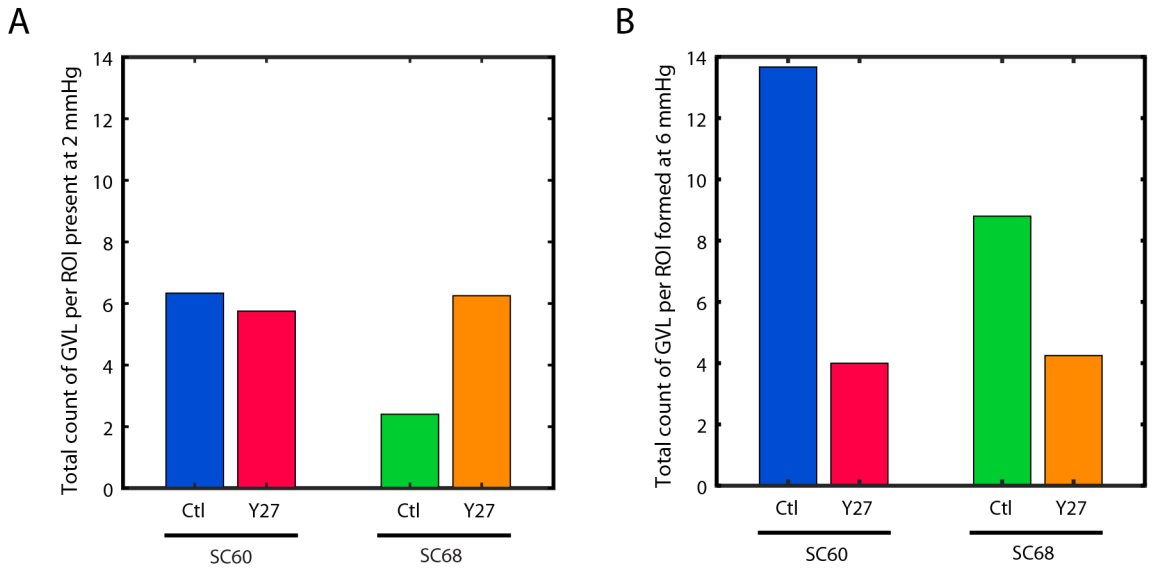


Figure 2.9: **Effects of Y-27632 on GVL formation. (A)** Effects of Y-27632 on the number of GVLs present at 2 mmHg. Most of the GVLs present at 2 mmHg were observed at the start of the time-lapse imaging. These GVLs had presumably formed during the acclimatisation of the cell layers before the start of time-lapse imaging. **(B)** Effects of Y-27632 on the number of all GVLs that formed while the pressure drop was maintained at 6 mmHg.

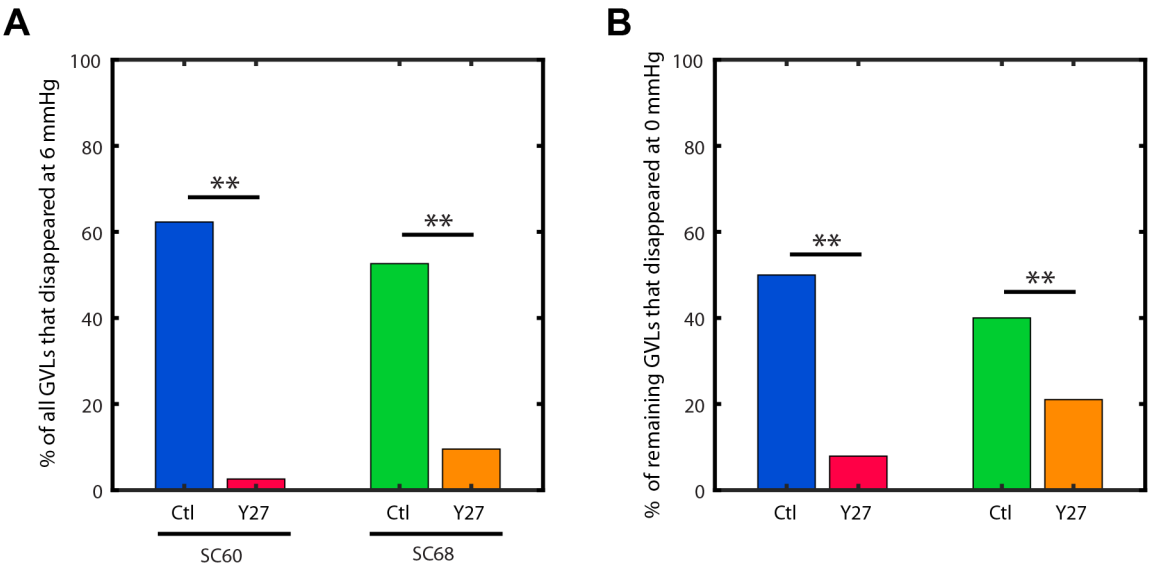


Figure 2.10: **Effects of Y-27632 on GVL disappearance. (A)** Effects of Y-27632 on the proportion of all GVLs that disappeared while the pressure drop was maintained at 6 mmHg. Statistically significant differences are indicated by (**) for $p < 10^{-5}$. **(B)** Effects of Y-27632 on the disappearance of remaining GVLs at 0 mmHg. The remaining GVLs correspond to the GVLs that were still present within the minute interval before the pressure drop was reduced from 6 mmHg to 0 mmHg. Statistically significant differences are indicated by (**) for $p < 10^{-5}$.

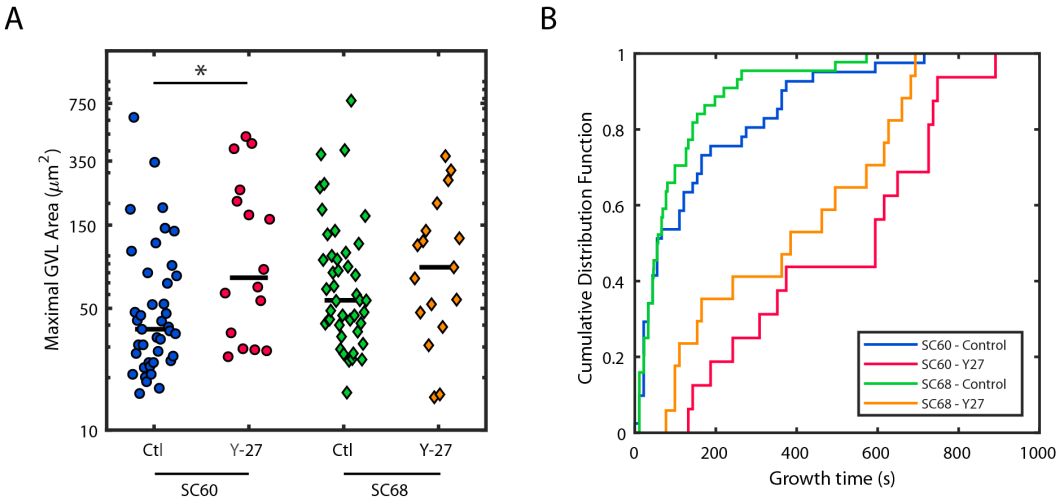


Figure 2.11: **Effects of Y-27632 on GVL maximum size and GVL growth time. (A)** Effects of Y-27632 on the maximum area reached by GVLs. For this analysis, all GVLs formed at 6 mmHg were included. Significant differences are indicated by (*) for $p < 0.02$. **(B)** Effects of Y-27632 on GVL growth time. For this analysis, all GVLs formed at 6 mmHg were included.

2.4 Discussion

Our study demonstrated the existence of a GVL life cycle in SCE cells perfused in the basal-to-apical direction at a fixed pressure drop, including a growth and a retraction phase. We found that GVL re-

traction occurred despite maintaining the pressure drop, and that the GVL retraction phase was longer than the GVL growth phase. Treatment with ROCK inhibitor Y-27632 led to a marked decrease in GVL formation at 6 mmHg and a significant reduction in GVL retraction both at 6 mmHg and 0 mmHg, likely as a result of decreased actomyosin contractility in the treated SCE cells. Together our data suggests that the dynamics of GVL depend both on pressure drop and on actomyosin contractility.

2.4.1 Pressure-dependence of GVL formation and survival

The inner wall endothelium resides within a demanding biomechanical environment. The basal-to-apical pressure drop across the endothelium tends to push the cells off their basement membrane leading to GV formation. The exact magnitude of the pressure drop across the inner wall endothelium is not known definitively and is subject to some controversy [12, 13, 19, 69], but most estimates place it in the range of $\sim$1 mmHg in the normal eye. In this study, we perfused SCE cells in the basal-to-apical direction at transendothelial pressure drops of 2 mmHg and 6 mmHg to drive the formation of GVLs. While the pressure drops applied across the SCE cells were supra-physiological, we did not observe any cell detachment nor cell death, which was consistent with a previous report [33].

To study the dynamics of GVLs we used an adapted version of an *in vitro* experimental platform that allowed for the real-time visualisation of GVL formation during basal-to-apical perfusion at a controlled trans-endothelial pressure drop [33]. There were two key design adaptation from the previous experimental set-up. First, the pressure drop in our current experimental set-up was controlled by a height-actuated fluid-reservoir rather than by a closed-loop fluid pump as used in the previous set-up [33]. Our current pressure-control method allowed for near instantaneous changes in pressure drop. Second, our microscopy acquisition system was synchronised with our pressure control such that we knew precisely the pressure drop at which each image was acquired. In virtue of both of these features, we were able to directly examine the role of pressure drop on the dynamics of GVL formation. This is an improvement compared to previous studies investigating the effects of pressure drop on true GVs *in situ* or on GVLs *in vitro* which were carried out by looking at perfusion-fixed eye tissue [34, 37, 53] and perfusion-fixed SCE cells [33, 93] respectively.

Previous studies in eye tissue demonstrated that true GVs *in situ* are pressure-dependent structures that increase in size and density with increasing transendothelial pressure drop, and that are largely absent in the absence of a transendothelial pressure drop across the inner wall endothelium [34, 37, 78]. In our current study, we observed that there was a peak in GVL formation in the minute interval following an acute step increase in pressure drop between 2 mmHg and 6 mmHg, and that GVL formation also continued to occur while the pressure drop was maintained at 6 mmHg for another tens of minutes. We also observed that no GVLs formed before the start of the transendothelial perfusion, and that reducing

the pressure drop to 0 mmHg resulted in an arrest of GVL formation. Together, our findings directly demonstrate that GVL formation depends on the existence of a transendohtelial pressure drop and that it occurs in response to both acute and sustained transendothelial pressure drop.

Within five mins after lowering the transendothelial pressure drop from 6 mmHg to 0 mmHg, there was a retraction and disappearance of between 40% to 50% of the GVLs remaining in the minute interval before the lowering of pressure drop. Comparatively, Brilakis and Johnson reported that there was $\sim$70% fewer GVLs in immersion-fixed human eyes that were fixed three minutes after the pressure drop had been lowered down to 0 mmHg compared to in perfusion-fixed eyes [78]. While the fraction of GVLs that disappeared after the removal of pressure drop was lower in our study than in that of Brilakis and Johnson, our results nonetheless directly confirm that GVL survival depends on the existence of a transendothelial pressure drop.

2.4.2 Effects of Y-27632 on the life cycle of GVLs

One of the most striking findings of this study was that after forming and growing, most GVLs retracted and disappeared while the pressure drop was maintained at 6 mmHg, demonstrating that GVLs do not remain open once formed but are instead cyclically forming and disappearing. Our observations directly confirms the existence of a GVL life cycle model as proposed by Tripathi in the 1970s [39] (also refer to 1.13 in 1). Furthermore, by perturbing actomyosin contractility in the cells with Y-27632 treatment, we were able to identify a possible mechanism for GVL retraction. Y-27632 treatment appeared to reduce the ability for GVL retraction to occur both while pressure drop was maintained at 6 mmHg and after the pressure drop was reduced to 0 mmHg. Taken together, these observations suggest that GVL retraction in part depends on actomyosin contractility, even after the removal of pressure drop. This finding may further help explain why GVL retraction time is shorter than GVL growth time as it suggests that each of these phases of the life cycle of GVLs may be governed by different mechanisms: GVL growth likely is largely pressure-driven and occurs by the passive filling of the GVL cavity whereas GVL retraction likely depends on actomyosin contraction against the pressure drop. As Y-27632 treatment results in reduced ability of GVLs to retract and to a lengthened GVL growth time, it is also possible that GVL retraction may be needed to arrest GVL growth.

In situ in the inner wall endothelium of SC, true GVs are associated to transendothelial pores. Together GVs and pores are thought to act as channels for the flow of aqueous humour across the endothelium [20, 29–31, 35, 42, 50, 51]. Cultured SCE cells have previously been reported to form transendothelial pores in response to basal-to-apical directed perfusion [17]. In this study, we did not directly assess pore formation, however given the known pore-forming ability of cultured SCE cells, it possible that the GVL retraction observed while the pressure drop remained fixed resulted from pore formation.

We speculate that pore formation in the GVL wall would lead to a reduction of the pressure drop across the GVL wall and to the release of the fluid contents from the GVL cavity. As retraction appears to be dependent on actomyosin contractility even when the pressure drop is lowered to 0 mmHg, we speculate that GVL retraction will require some actomyosin contraction even if a pore forms and reduces the pressure drop across the wall of the GVL. Alternatively, GVL retraction may result from the ability for the SCE cells to contract against an applied pressure drop, without the need for pore formation. A hypothetical schematic representation of the life cycle of GVLs and of the different retraction mechanisms possible is presented in Figure 2.12.

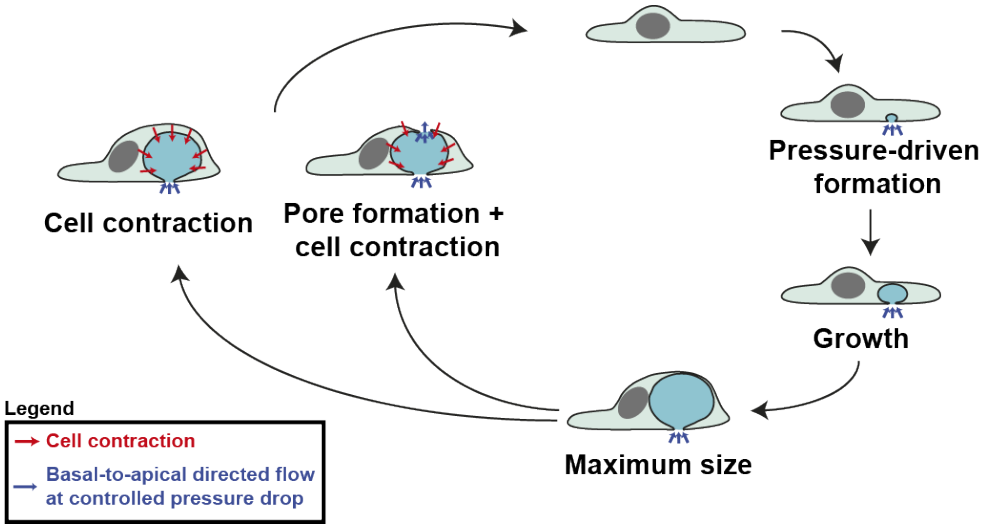


Figure 2.12: **Hypothetical GVL life cycle model.** The hypothetical life cycle model proposed is based from the conclusions drawn from this study. In this life cycle model, pressure drop leads to the local detachment of cell from its substrate leading to GVL formation. The GVL then grows as it fills with the inflow of fluid. Two GVL retraction mechanisms are considered: (i) retraction occurs only due the actomyosin contraction against the applied load, and (ii) a pore forms which reduces the pressure drop across the wall of the GVL, but actomyosin contraction is still needed to help retract the GVL. After retraction, the GVL disappears completing the life cycle. A new GVL can then form in the cell.

The reduction of GVL retraction and collapse observed in response to treatment with the ROCK inhibitor Y-27632 resulted in a longer GVL survival time. This is interesting to put in the context of the reduction in outflow resistance measured in porcine eyes treated with Y-27632 [86] and in monkey eyes treated with H-7 [63], another type of ROCK inhibitor. While it has previously been proposed that ROCK inhibitors affect outflow resistance by either decreasing the resistance through the JCT underlying the inner wall endothelium or by facilitating pore formation in the inner wall endothelium, neither of these hypotheses have been verified [81]. Our current results sheds light on another possible mechanism that would decrease outflow resistance by allowing flow pathways consisting of GVs and associated pores to remain open for longer before retracting.

We observed that Y-27632 treatment resulted in a reduction in GVL formation at 6 mmHg

compared to vehicle-treated cells. This was surprising as Y-27632 is known to decrease the stiffness in SCE cells [76] and to disrupt focal adhesions in SCE cells [86] and other cell types [85, 94, 95], both cellular events that would be expected to increase GVL formation in response to an applied load. This discrepancy may however be explained by the reduced ability of Y-27632 treated SCE cells to retract existing GVLs, which could be needed to then allow for the formation of new GVLs. In Y-27632 treated SCE cells we observed that the majority of GVLs identified were already present at 2 mmHg at the start of image acquisition. Although we did not visualise the formation of these GVLs given that they formed before the start of image acquisition, this suggests that GVL formation was not arrested at 2 mmHg. This further points to the possibility that GVLs formed at 2 mmHg may have been unable to retract, and it is possible that these persistent GVLs prevented the formation of new GVLs with further increases in pressure drop. Importantly, we note that our finding that Y-27632 treatment tended to increase GVL maximum size and GVL density is consistent with a previous study investigating the effects of Y-27632 treatment in porcine eyes [86].

2.4.3 Limitations of GVL contour tracking method

Using the active contour algorithm we were able to semi-automatically track GVLs over time. Our tracking method however suffered from a bias. Overall the percentage of trackable GVLs compared to the number of identified GVLs was between 30 % and 50 % for all donor cell lines and treatment conditions. The gap between the number of identified GVLs and the trackable GVLs was caused by the impossibility to track the thin and at times dimly fluorescent contour of certain GVLs. This included GVLs that formed very close to the cell edge as well as particularly large GVLs that highly attenuated the lining of the cell around the GVL. In these cases, the contour was not visible even by eye and could thus not be tracked. Another class of GVLs that were not examined in this study were GVLs with complex lobular shapes, which could not be not be tracked by the active contour algorithm (see red asterisk in Figure 2.5 for an example). In view of these limitations, our analysis of the dynamics of GVLs are therefore only representative of the class of GVLs that were tracked, and further studies will have to be conducted to confirm that our conclusions can be extended to most GVLs.

2.5 Conclusion

In conclusion, this study provides direct experimental evidence of the existence of a GVL life cycle as has been previously hypothesised by Tripathi in the 1970s ([53] and refer to Figure 1.13 for an illustration of his model). The life cycle of GVLs can be subdivided into two main phases, including a pressure-driven growth and retraction against an existing load that partly depends on actomyosin contractility. Our findings suggests that true GVs *in situ* may not remain open once formed and may instead be cyclically

opening and closing. This implies that GVs act as dynamic pressure-sensitive valves that may regulate outflow resistance and pressure drop across the inner wall endothelium. Further, the combined *in vitro* set-up and tracking method used in this study provides an opportunity to further investigate the cellular mechanisms that control GVL dynamics, which are likely involved in the regulation of outflow resistance and of IOP.

2.6 Supplementary Material: Movie Captions

Below are the captions for the movies included in the Digital Supplementary Material submitted with this thesis:

Movie 1 - Time-lapse image series of SCE cells (SC68) during basal-to-apical perfusion. Throughout the experiment, the pressure drop is increased from 2 mmHg to 6 mmHg and then is lowered down to 0 mmHg, while time-lapse images are acquired every 11s. GVLs are identified as elliptical void regions within the otherwise uniformly stained cytoplasm of the cells. At 2 mmHg, small and short-lived clusters of GVLs appear to be "bubbling" underneath the cells (magenta arrows) while a few larger GVLs are seen (magenta asterisk). A step increase in pressure drop from 2 mmHg to 6 mmHg results in the appearance of many new GVLs (yellow asterisks). While the pressure drop is kept fixed, many GVLs form, then grow to a maximum size, and finally retract and eventually disappear (inspect GVLs indicated by yellow asterisks as a representative example). Lowering the pressure drop from 6 mmHg to 0 mmHg cause most existing GVLs to retract and to disappear, although some GVLs still exist even 5 mins after the removal of pressure drop. Scale bar: 100 μm.

Movie 2 – Tracking of GVLs using an implementation of the active contour algorithm in Icy Bioimage. To track the GVL, the frame at which the GVL first appeared is identified by eye and a polygonal ROI is manually drawn around the GVL (green contour). The active contour algorithm then uses the user-inputted ROI and parameters to iteratively modify the contour until it converges (red contour). The algorithm then uses the contour it converged to in the first image as a starting contour for the following image in the time series and runs again. This iterative process continues until either the end of the image series is reached or until the contour has shrunk and disappeared (which is what occurs in this particular example). Scale bar: 10 μm.

Movie 3 – Time-lapse image series of SCE cells (SC60) treated with Y-27632 and perfused in the basal-to-apical direction. SCE cells treated with Y-27632 exhibit a narrower and more irregular morphology compared to vehicle-treated SCE cells. The pressure protocol used for the perfusion of the Y-27632-treated cells is identical as that used for vehicle-treated cells: the pressure drop is increased from 2 mmHg to 6 mmHg, and then is lowered down to 0 mmHg, while time-lapse images is acquired every 11s. In the perfused Y-27632-treated cells, GVLs (corresponding to elliptical void regions) are

seen, and these are similar in structure to those observed in the perfused vehicle-treated cells. Scale bar: 100 μm.

3

The F-actin and vimentin structures organised around GVLs in cultured SCE cells

3.1 Introduction

Aqueous humour flows across the inner wall endothelium of SC and generates a transendothelial pressure drop in the basal-to-apical direction. This pressure drop causes a local detachment of the SCE cells from their supporting basement membrane and inflates dome-shaped cellular outpouchings known as GVs [28, 30, 31, 34, 52]. GV formation leads to substantial thinning of the SCE cells and generates strains that likely exceed 50% [41, 69]. On individual electron microscopy sections, GVs have a "signet ring" appearance – SCE cells appear as a thin and continuous lining around the GV cavity, often with the nucleus deformed and bulging to one side. The ability for SCE cells to withstand the large stresses and strains imposed by GV formation likely depends on the composition, architecture and mechanical properties of the cytoskeleton surrounding GVs [69, 96]. The cytoskeletal arrangements surrounding GVs and how these influence GV biomechanics have however not been studied in detail.

While SCE cells contain all three of the main types of cytoskeletal building blocks (microtubules, intermediate filaments (IFs) and F-actin) [72], they are particularly enriched with F-actin and vimentin IFs [35, 71, 72, 74]. In eukaryotic cells, F-actin associates with crosslinkers and myosin motors forming different types of stiff and contractile structures including stress fibres, branched networks, and isotropic networks [96]. F-actin architecture is known to be dependent on imposed mechanical factors in many tissues, including in the inner wall endothelium of SC where it depends critically on the presence of transendothelial flow and pressure drop [64]. In the inner wall endothelium, F-actin is thought to to be important for the maintenance of cell-cell junction integrity and the anchorage of cells to their substrate [30, 35, 52, 64]. Vimentin filaments and networks are less stiff than actin filaments and networks respectively [97]. Unlike F-actin networks, vimentin networks stiffen with increasing strain and resist breakage even at high strains [97]. In virtue of these mechanical properties, vimentin is important in maintaining cellular shape and integrity in many cell types. In SCE cells *in situ*, vimentin likely helps support the large stresses and strains resulting from transendothelial flow and pressure drop across the inner wall endothelium. The F-actin and vimentin IF structures surrounding GVs requires further examination to determine their role in GV biomechanics.

Previously, we established an *in vitro* model to study the dynamics of GVLs that are morphologically similar to true GVs found in vivo in the inner wall endothelium of SC [33] (also refer to Chapter 2 of this thesis). Using this model, we found that transendothelial perfusion with the ROCK inhibitor Y-27632 modified GVL dynamics, and in particular the ability for GVLs to retract against a pressure drop. Given that Y-27632 is known to decrease on actomyosin contractility, this finding further suggests that the F-actin-based cytoskeleton influences GV biomechanics. The effects of Y-27632 on the cytoskeletal organisation surrounding GVs, however, remains to be determined. In this study, we used confocal fluor-

escence microscopy to visualise the F-actin and vimentin IF organisation in perfusion-fixed SCE cells, and in particular around GVLs, and compared this organisation with and without Y-27632 treatment.

3.2 Materials and methods

3.2.1 Experimental design

The aim of the study was first investigate the organisation of F-actin and vimentin IFs in perfusion-fixed SCE cells and particularly around GVLs, and second to look at the effects of Y-27632 treatment on the organisation of these cytoskeletal filaments.

Human SCE cells were isolated from a healthy donor (SC68, donor aged 30). The cells were seeded at passage 5 at 20,000 cells/cm^2 on the bottom-facing surface of a filter membrane held by a culture insert. The cells were cultured for 2 to 3 days after seeding, until they covered the filter membrane uniformly. The methods used for human SCE cells isolation and for cell seeding onto filter membranes were the same as those described in Chapter 2, and will not be repeated here.

The SCE cells were perfused in the basal-to-apical direction at controlled pressure drops, and were maintained in a temperature and CO_2-controlled incubator throughout the entire perfusion. The pressure drop was controlled using a custom-built perfusion system which measured both the pressure drop and the flow through the system. SCE cells were perfused first at 2 mmHg then at 6 mmHg, using a similar protocol as that described in Chapter 2. The SCE cells were perfused with filtered DMEM with 25 μM Y-27632 or filtered DMEM with the vehicle. After the end of the first part of the perfusion protocol, the SCE cells were perfusion-fixed at 6 mmHg by replacing the DMEM-based perfusate by fixative. Unperfused control cell layers seeded on the same day as the other cell layers, were treated either with Y-27632 or with the vehicle for the same duration as the perfused samples, and were then fixed at 0 mmHg.

Fixed samples were stained for the nucleus, the cytoplasm (to identify GVLs), F-actin and vimentin, and were imaged using Z-series confocal microscopy. Cytoskeletal structures found around GVLs were quantified and compared between the Y-27632 and control groups.

3.2.2 Sample preparation for perfusion

The experimental set-up used for the basal-to-apical perfusion and perfusion-fixation of the cell layers is showed in Figure 3.1. The inside of the cell culture inserts were washed to remove FBS and then filled with filtered DMEM with 1% PSG. A silicone stopper was subsequently fitted inside of the insert to create a leak-proof seal and to introduce a small chamber between the apical surface of the membrane and the silicone stopper. Prior to fitting the stopper inside of the insert, (i) a thin piece of tubing (length:

$\sim$ 50 mm; OD: 1.98 mm, ID: 1.02 mm, Portex 800/100/300, Smiths Medical, USA) was inserted in a punched 1.5 mm hole through the stopper, (ii) another longer thin piece of tubing was inserted in another punched 1.5 mm hole through the stopper (length: $\sim$ 100 mm), (iii) and a 19G needle was then threaded elsewhere through the stopper. The tubing and the needle fitted through the stopper served to shunt any pressure spikes that would otherwise damage the cells during the fitting of the stopper inside of the insert.

Once the stopper was placed inside of the insert, first a larger piece of tubing (OD: 3.2 mm; ID: 1.6 mm, C-Flex, 06422-02, Saint Gobain, France) filled with filtered DMEM was fitted onto the shorter thin tube ((i) in above paragraph) in the stopper. DMEM was then pushed through the tubing, into the chamber inside of the insert and out of the needle to flush out any bubbles. Next, as part of the set-up for perfusion-fixation, the longer thin tube ((ii) in above paragraph) was filled with DMEM and was then connected to a larger piece of tubing filled with 4% paraformaldehyde (PFA). The tubing line filled with PFA was shut off by a 3-way valve throughout the first part of the perfusion protocol, and was only open during the perfusion-fixation. This configuration ensured that no PFA was in contact with the DMEM inside of the culture insert before fixation had begun. After all tubes had been connected, the 19G needle ((iii) in above paragraph) was carefully threaded out of the stopper.

Immediately prior to perfusion, the culture insert and tubing assembly were placed in an insert adaptor (Artificial Membrane Adapter, 0420011301, Bioptech, USA) with the cells facing downwards, and the adapter was placed in a 35 mm dish that was filled with culture medium (81218-200, Ibidi, Germany). A custom-made 3D printed holder was adjusted over the insert and adapter to hold the culture insert and tubing still. The cell layers were then examined under a tissue culture brightfield microscope for integrity. Any cell layer damaged duringg preparation were discarded. The culture insert and tubing were placed in a tissue culture incubator.

3.2.3 Pressure-controlled perfusion system

To control the pressure drop applied across the culture insert filter and cells we used a custom-made perfusion system. The perfusion system was adapted from a previously described system (*iPerfusion* [90]). In this system, the pressure drop (ΔP) applied across the filter and cell layer is controlled using a reservoir filled with water coupled to a vertically mounted linear actuator (L35, Nanotech, Germany, resolution of 1.25 µm per step). The pressure applied across the filter and cells is monitored throughout the perfusion by a wet-wet differential pressure transducer (PX409, Omega Engineering, USA; measurement range: 0 to 50 mmHg, uncertainty: 0.04 mmHg). Flow through the filter and cells (Q) is also measured using an in-line thermal flow meter (SLI430, Sensirion, Switzerland; measurement range: -120 μl/min to 120 μl/min, uncertainty: 5% of measured value). A custom-written LabView (National Instruments, USA) program controls the whole system and is used to record the pressure and flow meas-

urements. Together, this perfusion system allows for an accurate control of the pressure drop applied, for almost immediate changes in the applied pressure, and for a precise measurement of ΔP and Q.

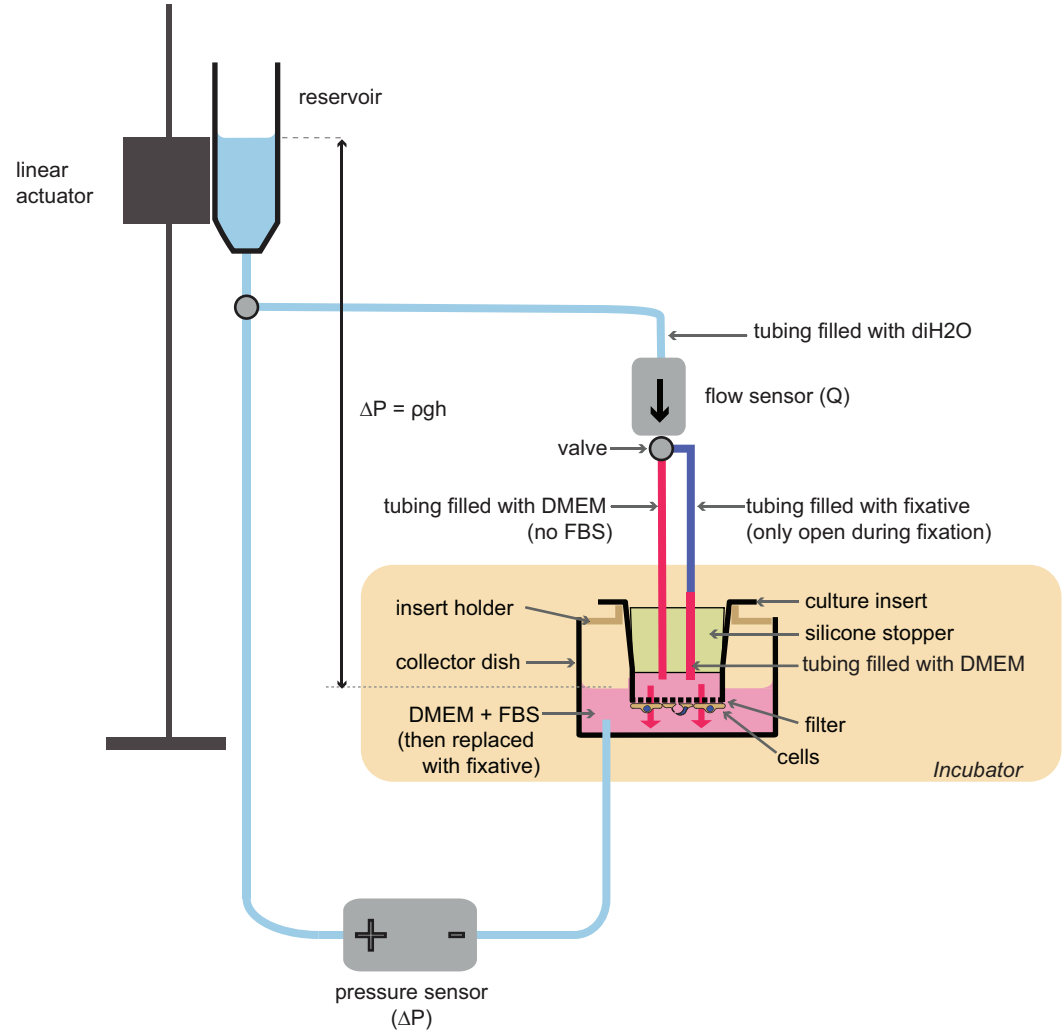


Figure 3.1: **Experimental set-up used for the basal-to-apical perfusion and perfusion-fixation of cultured SCE cell layers.** The pressure drop (ΔP) applied across the cells and filter is controlled by a reservoir filled with diH_2O coupled with a linear actuator. The applied pressure drop drives a basal-to-apical directed flow cross the cells and filter (red arrows). The culture inserts are maintained in a cell culture incubator throughout the entire perfusion. In the first part of the perfusion, the cells are perfused with DMEM without FBS, and the valve leading to the tubing filled with fixative remains closed. Throughout the first part of the perfusion the apical surface of the cell layer is in direct contact with culture medium containing serum (DMEM + 10% FBS). For fixation-perfusion, the valve leading to the tubing filled with DMEM is shut off and opened to the tubing filled with fixative instead. Fixative then flows into the culture insert, progressively replacing the DMEM inside the insert. When almost all of the DMEM inside the culture insert is replaced by fixative, we replace the culture medium in the culture dish with fixative while continuing to perfuse the cells with fixative. The ΔP and flow (Q) across the cells and filter are measured throughout the perfusion experiment. Note that the flow rate is low enough such that there is no significant mixing between the DMEM and diH_2O during the perfusion, and the volume of DMEM contained the tubing is always larger than the total volume perfused. ρ: density of the fluid in reservoir, g: gravitational acceleration, h: height or the fluid reservoir. Note that the end of tubing line containing fixative is filled with DMEM; this is to ensure that the cells are not exposed to fixative in the first part of the perfusion protocol

3.2.4 Perfusion protocol and fixation method

Once the system had been calibrated and tested, the tubing leading to the culture insert was connected to the perfusion system while the culture insert was still maintained in the incubator. The pressure drop initially applied across the filter and cells was set to 0 mmHg. Immediately prior to the start of the perfusion recordings, the pressure and flow measurements were both checked to confirm that they were very close to 0 mmHg and 0 μl/min respectively.

In this study, the SCE cells were first perfused following a similar pressure protocol as in Chapter 2. Briefly, after about 5 mins at 0 mmHg, a 2 mmHg pressure drop was applied across the filter and cells. As the SCE cells were seeded on the bottom-side of the filter membrane, a positive pressure drop drove perfusion medium to flow in the basal-to-apical direction across the cells. The pressure drop was held at 2 mmHg for approximately 45 mins. The pressure drop was then increased to 6 mmHg and held at this pressure for approximately 10 mins.

The cell layers were then perfused with fixative instead of DMEM in the basal-to-apical direction at 6 mmHg (Figure 3.1). After 10 to 15 mins of perfusion with fixative, DMEM in the chamber between the top-facing surface of the filter membrane and the silicone stopper was almost entirely replaced by fixative. The culture medium in the collector dish was then replaced by fixative such that the cell layers were in contact with fixative on both their apical and basal side. Perfusion at 6 mmHg continued for an additional 10 mins. The perfusion was stopped by lowering the reservoir to 0 mmHg, and the fixative in the collector dish was replaced with DPBS.

The culture inserts were detached from the perfusion system and the stopper was removed. Prior to removing the stopper, the tubing threaded through the stopper was opened to atmosphere to shunt any pressure spikes that would otherwise occur during stopper removal and could damage the cell layers. The culture inserts were then placed in a well-plate containing DPBS. The cell layers were examined to confirm that they were not damaged; undamaged cell layers were finally stored in DPBS at 4°C Unperfused control samples were fixed in a culture plate for 10 mins, and were then washed and placed in PBS and stored at 4°C.

3.2.5 Drug treatment

For each perfusion experiment, the cell layers were treated with either 25 μM Y-27632 or an equivalent volume of diH_2O (vehicle). Y-27632 (or the vehicle) was added to the perfusion medium in the tubing and to the culture medium in the collector dish. In this way the cell layers were in contact with Y-27632 (or the vehicle) both on their apical and basal side, and there was no dilution of the Y-27632 (or the vehicle) during perfusion. For each treatment condition, at three different cell layers were perfused.

3.2.6 Immunocytochemistry and fluorescent labelling

For preparation for confocal microscopy imaging, the cells were labelled to visualise the nuclei, vimentin IF, F-actin and the whole cell body. The membrane filter on which the cell layers were cultured was peeled off from the plastic housing of the culture insert using fine forceps, and it was placed cells facing up in a 48 well-plate filled with DPBS. Cells were permeabilised with 0.1% Triton-X buffer in DPBS for 10 mins then blocked with 10% goat serum and 0.2% Tween-20 for 1 hr. To visualise vimentin IF, the samples were incubated in 1:50 rabbit anti-vimentin IgG primary monoclonal antibody diluted in 0.2% Tween-20 and 1% goat serum (ab92547, Abcam, UK) overnight at 4°C. The primary antibody was then removed, the cells were washed in 0.2% Tween-20, then incubated for 1 hr at room temperature in 1:200 secondary antibody (Alexa 488 goat anti-rabbit, A-11034, Invitrogen, Thermo Fisher Scientific, USA), and finally washed with DPBS.

To visualise F-actin and the whole cell bodies, the cells were incubated for 30 mins in 1:200 fluorescent-labelled phalloidin (Alexa 568 phalloidin, A12380, Invitrogen, Thermo Fisher Scientific, USA) and in 1:100 HCS CellMask (HCS Cell Mask Deep Red/Alexa 647, H32721, Invitrogen, Thermo Fisher Scientific, USA) respectively. Finally, the nuclei were labelled by incubation in 1:1000 DAPI (D1306, Thermo Fisher Scientific, USA) for 10 mins.

After a thorough wash in DPBS, the samples were mounted onto a glass slide such as the cells faced up towards the coverslip. A 0.12 mm thick spacer was placed over the periphery of the filter membrane to hold it down and to avoid compression of the cell layer (in particular of the GVLs) by the coverslip. The samples were covered by mounting medium (Prolong Diamond Antifade, P37965, Invitrogen, Thermo Fisher Scientific, USA) and then with a coverslip.

3.2.7 Confocal imaging

Cell layers were imaged using a Leica SP-8 scanning confocal microscope (Leica Microsystems, Germany) equipped with four separate lasers (Diode 405, Argon 488, Diode 561 and Diode 633) and four different confocal acquisition channels permitting simultaneous visualization and collection of four different fluorophores. The confocal microscope was set-up automatically using the company-provided software to sequentially acquire by line scan four different fluorescent probes with minimal bleed through: DAPI (Emission/Excitation wavelength: 358/461 nm) , Alexa 488 (490/525), Alexa 568 (578/603) and Alexa 647(650/665). All images were acquired at 16-bit grey level scales and using a line averaging of 4.

Images were acquired using a 40x objective (oil immersion, NA: 1.3) for general cytoskeletal inspection and for the quantification of cytoskeletal structures around GVLs. For each cell layer, images

were acquired at a single ROI acquired at 1024x1024 pixels without additional optical zoom (square pixel resolution: 0.28 μm/pixel). A series of adjacent optical sections (Z-series) were acquired starting at the membrane filter just below the cell layer, and ending just above the cell layer where close to no fluorescent signal was observed. The pinhole opening was set to 1 Airy unit and the interval between Z-series was set to 0.28 μm to meet the Nyquist theorem requirements.

For detailed examination of the cytoskeletal structures surrounding individual GVLs, Z-series of ROIs containing putative GVLs were acquired using a 63x objective. The pinhole opening was set to 1 Airy unit and the interval between Z-series was set to 0.24 μm to meet the Nyquist theorem requirements. Images of 1024x1024, 1024x512 or 1024x256 pixel dimensions were acquired. Note that this did not change the resolution of individual pixels but simply decreased the area imaged to speed up acquisition. For some GVLs of interest, a zoom between 2 and 4 was applied such that the pixel resolution was close to that required by the Nyquist theorem. Images acquired at the Nyquist sampling rate were deconvolved using Huygens software (Scientific Volume Imaging, The Netherlands).

3.2.8 Cytoskeletal structure quantification

The number of nuclei and the number of GVLs with an F-actin band and/or a vimentin cage (refer Section 3.3.2) were quantified in the 40x Z-series acquired for each cell layer perfused. First, GVLs were identified by looking for elliptical voids within an otherwise uniformly fluorescent cell body labelling. To be considered GVLs, these voids also had to appear in multiple successive Z-sections in the Z-series acquired. All GVLs identified using this method were marked as a ROI in ImageJ and were then marked for the presence or not of a vimentin cage and/or an F-actin band.

3.3 Results

3.3.1 Effects of transendothelial pressure drop on F-actin and vimentin architecture

SCE cell layers were perfused in the basal-to-apical direction at 2 mmHg and subsequently at 6 mmHg for altogether approximately 1 hr, and they were then perfusion-fixed at 6 mmHg. Perfused cell layers were first inspected for integrity (Figure 3.2A). No large gaps were however observed in the cell layer that would have otherwise suggested that SCE cells had detached from the filter during perfusion. Compared to unperfused controls, perfused SCE cells had narrower bodies. The perfused cells appeared to overlap less, and there were wider and more frequent spaces intercellular spaces, as if they had retracted away from one another (compare Figure 3.2A and D). Inspection of cross-sections through the cell layers

revealed that perfusion led to an increase in the overall thickness of the cell layer (compare orthogonal views in Figure 3.3A and B). This morphological difference is likely due to the basal-to-apical direction of transendothelial pressure drop applied which tends to push the cells away from the filter.

Transendothelial perfusion led to the appearance of elliptical void regions with a smooth contour and within the otherwise uniformly stained cytoplasm of the cell (Figure 3.2D and Figure 3.3B). These void regions tended to extend along the length of SCE cells, and were visible on several consecutive Z-sections (Figure 3.4 and Figure 3.5). Inspection of cross-sections of these void regions along their short-axis revealed dome-like structures composed of an extracellular ellipsoidal cavity enclosed by a continuous cell lining (Figure 3.7). These structures were consistent with the classic "signet ring" appearance that was originally attributed to true GVs observed along the inner wall of SC [28], and with GVLs observed in perfused SCE cells [33](refer to Chapter 2).

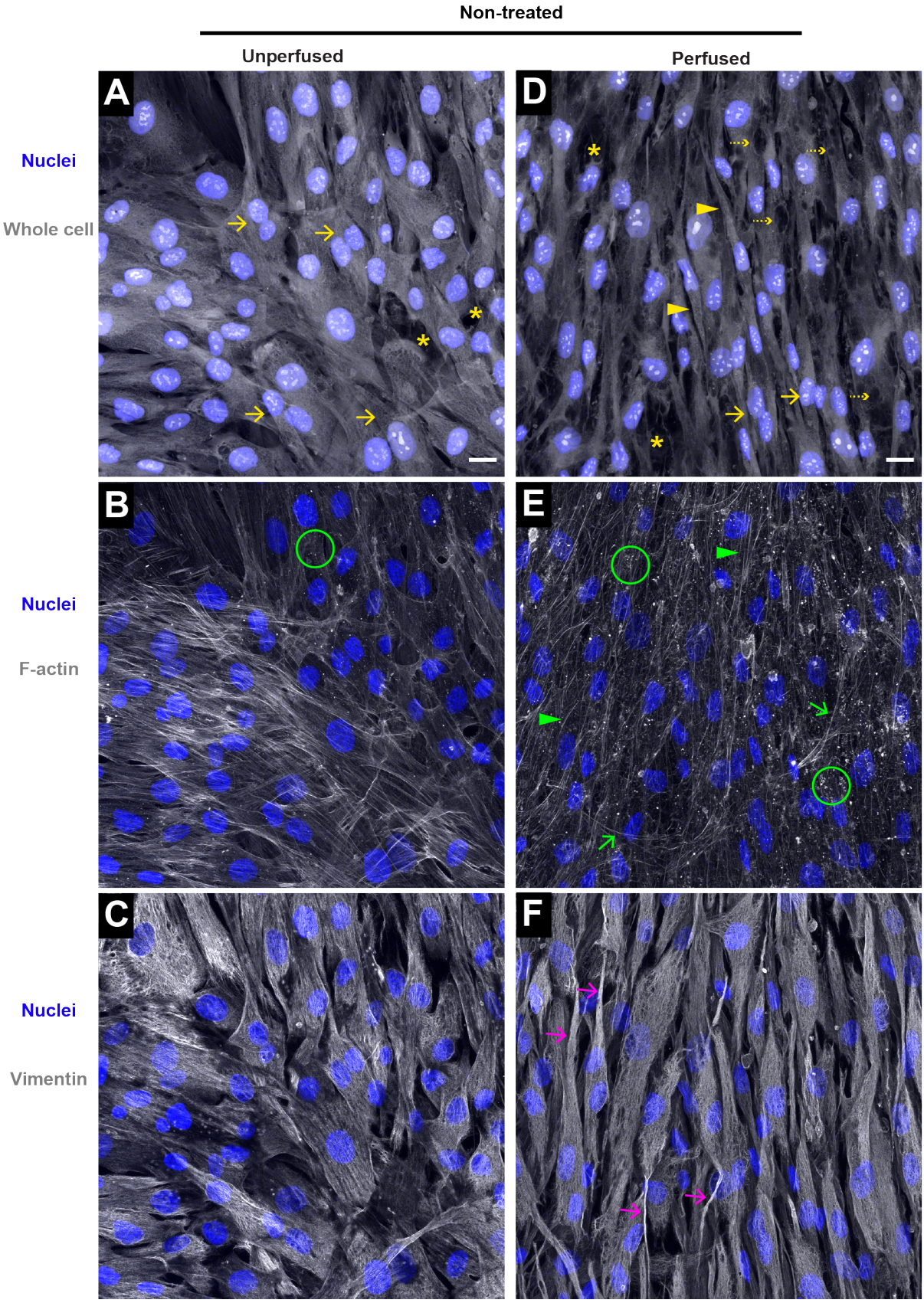


Figure 3.2: **Effects of transendothelial perfusion on SCE cell morphology, F-actin and vimentin architecture.** All images are maximum projections of a confocal Z-series acquired through the thickness of cultured SCE cells using a 40x objective. (Figure caption continues in the next page.)

Figure 3.2: (Continued from previous page.) **(A)** and **(D)** Yellow arrows point to cell-cell overlap identified due to the existence of overlapping nuclei; yellow asterisks indicate intercellular spaces in the cell layers; yellow arrowheads indicate thinned cell bodies in the perfused cell layers; yellow dashed arrows indicate GVLs (note that GVLs are not as sharp on maximum intensity projections as on individual Z-sections, due to the basal and apical cell lining that surrounds them). **(B)** and **(E)** Green circles indicate punctate F-actin staining in the cell layers; green arrowheads indicate some remaining stress fibres in the perfused cell layers; green arrows indicate long F-actin rich cell protrusions contacting neighbouring cells. **(C)** and **(F)** Magenta arrows indicate the thin cell extensions rich in vimentin. Scale bar: 20 μm.

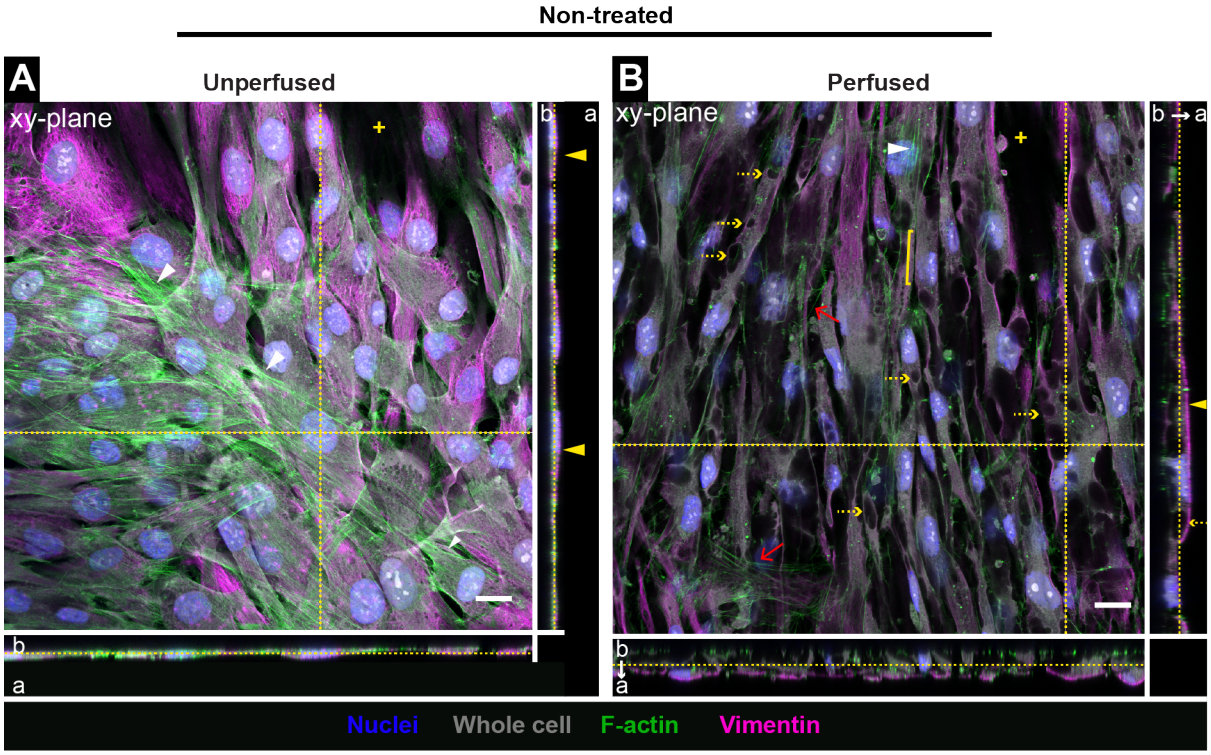


Figure 3.3: **Comparison of cross-section and thickness in unperfused and perfused cell layers.** The central panels of both panel A and B correspond to a confocal scanning micrograph in a single Z-section midway through the cell layer thickness. The lateral images correspond to orthogonal cross sections extracted along the doted yellow lines in the central panels (xz-plane in the bottom panel and yz-plane in the right hand-side of central images). The cross sections span the whole thickness of the cell layer from basal side (b) to the apical side (a); the white arrows in the vertical sections of panel B indicate the direction of flow during perfusion. White arrowheads indicate actin stress fibres; yellow crosses indicate areas that are out of focus at the current Z-section due to the fact that the samples are not perfectly flat; yellow arrowheads demonstrate the preferential apical distribution of vimentin in both unperfused and perfused cell layers; dashed yellow arrowheads indicate GVLs; red arrows indicate F-actin rich cell protrusions contacting neighbouring cells; yellow bracket indicates intercellular spaces between neighbouring cells. Scale bar: 20 μm.

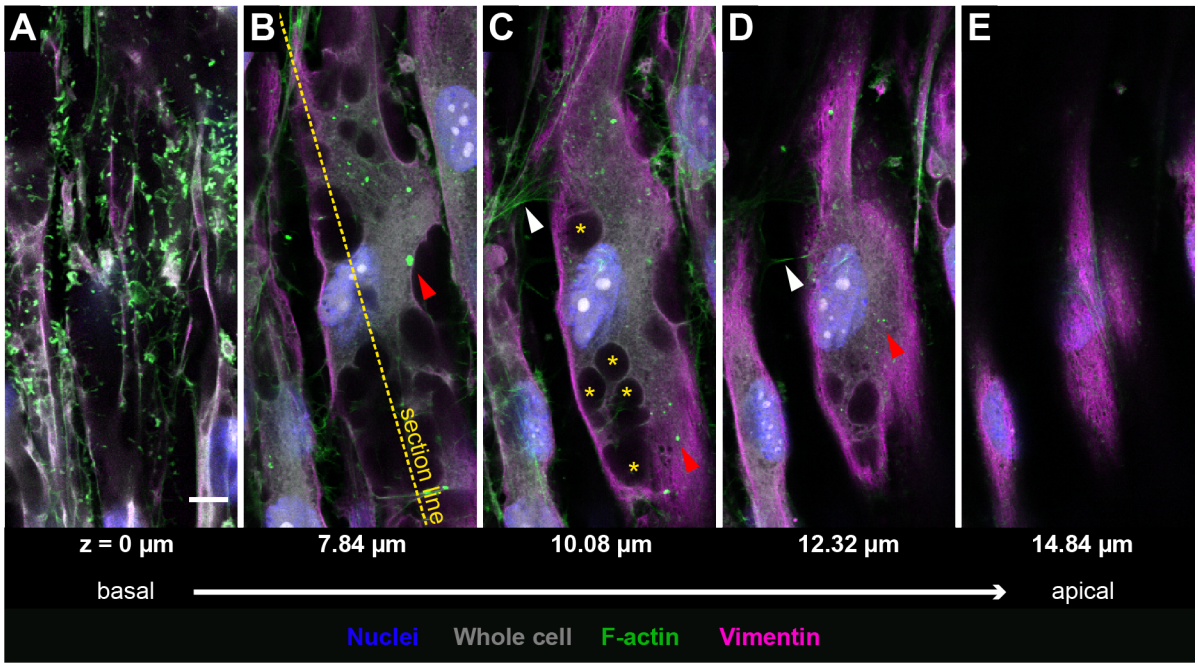


Figure 3.4: **Confocal scanning Z-series through an individual perfused SCE cell. (A)** to **(E)** Each image was image was acquired at a single Z-section (Z-section thickness is 0.28 µm). Note the disorganised and punctate staining of F-actin on the basal side of the SCE cell (red arrowheads). There is also visible punctate F-actin labelling visible within the cell (panel B). Narrow actin-rich processes are seen projecting between neighbouring cells (white arrowhead). Yellow asterisks indicate GVLs in the SCE cells; there are many in the same cell, with some organised into a cluster (panel C). Also note the mesh network organisation of vimentin on the apical side of the cell. The dotted line in panel B refers to the cross-section line for the images presented in Figure 3.5. Scale bar: 10 μm.

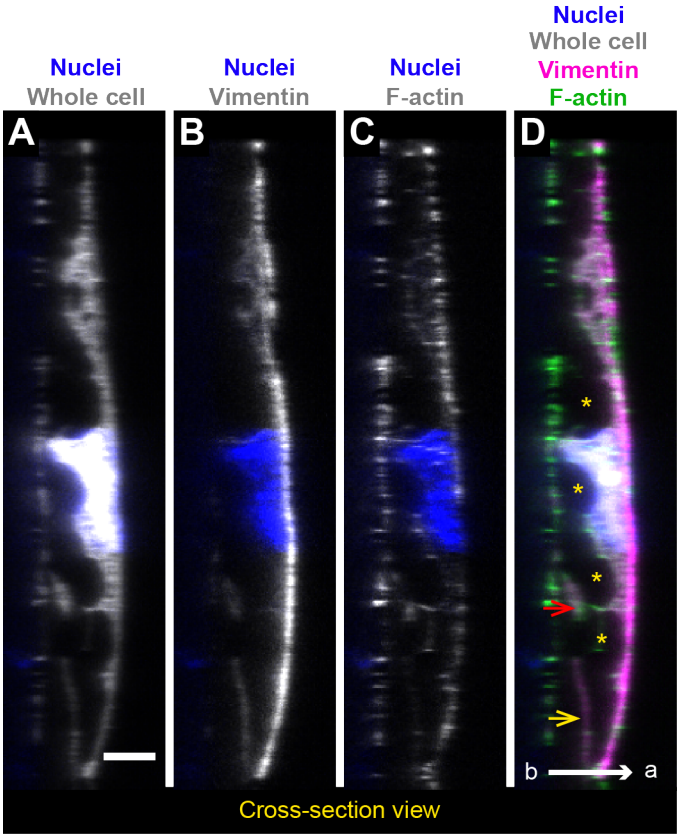


Figure 3.5: **Longitudinal cross-section through an individual perfused SCE cell. (D)** Yellow asterisks indicate GVLs; yellow arrow indicates the vimentin rich apical side of a neighbouring cell; red arrow indicates a septum separating two neighbouring GVLs; b: basal and a: apical. Note the significant nuclear deformation imposed by a GVL forming in the perinuclear region. The cell cytoplasm is very dim, particularly on the basal side of the cell, likely due to cell thinning. F-actin localises both on the apical and basal side of the cell. Vimentin is preferentially observed on the apical side of the cell. Scale bar: 10 μm.

On a number of cells, multiple GVLs of different sizes were visible and these tended to organise in clusters. An average of 1.3 $\pm$ 0.8 GVLs were present per cell nucleus (n = 3, mean $\pm$ SD, Table 3.1). Examination of cross-sections along the long-axis of cells with GVL clusters showed that the different GVLs appeared to be only separated by very thin cytoplasmic septae, which were sometimes enriched with F-actin and vimentin (Figure 3.5). In many cases, there was either a septa with an opening between the neighbouring GVLs, or no septa was present suggesting that fusion of neighbouring GVLs may have occured. It is however also possible that the septae were too thin to be resolved, either purely due to low septae thickness (below microscope resolution) or to low fluorescence intensity within the septae. Alternatively, single GVLs may have a lobular shape with an uneven height, giving the impression of multiple GVLs separated by cell cytoplasm when examining single Z-sections.

Transendothelial perfusion caused significant nuclear deformation (Figure 3.5). Many nuclei appeared to be elongated, perhaps as a result of cell thinning compared to those observed in the control samples (Figure 3.2E). Some GVLs appeared to have formed directly below the nucleus or in the

perinuclear region and caused obvious nuclear indentation and deformation.

Transendothelial perfusion resulted in significant changes in F-actin organisation*(compare Figure 3.2B and E). In control samples, F-actin was mostly organised in prominent stress fibres running through the entire cell and generally aligning along the long-axis of the cell. These findings were in agreement with previous reports [17, 86]. Bright punctate F-actin staining was also noted throughout the body of cells in the control samples. The punctate F-actin staining did not appear to be artefactual as it was only observed within cell boundaries and not in intercellular spaces. In the perfused cell layers, fewer stress fibres were visible in the central areas of the cells, and the overall organisation of F-actin was more irregular. Narrow cell processes filled with F-actin fibres were seen projecting towards neighbouring cells. In perfused cell layers, bright punctate F-actin labelling was also visible throughout the cell bodies, and appeared to be a more frequent occurrence than in the controls. In perfused samples, F-actin was organised differently on the apical and basal side of the cell (Figure 3.4). On the basal side, near the filter, F-actin mostly organised in focal spots, likely to support cell adhesions. On the apical side of the cell, F-actin was organised in randomly oriented short and thin strands.

The spatial distribution of vimentin IFs in SCE cells remained unchanged with transendothelial perfusion. In both the perfused and unperfused samples, vimentin was preferentially observed on the apical side of the cell, and was only faintly visible on the basal side of the cell. This spatial distribution of vimentin organisation is consistent with previous observations reported *in situ* in the human inner wall endothelium of SC [16]. On the apical side of the cell, vimentin was organised in a typical mesh-network. Unlike in other cultured endothelial cells [98, 99], a prominent ring of vimentin was not consistently observed around the nucleus and vimentin was generally not present below the nucleus. In the perfused cell layers, the vimentin was seen in tapered cell protrusions extending at the end of the long-axis of cells. A negative control for vimentin labelling is shown in Figure 3.6. It can be seen that there is some faint nonspecific labelling throughout the cells and occasional nonspecific punctate labelling, but that the overall level of nonspecific labelling is low.

*Out of the three perfusion-fixed samples that were imaged, two samples showed significant differences in F-actin organisation compared to controls. In the third sample inspected and imaged, the changes in the F-actin were more subtle even though, like in the other two samples, the cells were thinner and had many GVLs formed within them.

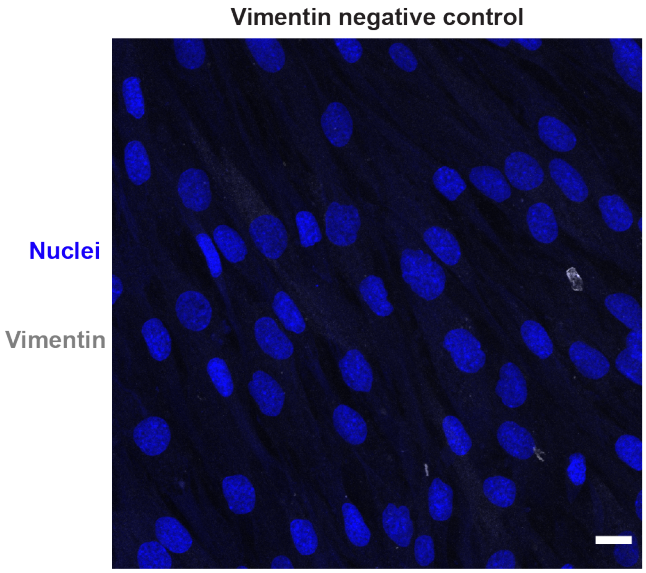


Figure 3.6: **Negative control for vimentin IF staining.** The image presented is a maximum projection of a confocal Z-series acquired at 40x through the thickness of the control cell layer. The control cell layer was not incubated with the vimentin primary antibody but only with the fluorescently-labelled secondary antibody. Scale bar: 20 μm.

3.3.2 F-actin and vimentin organisation around GVLs

F-actin organisation

A closer examination of the perfused cell layers revealed that F-actin lined the periphery of some GVLs, either continuously or partially (Figure 3.7). The F-actin lining was observed in several consecutive Z-sections, suggesting that F-actin was likely organised in a band around the GVL (Figure 3.8 and Figure 3.9). Interestingly, the F-actin lining was not consistently observed around all GVLs, even for GVLs that were on the same cell or even neighbouring one another. Out of 244 GVLs examined, 32% exhibited a peripheral F-actin band (pooled proportion from n = 3 cell layers imaged, Table 3.1).

Vimentin organisation

Vimentin mesh networks were consistently observed covering the apical side of GVLs, although in some GVLs the network appeared to be less dense than over the rest of the apical side of the cell (Figure 3.7). Very little vimentin was present on the basal side of GVLs. Inspection of consecutive Z-sections starting from the apical side of the cells revealed that vimentin also appeared to extend down laterally around the sides some GVLs, suggesting that a vimentin cage enveloped these GVLs (Figure 3.10 and Figure 3.11). Out of 244 GVLs examined, 25% exhibited a vimentin cage (Table 3.1).

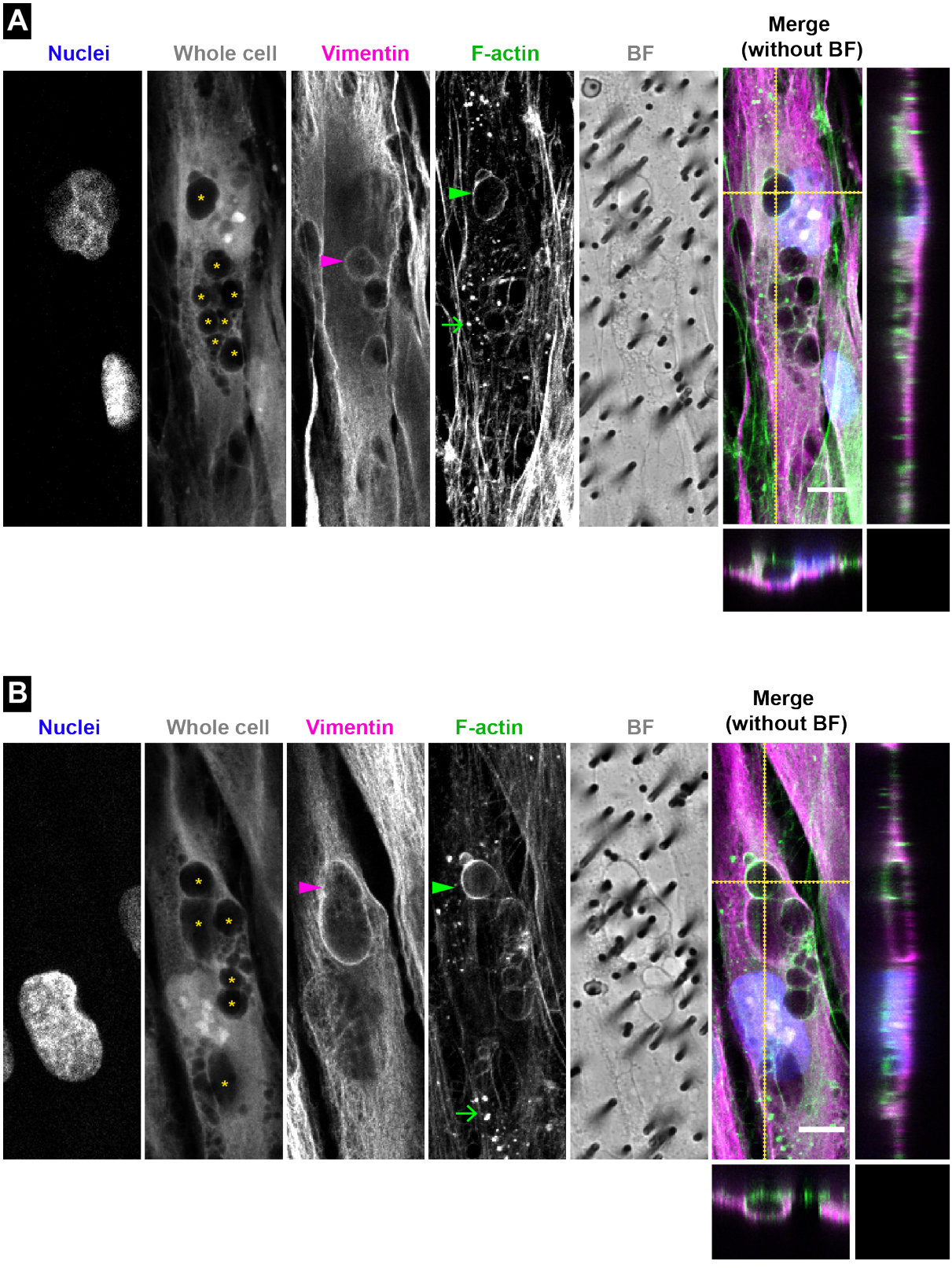


Figure 3.7: **F-actin and vimentin organisation around GVLs.** Panels **A** and **B** show two different cells. For each panel, the images for the different fluorescence channels have not all been acquired at the same Z-position - this is to illustrate specific features that are present at different Z-positions in the cell. The merged imaged is accompanied with orthogonal cross-sections along the dotted yellow lines. From the xz cross-sections (bottom), the typical dome-shaped morphology of the GVLs is visible. Yellow asterisks indicate GVLs; magenta arrowheads indicate the presence of vimentin around the periphery of some GVLs; green arrowheads indicate an F-actin band around the periphery of some GVLs; green arrows indicate punctate F-actin staining within the body of the cells. Scale bar: 10 μm.

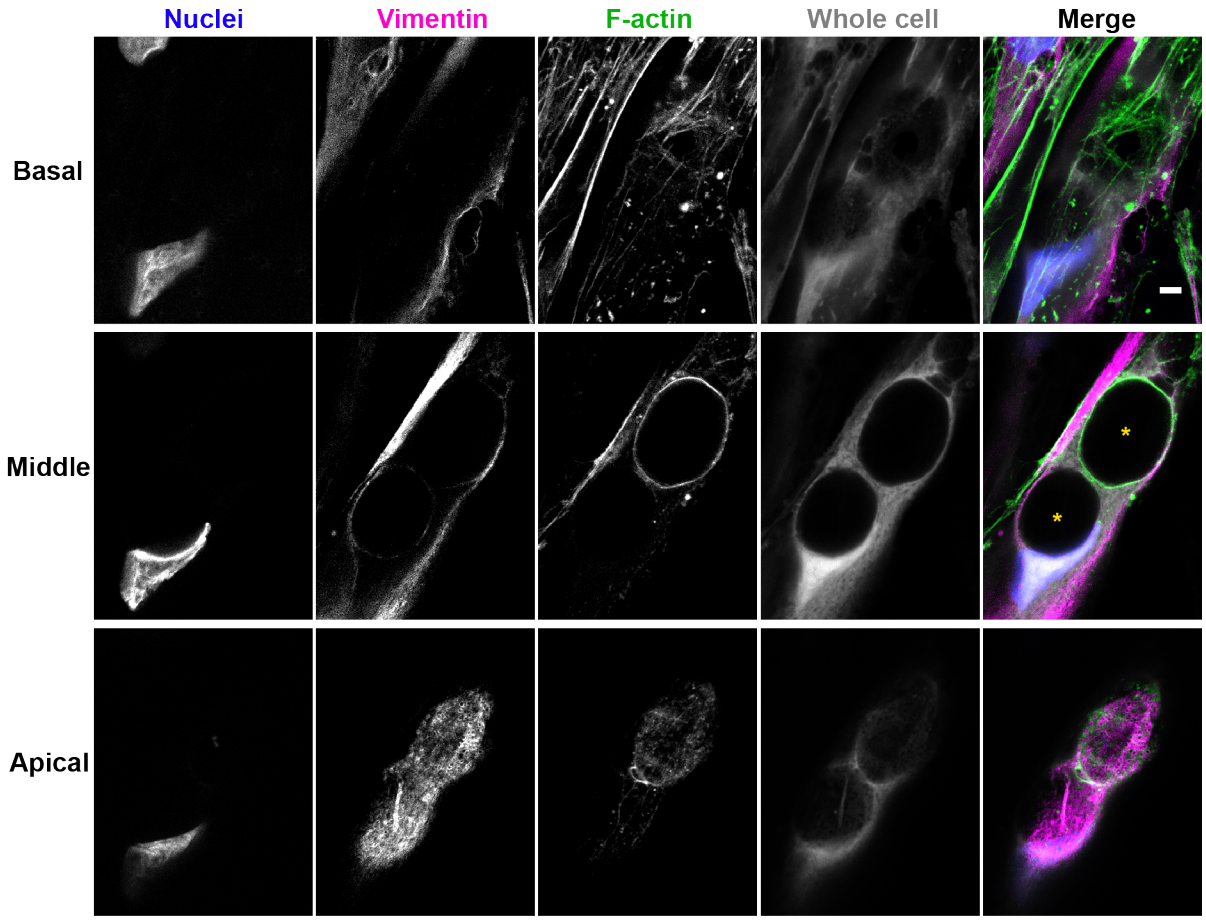


Figure 3.8: **F-actin and vimentin organisation at different Z-sections through a GVL (Part 1).** Note that the cell exhibits two GVLs (yelow asterisks), however only one of the two GVLs is surrounded by an F-actin band. Vimentin is only observed on the apical surface of both vacuoles, and does not form a cage around the rest of the GVL periphery. Scale bar: 5 μm.

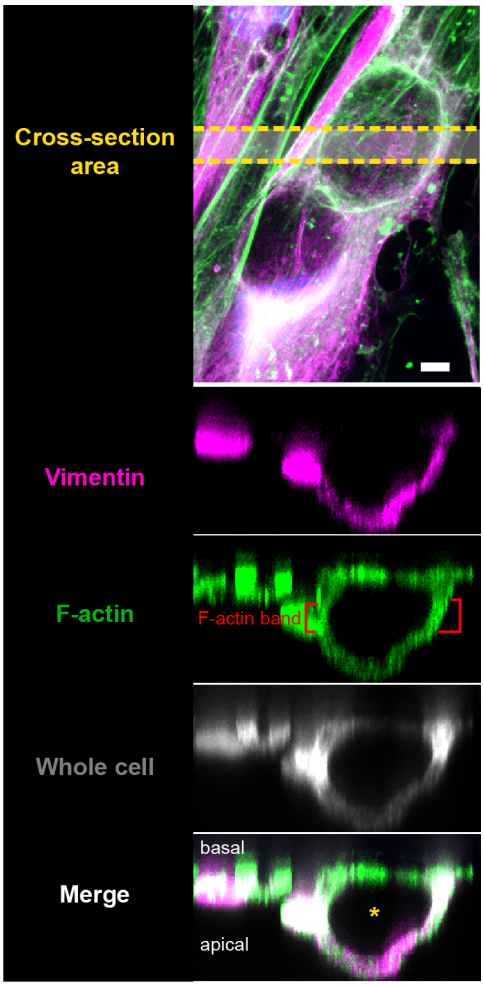


Figure 3.9: **Transversal section through a GVL surrounded by an F-actin band.** Transversal section through the GVL presented in Figure 3.8. The yellow asterisk indicates the GVL cavity. Note the presence of an F-actin band surrounding the GVL. Scale bar: 5 μm.

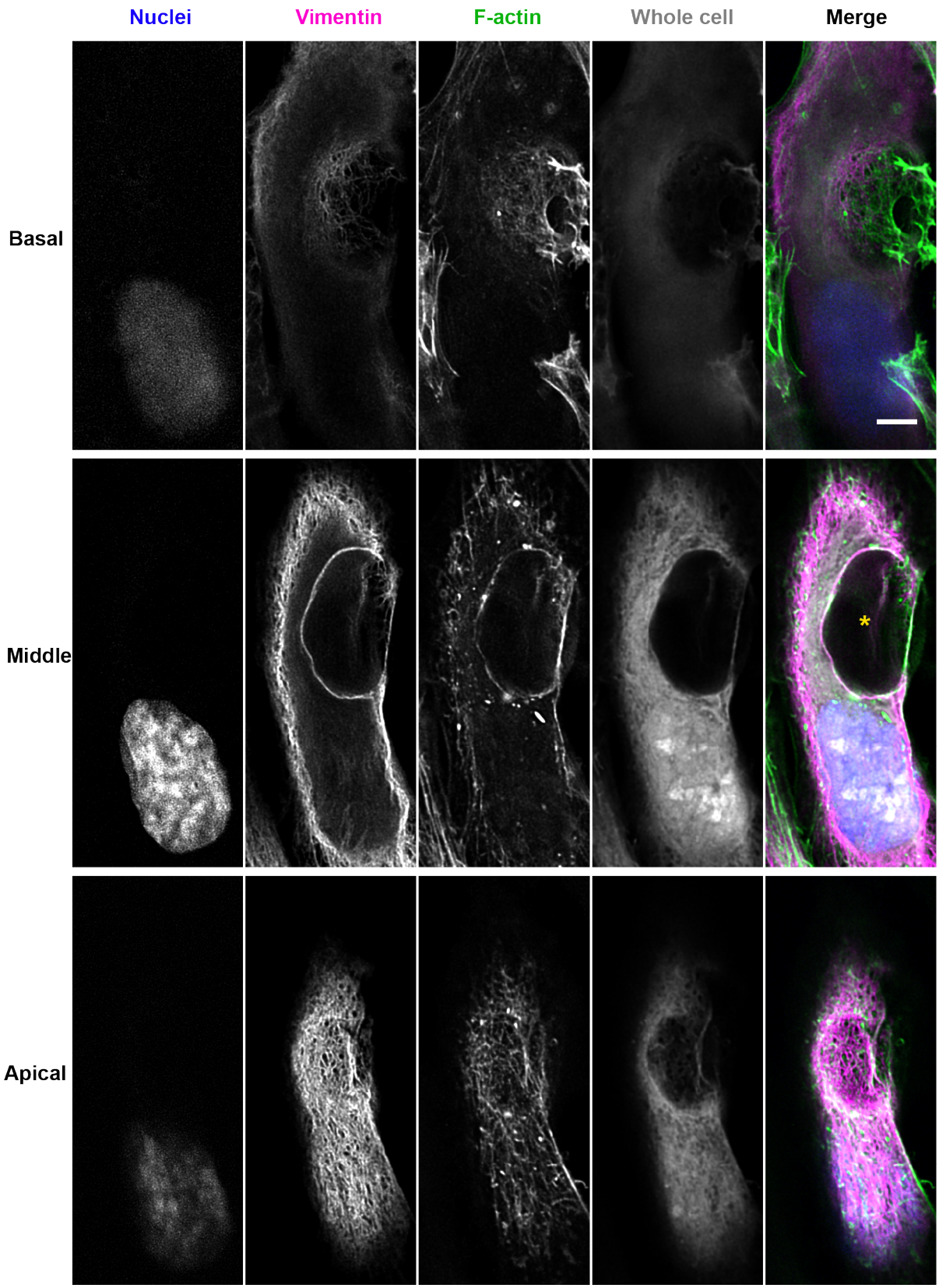


Figure 3.10: **F-actin and vimentin organisation at different Z-sections through a GVL (Part 2).** The images presented were deconvolved. Note the vimentin mesh network on the apical side of the GVL extending around the sides of the GVL and forming altogether a vimentin cage around the GVL. An partial F-actin band is also observed around the GVL. Scale bar: 5 μm.

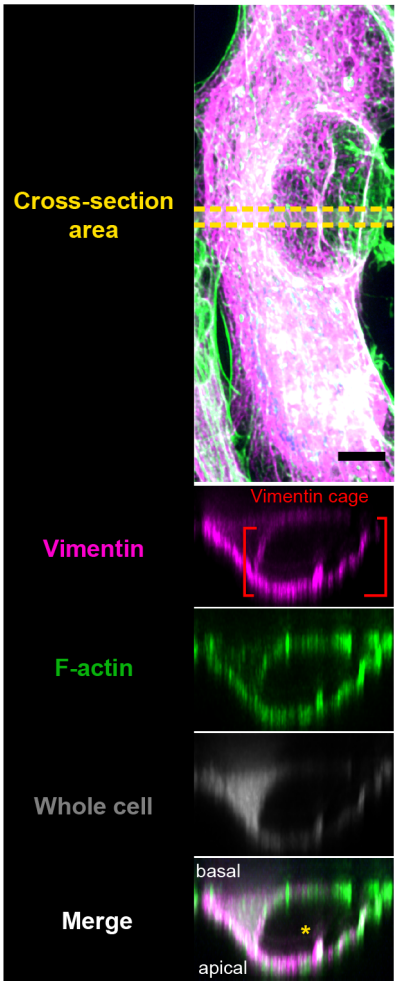


Figure 3.11: **Transversal section through a GVL with F-actin band and a vimentin cage.** Transversal section through the GVL presented in Figure 3.10. The yellow asterisk indicates the GVL cavity. Note presence of vimentin cage around the GVL. Scale bar: 5 μm.

3.3.3 Effects of Y-27632 on F-actin and vimentin architecture

To investigate the effects of decreasing actomyosin contractility on F-actin and vimentin organisation in SCE cells and around GVLs, we treated the SCE cells with Y-27632 (Figure 3.12). In non-perfused SCE cells, Y-27632 treatment led to the thinning of the cells and to more frequent and wider intercellular spaces compared to non-treated controls (compare Figure 3.12A and Figure 3.2A). Cell thinning due to Y-27632 treatment was also apparent from the pattern of vimentin staining , and many cells exhibited slender tapered vimentin-rich extensions along their long-axis. Y-27632 treatment did not however appear to affect the meshwork organisation of vimentin on the apical side of SCE cells (compare Figure 3.3A and Figure 3.13A). The F-actin architecture was severely disrupted in response to Y-27632 treatment, and this was consistent with previous reports [86] (compare Figure 3.12B and Figure 3.2B). Fewer elongated actin stress fibres were present throughout the cells, and many slender actin-rich cytoplasmic protrusions resembling filopodia were observed.

Perfused SCE cells treated with Y-27632 exhibited an irregular shape with a jagged and poorly defined contour. Treatment with Y-27632 treated SCE cells did not result in any significant cell detachment, as verified by quantifying the number of nuclei in cell layers perfused with and without Y-27632 treatment (less than a 10% difference, Table 3.1). Cell shape alterations observed in perfused cells treated with Y-27632 were accompanied by a disorganisation and a loosening of the vimentin mesh networks. F-actin appeared even more disorganised with Y-27632 treatment in perfused cells compared to unperfused cells, and very few actin stress fibres were present throughout the cell (Figure 3.12B and E). Most of the F-actin appeared instead to organise in short and irregular strands, and widespread punctate staining of different sizes was present throughout the cells.

3.3.4 Effects of Y-27632 on F-actin and vimentin organisation around GVLs

GVLs were present in perfused SCE cells with Y-27632 treatment, and these GVLs had a similar morphology to those observed in non-treated cell layers. Furthermore, no significant difference was found between the number of GVLs per nucleus in the treated and non-treated perfusion-fixed cell layers ($p = 0.58$, unpaired t-test, Table 3.1). The proportion of GVLs lined with F-actin, vimentin and both filaments combined was significantly higher in treated compared to non-treated cell layers ($p < 0.001$ for F-actin band, $p < 0.02$ for vimentin cage, $p \ll 0.001$ for both cytoskeletal structures combined, Figure 3.14 and Table 3.1).

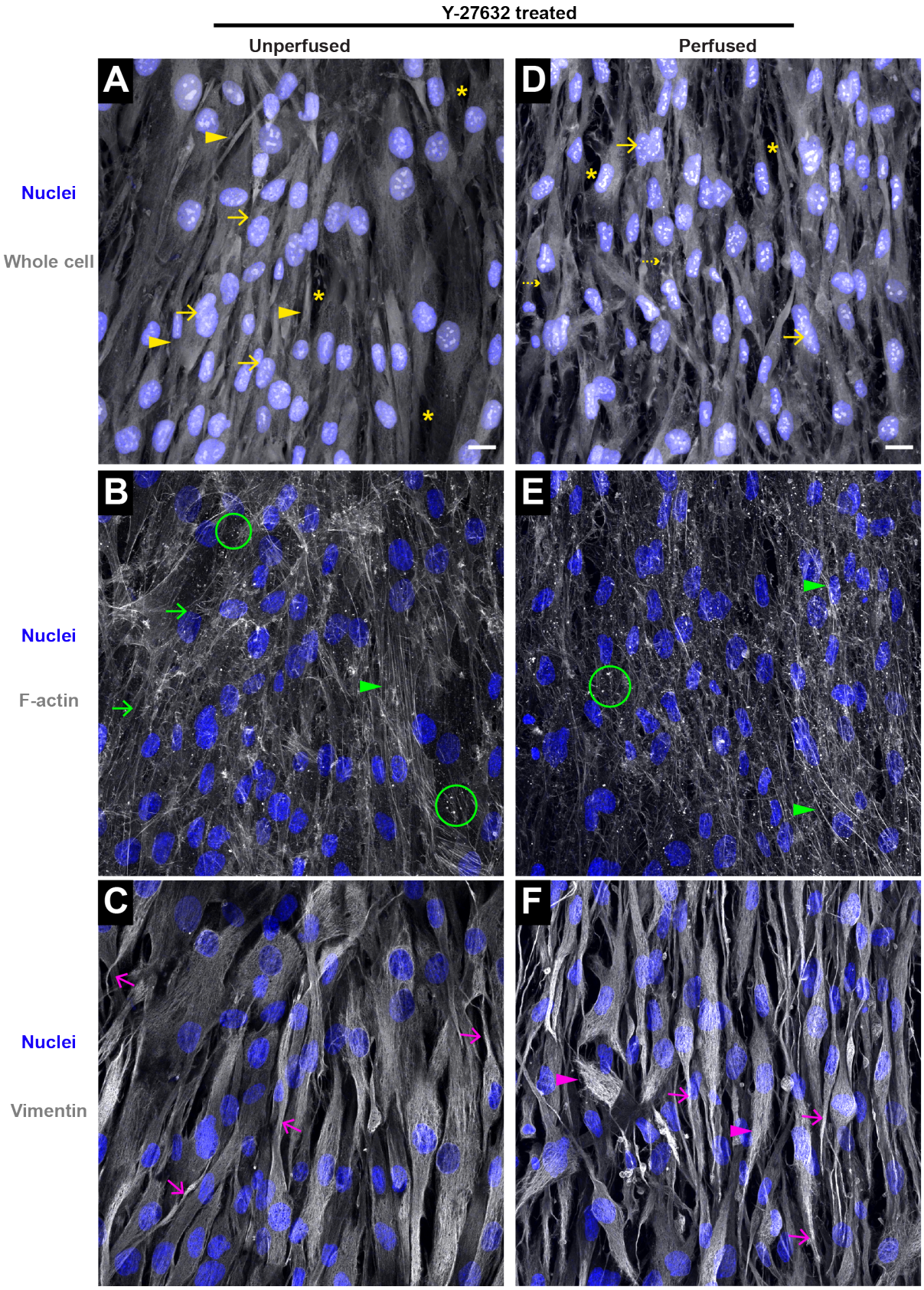


Figure 3.12: **Effects Y-27632 on cell morphology, F-actin and vimentin architecture in unperfused and perfused cell layers.** All images are maximum projections of a confocal Z-series acquired through the thickness of cultured SCE cells. Scale bar: 20 µm. (Figure caption continues in the next page.)

Figure 3.12: (Continued from previous page.) **(A)** and **(D)** Yellow arrows point to cell-cell overlap usually noticeable due to overlapping nuclei; Yellow asterisks indicate intercellular spaces in the cell layers; Yellow arrowheads indicate thinned cell bodies; Yellow dashed arrows indicate GVLs (Note that GVLs are not as sharp on maximum intensity projections as on individual Z-sections, due to the basal and apical cell lining that surrounds them). **(B)** and **(E)** Green circles indicate punctate F-actin staining in the cells; green arrowheads indicate stress fibres ; green arrows indicate filopodia. **(C)** and **(F)** Magenta arrows indicate thin cell extensions rich in vimentin; magenta arrowheads indicates a disorganised vimentin mesh network. Scale bar: 20 μm.

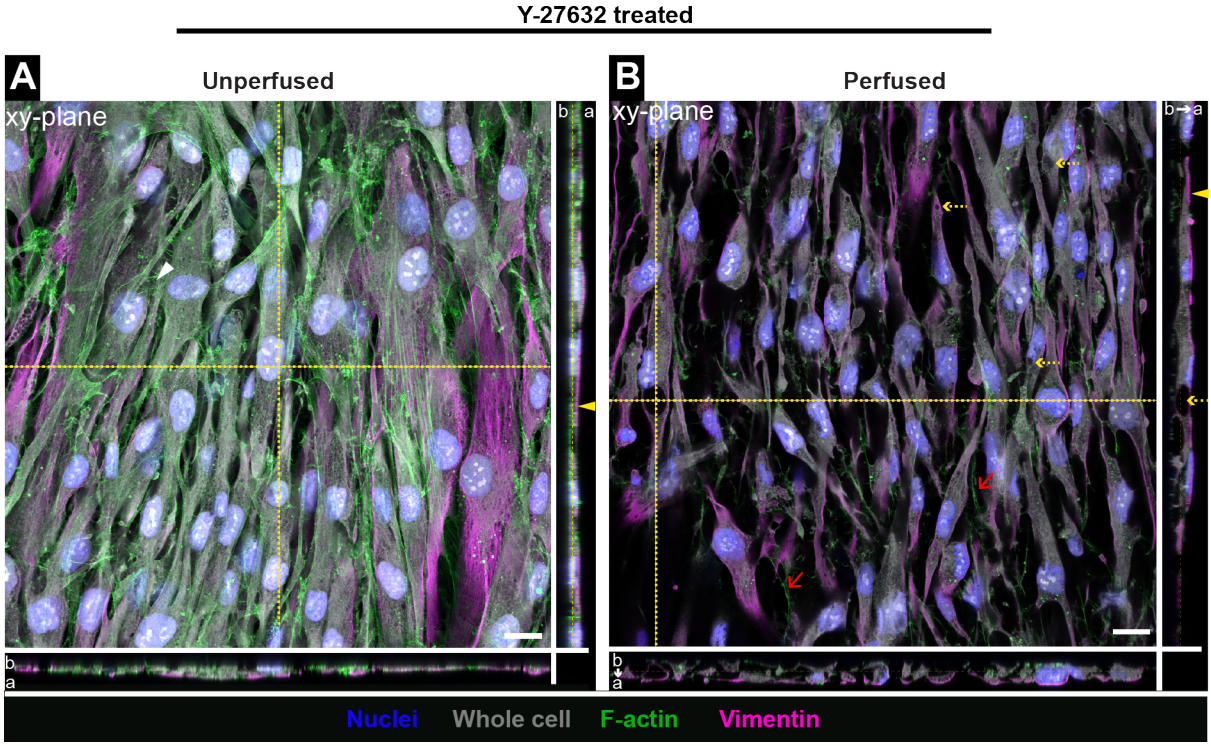


Figure 3.13: **Comparison of cross-section and thickness in unperfused and perfused cell layers treated with Y-27632.** The central panels of both panel A and B correspond to a confocal scanning micrograph at a single Z-position midway through the cell layer thickness. The lateral images correspond to orthogonal cross sections extracted along the doted yellow lines in the central panels (xz-plane in the bottom panel and yz-plane in the right hand-side of central images). The cross sections span the whole thickness of the cell layer from basal side (b) to the apical side (a); the white arrows in the vertical sections of Panel B indicate the direction of flow during perfusion. The white arrowhead indicates filopodia; red arrows indicate actin stress fibres; yellow dashed arrows indicate GVLs; yellow arrowhead demonstrate the preferential apical distribution of vimentin in the cell layers.

Cell layer imaged	GVL count	Nuclear count	GVLs per nucleus	% GVLs w/ actin band	% GVLs w/ vimentin cage	% of GVLs w/ both
Non-treated 1	46	101	2.2	19%	18%	3%
Non-treated 2	71	72	1.0	36%	36%	13%
Non-treated 3	119	71	0.6	45%	23%	18%
Non-treated all	79 ± 21	81 ± 10	1.3 ± 0.5	32%	25%	10%
Y-27632 Treated 1	54	41	1.3	42%	38%	28%
Y-27632 Treated 2	56	83	0.7	39%	30%	18%
Y-27632 Treated 3	78	88	0.9	64%	38%	36%
Y-27632 Treated all	71 ± 15	63 ± 8	0.9 ± 0.2	50%	35%	28%

Table 3.1: **Summary of nuclear counts, GVL counts, GVLs per nucleus and proportion of GVLs with an actin band, a vimentin cage or both features in each cell layer imaged.** For each cell layer, quantification was carried out from a Z-series acquired with a 40x objective at a single region of interest. The nuclear count, GVL counts and GVLs per nucleus for all the non-treated cell layers and all the treated cell layers correspond to mean $\pm$ SEM. The proportions for all the non-treated cell layers and all the treated cell layers correspond to pooled proportions.

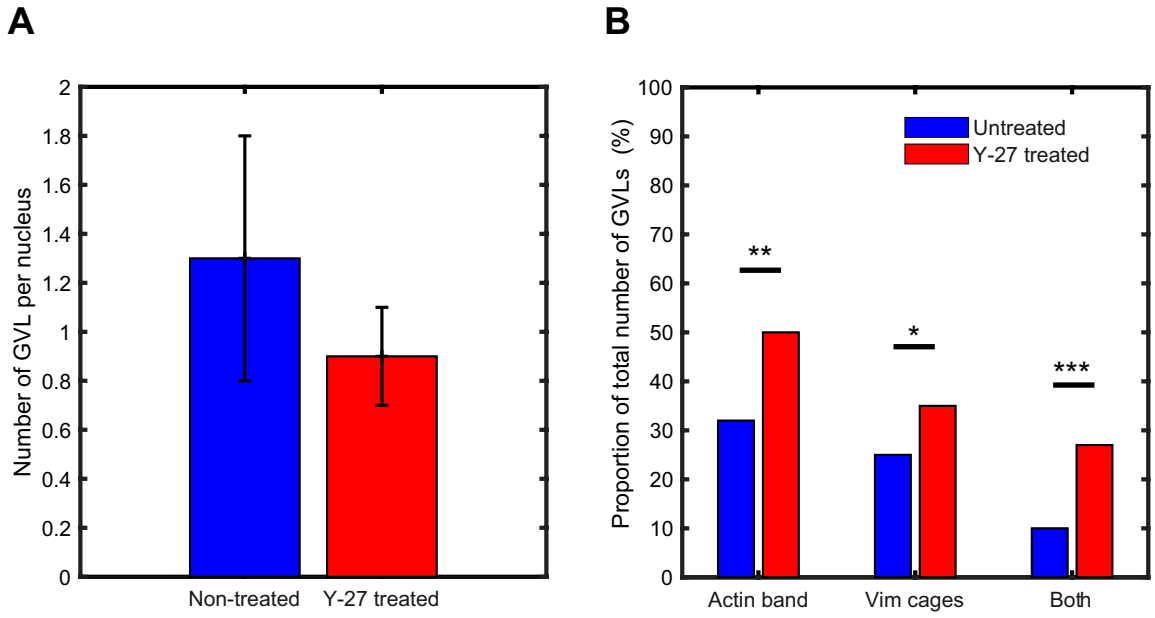


Figure 3.14: **Effects of Y-27632 treatment on (A)** the average number of GVLs per nucleus for the non-treated and Y-27632 treated cell layers represented as mean $\pm$ SEM, and **(B)** on the proportion of GVLs with F-actin band, vimentin cage and both structures together for the non-treated and the Y-27632 treated cell layers. Statistically significant changes due to Y-27632 are indicated by (*) for $p < 0.02$, (**) for $p < 0.001$ and (***) for $p \ll 0.001$.

3.4 Discussion

In this study our aim was first investigate the organisation of F-actin and vimentin IFs in perfusion-fixed SCE cells and particularly around GVLs, and second to look at the effects of ROCK inhibitor Y-27632 treatment on the organisation of these cytoskeletal filaments. We found that transendothelial perfusion led to an alteration in the F-actin organisation in SCE cells, and that both treatment with Y-27632 alone and treatment combined with transendothelial perfusion led to a severe disruption of the F-actin organisation. We next demonstrated that a proportion of GVLs were surrounded by either an F-actin band, or a vimentin cage, or both structures together, and that treatment with Y-27632 increased the proportion of GVLs surrounded by these cytoskeletal structures.

3.4.1 Effects of transendothelial perfusion on F-actin architecture

The inner wall endothelium of SC resides within a demanding biomechanical environment where the basal-to-apical pressure drop across the endothelium imposes significant forces. These forces have been estimated to be approximately 60 nN for a physiological pressure drop of 1 mmHg, with larger forces expected for higher pressure drops [41]. These forces are higher than that exerted at focal adhesions during cell contraction which are typically on the order of $\sim$ 10 nN [65, 66], and are likely to drive cytoskeletal remodelling in SCE cells.

In this study, we perfused SCE cells at a fixed transendothelial pressure drop of 6 mmHg across cultured SCE cells. While the pressure drop applied was likely supra-physiological, the SCE cells were able to withstand the pressure drop applied across them without peeling off the filter membrane they were seeded on. Transendothelial perfusion however led to a significant remodelling of F-actin in SCE cells, predominantly resulting in a reduction of stress fibres throughout the cells, an increase of shorter and thinner strands, and an increase of punctate F-actin staining. F-actin staining was particularly altered towards the basal side of the cell, suggesting a re-organisation of focal adhesions.

3.4.2 Effects of Y-27632 on F-actin architecture

Y-27632 selectively inhibits both ROCK1 and ROCK2, which are effectors of the Rho GTPases family and are recognised to control the formation of actin stress fibres, focal adhesions, and the contractile state of cells [85, 95, 100]. By inhibiting ROCK, Y-27632 acts to inhibit the phosphorylation myosin light chain, reducing myosin-actin interactions and the formation of stress fibres and focal adhesion complexes [94, 95, 100]. Y-27632 also results in the de-phosphorylation of LIM-kinase leading to the activation of cofilin-mediated actin-filament disassembly and to a decrease in actin filament density, rigidity, and stability [100]. Consistent with the known mechanism of action of Y-27632, we observed that treatment

with Y-27632 led to a disruption of the F-actin organisation throughout SCE cells and a reduction of F-actin stress fibres. In this study, some stress fibres persisted despite the treatment with Y-27632, and this is consistent with previous reports suggesting that the effects of Y-27632 on F-actin organisation [86], cell contractility [101] and stiffness [76] is dose-dependent. The overall decrease in F-actin stress fibres in Y-27632 treated SCE cells is consistent with the reduction in SCE cell stiffness with Y-27632 treatment [76].

3.4.3 Effects of transendothelial perfusion and Y-27632 on vimentin architecture

Both transendothelial perfusion and Y-27632 treatment did not alter the general cytoplasmic network organisation and spatial distribution of vimentin. In all cases, vimentin was organised in a typical mesh network, and was preferentially found on the apical side of cells. The maintenance of the mesh organisation and spatial distribution of vimentin is consistent with the fact that vimentin networks stiffen with increasing strain and can resist breakage at much higher strains than F-actin and microtubules [97, 102].

Transendothelial perfusion and treatment both led to a thinning of cells, which appeared to be accompanied by a deformation of the vimentin networks. While IF networks are known to be important for maintaining cell shape, it is unclear from our study whether the change in cell shape was due to a local remodelling of vimentin IFs. While ROCK inhibitors do not have any known effects on vimentin IFs, given the effects of Y-27632 on focal adhesions [85, 86, 95], it is possible that the changes in cell shape observed were due to changes in adhesions pattern, and that in turn vimentin re-arranged in response to changes in cell shape. Similarly, as our results suggest that transendothelial perfusion may also affect focal adhesions such that the same argument made for the effects of Y-27632 on cell shape can be made for the effects of transendothelial perfusion on cell shape.

3.4.4 F-actin and vimentin structures surrounding GVLs

We found that transendothelial pressure drop led to the formation of GVLs, and multiple GVLs were often found to cluster on single cells. The ability for the SCE cells to withstand the pressure drop applied and GVL formation was likely due to the cytoskeletal structures observed around GVLs. In fact one of the most striking findings in this study is that a proportion of GVLs were surrounded by either an F-actin band, or a vimentin cage or both structures together.

Strikingly, only a proportion of all GVLs identified exhibited an F-actin band and/or a vimentin cage. We speculate that this may be linked to the transient nature of GVLs as demonstrated in Chapter 2. It is possible that the F-actin band observed around GVLs only assemble and exist at a certain stage during the life-cycle of the GVL. As the cells were fixed in this study, we were only offered a snapshot

in time of what is otherwise a dynamic process. Further experiments in live-cells specifically looking at the distribution of F-actin and vimentin in the cell during basal-to-apical directed perfusion should be carried out to verify this hypothesis.

Possible biomechanical relevance of F-actin bands surrounding GVLs

We speculate that the F-actin band observed around a proportion of GVLs is contractile, although co-staining with myosin II will be needed to verify this claim. The possibility that the F-actin in bands observed were contractile is substantiated by their structural similarity to other contractile band-like F-actin organisations found in other cell events. This includes the F-actin ring that is assembled during cytokinesis [103]: the F-actin ring found in the furrow between dividing cells is known to be associated to myosin II and to be responsible for contraction leading to the approximation and the fusion of the lipid membranes during cell division. Another example of a band-like contractile F-actin structure is that of actin coat found around secretory vesicles [104]: the coats of actin nucleate around vesicles after their fusion with the cell membrane, and when associated to myosin they contract to release the content of the vesicles out of the cell. Based on these reports, we further speculate that in SCE cells, the existence of a contractile F-actin band around GVLs could act to contract against the GVLs which would limit their growth or even cause them to shrink. Interestingly, in Chapter 2 we found that GVLs shrink and disappear even when the pressure drop is maintained at 6 mmHg. Together the findings of the study presented in Chapter 2 and this current study suggest that GVL retraction against a load could be induced or aided by active contraction of an F-actin band surrounding GVLs.

Surprisingly, treatment with Y-27632 led to an increase in the proportion of GVLs surrounded by an F-actin band. We speculate that while the F-actin band is able to assemble in Y-27632 cells, this band may have not been contractile due to the reduction in actomyosin contractility caused by Y-27632 [94]. Our speculation is supported by a study by Segal et al. [104] on F-actin coats around secretory vesicles that demonstrated that unlike contraction, F-actin nucleation around the vesicle was independent of Rho. Segal et al. reported that treatment with Y-27632 did not hamper the assembly of F-actin around vesicles but did interfere with contraction such that many vesicle stayed open for a long time and accumulated in the cell. It is interesting to point out that if a contractile F-actin band is needed for GVL retraction then reduced actomyosin contractility would impair GVL retraction. This is in surprising agreement with our observations in Chapter 2.

Possible biomechanical relevance of vimentin cages surrounding GVLs

The existence of vimentin cages around GVLs may help maintain the integrity of the SCE cells during GVL formation. Strikingly, the preferential apical distribution of vimentin in cultured SCE cells and the

presence of vimentin cages has been reported to be similar *in situ* in the inner wall endothelium [16]. Vimentin is less stiff than both filamentous actin and tubulin at low strains, but stiffen with increasing strain [97]. Vimentin both as a single filament and as a purified gel, can withstand strains well in excess of 100% without rupture [97] in contrast to F-actin and vimentin which break at much lower strains. The resilient properties of vimentin may be important for SCE cells to support the strain imposed by GVLs, which likely exceeds 50% [41]. Furthermore, the stiffening of vimentin with increasing strain may be important to restrict the growth of GVLs and maintain cell integrity. Further investigation into the role of vimentin in GVL dynamics and structure should be carried out, possibly by disrupting vimentin in SCE cells during transendothelial perfusion.

Given the structure of the vimentin cages and the preferential apical distribution of vimentin in SCE cells, we speculate that these cages might result from a stretching of the vimentin apical network around the expanding GVL. As the GVL expands and forces the cell to bulge outwards, the cellular lining surrounding the GVL, which includes the vimentin network, must stretch. This hypothesis would predict that larger GVLs would be more likely to exhibit a vimentin cage around them and may explain why only a proportion of GVLs exhibit a vimentin cage. This hypothesis is in part consistent with the observation that Y-27632 both increased the proportion of GVLs with a vimentin cage and tended to increase GVL size (refer to Chapter 2).

3.4.5 Conclusion

In conclusion, we found that basal-to-apical directed perfusion of SCE cell layers led to cytoskeletal remodelling, and that a proportion of GVLs formed in the perfused cell layers were surrounded by an F-actin band, a vimentin cage or both features together. This finding is consistent with the assumed role of F-actin and vimentin as mechanical supports for the large stresses and strains experienced by SCE cells during GVL formation. Further, consistent with the apparent role of cellular contractility in GVL retraction reported in Chapter 2, we speculate that the F-actin bands surrounding GVLs may be contractile structures involved in the process GVL retraction.

4

Characteristics and limitations of hydraulic resistivity measurements in cultured SCE cell layers

4.1 Introduction

The bulk of outflow resistance is generated in the vicinity of the inner endothelium of Schlemm's canal [10, 11], and elevated outflow resistance is the cause of ocular hypertension associated with glaucoma. While the exact mechanism for outflow resistance generation is still a matter of debate, it is now accepted that aqueous humour crosses the inner wall endothelium in the basal-to-apical direction through micron-sized pores [12, 19, 41]. As pores provide flow passageways through an otherwise continuous endothelium, they likely act as modulators of outflow resistance [13, 61]. Importantly, pore density is reduced in glaucoma [14, 15], possibly contributing to obstructed outflow and IOP elevation. Little is known, however, about the mechanisms that regulate pore density in the inner wall endothelium of SC.

Pores often associate with dome-shaped cellular outpouchings known as GVs [30, 54], which result from the basal-to-apical direction of pressure drop across the inner wall endothelium [33, 34]. GVs generate biomechanical strains likely in excess of 50% [41, 69], and strain has been shown to induce pore formation in cultured SCE cells [32]. While GVs and pores are thought to be driven by transendothelial pressure drop [34, 42, 67, 77], the relationship between pressure drop and outflow resistance still remains unknown.

Investigation of the relationship between transendothelial pressure drop and the regulation of outflow resistance requires a model system that allows access to the surface of SCE cells and that facilitates controlled perturbations. To this end, previous investigators have developed *in vitro* models of human SCE cells that can be perfused in the basal-to-apical direction [33, 93]. These models reproduce key morphological features of the inner wall endothelium exhibiting GVLs similar to true GVs and transendothelial pores [17, 33, 93]. GVLs are absent and pore density is low in SCE cells cultured under static conditions,[17, 33, 93] (also refer to Chapter 2 and Chapter 3). GVL size and pore density both increase with increasing pressure drop [17, 33], while the hydraulic resistivity of SCE cell layers decreases with pressure drop [33]. Furthermore, our own *in vitro* studies have shown that GVLs are dynamic structures that form and disappear within minutes, even when the pressure drop is kept constant (refer to Chapter 2). It is currently not known whether the hydraulic resistivity of SCE cell layers exhibits a time-dependence that reflects the time-dependent biomechanical response of SCE cells under a fixed transendothelial pressure drop.

In this study, we used a custom-built pressure-controlled perfusion system to measure the hydraulic resistivity, R_p, of SCE cell layers at two successive transendothelial pressure drops. Time-resolved measurements enabled us to investigate the temporal change in R_p at a given transendothelial pressure drop. Additionally, by perfusing individual monolayers over two successive pressure drops rather than at a single pressure drop [33], we were able to more fully characterise the pressure-dependent

changes in R_p.

4.2 Materials and methods

The R_p measurements presented in this chapter were acquired during the basal-to-apical perfusion of SCE cells in preparation for perfusion-fixation. The perfusion-fixed samples were subsequently immunostained and used to image GVLs and the surrounding cytoskeleton, as presented in Chapter 3. The detailed methods for cell seeding onto filter membranes and sample preparation for perfusion were already outlined in Chapter 3 and will not be repeated in full here. For clarity, we will present an overview of the general experimental design, and of the perfusion system and protocol used to measure R_p across SCE cell layers.

4.2.1 Experimental design

Briefly, human SCE cells isolated from healthy donor eyes (SC68, Donor age: 30 yrs) were seeded at passage 5 on the bottom-facing surface of a filter membrane held by a culture insert. Perfusion experiments were carried out approximately 2 to 3 days after cell seeding, once the SCE cells covered the filter membrane uniformly. SCE cells were held in a temperature and CO_2-controlled incubator while being perfused at a series of controlled basal-to-apical directed pressure drop using a custom-built perfusion system. Basal-to-apical R_p of SCE cells was measured throughout the entire perfusion experiment.

4.2.2 Pressure-controlled perfusion system

We used a custom-made perfusion system to control the pressure drop applied across the filter and cells (see Figure 3.2 in Chapter 3). The perfusion system was adapted from a previously described system (*iPerfusion* [90]). In this system, the pressure drop applied across the filter and cells (ΔP) is controlled using a reservoir filled with water coupled to a vertically mounted linear actuator (L35, Nanotech, Germany, resolution of 1.25 µm per step). The pressure applied across the filter and cells is monitored throughout the perfusion by a wet-wet differential pressure transducer (PX409, Omega Engineering, USA; measurement range: 0 to 50 mmHg , uncertainty: 0.04 mmHg). Flow through the filter and cells (Q) is also measured using an in-line thermal flow meter (SLI430, Sensirion, Switzerland; measurement range: -120 μl/min to 120 μl/min, uncertainty: 5% of measured value). A custom-written LabView (National Instruments, USA) program controls the whole system and is used to record the pressure and flow measurements. Together, this perfusion system allows for an accurate control of the pressure drop applied, for an almost immediate changes in the applied pressure, and for a precise measurement of pressure drop and flow rate.

4.2.3 Perfusion protocol

Before the beginning of the experiment, the perfusion system was calibrated and tested following the methods described by Sherwood et al. ([90]). First, the pressure sensor was calibrated by using an automated 8-point calibration with the automated linear actuator. Subsequently, the resistance of a glass capillary of a known-resistance comparable to the filter and cells was measured to confirm that the system was functioning as expected. The system was always checked for bubbles and leaks before starting an experiment.

Once the system had been calibrated and tested, the tubing leading to the culture insert assembly (see methods section in Chapter 3) was connected to the perfusion system. The culture insert was then placed in the incubator in which it remained throughout the entire perfusion experiment. The pressure drop applied across the filter and cells was initially set to 0 mmHg. Immediately prior to the start of the perfusion recordings, the pressure and flow measurements were both checked to confirm that they were very close to 0 mmHg and 0 μl/min respectively.

After about 5 mins at 0 mmHg, a 2 mmHg pressure drop was applied across the filter and cells. As the SCE cells were seeded on the bottom-facing surface of the filter membrane, a positive pressure drop drove perfusion medium to flow in the basal-to-apical direction across the cells, mimicking *in vivo* conditions. The pressure drop was held at 2 mmHg for approximately 45 mins. The pressure drop was then increased to 6 mmHg and held at this pressure drop for approximately 10 mins. The pressure drop and flow through the cell layer and filter were measured throughout the length of the perfusion experiment.

4.2.4 Hydraulic resistivity measurement

Using the recorded pressure drop and flow rate measurements, the hydraulic resistivity R_p of the cell layer was computed as previously reported by others [33, 93]:

$$R_p = (\frac{\Delta P}{Q} - R_F) * A \tag{4.2.1}$$

where R_F is the resistance of the filter membrane alone (measured value of 0.050 mmHg.min. μl^{-1}) *, and A is the perfused area of the filter membrane (0.33 cm^2).

The initial R_p, R_{p_i}, was computed by averaging R_p over a 30 s window immediately after the step increase in pressure drop from 0 mmHg to 2 mmHg. The final R_p, R_{p_f}, was computed by averaging R_p over the last 30 s of the pressure step. The time to steady state was evaluated by computing the slope of the conductance , which is equivalent to the inverse of resistance ($Q(t)/\Delta P(t)$), over a 5 mins window.

When the relative change in conductance over a 5 mins window was less than 5% (which corresponds to the uncertainty on the flow sensor reading) we considered that steady state was reached. R_{p_i}, R_{p_f}, and the time to steady state were also computed after the pressure drop was increased from 2 mmHg to 6 mmHg.

4.3 Results

We perfused SCE cells seeded on a filter membrane, and measured R_p in response to a step change in basal-to-apical transendothelial pressure drop from 0 mmHg to 2 mmHg. A representative plot of the flow and pressure measured through the cells, and the corresponding R_p measurement is shown in Figure 4.1. We found that a step change in pressure drop from 0 mmHg to 2 mmHg resulted in a time-dependent increase in flow rate, which corresponded to a time-dependent decrease in R_p. We confirmed that the filter membrane had a constant resistance (Figure 4.2), and concluded that the time-dependent change in R_p was due to a response of the cells to the applied pressure drop. We characterised the time for R_p to reach steady state in 8 cell layers (Figure 4.3, left panel, Table 4.1, left column and refer to Methods Section 4.2.4 for a definition of steady state). On average, R_p reached steady state after 23.7 $\pm$ 8.0 mins (mean $\pm$ SD, n = 8), bounded by a minimum measured transient time of 12.8 mins and a maximum measured transient time of 36.7 mins.

After a step increase in pressure drop from 0 mmHg to 2 mmHg, for each sample the average initial R_p was computed immediately after the step in pressure drop (termed R_{p_i}), and the average final R_p was computed at the end of the pressure step (termed R_{p_f}). Given the apparent disparity and skewness in the data, the distribution of R_{p_i} and R_{p_f} were separately tested for normality. We applied a Shapiro-Wilk test to each distribution, and we found that both distributions were significantly different from a Gaussian-normal distribution ($p < 0.03$ for R_{p_i} and $p < 0.01$ for R_{p_f}). After logarithmic transformation of R_{p_i} and R_{p_f}, this difference was however eliminated ($p < 0.66$ and $p < 0.69$ respectively), suggesting that both variables are lognormally distributed rather than normally distributed. Accounting for the lognormal distribution, the mean R_{p_i} across all samples was 0.074 $^{\times}/$ 2.229 mmHg.min.cm^2.μl^{-1} (geometric mean $^{\times}/$ multiplicative SD, n = 8) and the mean R_{p_f} across all samples was 0.018 $^{\times}/$ 2.973 mmHg.min.cm^2.μl^{-1}. Overall R_{p_i} and R_{p_f} were significantly different from one another ($p \ll 0.001$, paired t-test on log-transformed R_p data).

When the same samples were subjected to a step change in pressure drop from 2 mmHg to 6

*Here it is assumed that the extracellular matrix (ECM) secreted by the endothelial monolayers over a period of days did not add significantly to the measured flow resistance across the filter membrane. This assumption is consistent with a prior study in which the permeability of the filter plus ECM secreted by endothelial monolayers was measured after removing the cells with EGTA [105]. Warboys and colleagues reported that the ECM secreted by monolayers cultured over a period of 9 days did not significantly add to the permeability of the filter alone [105]. Of importance, Warboys et al. also used the same type of filter (track-etched) and with the same porosity (and therefore expected resistivity) as the filter used in this current study.

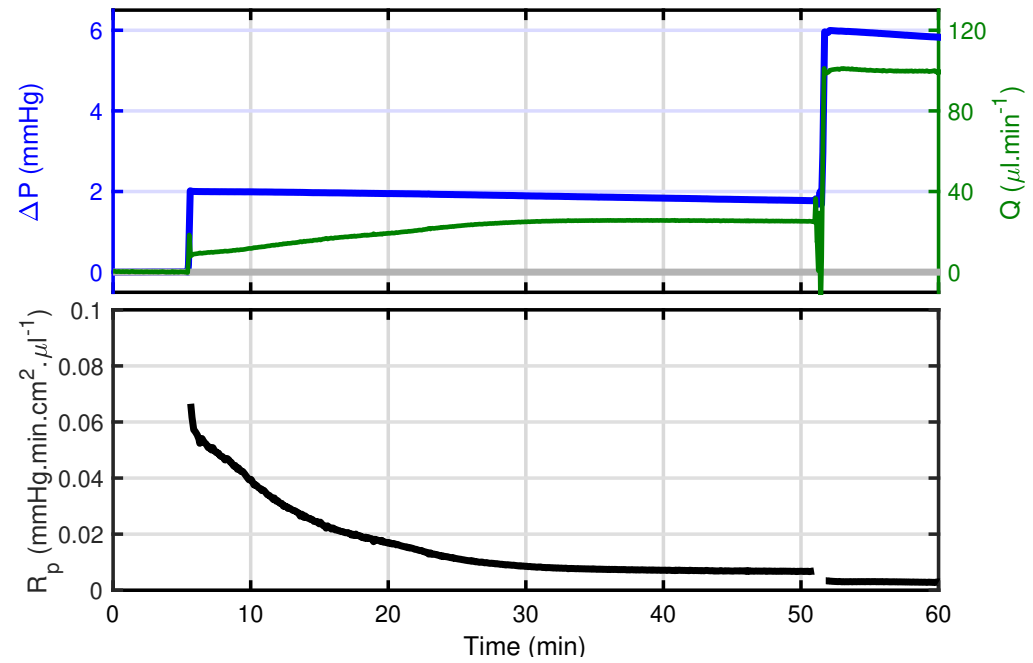


Figure 4.1: **Representative plot of measured ΔP and Q through the cells and filter, and of the corresponding R_p.** The pressure drop is first increased from 0 mmHg to 2 mmHg, and is maintained at 2 mmHg for approximately 45 mins, then it is increased from 2 mmHg to 6 mmHg and is maintained at 6 mmHg for approximately 10 mins. R_p is computed according to Equation 4.2.1.

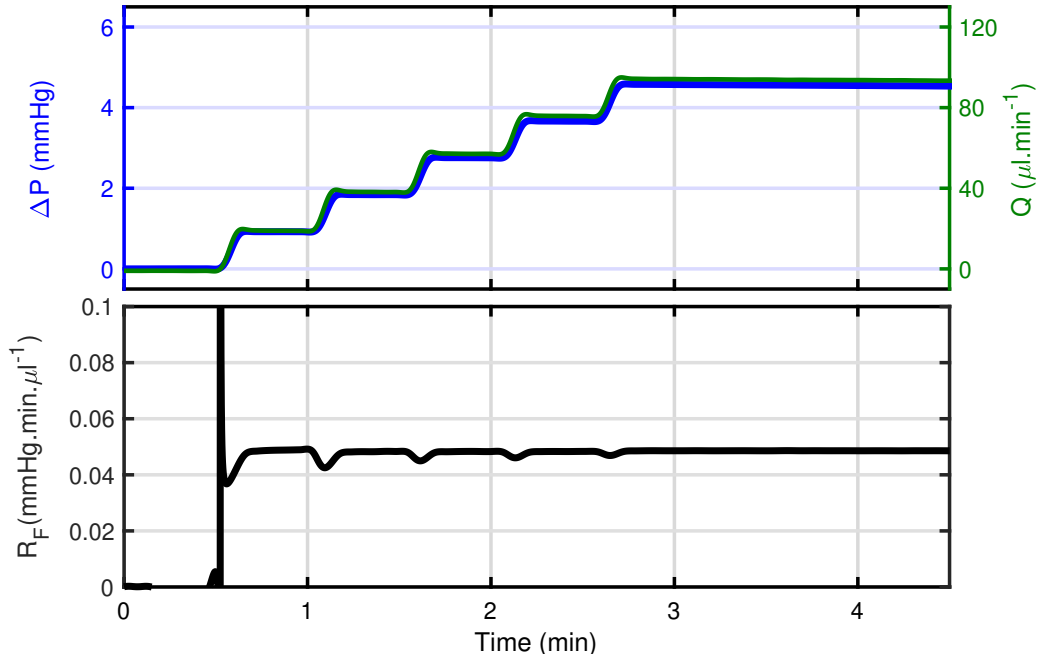


Figure 4.2: **ΔP and Q measurement through the filter membrane, and corresponding R_F measurement.** Both ΔP and Q reach stability almost instantaneously demonstrating that there is negligible compliance in the perfusion system. R_F is constant over time and pressure drop.

mmHg, there was an immediate drop in the measured R_p in all samples perfused (Figure 4.3, right panel, and Table 4.1, right column). In 3 out of 8 of the samples, the immediate drop in R_p observed in response

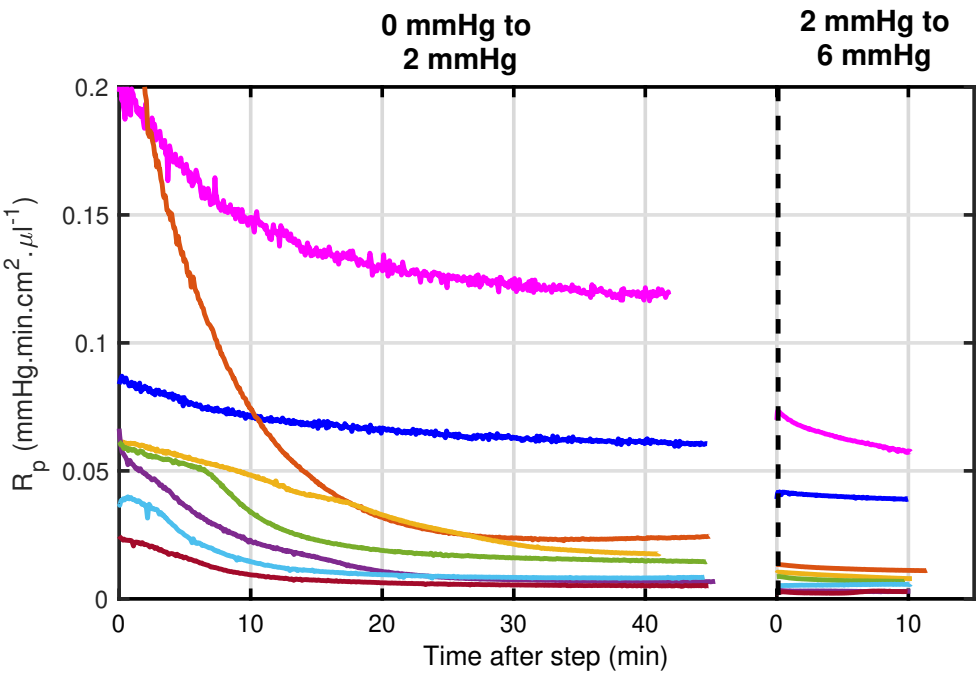


Figure 4.3: **Time and pressure-dependent changes in R_p for all cell layers.** Each curve represents the R_p measurement for each cell layer perfused after a step in pressure from 0 mmHg to 2 mmHg, and then from 2 mmHg to 6 mmHg. Note that the decrease in R_p measured in all cell layers following the step increase in pressure drop from 2 mmHg to 6 mmHg is immediate.

Samples	Step from 0 mmHg to 2 mmHg				Step from 2 mmHg to 6 mmHg				Ratio R_{p_f} at 6 vs 2 mmHg
	R_{p_i} (UR)	R_{p_f} (UR)	R_{p_f}/R_{p_i}	Time to *ss* (mins)	R_{p_i} (UR)	R_{p_f} (UR)	R_{p_f}/R_{p_i}	Time to *ss* (mins)	
1	0.086	0.061	0.708	12.8	0.041	0.040	0.949	5.0	0.646
2	0.195	0.119	0.610	17.7	0.072	0.059	0.810	$> 10^{\dagger}$	0.494
3	0.266	0.024	0.091	30.2	0.013	0.011	0.833	5.5	0.462
4	0.061	0.018	0.291	36.7	0.010	0.008	0.787	6.6	0.460
5	0.058	0.007	0.116	28.5	0.003	0.003	0.874	5.0	0.425
6	0.060	0.015	0.245	25.7	0.008	0.007	0.800	5.6	0.472
7	0.038	0.008	0.217	20.5	0.005	0.006	1.091	5.0	0.682
8	0.023	0.005	0.219	17.5	0.003	0.003	1.1517	5.0	0.574
All	$0.074\ ^{\times}/$ 2.229	$0.018\ ^{\times}/$ 2.973	$0.250\ ^{\times}/$ 2.041	23.7 ± 8.0	$0.106\ ^{\times}/$ 3.216	$0.010\ ^{\times}/$ 3.020	$0.903\ ^{\times}/$ 1.158	5.9 ± 0.6	0.523 ± 0.096

Table 4.1: **Summary of time and pressure-dependent change in R_p across all samples perfused.** All R_p values are in units of resistivity (UR: mmHg.cm^2.min.μl^{-1}). Time to ss corresponds to the time to steady state. The average R_p values indicated in the last row of the table represent the geometric mean $^{\times}/$ multiplicative SD including all cell layers (assumed log-normal distribution, see text for more details). The average time to steady state indicated in the last row of the table represents the mean $\pm$ SD including all cell layers (assumed Gaussian distribution). The average ratio of R_{p_f} at 6 mmHg versus at 2 mmHg indicated in the last row of the table represents the mean $\pm$ SD including all cell layers (assumed Gaussian distribution).

to a step in pressure drop was followed by a short time-dependent decrease in R_p, and steady state was reached on average 5.9 ± 0.6 mins after the step in pressure drop from 2 mmHg to 6 mmHg. In another 4

out of 8 samples, the time-dependent change in R_p was shorter than 5 mins, corresponding to the length of the time window used to evaluate stability. In 1 out of 8 samples, the time-dependent decrease in R_p had not reached steady-state after 10 mins, which corresponded to the end of the recording at 6 mmHg.

Taking all samples into account, the mean R_{p_i} and mean R_{p_f} at 6 mmHg across all samples were not significantly different within each sample (p = 0.09, paired t-test on log-transformed R_p data), and the mean R_{p_f} was 0.010 $^{\times}/$ 3.020 mmHg.min.cm^2.μl^{-1} (Table 4.1). The mean R_{p_f} at 6 mmHg was however 2-fold lower than the mean R_{p_f} at 2 mmHg ($p \ll 0.001$, paired t-test on log-transformed R_p data)(Figure 4.4).

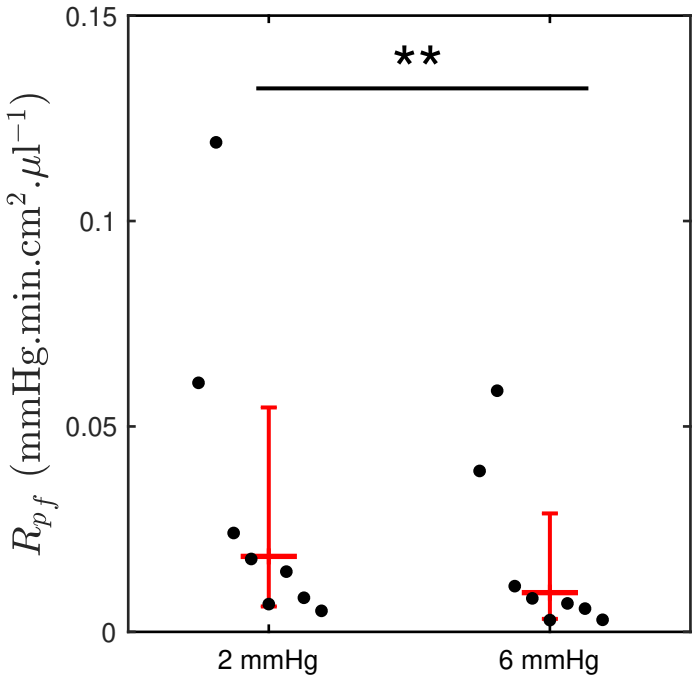


Figure 4.4: **Comparison of R_{p_f} at 2 mmHg and at 6 mmHg.** Each black dot represents the R_{p_f} measurement from a single cell layer, and the red error bar represents the geometric mean $^{\times}/$ the multiplicative SD of all cell layers. There is a statistically significant two-fold decrease in paired R_{p_f} measurements between 2 mmHg and 6 mmHg. The statistical significance difference is indicated by (**) for $p \ll 0.001$.

4.4 Discussion

In this study, we demonstrated that the basal-to-apical R_p measured across SCE cell layers exhibits both time and pressure-dependent characteristics.

[†]The R_p of this cell layer did not reach steady state by the end of the recording.

4.4.1 Time and pressure-dependent characteristics of *in vitro* $\mathbf{R_p}$

We found that, following a step increase in pressure drop from 0 mmHg to 2 mmHg, the R_p of SCE cell layers exhibited an exponential-like decay lasting several tens of minutes while the pressure drop was maintained at 2 mmHg. After 45 mins at 2 mmHg, R_p had lowered down to 25% of its initial value. This large time-dependent R_p decrease likely reflected changes in cell layer morphology suggesting that the cells were acclimatising to the transendothelial pressure drop and flow. Interestingly, there was an immediate drop in R_p following a further step increase in pressure drop from 2 mmHg to 6 mmHg, but there was only a negligible time-dependent decay in R_p while the pressure drop was maintained at 6 mmHg. These findings suggest that once the cell layers had acclimatised to pressure drop and flow, they continued to respond to acute changes in pressure drop but only weakly responded to sustained changes in pressure drop.

Time-dependent R_p changes have previously been reported in other types of endothelial cells [106, 107], but surprisingly not in SCE cells [33, 93]. Tarbell et al. and Dull et al. [106, 107] reported that, following a step increase in pressure drop, bovine aortic endothelial cells [106] and bovine lung microvascular cells [107] first exhibited a time-dependent increase in R_p over around an hour, followed by a time-dependent R_p decrease occurring over several hours. The initial transient R_p increase, called the sealing effect, was observed even when the cells were fixed prior to the application of a step in pressure drop [108]. The reason why we did not observe a sealing behaviour in our study may be due to the perfusion direction applied: in those other studies, endothelial cells were perfused in the apical-to-basal direction which tends to push the cells onto their substrate and likely causes flow pathways between the cells and the filter to seal off, thereby obstructing flow. In contrast, in this current study we perfused SCE cell layers in the basal-to-apical direction which tends to push the cells away from their filter and likely results in the opening of flow pathways. In SCE cells, these flow pathways presumably include transendothelial pores, loose cell-cell junctions and intercellular gaps. The hypothesised asymmetry in R_p measurements is substantiated by a previous study showing that the apical-to-basal R_p of SCE cell layers is 10-fold larger than the basal-to-apical R_p [93].

We found a 2-fold difference between R_p at 2 mmHg and at 6 mmHg. Similar pressure-induced changes have been reported in bovine aortic endothelial cells [106] and bovine lung microvascular cells [107] perfused in the apical-to-basal direction, and in another study using SCE cells perfused in the basal-to-apical direction [33]. Interestingly, in this last study, Pedrigi et al. [33] used SCE cells from different donors and reported a similar two-fold difference between R_p measured at 2 mmHg and at 6 mmHg in SCE cells perfused in the basal-to-apical direction.

The morphological changes in SCE cell layer associated with the pressure and time-dependent changes in R_p were not directly assessed in this study. We speculate, however, that there are four possible

perfusion-induced scenarios that may account for the R_p changes measured: (i) the blowing off of the cells from the filter membrane, (ii) the existence of a flow bypass between the cells and the filter due to the slight lift off of cells from the filter, (iii) the formation of GVLs and associated transendothelial pores and (iv) the retraction of cells due to a remodelling of cell-substrate adhesions (Figure 4.5). We can eliminate the scenario of cells blowing off the filter as we did not observe a loss of cell layer integrity with basal-to-apical perfusion (refer to Figure 2.4 in Chapter 2 and to Figure 3.2B in Chapter 3). It is possible that the basal-to-apical direction of perfusion may have caused the cells to slightly lift off the filter allowing for fluid to flow between the cells and filter, thus creating a flow bypass. We however do not have any means to assess the probability of this hypothetical scenario at this time.

It is tempting to speculate that the measured time and pressure-dependent changes in R_p result from GVL and associated transendothelial pore formation, which are known to form under transendothelial basal-to-apical directed flow in cultured SCE cells [17, 33, 93]. Other studies have already demonstrated that in cultured SCE cell layers, GVLs and pores are largely absent at 0 mmHg, and that basal-to-apical perfusion results in GVL [33] (also see Chapter 2 and Chapter 3 of this thesis) and pore formation [17]. Pore density may progressively increase over time following a step increase in pressure drop. This putative progressive increase in pore density could explain the time-dependent decrease in R_p observed. Furthermore, it is known that with increasing pressure drop, GVL size [33] and pore density increases [17]. The pressure-dependent changes in GV size and pore density may thus explain the pressure-induced decrease in R_p measured.

Assuming that the R_p of the SCE cell layer only depends on transendothelial pores and that the average pore size does not change with increasing pressure drop, then we can estimate the relative change in R_p that would be caused by the pressure-dependent increase in pore density. Overby et al. [17] reported that the average pore density formed at a basal-to-apical perfusion pressure drop of 0 mmHg was approximately 40 pores/mm^2, at 2 mmHg it was 150 pores/mm^2 and 6 mmHg it was 190 pores/mm^2 respectively. Using these numbers, we estimate that increases in pore density in response to an increasing step in pressure drop from 0 mmHg to 2 mmHg would cause a 75% decrease in R_p, and an increasing step in pressure drop from 2 mmHg to 6 mmHg would cause a 25% decrease in R_p [‡]. The results of this simple estimation are strikingly similar to the measured time-dependent decrease in R_p in response to a pressure step between 0 mmHg and 2 mmHg($\sim$ 75%) . The results of this estimation for a step increase in pressure drop from 2 mmHg to 6 mmHg are however lower than those measured in this current study ($\sim$ 50% measured).

[‡]To evaluate the change in resistivity due to the opening of pores, we assumed that the cell layer was fully confluent and that flow could only pass through the pores. Using this assumption, the resistivity of the cell layer could be estimated by the expression: $R_p = (R_{pore}/(n_{pore} * A))$ where R_{pore} is the radius of an average pore, n_{pore} is the pore density and A is the surface area of the filter. We further assumed that the average pore size did not change with increasing pore density, such that the change in resistivity with increasing pressure drop could be estimate based on the change in pore density alone.

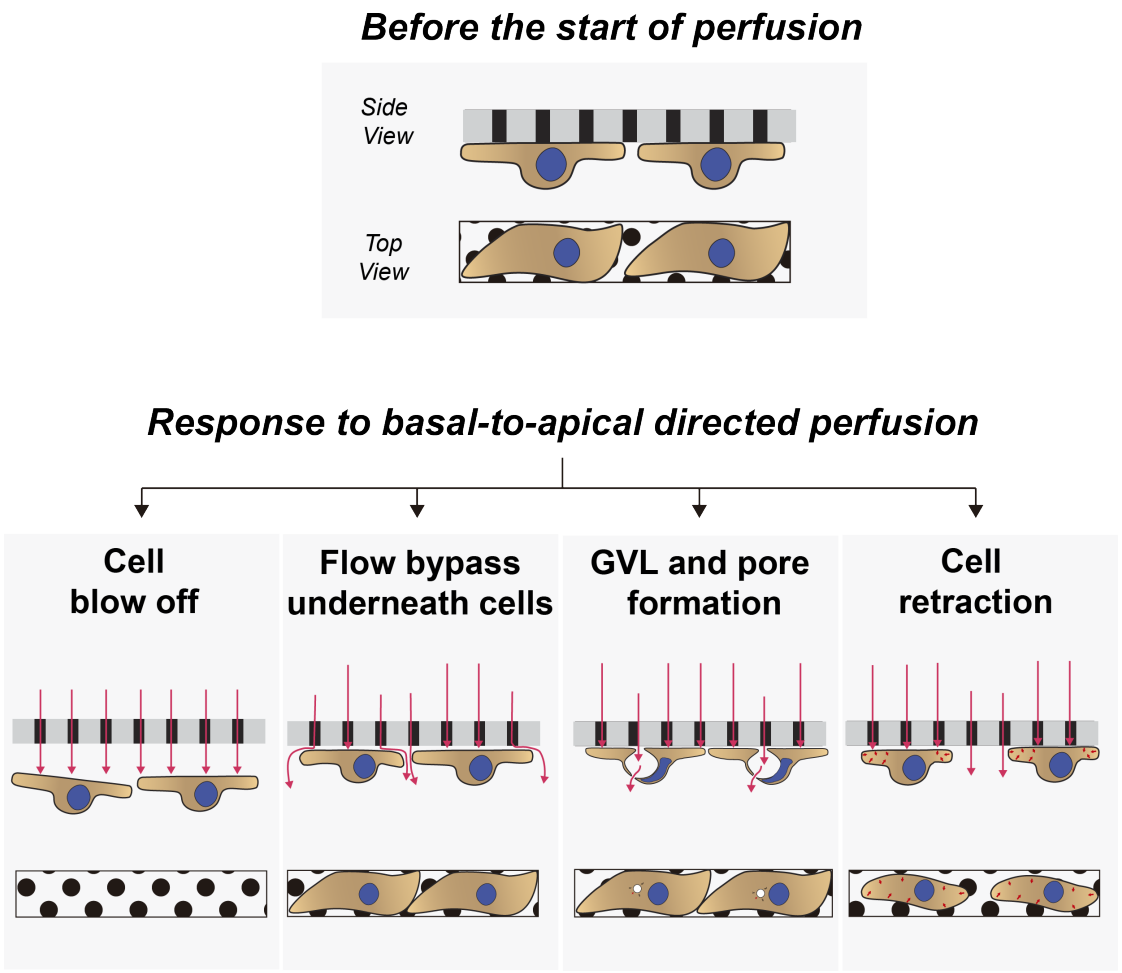


Figure 4.5: **Hypothetical scenarios of cell morphological changes accounting for time and pressure-dependent changes in R_p.** See text for further details.

The estimation proposed above has at least one limitation: cultured SCE cell layers are known to exhibit non-physiological micron-sized intercellular gaps or imperfections related to weak cell-cell junctions [12], and as a result the absolute measured value R_p almost certainly does not only depend on the density of transendothelial pores. Considering this limitation, it is possible that the observed time-dependent and pressure-dependent changes in R_p may be due to the widening of intercellular spaces. In fact, in time-lapse images acquired during basal-to-apical perfusion of SCE cells (see Chapter 2) we observed a visible widening of spaces between cells immediately after a step-change in pressure drop. An alternative and more probable scenario is that both pore formation and intercellular space widening may concurrently occur, and affect R_p (see Appendix A, Section 4.6).

4.4.2 Comparison with *in situ* R_p and other reported *in vitro* R_p

As mentioned above, a limitation of the current *in vitro* model is that cultured SCE cell layers exhibit micron-sized intercellular gaps or imperfections [93, 109] (also refer to Chapter 2 and 3 of this thesis).

This is in stark contrast to the continuous cell monolayer with tight-junctions observed *in situ* in the inner wall endothelium of SC [23, 110]. It is well-recognised that similar intercellular gaps exist in *in vitro* model of vascular endothelia [111]. In these models, *in vitro* R_p is 10-100 times lower than *in situ*, and this is thought to be attributable to the presence of intercellular gaps [111–113]. The gaps observed in SCE cell layers are likely associated with the lack of mature cell-cell junctions, particularly of tight junctions, and altered junctional protein expression and localisation [79, 80, 109, 114].

The *in vitro* R_p values measured in this study were comparable to the lower bound *in situ* R_p estimates (Table 4.2). This is consistent with the existence of gaps in the cultured SCE layers which presumably lower the absolute value of *in vitro* R_p. Surprisingly, the *in vitro* R_p values measured in this current work are however over an order of magnitude lower compared to those measured by Pedrigi et al. [33] at the same pressure drops and using a similar cell culture model (i.e. SCE cells cultured on filter membranes with defined cylindrical pores). Pedrigi et al. reported *in vitro* R_p values that were higher than the estimated upper bound of *in situ* R_p. Given the widely reported existence of non-physiological intercellular gaps in cultured SCE cell layers [93, 109], it is difficult to explain the absolute R_p values measured by Pedrigi and colleagues. We note that Pedrigi et al. used a different perfusion system (pressure was controlled by closed-loop fluid pump based system rather than with a height-actuated fluid reservoir), and this difference in experimental methods may in part explain our different results.

	Current study	**Measured *In vitro*** [33]	**Estimated *in situ*** [19]
$\mathbf{R_p}$	At 2 mmHg: 0.02	At 2 mmHg: 0.87	Lower bound: 0.01-0.03
mmHg.min.cm^2.μl^{-1}	At 6 mmHg: 0.01	At 6 mmHg: 0.47	Upper bound: 0.14-0.33

Table 4.2: **Comparison of measured $\mathbf{R_p}$ with other published values.** The lower bound *in situ* R_p values presented are estimated based on the assumption that only 10% of the total pressure drop ($\sim$0.5 mmHg) that exists across the outflow pathway occurs across the inner wall endothelium. This assumption is based on the quantification of pore density and size in the endothelium [20]. The upper bound *in situ* R_p values presented are estimated based on the assumption that the entire pressure drop occurs across the inner wall endothelium ($\sim$5 mmHg). We note that lower and upper bound estimated are most likely an underestimation and an overstimation respectively of the true outflow resistance generated by the inner wall endothelium as reviewed by Johnson [12] and Overby et al. [13].

A key assumption in the computation of *in vitro* R_p of the SCE cell layer (Equation 4.2.1) is that the membrane filter and cells act as resistances in series. In a first scenario in which the filter membrane is covered by a confluent cell monolayer, there is only one flow pathway available: the entire flow must cross both the filter and the cells. In this first scenario, the filter and cells are resistances in series and R_p computed using Equation 4.2.1 corresponds to the true resistivity of the cell layer. In a second scenario in which the membrane filter is covered by a non-confluent cell layer with intercellular gaps, there are now two fluid pathways available: in some areas, fluid will cross both the filter and the cells, and in other areas, fluid will only cross the filter. In this second scenario, the filter and cells can no longer be considered as resistances in series and the R_p computed using Equation 4.2.1 no longer

corresponds to the true cell layer resistivity. Additionally, in the second scenario it seems certain that the resistance generated in areas where the filter is not covered by cells will depend on the resistance of the filter. As a result, the R_p computed in the second scenario will depend on the resistance of the filter used. This observation may be important to explain the discrepancy between the R_p values measured in this study and the R_p values reported by Pedrigi et al. [33] as filters with different resistances were used in these two studies. The effect of the filter resistance on measured R_p in a non-confluent cell layer is discussed in Appendix A.

4.5 Conclusion

In conclusion, this study has shown that the basal-to-apical R_p of cultured SCE cell layers exhibits both time and pressure-dependent changes. These changes likely reflect alterations in the morphology of SCE cell layers, including both pore formation and intercellular gap widening (see Appendix A, Section 4.6). The absolute value of R_p measured in this study is close to the estimated lower bound value of *in situ* R_p, but it is also almost certainly influenced by the presence *in vitro* of non-physiological intercellular gaps associated with poorly developed cell-cell junctions. Furthermore, due to the existence of intercellular gaps, the computed R_p values using a series resistance model is invalidated and no longer yields the true cell layer resistivity (see Appendix A, Section 4.6). In Chapter 5, we propose that culturing SCE cells under a long-term basal-to-apical pressure drop to mimic the *in vivo* biomechanical environment of these cells, may be key to maintaining the native barrier function and moprhology of SCE cell layers.

4.6 Appendix A: Parallel Resistances Model

4.6.1 Introduction

The *in vitro* measurement of R_p of cultured SCE cell layers assumes that the cells and the filter membrane act as resistances in series. For this assumption to hold true, the SCE cell layer must fully cover the filter membrane such fluid must everywhere cross both the filter membrane and the cell layer. However, it is well-recognised that cultured SCE cell layers exhibit micron-sized intercellular gaps [12, 69]. In that case, as the filter membrane is only partially covered by the cell layer, two flow pathways are available: in some areas, fluid will cross both the filter and the cells, and in other areas, fluid will only cross the filter. As a result, the R_p value computed using usual methods (Equation 4.2.1) does not correspond to the true resistivity of the cell layer. In addition, the R_p computed in that case will likely depend on the resistance of the filter used. This observation may be important to explain the discrepancy between the R_p values measured in this study and the R_p values reported by Pedrigi et al. [33] as filters with different resistances were used in these two studies. In the following appendix, we propose that a system of parallel

resistances may be a better model for sub-confluent SCE cell layers seeded on filter membranes. Using this model, we first examine the effect of changing the filter resistance on the computed R_p value. We next use the model to evaluate the contribution of intercellular gap widening on the time-dependent R_p decrease measured.

4.6.2 Parallel resistances model

We propose that for a sub-confluent cell layer cultured on a filter (see illustration in Figure 4.5), the total resistance of the filter and cells can be modelled as a system of parallel resistances as represented in Figure 4.6.

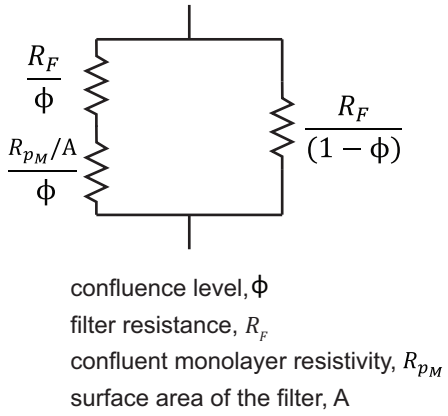


Figure 4.6: **Model of parallel resistances for subconfluent cell layers cultured on a filter membrane.**

The total resistance of this parallel flow pathway model is given by:

$$R_{tot} = \left(\frac{1-\phi}{R_F} + \frac{\phi}{R_F + R_{p_M}/A}\right)^{-1} \tag{4.6.1}$$

where ϕ is the cell layer confluence, R_F is the resistance of the filter membrane, and R_{p_M} is the true resistivity of the confluent cell monolayer, A is the surface area of the filter and R_{p_M}/A is therefore the true cell layer resistance of the cell layer monolayer. When the cell layer is fully confluent, ϕ is equal to 1 and R_{tot} simplifies to the series resistances $R_F + R_{p_M}/A$. When there is no cell layer, ϕ is equal to 0 and R_{tot} is equal to R_F. We consider that R_{tot} corresponds to the resistance of the cell layer and filter measured using the perfusion system (i.e. $R_{tot} = \frac{\Delta P}{Q}$).

We henceforth use the term R_{p_S} to refer to the resistivity usually computed using the conventional series model:

(4.6.2) $$R_{p_S} = (\frac{\Delta P}{Q} - R_F) * A$$

(4.6.3) $$R_{p_S} = (R_{tot} - R_F) * A$$

(4.6.4) $$R_{p_S} = ((\frac{1-\phi}{R_F} + \frac{\phi}{R_F + R_{p_M}/A})^{-1} - R_F) * A$$

4.6.3 Effects of different filter resistances on R_{p_s}

Parameters

We used the parallel resistances model to evaluate the effect of changing the filter resistance, R_F on the resistivity value conventionally computed using the series model R_{p_S}. To compute R_{p_S} using Equation 4.6.4, we used the resistances of the filter used in the current study (1 μm diameter pores, 2*10^6 pores/cm^2 and 11 μm thickness) and that used by Pedrigi et al. [33] (0.4 μm diameter pores, 4*10^6 pores/cm^2 and 10 μm thickness) as summarised in Table 4.3.

In this analysis, the confluent cell layer resistivity value R_{p_M} used to compute R_{p_S} corresponded to the estimated upper bound *in situ* resistivity of the inner wall endothelium (0.33 mmHg.min.cm^2.μl^{-1} [19], see Table 4.2). While R_{p_S} was evaluated at all values of ϕ from 0 to 1, we highlighted the range of typical ϕ values usually observed for SCE cell layers based on microscopic evaluation (between 0.80 and 0.95). All the parameters and values used to compute R_{p_S} are summarised in Table 4.3.

Model predictions

The parallel flow pathways model predicts that for a fixed R_{p_M} value, R_{p_S} will decrease with decreasing ϕ values (Figure 4.7). In addition, for any value of ϕ <1 and a given R_{p_M}, R_{p_S} will be lower for lower R_F values. For decreases in ϕ in the range of 0.80 to 0.95, the decrease in R_{p_S} is more drastic for smaller $R_F * A$ (filter resistivity) values, and approaches a linear behaviour for values of R_F larger than R_{p_M}. Note that these predictions can be quantitatively verified in future experiments by directly comparing R_{p_S} measurements across SCE samples seeded on filters with different resistances. Of significance, such an experiment could allow us to estimate the value of the true cell layer resistivity R_{p_M}.

Parameters	Symbols	Units	Pedrigi et al. study [33]	Current study
Filter resistance	R_F	mmHg.min.μl^{-1}	1.04	0.05
Confluent monolayer resistivity	R_{p_M}	mmHg.min.cm^2.μl^{-1}	0.33 (*in situ* estimate from [19])	
Filter surface area	A	cm^2	0.33	
Confluence	ϕ	U	0.7 - 0.95	
Measured resistivity at 2 mmHg	R_p at 2 mmHg	mmHg.min.cm^2.μl^{-1}	0.87	0.018
Measured resistivity at 6 mmHg	R_p at 6 mmHg	mmHg.min.cm^2.μl^{-1}	0.47	0.010

Table 4.3: **Parameters used to estimate the effects of R_{ps} on the computed R_p.**

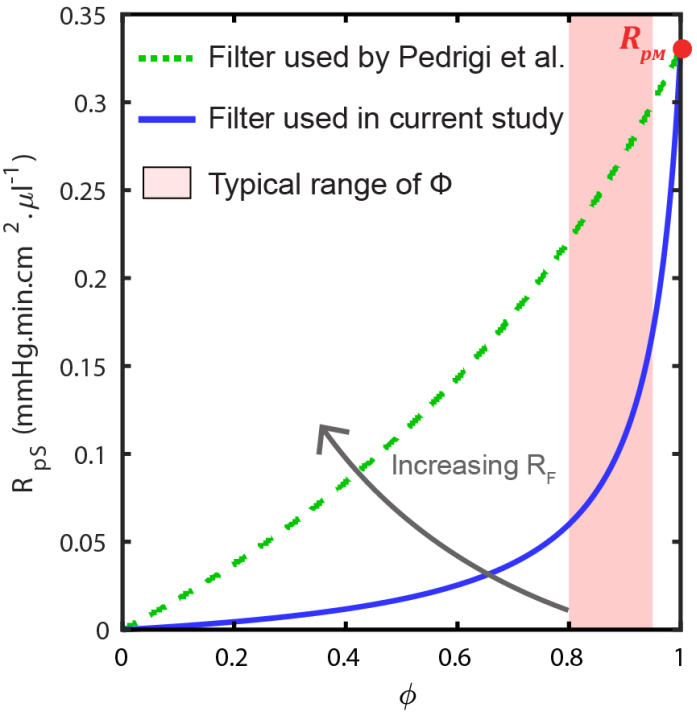


Figure 4.7: **Predicted R_{ps} for different filter resistances.** For this analysis, the resistivity R_{p_M} is assumed to be the the upper bound estimated resistivity of the inner wall endothelium of SC (Table 4.3).

4.6.4 Contributions of changes in ϕ to the measured time-dependent changes in R_{p_s}

Parameters

We next used the parallel resistances model to investigate the contribution of changes in the cell layer confluence, ϕ, to the measured time-dependent changes in R_p presented in Figure 4.3 and Table 4.1. In this analysis, we considered that R_{p_M} is constant and only ϕ varies over time. We used the measured R_{p_i} and R_{p_f} reported in Table 4.1 to solve the change in ϕ over time. We used ϕ_i = 0.95 as a starting condition, and estimated the corresponding R_{p_M} value by solving Equation 4.6.4 using the R_{p_i} value measured for each cell layer. We then allowed ϕ to vary until the computed R_{p_S} matched the measured R_{p_f} value, and reported the predicted final ϕ_f value.

Model predictions

The results are presented in Table 4.4. We observed that for most cell layers, the confluence would have to go below 60% to account for the entire change in R_p measured over time. This is significantly lower than the range of ϕ values observed by microscopy which are typically between 0.80 and 0.95. This analysis suggests that changes in ϕ alone, which would correspond to the opening and widening of paracellular gaps, cannot account for the entire time-dependent changes in R_p measured. The time-dependent changes in R_p are likely due to the combination of the widening of intercellular gaps and the change in the resistivity of the confluent cell layer R_{p_M}, which would likely involve GVL and pore formation.

Sample	ϕ_i	R_{p_M} (UR)	ϕ_f
1		0.12	0.89
2		0.55	0.90
3		1.84	0.60
4	0 .95	0.08	0.62
5		0.08	0.35
6		0.08	0.57
7		0.05	0.46
8		0.03	0.39

Table 4.4: **Predicted change in cell confluence needed to account for the measured time-dependent change in R_p.** UR are units of resistivity mmHg.min.cm^2.μl^{-1}.

5

Effects of long-term transendothelial pressure conditioning on cultured SCE cells

5.1 Introduction

The bulk of aqueous humour outflow resistance is generated in the vicinity of the inner wall endothelium of SC [10, 11, 115] and the same tissues are implicated in the pathological increase of outflow resistance associated with ocular hypertension and glaucoma [11]. The mechanisms by which the inner wall endothelium regulates outflow resistance is still, however, poorly understood [12, 13, 69].

The inner wall endothelium of SC has an unusual combination of structure, barrier function and biomechanical environment compared to other endothelia [12, 25, 69]. First, SCE cells are joined to one another by continuous tight junctions, yet these cells lie on a discontinuous basement membrane [23, 52, 110]. Second, despite the presence of continuous tight junctions between SCE cells, the inner wall endothelium has a remarkably low hydraulic resistivity ($R_p \sim 0.33$ mmHg.min.cm^2.μl^{-1}), even when compared to fenestrated endothelia (R_p in the order of magnitude of 1 to 10 mmHg.min.cm^2.μl^{-1}) [12, 19]. The low hydraulic resistivity of the inner wall endothelium is attributable to the existence of transendothelial micron-sized pores, which provide flow pathways across the otherwise continuous endothelium [29, 51, 52]. Third, aqueous humour flows across the inner wall endothelium in the basal-to-apical direction and generates a transendothelial pressure drop in the same direction. In the healthy eye, this basal-to-apical transendothelial pressure drop is of sufficient magnitude to cause cells to locally detach off their basement membrane and to inflate large cellular outpouchings known as GVs [34, 40] (also see Chapter 2 and Chapter 3). GVs cause severe thinning of SCE cells and this is thought to be associated to pore formation [16]. The relationship between the biomechanical environment and the barrier morphology and function of the inner wall endothelium remains to be determined.

Detailed studies of the cellular and molecular processes underlying the regulation of outflow resistance require a model system that allows access to the surface of SCE cells and that facilitates controlled perturbations. To this end, previous investigators have developed *in vitro* models of human SCE cells that can be perfused over a short time (a few minutes to a couple of hours) in the basal-to-apical direction [33, 93]. These models reproduce key morphological features of the inner wall endothelium exhibiting GVLs similar to true GVs and transendothelial pores [17, 33, 93]. However, SCE cells do not form a continuous monolayer *in vitro*, which limits the use of such models in the study of barrier function regulation.

In culture SCE cells lose the expression of key endothelial differentiation markers (vWF and PECAM-1) [79], exhibit non-physiological intercellular gaps and organise into multi-layers rather than monolayers [33, 93, 109] (also see Figure 2.4 in Chapter 2 and Figure 3.2 in Chapter 3). Although cultured SCE cells express tight junction proteins claudin 11 and tricellulin, tight junction-associated protein zonula occludens 1 (ZO-1), and adherens junction protein VE-cadherin [26, 80, 93, 114], these proteins

are only discontinuously localised at the cell membrane. Further, while *in situ* F-actin is organised in a peripheral band around SCE cells and is associated with tight junctions, *in vitro* F-actin is organised in stress fibres that run along the length of the cell [17, 64, 116] (also see Chapter 3). Together, these observations suggest that cultured SCE cells lack mature cell-cell junctions, and particularly tight junctions. This is substantiated by another study using transmission electron microscopy that showed that cultured SCE cells do not form continuous tight junctions [109].

It is well-recognised that mechanical forces are an important driving factor of endothelial cell phenotype, affecting cytoskeletal re-arrangement, cellular orientation, adhesion molecule expression, and junction formation [117–122]. Further, exposure of cultured vascular endothelial cell monolayers to physiologically relevant mechanical forces over a long period (days) has been shown to enhance tight junctions and to decrease monolayer permeability [105, 123–125]. Here, we hypothesise that the unusual biomechanical environment of the inner wall endothelium, namely the basal-to-apical directed pressure drop and associated transendothelial flow, is key to maintaining the endothelial identity and the barrier morphology and properties of the SCE cell layer. This hypothesis implies that the absence *in vitro* of a physiologically relevant mechanical environment contributes to the loss of endothelial differentiation markers, mature cell-cell junctions and monolayer organisation *in vitro*.

The goal of this study was to investigate the effects of culturing SCE cells under a long-term basal-to-apical transendothelial pressure drop mimicking the *in vivo* biomechanical environment of the endothelium. To this end, we developed a conditioning system to subject SCE cells to a basal-to-apical directed transendothelial pressure drop over several days. We compared two groups: conditioned cell layers which were subjected to a 4 mmHg pressure drop, and static control cell layers that were held in the same system but subjected to a pressure drop below 0.5 mmHg. After the conditioning period, we assessed the barrier function of SCE cell layers by measuring their hydraulic resistivity, R_p. Next, the SCE cells were fixed, and using widefield fluorescence imaging we assessed the effect of conditioning on SCE cell confluence and density. Using confocal microscopy, we then examined the effects of conditioning on cell morphology and F-actin distribution. Finally, we evaluated the effects of conditioning on cell layer thickness and multicellular arrangement.

5.2 Materials and Methods

5.2.1 Experimental design

The aim of this study was to culture SCE cells under a long-term basal-to-apical transendothelial pressure conditioning of SCE cell layers and to investigate of conditioning on barrier morphology and properties. To this end, we designed an experimental set-up to compare two groups of SCE cell layers: (i) the

conditioned cell layers, which were subjected to a basal-to-apical transendothelial pressure drop of 4 mmHg, and (ii) the static control cell layers, which were subjected to a basal-to-apical pressure drop below 0.5 mmHg. The low pressure drop applied across the static control cell layers allowed for medium exchange necessary for cell survival.

Although a study has suggested that cell-cell junctions in SCE cell layers continue to mature over weeks in response to external stimulation (Underwood et al., 1999), in this study it was not practicable to condition the cell layers for such a long period of time given the required amount of medium and FBS volume needed for each day of perfusion (several tens of mL). Two more recent studies have reported that SCE cells exhibited significant changes in barrier function, morphology or junctional protein expression level between 5 days up to a week after the beginning of chemical or mechanical stimulation (Ashpole et al., 2014; Perkumas et al., 2012). We therefore conditioned SCE cells for 5 days (SC60) or 8 days (SC68).

For each cell line, a minimum of 10 samples were seeded per experimental run (5 conditioned and 5 static controls samples) (Figure 5.1). In the SC60, three additional samples were seeded and fixed on the same day as the conditioning experiment was started; these samples served as a benchmark for cell density and morphology before conditioning.

A hydrostatic transendothelial basal-to-apical pressure drop was applied across the SCE cell layers. The entire set-up was designed to fit into a cell culture incubator. A key design criterion in the development of the conditioning system was the requirement to perfuse the samples with DMEM without FBS. This requirement was based on preliminary experiments that demonstrated that perfusion with DMEM containing FBS led to significant clogging of the filter membrane (see Supplementary Figures, Figure 5.11 and [126]). SCE cells, however, do not survive for prolonged periods of time in the absence of FBS. To resolve these two conflicting requirements, all conditioned and static control samples were placed together in the same well of a plate containing a large volume of complete medium (DMEM with 10% FBS) such that the apical surface of the cell layers were in contact with serum. The cell layers were then perfused with filtered DMEM without serum. The FBS concentration in the receiving plate decreased over time due to the inflow of the DMEM perfusate, nevertheless the FBS concentration never dropped below 2.5 %. The effects of fluctuations in FBS concentrations was controlled for as all samples were placed in the same well and thus experienced the same FBS conditions at all times.

R_p was measured at the end of the conditioning period in each of the conditioned and static control samples. The samples were then immersion-fixed in 4% PFA and immunostained to examine cell morphology and F-actin architecture by fluorescence microscopy. In SC60, we also quantified nuclei density, cell confluence and cell layer thickness.

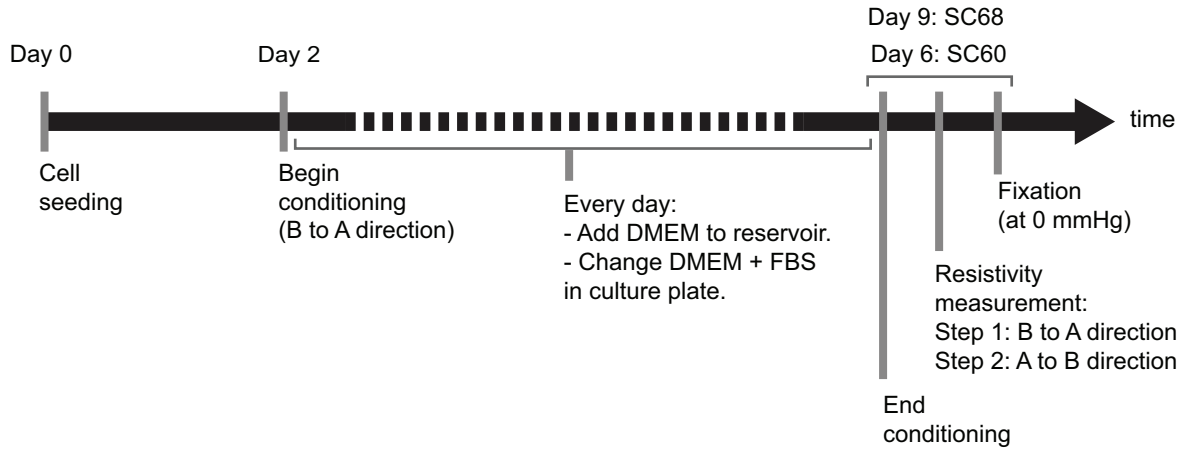


Figure 5.1: **Timeline of conditioning experiment.** B to A: Basal-to-apical. See text for further details.

5.2.2 Cell isolation, culture and seeding on porous membranes

The two human SCE cells lines used in this study were isolated from healthy donor eyes by K. Perkumas (Prof WD Stamer lab, Duke University, USA) and sub-cultured following standard tissue culture methods described in Chapter 2, Section 2.2.2. Two days prior to the start of conditioning (day 0 on the timeline, Figure 5.2), the cells were seeded at 20,000 cells/cm^2 onto the bottom-facing surface of filter membranes held by culture inserts (refer to the methods section in Chapter 2 for detailed procedures).

5.2.3 Experimental set-up for long-term conditioning

In preparation for the conditioning experiment, the inside of the culture inserts were washed to remove the DMEM with FBS used in culture, and they were then filled with filtered DMEM with 1% Pen-Strep-Glutamine (PSG). A silicone stopper was subsequently fitted inside of the insert to create a leak-proof seal and to introduce a small chamber between the apical surface of the membrane and the silicone stopper. Prior to fitting the stopper inside of the insert, first a thin piece of tubing (length: $\sim$ 50 mm; OD: 1.98 mm, ID: 1.02 mm, Portex 800/100/300, Smiths Medical, USA) was inserted through a punched 1.5 mm hole in the stopper, and a 19G needle was then threaded elsewhere through the stopper. During the fitting of the stopper inside of the insert, both the tubing and the needle served to shunt any pressure spikes that would otherwise damage the cells. Once the stopper was placed inside of the insert, a larger piece of tubing (OD: 3.2 mm; ID: 1.6 mm, C-Flex, 06422-02, Saint Gobain, France) filled with filtered DMEM was fitted onto the thin tube in the stopper. DMEM was then pushed through the tubing, into the chamber inside of the insert and out of the needle to flush out any bubbles. The larger tubing was connected to a manifold (Figure 5.2, Panel B) and closed off, and the needle was delicately threaded out of the stopper.

During conditioning, a basal-to-apical directed pressure drop across the SCE cells was applied

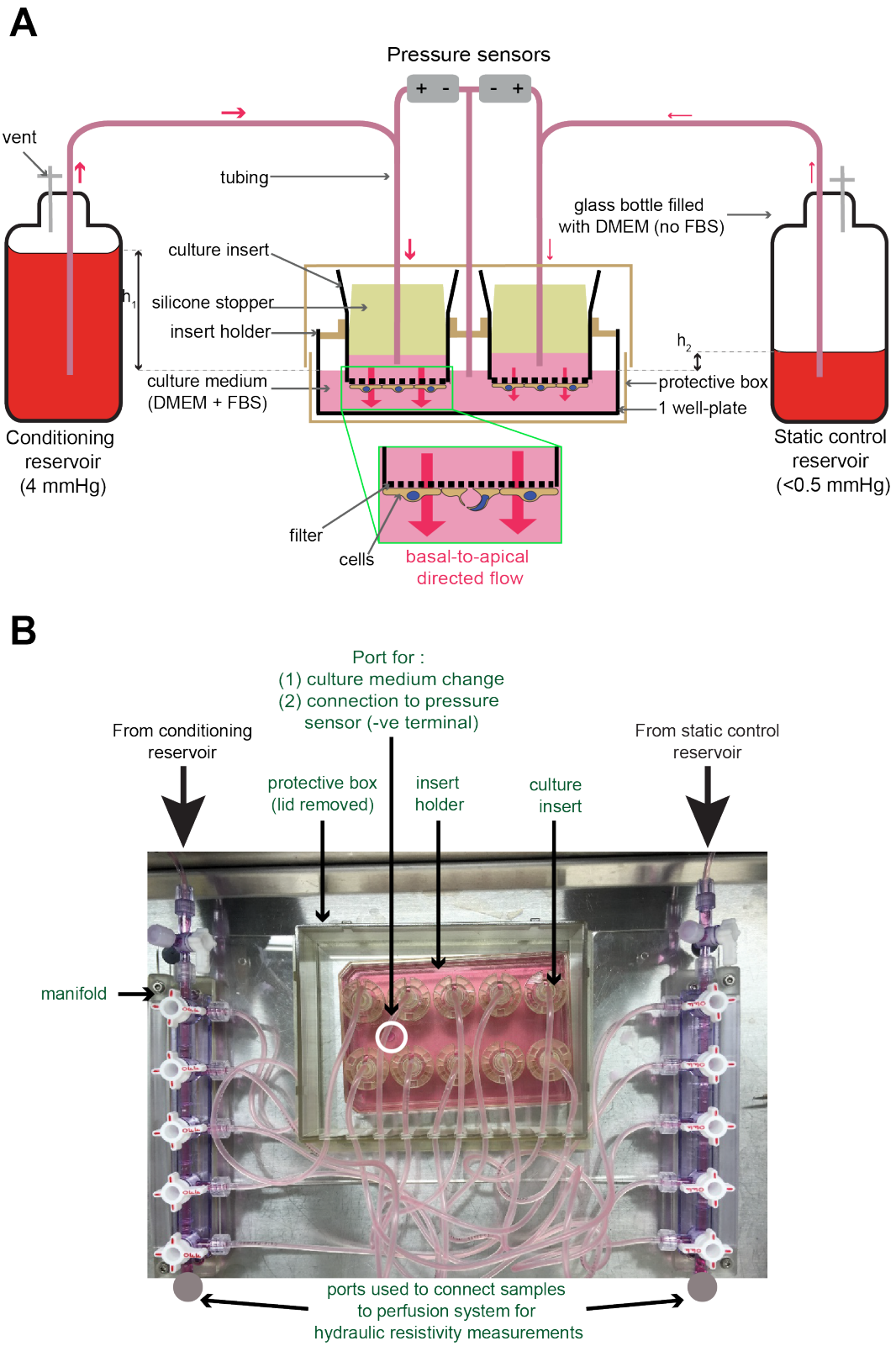


Figure 5.2: **Long-term transendothelial pressure conditioning system. (A)** Schematic of the perfusion system used for the long-term conditioning of SCE cells. Cells are seeded on the bottom face of the permeable membrane of a culture insert.(Figure caption continues in the next page.)

Figure 5.2: (Continued from previous page.) Culture inserts are held in a custom-made 3D printed holder placed in a one-well receiving plate filled with culture medium containing 10% FBS. The receiving plate and culture inserts are placed inside a custom-made protective box, to prevent contamination. A sealed chamber is created above the culture insert using a silicone stopper. The chamber created inside the culture insert is then connected via tubing to a sterilised glass bottle filled with filtered DMEM that serves as a hydrostatic reservoir. There are two reservoirs: one used for conditioning and one used for static controls. The height of difference between the DMEM inside the reservoir and the culture medium inside the receiving plate is adjusted to initially apply a pressure drop of either 4 mmHg or less than 0.5 mmHg. The whole system is kept in at 37 °C, 5% CO2 and 100% humidity in an incubator throughout the conditioning period. **(B)** Conditioning set-up. The culture inserts are connected to either the conditioning or the static control reservoir via a manifold and individual tubing. The other end of the manifolds is used to connect the culture inserts to the pressure sensor for measurements during conditioning, and later to the full perfusion system for hydraulic resistivity measurements at the end of the conditioning period. Medium inside the one-well plate is changed via tubing connected to an open-port in the insert holder (tubing not shown here). The same port is also used to connect to the pressure sensor for measurements during and at the end of the conditioning period.

using a reservoir consisting of a sterilised 500 mL glass bottle filled with filtered DMEM with 1 % PSG (Figure 5.2, panel A). The inside of the bottle was connected to atmospheric air via a syringe filter connected to port on the cap of the bottle to prevent contamination. There were two DMEM bottles to apply either a pressure drop of 4 mmHg (conditioning reservoir) or 0.5 mmHg (static control reservoir) across the samples. Each reservoir was connected to 5 culture inserts via a manifold and individual flexible tubing leading to the culture inserts (Figure 5.2, panel B). All 10 culture inserts used for each experimental run were held in a custom-made holder placed over a 1-well plate *filled with 30 mL DMEM with 10% foetal bovine serum (FBS) (Figure 5.2). The 1-well plate and culture insert adaptor was placed inside a custom-made 3D printed protective box with a clear Plexiglas® top and bottom to prevent contamination of the samples.

The pressure drop applied by each reservoir was monitored throughout the experiment using two differential pressure sensors connected at one end to one of the reservoirs and on the other end to the 1-well plate (Figure 5.2, Panel A). As DMEM flowed from the conditioning reservoir through the filter and cells and into the 1-well plate, the height difference between the fluid in the conditioning reservoir and the fluid in the 1-well plate decreased over time. As a result, the pressure drop applied across the conditioned samples also decreased over time (see Figure 5.12). Given the large surface area of the reservoirs (50 cm^2) and that of the 1-well plate (95 cm^2), the pressure drop across the conditioned samples decreased by approximately 0.2 mmHg for every 10 mL perfused. The inflow of the DMEM perfusate into the 1-well plate also resulted in a decrease in FBS concentration in the culture plate over time. The FBS concentration dropped from 10% to approximately 3% after 60 mL of perfused DMEM. There was little flow through the static control samples over time and the height of fluid in the control

*To clarify, a 1-well plate has the format of a traditional well-plate but only has a single well with no additional compartments.

reservoir did not change significantly. The pressure drop across these samples did nonetheless decrease to values between zero to slightly below zero over time because the 1-well plate filled up with DMEM coming from the conditioned samples. Note that small pressure drops below zero drove small apical-to-basal flow through the filter and cells.

The reservoirs were periodically re-filled with filtered DMEM to reset the pressure drop to 4 mmHg, and the culture medium in the plate was replaced to restore the FBS concentration to 10%. Reservoir re-filling and culture medium changes were carried out after approximately 60 mL of DMEM had been perfused. This volume of perfusate corresponded to a decrease in pressure drop of approximately 1.2 mmHg and to a decrease in FBS concentration in the culture medium in the plate of approximately 3%. The time interval between changes in reservoir re-filling and culture medium changes was generally approximately 6 h, and could be carried out without opening nor the reservoir nor the 1-well plate helping to avoid contamination. The reservoirs were re-filled using a syringe and filter connected to a port through the cap of the glass bottles (not shown on Figure 5.2 for diagramatic simplicity). The medium in the one-well plate was also replaced via a port in the one-well plate connected to a piece of tubing (Figure 5.2, panel B).

The pressure conditioning setup was entirely assembled in a tissue culture hood to prevent contamination. All materials used in the perfusion set-up, with the exception of the manifolds and the well-plate protective box, were either sterilised by autoclaving or were used new as provided sterile by the manufacturers. The manifolds used were always new, but as they were not sterilised by the manufacturer, they were sterilised with 70% ethanol. The plate holder and accompanying lid were not compatible with autoclaving and were therefore also sterilised with UV exposure and 70% ethanol.

5.2.4 Hydraulic resistivity measurements

Conditioning was stopped after 5 days (SC60) or 8 days (SC68) (day 6 and 9 on the timeline, Figure 5.2) and R_p was measured across all samples in both the basal-to-apical and then in the apical-to-basal direction at 4 mmHg. R_p was measured using a modified version of the *iPerfusion* system similar to that described in Chapters 2 and 3. Using this set-up, two samples (one from the conditioned group and one from the control group) were measured simultaneously (Figure 5.3, Panel A). Briefly, the perfusion system for R_p measurement was connected to the conditioning system via a port at the end of the manifold (see Figure 5.2, Panel B). During R_p measurements, the pressure drop was controlled and measured across two samples using the a single actuated reservoir and differential pressure transducer. Each sample was individually connected to a different thermal flow sensor to measure flow rate.

R_p was measured first in the basal-to-apical direction at 4 mmHg, corresponding to the physiological direction of flow across the inner wall endothelium. R_p was then measured in the apical-to-basal

direction at 4 mmHg (Figure 5.3, Panel B). Previous studies have shown that apical-to-basal transendothelial flow (unlike basal-to-apical transendothelial flow) does not drive the GV and pore formation [17, 93]. It was thus reasoned that R_p measurements in the apical-to-basal direction would be an assessment of the filtration properties of the cell layer attributable to confluence and cell-cell junctions alone.

5.2.5 Fluorescent labelling

After R_p was measured through all samples, these were removed from the conditioning set-up, and were then quickly washed with PBS and immersion-fixed in 4% PFA for 10 mins. The samples were then stored in DPBS at 4°C. Note that samples were fixed between 30 mins to a few hours after the end of conditioning, corresponding to the time to measure R_p of each sample and to remove the samples from the set-up.

In preparation for fluorescence imaging, the SCE cells were labelled to visualise the nuclei, F-actin and the whole cell body. For each sample, the filter membrane was delicately peeled off from the plastic housing of the insert, and it was placed cells facing up in a 48 well-plate filled with DPBS. Cells were permeabilised with 0.1% Triton-X buffer in DPBS for 10 mins then blocked with 10% goat serum and 0.2% Tween-20 for 1 hr. F-actin and the whole cell body were labelled simultaneously by incubation for 30 mins in 1:200 phalloidin (Phalloidin Alexa 568, A12380, Invitrogen, Thermo Fisher Scientific, USA) and 1:100 HCS CellMask (HCS Cell Mask Deep Red/Alexa 647, H32721, Invitrogen, Thermo Fisher Scientific, USA). The nuclei were labelled by incubation in 1:1000 DAPI (D1306, Thermo Fisher Scientific, USA) for 10 mins.

After a thorough wash with DPBS, the samples were mounted onto a glass slide with the cells facing up and away from the slide. A 0.19 mm spacer was placed over the periphery of the filter membrane to hold the sample in place and prevent the compression of sample during mounting. This was particularly important for the thickness measurements of the cell layer. The samples were then covered by mounting medium (Prolong Diamond Antifade, P37965, Invitrogen, Thermo Fisher Scientific, USA) and then with a coverslip.

5.2.6 Fluorescence imaging

The samples were examined and imaged using two different imaging modalities: widefield and confocal imaging. Widefield fluorescence imaging was used to collect image tiles through the entire samples and create a montage. The montages were then used to examine the overall morphology of the cells in different conditions, quantify the number of nuclei in each sample over a large area, and estimate confluency. Confocal fluorescence imaging was used to acquire optical sections through areas of the cell

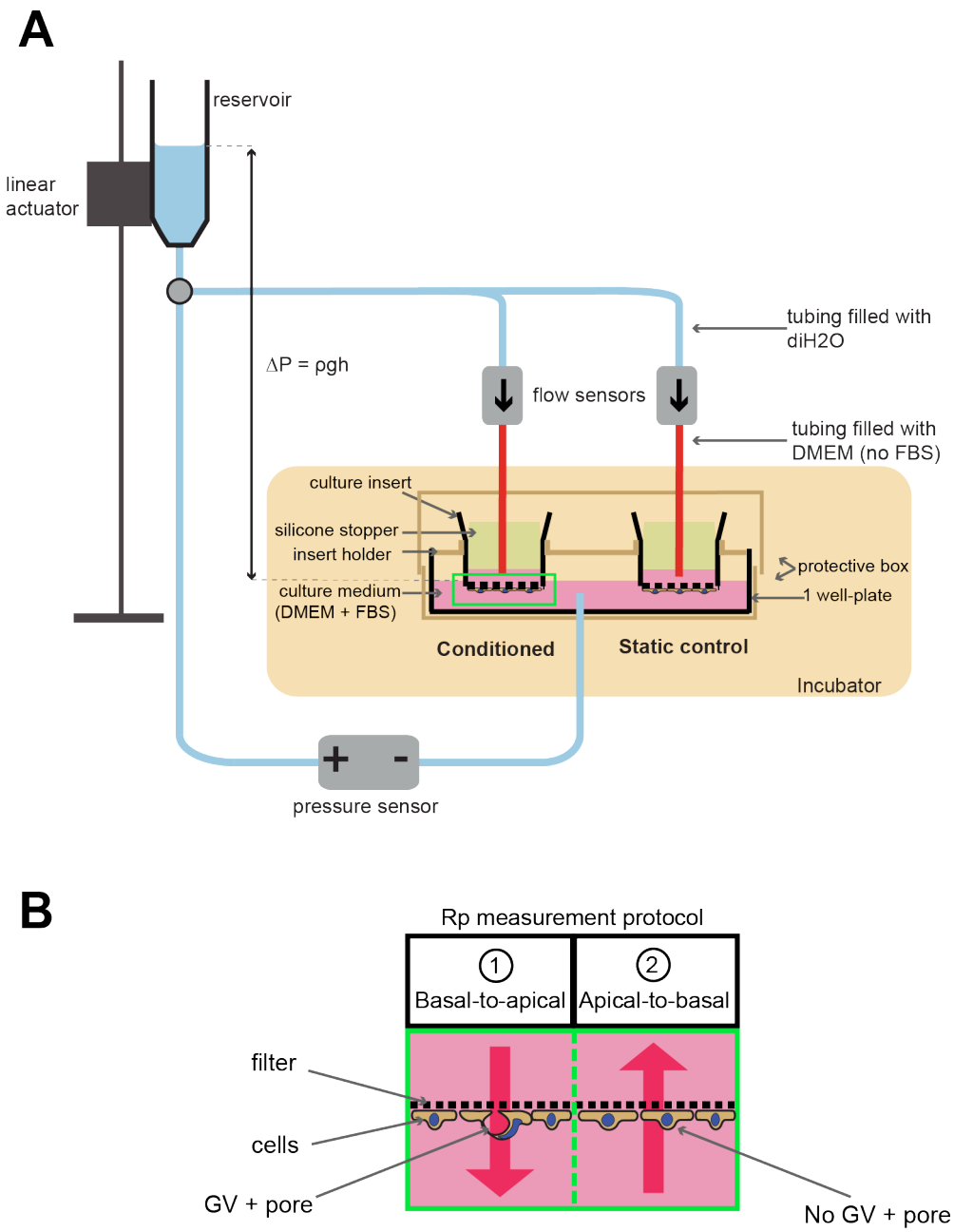


Figure 5.3: **Set-up and protocol for hydraulic resistivity measurements. (A)** The perfusion system used to measure R_p could be directly connected to the conditioning system such that minimal manipulation was needed. **(B)** Two samples could be measured at once for time-efficiency: one conditioned and one static control sample. ρ: density of the fluid in reservoir, g: gravitational acceleration, h: height or the fluid reservoir. This schematic is not to scale.

layers. The Z-stacks collected were used to examine cell and F-actin more closely, and to quantify the thickness of the cell layer in the conditioned and static control cell layers.

Image tiles of the entire samples were acquired using a Zeiss AxioVert 200M inverted widefield microscope (Zeiss, Germany) and a 10x objective (EC Plan-Neofluar 10x 0.30 Ph1, Zeiss, Germany). The tiles were then stitched and fused to create a montage image using Zen software (Zeiss, Germany). The widefield microscope was set-up automatically using the company-provided software to sequentially acquire the signal from same three different fluorescent probes.

To image the general morphology of the cells, and measure the thickness of the cell layer, the samples were imaged using a Leica SP-8 scanning confocal microscope (Leica Microsystems, Germany). For general morphology imaging, the cells were imaged using a 20x objective (Oil immersion, NA: 1.3) without zoom. Three separate lasers were used to excite the three different fluorophores: Diode 405, Diode 561 and Diode 633. The confocal microscope was set-up automatically using the company-provided software to sequentially acquire by line scan three different fluorescent probes with minimal bleed through: DAPI (Emission/Excitation wavelength: 358/461 nm), Alexa 568 (578/603) and Alexa 647(650/665). Images were acquired at 16-bit grey level scales, at 1024x1024 pixels, and using a line averaging of 4. Z-series were acquired at Nyquist sampling rate with a Z-slice interval of 0.24 μm and a pinhole opening set to 1 Airy unit.

For thickness measurement a 63x objective (oil immersion, NA: 1.4) was used without additional zoom. To speed up acquisition, the images of dimension 1024x256 pixels were acquired and only one fluorescent channel was used to image the probe for the whole cell stain (Alexa 647, Em/Ex: 650/655). Z-series were acquired at the Nyquist sampling rate with a Z-slice interval of between 0.24 μm and 0.30 μm and a pinhole opening set to 1 Airy unit. To acquire the full thickness of the cell layer, the first Z-plane was acquired on the basal side of the cell layer, near the filter membrane, before any fluorescent signal was visible. The last Z-plane was acquired on the apical side of the cell layer, after no more fluorescent signal was visible.

5.2.7 Image analysis and quantification

Nuclei were counted using the widefield images captured of the SC60 samples. Using ImageJ, the images were pre-processed by subtracting the background, enhancing the contrast and applying a Gaussian filter to the image. The nuclei were identified automatically using an Otsu thresholding, followed by a watershed separation on the resulting binary image (to separate connected nuclei) and finally by finding particles of size 100 μm^2 and above. The nuclei identified were then manually checked, and any connected nuclei that were not separated by the watershed algorithm were manually added to the nuclear count. For each sample, the nuclei were counted across 9 different square ROIs of 1 mm^2 (out of the

total filter area of 33 mm^2). For confluence quantification, the whole cell stain channel was thresholded manually using the background fluorescence as the cut-off intensity. The percentage of pixels above the threshold to total pixels in the image was then measured and interpreted as confluence percentage.

Thickness quantification was carried out in Matlab by first averaging the intensity along the y-axis for each x-position in the image. The process was repeated for every Z-plane image, yielding an orthogonal xz plane image of the cell layer (Figure 5.4). The resulting image was thresholded using the Ostu thresholding algorithm, and the thickness of the cell layer was based on the total number of white pixels divided by the length of the image (Figure 5.4).

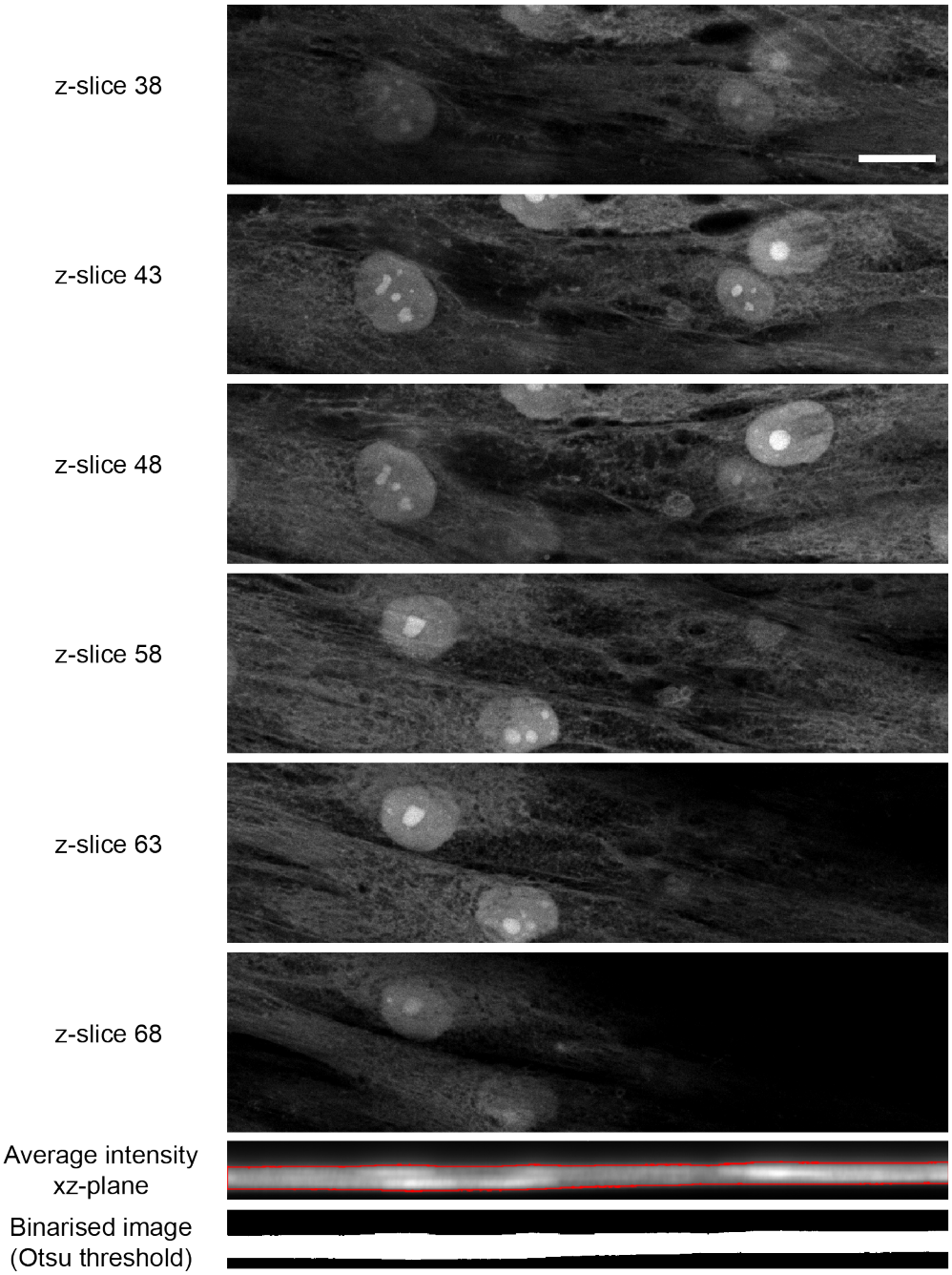


Figure 5.4: **Method for cell thickness measurement.** To measure the thickness of the cell layers, we acquired a Z-series of 1024x256 pixel images of the whole-cell stain fluorophore through the entire cell layer and with a Z-slice interval of 0.30 μm. Using the stack of images, we then computed the average intensity along the y-axis at each x-position to obtain a xz-plane image (second image from the bottom). The resulting xz-plane image was then thresholded using the Otsu thresholding algorithm and the mean thickness of the cell layer was computed by the taking the ratio of the total number of pixels above the threshold over the total length of the image in pixels.

5.3 Results

5.3.1 Effects of conditioning on R_p

To assess the effects of transendothelial pressure conditioning on the barrier function of SCE cells, we measured R_p at a pressure drop of 4 mmHg first applied in the basal-to-apical direction and then applied in the apical-to-basal direction (Figure 5.5). In the two cell lines used, SC60 and SC68, there was no difference in average R_p measured in the basal-to-apical direction between the static control and the conditioned samples (p = 0.7, unpaired Student's t-test). In all static control samples (SC60: n = 5, SC68: n = 3), the flow rate measured in the apical-to-basal direction was below the detection limit of the flow sensor (0.1 μl.min^{-1} [†]). In other words, R_p measured in the apical-to-basal direction was at least higher than 132 mmHg.min.cm^2.μl^{-1}, corresponding to the maximum R_p value measurable at 4 mmHg using the perfusion system. In conditioned samples, R_p measured in the apical-direction was significantly higher than R_p measured in the basal-to-apical direction (SC68: p < 0.02, n = 5; SC60: p $\ll$ 0.01, n = 4, paired Student's t-test). In the conditioned SC68 samples, R_p measured in the apical-to-basal was on average 8.43 $\pm$ 4.67 times higher (mean $\pm$ SD) than R_p measured in the basal-to-apical direction. In the conditioned SC60 samples, R_p measured in the apical-to-basal direction was on average 4.31 $\pm$ 0.64 times higher than R_p measured in the basal-to-apical direction.

5.3.2 Effects of conditioning on cell distribution, cell confluence and nuclei density

We next examined the effects of transendothelial pressure conditioning on SCE cell distribution and confluence (SC60: Figure 5.6; SC68: in Supplementary Figures, Figure 5.13). Using fluorescence widefield imaging, we confirmed that there was no obvious damage to the cell layers after the end of the conditioning period. In the static control samples of both cell lines, the SCE cells fully covered the filtration area of the filter and appeared to grow over one another in some areas, particularly in the SC68 (SC60: middle images in Figure 5.6A and 5.6B; SC68: in Supplementary Figures, left images in Figure 5.13A and Figure 5.13B). In the conditioned samples of both cell lines, the SCE cells were uniformly distributed across the filter membrane surface, but did not fully cover the filter and there were visible open spaces between the cells (SC60: right images in Figure 5.6A and 5.6B; SC68: in Supplementary Figures, right images in Figure 5.13A and Figure 5.13B). For a single cell line (SC60), we evaluated the cell confluence in the static control samples, conditioned samples, and the samples fixed before the beginning of the conditioning period (on day 2 of experimental timeline, see Figure 5.1 and Figure 5.6C). Cell confluence

[†]The lower detection limit of the flow sensor is taken to be the accuracy of the flow sensor at low flow rates supplied by the manufacturer.

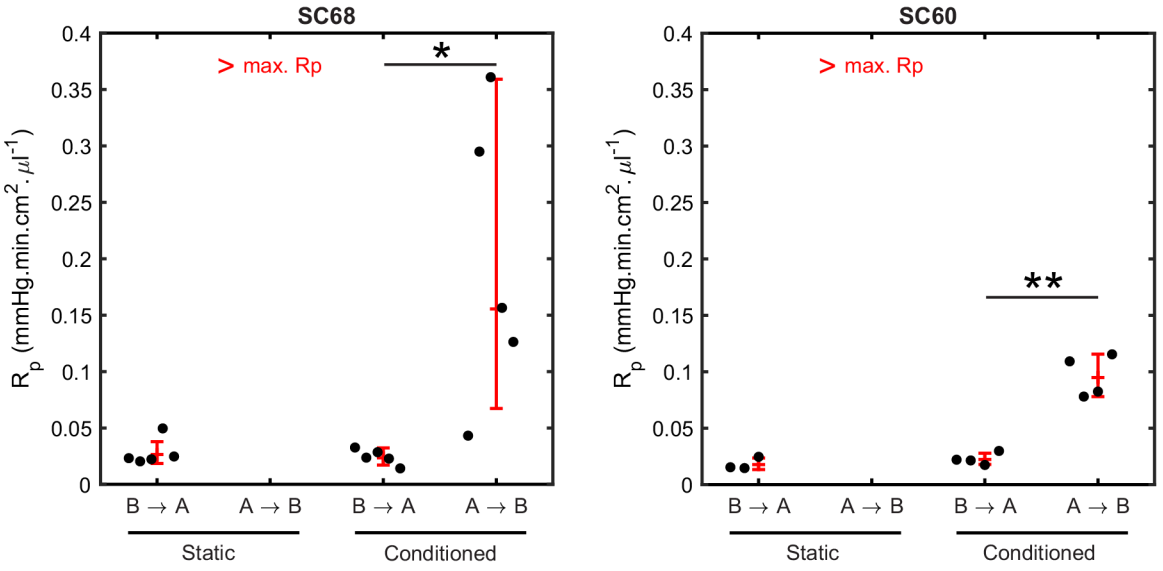


Figure 5.5: R_p **measurements at 4 mmHg in the basal-to-apical (B → A) and apical-to-basal (A → B) direction in SC68 and SC60.** All R_p were measured immediately after the end of conditioning (day 9 for SC68 and day 6 for SC60 on the timeline, Figure 5.1). In each cell line, direction and sample, R_p was computed once steady state had been reached. Black dots are individual measurements and red bars are the corresponding geometric mean $^{\times}/$ multiplicative SD (assuming a log-normal distribution, refer to Results section in Chapter 4). R_p measured in the apical-to-basal direction in all the static control samples was larger than the maximum R_p value measurable at 4 mmHg using the perfusion system. Statistically significant differences between R_p measured in the basal-to-apical and apical-to-basal direction in the conditioned samples are indicated by (*) for $p < 0.02$ and (**) for $p \ll 0.01$.

decreased with conditioning: there was a difference of 17% between the before conditioning and conditioned group ($p < 0.05$, $n = 3$ in each group), and a 26% between the static control and the conditioned group ($p < 0.01$, $n = 3$ in each group) respectively.

Given the differences in cell confluence observed in SC60, we examined the effect of long-term conditioning on nuclei density (Figure 5.6D). The differences in nuclei density between the experimental groups (i.e. before conditioning, static control and conditioned) were borderline significant (One-way ANOVA, $p = 0.07$). A multiple comparison approach revealed that only the conditioned and static control groups tended to be different (multiple comparison using Tukey's honest significant difference criterion, $p = 0.06$), and that there was no statistical difference between the other groups ($p > 0.2$).

We evaluated whether the difference in nuclei density could account for the differences in cell confluence between the before conditioning and conditioned groups. We first estimated the average cell area in the conditioned group by dividing the total area covered by cells by the nuclei count over the same area. Using the calculated average cell area (approximately 2400 μm^2), we then estimated that approximately 26% additional cells would be needed in the conditioned group to reach the same cell confluence as the one observed in the before conditioning group. Comparatively, the nuclei count difference actually measured between the conditioned and the before conditioning groups was only approximately 13%. The

discrepancy between the measured and estimated difference in nuclei density between the conditioned group and the before conditioning group suggests that the difference in measured cell confluence between these groups may be in part due to a change in cell area.

5.3.3 Effects of conditioning on cell morphology and F-actin organisation

Using fluorescence confocal imaging, we looked more closely at the effects of transendothelial pressure conditioning on cell morphology (SC60: Figure 5.6B; SC68: in Supplementary Figures, Figure 5.13B). In the static control samples, the SCE cells were elongated and frequently overlapped. In the conditioned samples, SCE cells tended to exhibit a polygonal-like morphology. Cell overlap was less frequently observed in the conditioned cell layers compared to in the static control cell layers, gaps were visible between the cells, and neighbouring cells appeared to arrange next to one another forming an irregular cobblestone pattern. In the before conditioning samples, the SCE cells had an elongated morphology and tended to overlap as was observed in the static control samples. Unlike in the static control samples, however, in the before conditioning samples there were visible gaps between the cells.

Confocal Z-stack imaging through the cells layers revealed that conditioning altered the organisation of F-actin (SC60: Figure 5.7 and Figure 5.8; SC68: in Supplementary Figures, Figure 5.14 and Figure 5.15). In the static controls, F-actin was organised in long stress fibres oriented parallel to the length of the cells. In addition, there appeared to be multiple layers of cells in the static control samples (particularly in SC68) as suggested by the frequent crossing of actin fibres and nuclei overlap. In the conditioned samples SC68, the SCE cells exhibited a more complex F-actin architecture, with both long and shorter actin fibres. Long F-actin strands were generally observed near the apical side of the cell. Shorter and randomly oriented F-actin stress fibres were generally observed near the basal side of the cell. In SC60, the difference in F-actin organisation between the static control and conditioned group was similar yet less pronounced than in the SC68; specifically, the SC60 conditioned samples tended to exhibit many more long-strands of F-actin than the same group in SC68.

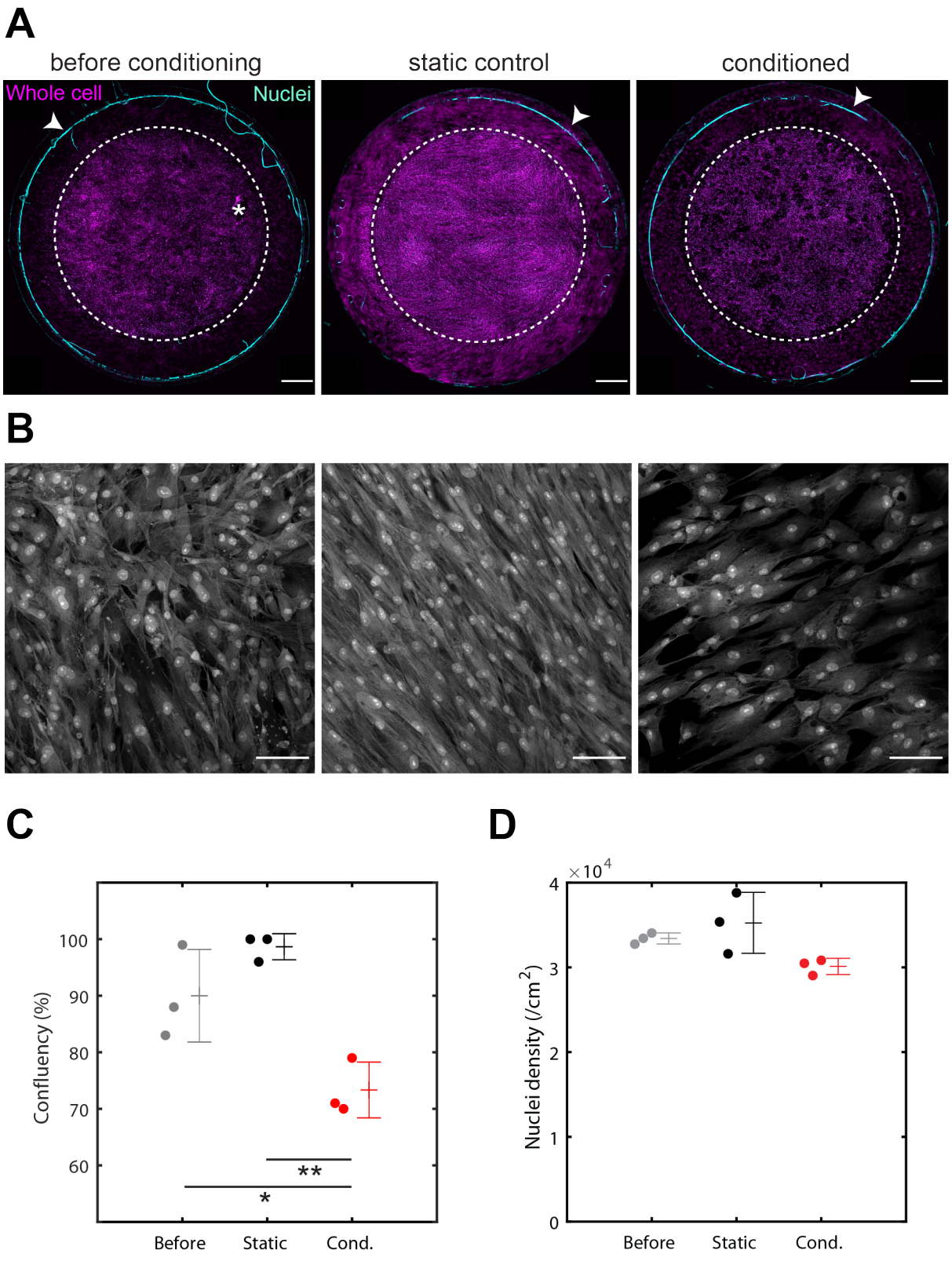


Figure 5.6: **Comparison of cell confluence, morphology and nuclei density. (A)** Representative images of the entire SC60 sample area in each condition: samples fixed before the beginning of the conditioning period (left), static control samples (centre) and conditioned samples (right). All images are a stitched tile-scan image acquired with a fluorescence widefield microscope and a 10x objective. Two fluorescence channels were acquired: that of the whole-cell stain (magenta) and that of DAPI (blue). (Figure caption continues in the next page.)

Figure 5.6: (Continued from previous page.) The area inside the white dashed circle corresponds to the filtration area of the membrane. The area outside the white dashed circle corresponds to the the part of the membrane that is glued to the culture insert housing. In the left panel, the filter and cells outside of the dashed circle are out of focus, explaining the lack of fluorescence visible in that region. The white asterisk in the left panel corresponds to a defect in the cell layer that arose following the preparation of the sample for immunofluorescence. Scale bars: 1000 μm. **(B)** Maximum intensity projection of confocal Z-series images acquired using a 20x objective of the whole-cell stain fluorophore. Scale bars: 100 μm. **(C)** Confluence level in each condition (quantified over n = 3 samples for each condition). Statistical significant differences in confluency between each condition are indicated by (*) for $p < 0.05$ and (**) for $p < 0.01$. **(D)** Nuclei density (quantified over n = 3 samples for each condition).

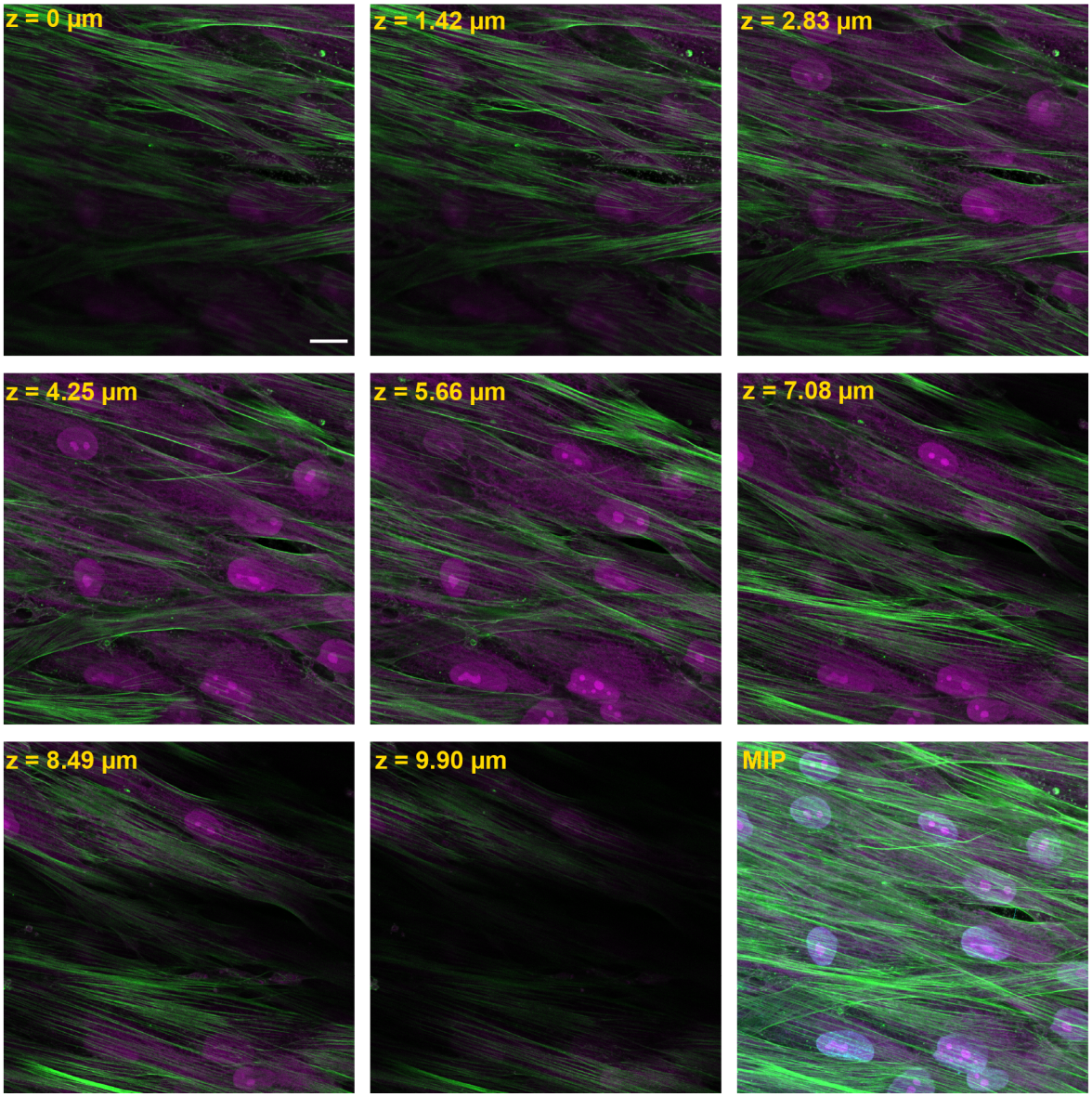


Figure 5.7: **F-actin distribution in static control SC60 cell layers.** The images presented are extracted from a confocal Z-series. F-actin is labelled green, the whole-cell body is labelled magenta. In the MIP image, nuclei are labelled in blue. The SCE cells exhibit an elongated morphology, and there is clear cell-cell overlap. The F-actin is organised in stress fibres and extends along the length of the cells. MIP: Maximum intensity projection. Scale bar: 20 μm.

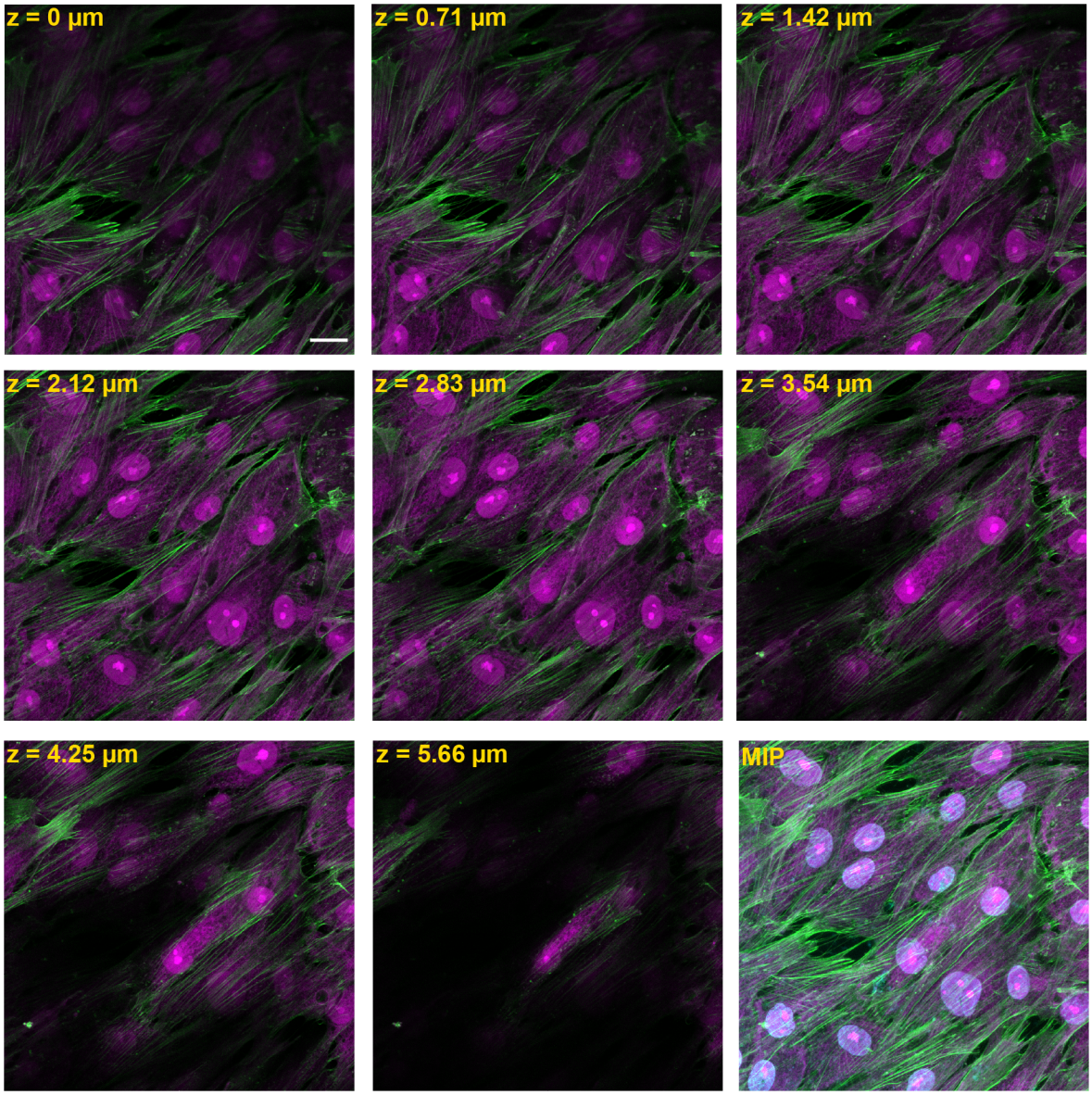


Figure 5.8: **F-actin distribution in conditioned SC60 cell layers.** The images presented are extracted from a confocal Z-series. F-actin is labelled green and the whole-cell body is labelled magenta. In the MIP image, nuclei are labelled in blue. The SCE cells exhibit a polygonal morphology, and there is little overlap between neighbouring cells. F-actin is mainly found at the periphery of SCE cells, and there are fewer stress fibres throughout the cell bodies compared to the static control presented in Figure 5.15. Scale bar: 20 μm.

5.3.4 Effects of conditioning on multicellular organisation

Given the observed tendency for SCE cells to overlap more in the static control group compared to in the conditioned group, we compared the cell layer thickness between the two groups using Z-stack confocal microscopy. In SC60, the cell layer thickness significantly decreased with conditioning, compared to the static controls ($p < 0.01$, unpaired t-test, Figure 5.9A). These measurements were corroborated by brightfield images of semi-thin sections through the SC68 and SC60 cell layers (SC60: Figure 5.9B and

SC68: in Supplementary Figures, Figure 5.16). In the static controls, SCE cells were organised in a thick multilayer. In the conditioned samples, SCE cell layers were thinner, and while cell-cell overlap was still seen in places, the cells were generally organised in a single layer.

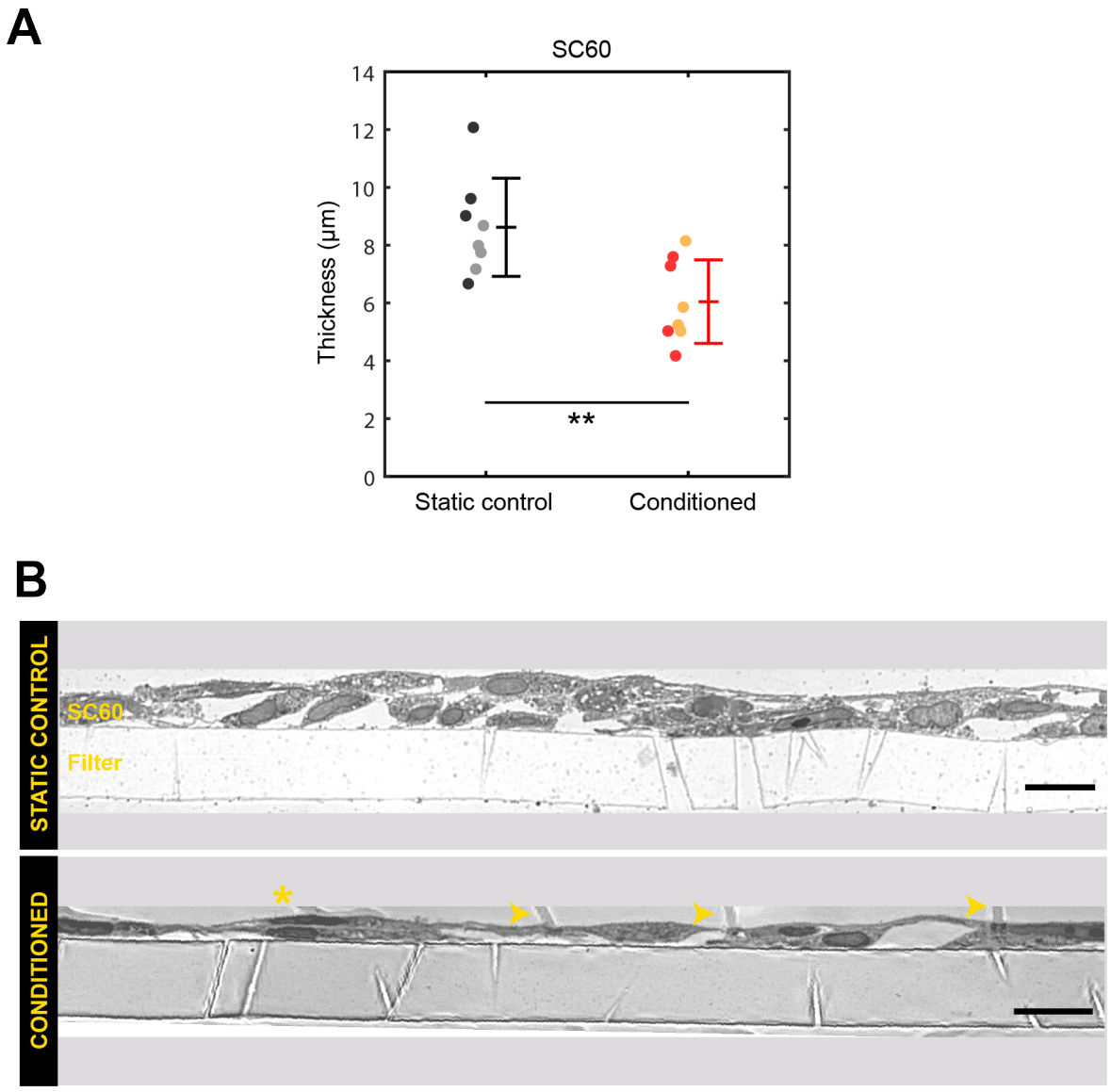


Figure 5.9: **Cell layer thickness and multicellular arrangement of static control and conditioned SC60 cell layers. (A)**. Thickness measurements of SC60 cell layers in the static control and conditioned groups using confocal microscopy (see Figure 1.5 for methods). For each condition, the dots represent measurement repeats in different areas of the cell layers (4 repeats for each sample). The two colours of dots for each condition represents two different cell layers in which the thickness was measured. The line and errorbars indicate the mean ± SD. The statistical significant difference in thickness between the static control and the conditioned cell layers is indicated by (**) for $p < 0.01$. **(B)** Brightfield images of semi-thin sections of SC60 cell layers cultured under static (top) and the conditioned (bottom) conditions. The yellow arrowheads indicate folds and preparation defects in the sections. The yellow asterisk in the bottom panel indicates an area where two cells overlap. Scale bar: 10 μm.

5.4 Discussion

The inner wall endothelium of SC likely is centrally involved in the generation of aqueous humour outflow resistance and the regulation of IOP [12, 13, 69]. Cell culture models are attractive for probing SCE cell mechanobiology, but their value is limited because they poorly replicate the barrier morphology and properties of the *in situ* SC endothelium. We hypothesise that the barrier organisation and function of the SCE endothelial cells is regulated by their biomechanical environment, namely the basal-to-apical pressure drop and flow that they experience *in vivo*. To test this hypothesis, we developed an *in vitro* set-up to condition SCE cells to a basal-to-apical transendothelial pressure drop sustained over a period of several days. We demonstrated that compared to static controls, conditioned SCE cells decreased in size, shifted from an elongated towards a more polygonal cell morphology and exhibited fewer central F-actin stress fibres. Likely due to the decrease in cell size, we observed that pressure conditioning also led to a decrease in cell confluence. The changes at the individual cell scale were accompanied with a multicellular re-organisation indicated by a decrease in cell layer thickness and a transition towards a monolayer arrangement. Despite the cellular and multicellular changes observed, we found that conditioning did not however lead to a change in basal-to-apical R_p, and in fact resulted in a decrease in apical-to-basal R_p compared to static control.

The inner wall endothelium of SC resides within a demanding biomechanical environment characterised by an unusual basal-to-apical directed transendothelial pressure drop. The exact magnitude of the basal-to-apical pressure drop is not known and is still a matter of controversy [12, 13, 69] as it depends on parameters that are not definitively known (i.e. transendothelial pore density and size in the endothelium). It is however thought to lie in the range of 0.7 mmHg to 5 mmHg. Regardless of the exact magnitude of the pressure drop experienced by the SC endothelium *in vivo*, it is known to drive GV formation which results in significant cellular strains and stresses.

In this study, we applied a transendothelial pressure drop of 4 mmHg across the filter and SCE cells. It is not possible to measure the exact pressure drop experienced by the cells individually, but it is likely only a proportion of the pressure drop applied due to the upstream resistance of the filter. Our previous results have shown that *in vitro* SCE cells are able to withstand pressure drops of at least 6 mmHg, and that pressure drops between 2 mmHg and 6 mmHg drive the formation of GVLs with similar characteristics as true GVs observed *in situ* in the inner wall endothelium of SC (see [33] and Chapter 2 and Chapter 3 of this thesis). Our choice of pressure drop magnitude for long-term conditioning assumed that GVL formation and the resulting stresses imposed are important biomechanical cues necessary to mimic the *in situ* environment.

5.4.1 Effect of conditioning on SCE cell morphology, multicellular arrangement and F-actin architecture

In static culture, vascular endothelial cells maintain a polygonal-shape, monolayer arrangement and form cell-cell junctions, although these are less mature than those found *in situ* and intercellular gaps exist [111]. Comparatively, SCE cells cultured under static conditions remain highly elongated and wide, and they do not maintain a monolayer organisation as found *in situ* but tend instead to grow into multilayers. In static culture, SCE cells also appear to lose the ability to form well-developed junctions, and have a lower expression of junctional proteins such as PECAM-1 [26, 79], and VE-cadherin [80], and discontinuous localisation at cell-cell junctions of tight junction proteins claudin 11 and tricellulin and tight junction associated protein ZO-1 [114]. In this study, we observed that compared to static controls, SCE cells conditioned under a basal-to-apical transendothelial pressure drop were smaller and more polygonal, and that neighbouring cells tended to arrange in a cobblestone-like pattern and appeared to organise in a monolayer. Together, these observed changes suggest that transendothelial pressure drop drives a morphological adaptation of SCE cells and a re-arrangement into a monolayer.

In SCE cells cultured under static condition, F-actin was found throughout the cells organised in long stress fibres running along the major axis of the cells. Conditioning led to a decrease in the occurrence of long stress fibres in the central regions of the cells, and also led, in some cells, to the appearance of shorter strands of actin and of actin fibres near the cell periphery. Interestingly, *in situ*, F-actin organises into a prominent peripheral band around the SCE cell and into thin long fibres in the central aspects of the cells [64]. While the F-actin organisation observed in conditioned SCE cells does not fully replicate the *in situ* organisation, it does appear to shift towards it. There is however at least one caveat to the F-actin observations made in this study. The cell layers were all only fixed between one hour and a few hours after the removal of transendothelial pressure drop. This corresponded to the time needed to measure R_p in all cell layers (refer to Figure 5.1 for experimental timeline). As a result of the delay between the removal of transendothelial pressure and fixation, it is possible that there was a re-arrangement in the F-actin cytoskeleton before the cells were fixed. To address this potential caveat, future experiments should be run in which the SCE cells are either fixed while the transendothelial pressure is still applied or immediately after its removal.

While some investigators have previously stated SCE cells were contact-inhibited [79, 80], other investigators have previously alluded to the issue of SCE cells growing into layers [33]. In our hands, cultured SCE cells often grew over one another rather than beside one another, forming layers of multiple cells (Figure 5.9) even when the cells were sub-confluent (Figure 5.6, Panel B, left figure). The multi-layer organisation of SCE cells culture under static condition is in stark contrast with the monolayer

arrangement of SCE cells observed in the inner wall endothelium of SC *in situ*. A striking finding of this current study was that pressure conditioning led to decrease in cell layer thickness associated with a reduction in cell layering and a shift towards a monolayer organisation resembling that observed *in situ*.

Pressure conditioning of SCE cells led to a significant decrease in cell confluence compared to both the static controls and the samples fixed before conditioning. There was however no significant difference in apparent cell density (estimated using nuclear counts) between these same groups. Given the estimated size of the SCE cells in the conditioned samples, we found that the observed difference in apparent cell density could not account for the significant difference in confluence level before and after the conditioning. This suggests that the morphological changes observed after conditioning were associated with a decrease in cell size. Based on the confluence level and the apparent cell density, we found that cell area in the conditioned samples was approximately 2400 μm^2. We were unable to accurately estimate the cell area in the static controls due to the frequent occurrence of cell-cell overlap and the difficulty to discern clear cell boundaries in these samples. As a comparison, however, Pedrigi et al. [33] previously reported that SCE cells cultured under static conditions were approximately 5000 μm^2. Despite being smaller than the value reported by Pedrigi et al. for SCE cells cultured under static conditions, the estimated cell area in our study in conditioned samples is still 5 to 6 times larger than the size of SCE cells *in situ*, which has been reported to be 409-480 μm^2 [20, 24]. Nonetheless, the observed decrease in cell size observed with pressure conditioning does further suggest a transition towards a morphology closer to that found *in situ*. We note, however, that as pressure conditioning appears to lead to a decrease in cell size and to a resulting decrease in cell confluence further optimisation experiments will be needed to achieve a confluent conditioned SCE cell layer, including testing for higher initial seeding densities, longer growth time before the of conditioning, etc.

Weakened cell-cell junctions and the existence of non-physiological intercellular gaps are a common limitation of vascular endothelial cell monolayers [69, 111]. As a result, the hydraulic resistivity of cultured vascular endothelial monolayers tends to be appreciably lower than the *in situ* hydraulic resistivity of endothelial monolayers [12, 107, 108, 127]. Similarly, the permeability of cultured endothelial cells to larger solutes such as albumin is often 10 - 100 times larger than *in situ* [111], and it has been reported to increase with increasing passage number [128]. In vascular endothelial cells, barrier function and cell-cell junctions, particularly tight junctions, have been shown to be improved by culturing cells in medium supplemented with sphingosine-1-phosphate (S1P) [129, 130] or with dexamethasone [131] or, in the case of brain microvascular endothelial cells, in astrocyte-conditioned medium [132]. Only a few studies have reported on possible culture methods to improve intercellular junctions and barrier function in SCE cell layers. These include dexamethasone treatment [109], culture in medium containing adult bovine serum (rather than FBS) [80] and culture on a hyaluronic acid-based substrate [133]. Using these

studies as well as knowledge developed in the vascular endothelial field, future investigation should aim to identify cell culture methods to improve intercellular junctions in cultured SCE cells. These methods could then be easily combined with long-term transendothelial pressure conditioning of SCE cells to achieve an *in vitro* model that better replicates the *in situ* inner wall endothelium of SC.

In this study, we chose to sustain conditioning over a period of 5 to 8 days. This experimental design feature was based on previous studies that have highlighted the slow response of SCE cells to mechanical and chemical stimuli. Ashpole et al. [134] showed that while vascular endothelial cells subject to shear stress elongate and orient in the direction of flow within 24 h of the onset of flow, SCE cells only show a similar response 7 days after the onset of flow. Perkumas et al.[80] demonstrated that treatment of SCE cells with adult bovine serum led to an increase transendothelial electrical resistance and VE-cadherin expression only after the 5th day of treatment. Underwood et al. [109] showed that the hydraulic resistivity of SCE cell layers continue to increase even 7 weeks after the start of treatment with dexamethasone suggesting that cell-cell junctions may continue to mature over weeks[‡]. Given these results, we reasoned that a conditioning time of several days may be necessary to observe a response in SCE cells. Our current study was not designed to characterise the timeline of the observed morphological changes. In our other studies of SCE cells fixed after short-term pressure-controlled perfusion, we however did not observe the change in phenotype presented here, suggesting that it occurred at least on a timescale longer than a couple of hours (refer to Chapter 3). It is unclear from our current results whether conditioning SCE cells for longer than 8 days would lead to a transition towards a *in situ*-like continuous monolayer with junctions. Further experiments are necessary to optimise the length of conditioning and to determine the timeline of changes in morphological and multicellular organisation during conditioning.

We would remiss if we did not mention that microenvironmental factors other than mechanical forces may account for the loss of endothelial differentiation and of barrier morphology and function in cultured SCE cells. Once isolated from their native microenvironment, SCE cells are in contact with a substrate of higher stiffness and of different composition, they are exposed to different chemical agents (cell culture medium does not fully replicate these), they no longer interact (physically and chemically) with neighbouring cells, and they are driven into a proliferation state (due to the presence of FBS in the medium). All of these factors likely affect the differentiation state and function of these cells. Furthermore, given the very low number of cells yielded during isolation from SC endothelium, SCE cells will initially be seeded at a very low density and will be driven into a prolonged and unphysiological proliferation state. This may also lead these cells to lose contact inhibition and to lose differentiation markers. We note that partly due to the scarcity of human SCE cells, it is a standard in the field to use

[‡]Note that Underwood et al. [109] did not report at which time point the hydraulic resistivity started to increase after the start of the treatment with dexamethasone.

these cells up to passage 5 or 6, limit after which they have been found to be senescent [17, 32, 33, 76, 86, 134]. However, repeated sub-culturing may lead to further loss in differentiation and function, and therefore earlier passage cells should be used whenever possible.

5.4.2 Effect of conditioning on R_p

R_p was higher when measured in the apical-to-basal direction than in the basal-to-apical direction in both the conditioned and in the static control group. This finding was consistent with previous reports by Alvarado et al. [93]. We speculate that the observed difference in R_p may be due to the opening of flow pathways in the basal-to-apical direction compared to the obstruction of pathways in the apical-to-basal direction (Figure 5.10). In the basal-to-apical direction, SCE cells tend to be pushed away from the filter opening intercellular spaces and forming GVs and pores, and leading to an overall opening of flow pathways and to a decrease in R_p. In the apical-to-basal direction, GVs and pores do not form as the SCE cells are pushed against the filter, likely flattening the cells and further narrowing intercellular spaces, leading to an overall decrease in obstruction of flow pathways and resulting in an increase in R_p. In the case of cells organised in a multilayer covering the entire filter, we speculate that the compression of the multiple layers of cells over one another leads to a severe obstruction of flow pathways resulting in very high R_p values in the static control samples compared to in the conditioned samples.

The experimental aim behind measuring R_p in the apical-to-basal direction was to assess the effects of conditioning on R_p caused by changes in the cell-cell junctions alone, as GVs and pores do not form in this direction of flow. However, due to cell layering, the apical-to-basal R_p measured in the static control samples did not serve as an appropriate benchmark against which to compare the apical-to-basal R_p measured in the conditioned samples. In the future, the apical-to-basal R_p of SCE cells before the start of the conditioning experiment should be measured to be used as a benchmark value for comparison with conditioned SCE cells.

We observed no difference in R_p measured in the basal-to-apical direction between the conditioned and static control groups. This was surprising given that the cell confluence was significantly larger in the static control group compared to the conditioned group. In view of the study presented in Chapter 4 that looked at the effects of cell confluence on R_p, we do not entirely understand this result. A possible limitation is that the layering of SCE cells cultured under static conditions is not taken into account when looking at the cell confluence data alone. We speculate that while the cells in the static control appear to cover the filter entirely, they may not be growing directly on the filter but may instead be growing over one another (see Figure 5.10, right column). Due to the known weak junctions between the cells, it is possible that during perfusion, gaps between layers of cells widen and flow paths open such that the R_p is similar between the conditioned and the static controls. Alternatively, it may be that

the junctions between SCE cells in the conditioned group may have strengthened, thus compensating for the less confluent state of the cell layer.

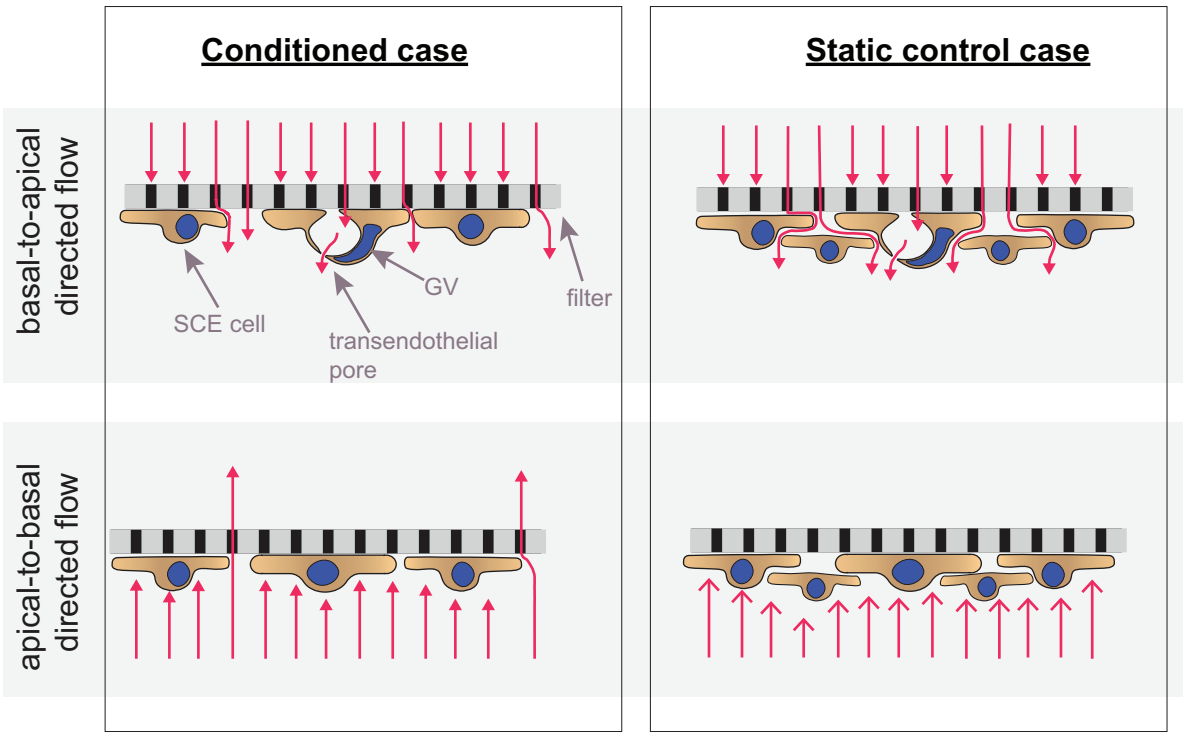


Figure 5.10: **Hypothetical model comparing the existing flow pathways through conditioned and static control cell layers perfused in the basal-to-apical and apical-to-basal direction.** The hypothetical model proposed aims to explain the differences in the R_p values of the conditioned and static control cell layers measured in the basal-to-apical and apical-to-basal direction (refer to Figure 5.5). See text for further details.

5.4.3 Strengths and limitations of the experimental set-up

We developed a system to condition SCE cells to a basal-to-apical directed transendothelial pressure drop over a period of days. The system allowed simultaneous conditioning of multiple samples to allow for statistical analysis of experimental measurements. The system was developed in a way to avoid manipulating the samples during the conditioning period, thus reducing the risk of contamination.

There were two important and related experimental design features in the conditioning system developed. The first experimental design feature was the choice of filtered DMEM alone as the perfusate to avoid clogging of the filter by the accumulation of protein in the FBS. Because FBS is needed for SCE cell survival, the second experimental design feature consisted of placing all samples together in a single well of a receiving plate containing a large volume of culture medium supplemented with FBS such that the apical surface of the cells was always in contact with FBS. B placing all the samples together in the same well with large volume of culture medium we minimised the dilution of FBS content by the inflow of DMEM perfusate during conditioning, and we also ensured that all the samples experienced

the changes in FBS concentration over time. However, one potential limitation of holding all the samples in the same plate was that any chemical factors released by one group of samples could affect the other group. This effect was however likely minimised by the large volume of medium contained in the 1-well plate (a few tens of millilitre) maintaining the any potentially synthesised chemical factor at a low concentration.

A limitation of the conditioning system designed was the fluctuation in pressure drop applied across the SCE cells over time. The pressure drop across the cells depended on the height difference between the DMEM contained in the reservoir, and the culture medium contained in the receiving plate in which the samples were held. Throughout the conditioning period, the difference in height between the two containers decreased as DMEM flowed from the reservoir through the samples and into the receiving plate. The SCE cells hence experienced a decreasing pressure drop over time, with punctual step increases when the reservoir was re-filled with DMEM. The choice of a reservoir and a receiving plate with a large surface area, however, minimised the changes in pressure over time. In the configuration used in this study, the conditioned SCE cells almost continuously experienced a pressure drop between 4 mmHg down to 2.5 mmHg, compared to the static control samples that experienced a pressure drop that was always below 0.5 mmHg. Although the current design would not be appropriate to study the effect of different pressure drop levels on SCE cells, it is nonetheless an appropriate set-up to study the differences between SCE cells cultured under a transendothelial pressure drop compared to under static conditions.

5.5 Conclusion

In conclusion, we hypothesised that transendothelial pressure drop is a major driving factor in the maintenance of the endothelial barrier morphology and function of SCE cell layers. To test this hypothesis, we have developed a system for the long-term conditioning of SCE cells to a basal-to-apical directed transendothelial pressure drop. We have shown that pressure conditioning leads to changes in cell morphology, F-actin architecture and multicellular arrangement that suggest a shift towards a SCE cell layer that better replicates the *in situ* SC endothelium morphology. While further optimisation experiments are required to achieve a confluent layer of cultured SCE cells with conditioning and to confirm that conditioning leads to improved cell-cell junctions and barrier function, our results are a promising first step to establishing an improved cell culture model of the inner wall endothelium of SC. Such a culture model would open new opportunities to investigate the mechanisms by which the inner wall endothelium of SC generates outflow resistance, and how these mechanisms are affected in glaucoma.

5.6 Supplementary Figures

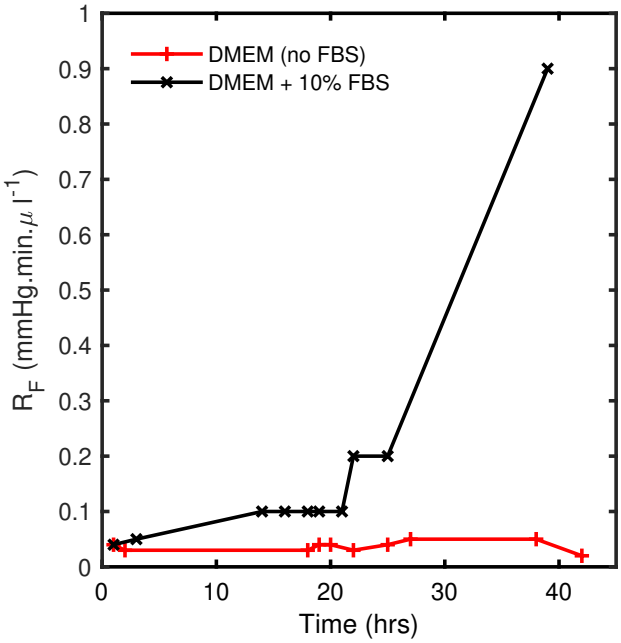


Figure 5.11: **Filter clogging due to the presence of serum in the cell culture medium.** The filter resistance, R_F increases over time when serum (FBS) is added to the culture medium, while it remains constant in the absence of serum. Note that the clogging of the filter by serum is not consistent between different experiments, and is therefore unpredictable, justifying the use of DMEM for the long-term conditioning of SCE cell layers.

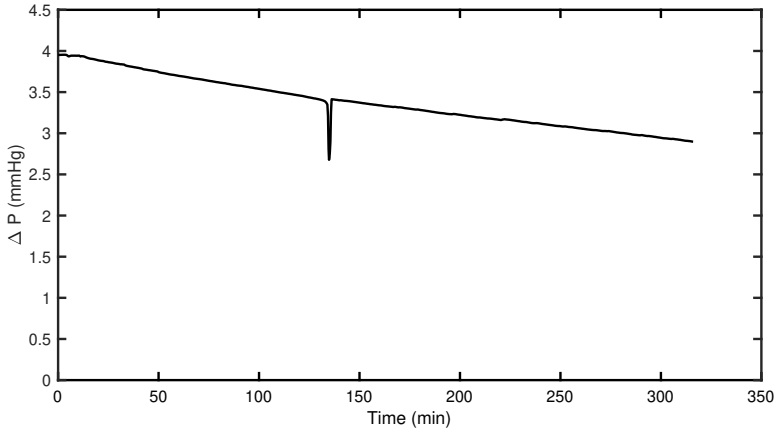


Figure 5.12: **Representative plot of the change over time in the pressure drop across the conditioned samples.** The spike observed at approximately 150 mins was caused by the opening and closing of the cell culture incubator during the pressure drop measurement.

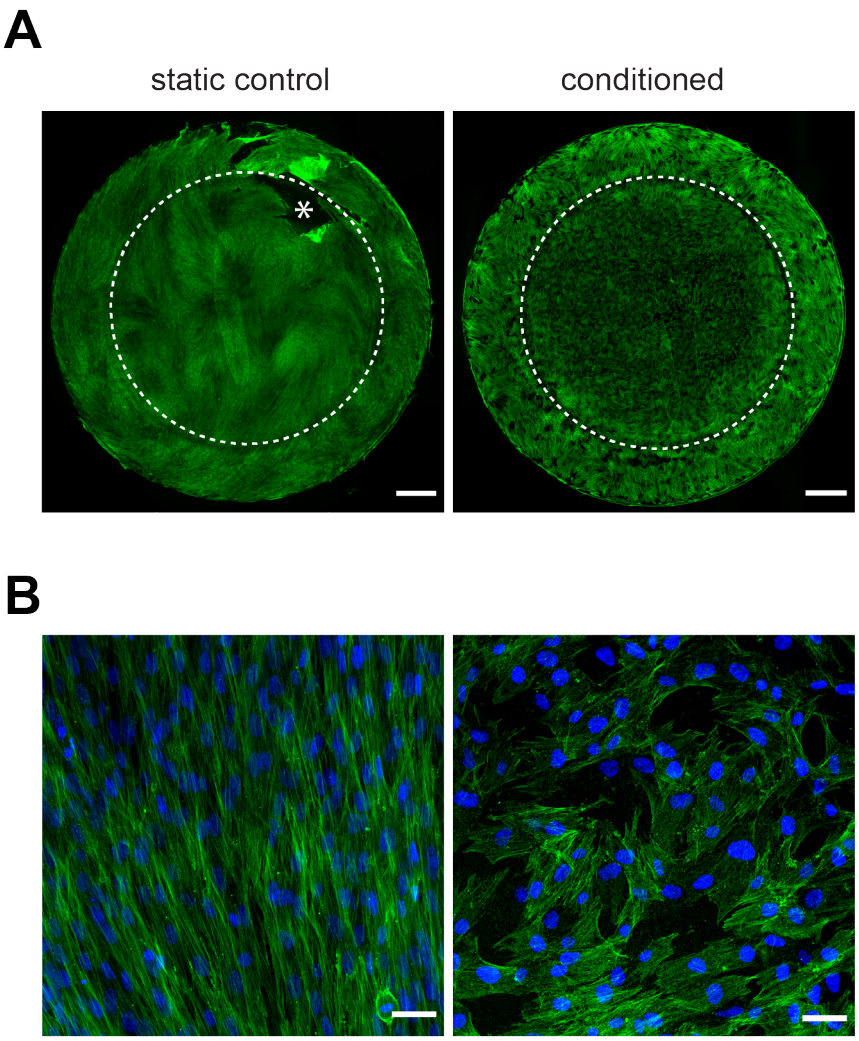


Figure 5.13: **Morphology and arrangement of SC68 cells in the static control and conditioned group. (A)** Representative images of the entire static control and conditioned SC68 cell layer area. The cells were fluorescently labelled for F-actin in these images (green). The area outside the white dashed circle is the part of the filter membrane that is glued to the culture insert housing. The white asterisk in the left panel corresponds to a defect in the cell layer that arose following the preparation of the sample for immunofluorescence. Scale bar: 1000 μm; **(B)** Maximum intensity projection of confocal Z-series images acquired using a 20x objective. The cells were fluorescently labelled for F-actin (green) and the nuclei (blue). Scale bar: 50 μm

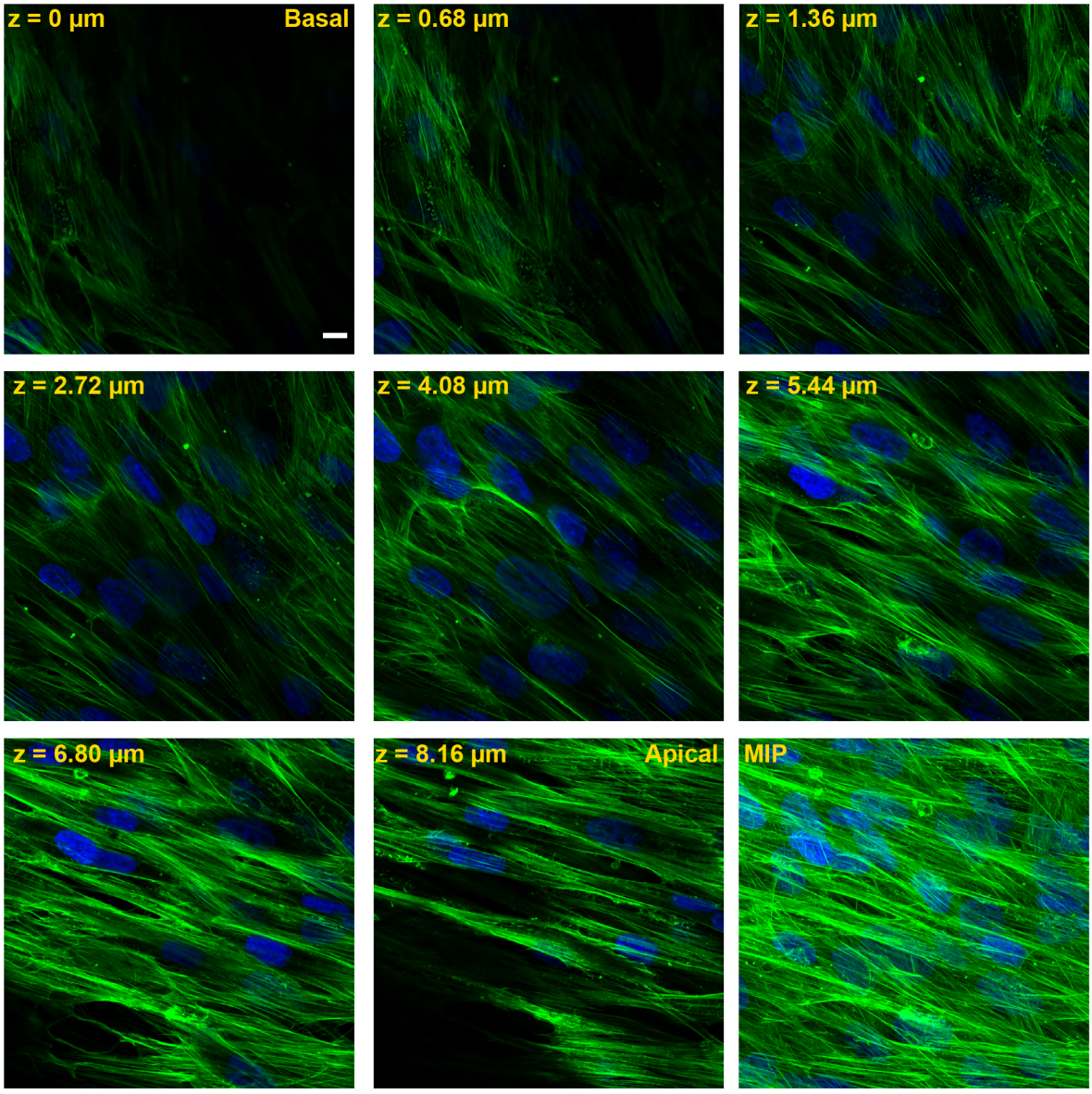


Figure 5.14: **F-actin organisation in static control SC68 cell layers.** The images presented are extracted from a confocal Z-series. F-actin is labelled green, and the nuclei are labelled blue. The SCE cells exhibit an elongated morphology, and there is clear cell-cell overlap. The F-actin is organised in stress fibres and extends along the length of the cells. MIP: Maximum intensity projection. Scale bar: 10 μm

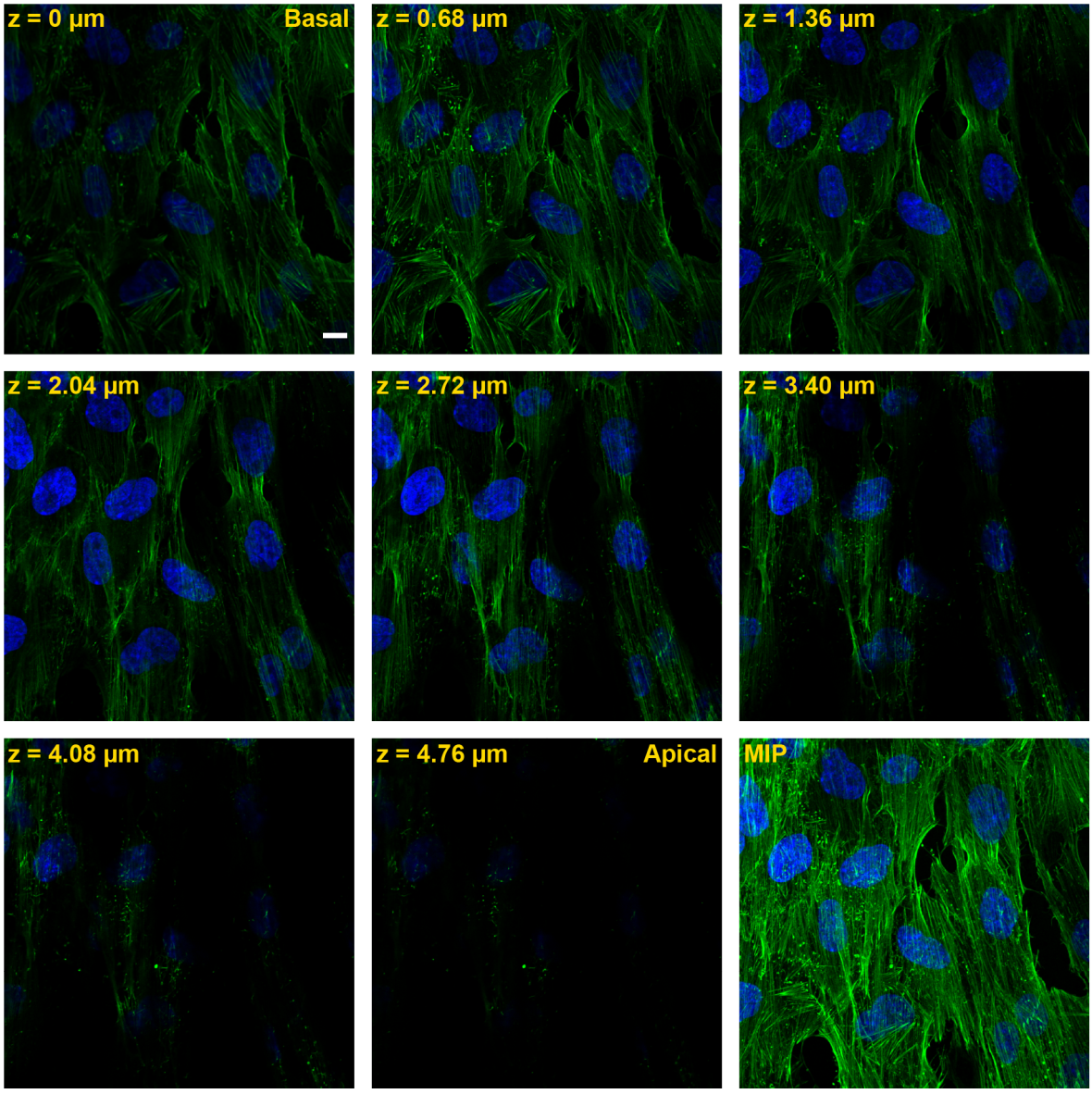


Figure 5.15: **F-actin organisation in conditioned SC68 cell layers.** The images presented are extracted from a confocal Z-series. F-actin is labelled green and the nuclei are labelled blue. The SCE cells exhibit a polygonal morphology, and there is little overlap between neighbouring cells. F-actin appeared to organise in different directions rather than only as long fibres extending along the long-axis of the cells as in the static control (refer to Figure 5.14). MIP: Maximum intensity projection. Scale bar: 10 μm



Figure 5.16: **Brightfield images of semi-thin sections (0.5 μm) through conditioned and static control SC68 cell layers.** The yellow arrowheads indicate folds and preparation defects in the sections. The yellow asterisk in the top panel indicates a region where two neighbouring brighfield images of the cell layer have been stitched. Note that the cell layer is organised in multilayers, whereas the conditioned cell layer appears to organise as a monolayer. Scale bar: 10 μm

6

Conclusions

The bulk of aqueous humour outflow resistance is generated in the vicinity of the inner wall endothelium of SC, and elevated outflow resistance leads to ocular hypertension in glaucoma. In this thesis, we examined the hypothesis that the biomechanical forces acting on the inner wall endothelium are key determinants of its barrier morphology and properties. The basal-to-apical directed pressure drop across the endothelium of the inner wall of SC tends to push the SCE cells off their basement membrane and drives GV formation. GVs generate biomechanical strains likely in excess of 50% and these strains are thought to be associated with the formation of transendothelial pores that provide a flow pathway across the inner wall endothelium. By causing cytoskeletal and intercellular junction remodelling, the transendothelial pressure drop may also be important to maintaining the barrier morphology of the endothelium. Our hypothesis further predicts that the biomechanical properties of SCE cells are important modulators of the transport mechanism across the inner wall endothelium and may thereby modulate outflow resistance. The main goal of this thesis was to investigate the interaction between the basal-to-apical directed transendothelial pressure drop, the cellular processes governing GV dynamics, and the barrier morphology and properties of SCE cell layers.

In Chapter 2, we described the life cycle of GVLs formed in cultured SCE cells during basal-to-apical transendothelial perfusion at controlled pressure drop. Unlike previous studies on GVL dynamics, we tracked the contour of GVLs identified in time-lapse images acquired during the perfusion. We showed that while GVL formation and growth appears to be largely pressure-dependent, GVLs are able to retract while the pressure drop is maintained. We found that treatment with ROCK inhibitor Y-27632 impairs GVL retraction both while pressure drop is maintained and after it is removed, suggesting that GVL retraction depends on actomyosin contractility. These findings suggest that while GVL dynamics are pressure-dependent, they also depend on other factors including cell contractility. Extending our conclusions to the dynamics of true GVs in the inner wall endothelium of SC, our results predict that GVs and associated transendothelial pores may be cyclically opening and closing over time, rather than remaining open once formed. This further implies that SCE cells may be able to directly regulate outflow resistance and IOP by modulating GV (and perhaps pore dynamics) dynamics through an actomyosin-dependent process.

In Chapter 3, we examined the F-actin and vimentin IFs organisation in perfusion-fixed SCE cells, and specifically around GVLs. We found that basal-to-apical directed perfusion led to cytoskeletal remodelling, and that a proportion of GVLs are surrounded by an F-actin band, a vimentin cage or both features together. The presence of F-actin bands surrounding GVLs is consistent with the role of actomyosin contractility in GVL retraction reported in Chapter 2, and we speculate that these F-actin bands may contract against the GVL wall during GVL retraction. Furthermore, given that vimentin IFs can undergo large deformations before rupturing and that they stiffen in response to increasing deformation,

the vimentin cages found surrounding GVLs likely are important to help SCE cells withstand the large biomechanical stresses and strains generated by GVL formation.

Together, our findings from Chapter 2 and 3 have generated new testable hypotheses on the cellular processes and biomechanics involved in the different phases of the life cycle of GVLs. Importantly, due to the association of transendothelial pores with true GVs in the inner wall endothelium of SC, these results are a step forward toward understanding the known relationship between the mechanical properties of SCE cells and outflow resistance. This is of significance as increased cellular stiffness in glaucomatous cells has been correlated to a decreased pore forming ability, and the reduced pore density observed in the inner wall endothelium of SC in glaucoma is the only known morphological alteration that might explain the elevated outflow resistance.

In Chapters 4 and 5, we investigated the effects of short-term and long-term pressure drop application on the barrier function of SCE cell layers cultured on porous filter membranes. In Chapter 4 we showed that the hydraulic resistivity of SCE cell layers is both time and pressure-dependent. We speculate that the observed time and pressure-dependent changes in hydraulic resistivity are associated with morphological changes in the SCE cell layers. In Chapter 4 we also highlighted that the existence of non-physiological intercellular gaps in cultured SCE cell layers limits the interpretation of resistivity values computed using a series resistance model, and we proposed that a parallel resistance model may better represent the resistivity of a cell layer with intercellular gaps.

Intercellular gaps most likely result from a loss mature cell-cell junctions *in vitro* . In Chapter 5, we examined the hypothesis that the basal-to-apical pressure drop experienced by SCE cells *in vivo* may be key to the maintenance of their barrier morphology and function. We demonstrated that long-term pressure conditioning of cultured SCE cell layers led to changes in cell morphology, F-actin architecture and multilayer organisation consistent with a transition towards a more *in situ*-like barrier morphology.

In vitro models of the inner wall endothelium are attractive to probe the SCE cell biomechanical processes involved in outflow resistance generation and to investigate how alterations in biomechanical function contribute to elevated outflow resistance in glaucoma. Our findings in Chapter 4 and 5 improve our understanding of the properties and limitations of current *in vitro* models of the inner wall endothelium of SC, and provide insight into the biomechanical factors that drive barrier morphology and properties *in situ*. Our current findings are a step forward for the development of an improved *in vitro* model of the inner wall endothelium of SC that may be used in the future to study the relationship between transendothelial pressure drop and outflow resistance regulation, and to develop promising new therapeutics with long-lasting IOP lowering effects for glaucoma therapies.

6.1 Future work

The results presented in this thesis improve our understanding of the biomechanical regulation of GV formation and of the barrier function of SCE cell layers, while also raising further research questions.

What are the dynamics of F-actin that accompany the life-cycle of GVLs and are F-actin bands surrounding GVLs contractile?

In Chapter 2, we found that GVLs formed in cultured SCE cells exhibit a life-cycle including a growth and a retraction phase. In Chapter 3, we observed that transendothelial perfusion resulted in F-actin remodelling in SCE cells, and that a proportion of GVLs were surrounded by a band of F-actin. We speculate that the F-actin band may be contractile, and that it likely assembles around GVLs at the initiation of their retraction phase. This speculation is consistent with the dynamics of other similar F-actin structures found in cells, such as the actin ring found at the cleavage furrow in dividing cells [103], and around secretory vesicles [104]. To confirm this hypothesis, future work should involve (i) time-lapse imaging of GVLs formation in live SCE cells fluorescently labelled for F-actin, and (ii) double staining of perfusion-fixed SCE cells with F-actin and myosin II.

What is the biomechanical function of vimentin cages found around GVLs?

In Chapter 3, we observed that proportion of GVLs were surrounded by a vimentin cage. We hypothesise that these vimentin cages provide mechanical support to the SCE cells, allowing them to withstand the high strains imposed by GVL formation. To test this hypothesis, it would be interesting to treat SCE cells with compounds inhibiting vimentin (e.g. Withaferin) and investigate their effects on GV dynamics and structure.

What are the effects of elevated subcortical stiffness on the GVL life-cycle?

Increased subcortical stiffness in glaucoma is associated with decreased pore formation [17]. Furthermore, drugs that typically increase outflow resistance have been shown to systematically cause increased cell stiffness, while drug that typically decrease outflow resistance cause decreased cell stiffness [76]. It has been hypothesised that increased cell stiffness decreases the ability for SCE cells to form GVs, leading to decreased pore formation. The effects of increased cell stiffness on GVL dynamics and structure are however not known, and should be investigated.

A possible method to increase SCE cell stiffness would be treatment with connective tissue growth factor (CTGF). Overexpression of CTGF in the mouse eye has been shown to lead to ocular hypertension and optic nerve damage, and treatment of trabecular meshwork cells has been shown to increase cell contractility [135]. In addition, CTGF expression is increased in glaucomatous SCE cells. Treatment of

perfused SCE cells with with CTGF may therefore be a good model to study the effects of glaucomatous cell stiffness increase on GVL dynamics and structure, providing further insight into the pathophysiology of glaucoma.

What are the morphological alterations associated with time-dependent changes in hydraulic resistivity measurements in cultured SCE cells?

In Chapter 4, we found that there was time-dependent decrease in the hydraulic resistivity. We hypothesised that these changes are associated with morphological changes in the SCE cell layers, particularly GV and pore formation and intercellular gap widening. To verify the validity of this hypothesis, it would be interesting to evaluate changes in layer confluency and GV formation while measuring the time-dependent change of hydraulic resistivity. To this end, time-lapse images of the SCE cell layer should be acquired immediately after the initiation of the perfusion (unlike in our studies where the cell layer was only examined after acclimatisatoin), and until resistivity has stabilised.

A

Permissions to reprint

ELSEVIER LICENSE
TERMS AND CONDITIONS

Apr 09, 2019

This Agreement between Imperial College London -- Alice Spenlehauer ("You") and Elsevier ("Elsevier") consists of your license details and the terms and conditions provided by Elsevier and Copyright Clearance Center.

License Number	4564700020532
License date	Apr 09, 2019
Licensed Content Publisher	Elsevier
Licensed Content Publication	Experimental Eye Research
Licensed Content Title	Mechanism of the aqueous outflow across the trabecular wall of Schlemm's canal
Licensed Content Author	Ramesh C. Tripathi
Licensed Content Date	Jan 1, 1971
Licensed Content Volume	11
Licensed Content Issue	1
Licensed Content Pages	1
Start Page	116
End Page	IN39
Type of Use	reuse in a thesis/dissertation
Portion	figures/tables/illustrations
Number of figures/tables/illustrations	5
Format	both print and electronic
Are you the author of this Elsevier article?	No
Will you be translating?	No
Original figure numbers	Plate 1, 2, 6, 17 and Figure 1
Title of your thesis/dissertation	The mechanobiology of the inner wall endothelium of Schlemm's canal
Expected completion date	Jun 2019
Estimated size (number of pages)	150
Requestor Location	Imperial College London Department of Bioengineering Royal School of Mines Prince Consort Road London, SW7 2BP United Kingdom Attn: Imperial College London
Publisher Tax ID	GB 494 6272 12
Total	0.00 GBP
Terms and Conditions	

INTRODUCTION

1. The publisher for this copyrighted material is Elsevier. By clicking "accept" in connection with completing this licensing transaction, you agree that the following terms and conditions apply to this transaction (along with the Billing and Payment terms and conditions

ELSEVIER LICENSE
TERMS AND CONDITIONS

Jan 04, 2020

This Agreement between Imperial College London -- Alice Spenlehauer ("You") and Elsevier ("Elsevier") consists of your license details and the terms and conditions provided by Elsevier and Copyright Clearance Center.

License Number	4563820814737
License date	Apr 07, 2019
Licensed Content Publisher	Elsevier
Licensed Content Publication	American Journal of Ophthalmology
Licensed Content Title	Aqueous Humor Pathways Through The Trabecular Meshwork and Into Schlemm'S Canal in the Cynomolgus Monkey (Macaca Irus) An Electron Microscopic Study
Licensed Content Author	Hajime Inomata,Anders Bill,George K. Smelser
Licensed Content Date	May 1, 1972
Licensed Content Volume	73
Licensed Content Issue	5
Licensed Content Pages	30
Start Page	760
End Page	789
Type of Use	reuse in a thesis/dissertation

Portion	figures/tables/illustrations
Number of figures/tables/illustrations	5
Format	both print and electronic
Are you the author of this Elsevier article?	No
Will you be translating?	No
Original figure numbers	Figs.1, 2, 16, 21, 27
Requestor Location	Imperial College London Department of Bioengineering Royal School of Mines Prince Consort Road London, SW7 2BP United Kingdom Attn: Imperial College London
Publisher Tax ID	GB 494 6272 12
Total	0.00 GBP

Terms and Conditions

INTRODUCTION

1. The publisher for this copyrighted material is Elsevier. By clicking "accept" in connection with completing this licensing transaction, you agree that the following terms and conditions apply to this transaction (along with the Billing and Payment terms and conditions established by Copyright Clearance Center, Inc. ("CCC"), at the time that you opened your Rightslink account and that are available at any time at http://myaccount.copyright.com).

GENERAL TERMS

2. Elsevier hereby grants you permission to reproduce the aforementioned material subject to the terms and conditions indicated.

3. Acknowledgement: If any part of the material to be used (for example, figures) has appeared in our publication with credit or acknowledgement to another source, permission must also be sought from that source. If such permission is not obtained then that material may not be included in your publication/copies. Suitable acknowledgement to the source must be made, either as a footnote or in a reference list at the end of your publication, as follows:

ELSEVIER LICENSE
TERMS AND CONDITIONS

Aug 04, 2019

This Agreement between Imperial College London -- Alice Spenlehauer ("You") and Elsevier ("Elsevier") consists of your license details and the terms and conditions provided by Elsevier and Copyright Clearance Center.

License Number	4641551159855
License date	Aug 03, 2019
Licensed Content Publisher	Elsevier
Licensed Content Publication	American Journal of Ophthalmology
Licensed Content Title	Pressure-Dependent Changes in Structures of the Aqueous Outflow System of Human and Monkey Eyes
Licensed Content Author	Murray A. Johnstone,W. Morton Grant
Licensed Content Date	Mar 1, 1973
Licensed Content Volume	75
Licensed Content Issue	3
Licensed Content Pages	19
Start Page	365
End Page	383
Type of Use	reuse in a thesis/dissertation
Portion	figures/tables/illustrations
Number of figures/tables/illustrations	1
Format	both print and electronic
Are you the author of this Elsevier article?	No
Will you be translating?	No
Order reference number	Johnstone1973Illustration
Original figure numbers	Figure 19
Title of your thesis/dissertation	The mechanobiology of the inner wall endothelium of Schlemm's canal
Expected completion date	Jun 2019
Estimated size (number of pages)	150
Requestor Location	Imperial College London Department of Bioengineering Royal School of Mines Prince Consort Road London, SW7 2BP United Kingdom Attn: Imperial College London
Publisher Tax ID	GB 494 6272 12
Total	0.00 USD
Terms and Conditions	

INTRODUCTION

ELSEVIER LICENSE
TERMS AND CONDITIONS

Aug 04, 2019

This Agreement between Imperial College London -- Alice Spenlehauer ("You") and Elsevier ("Elsevier") consists of your license details and the terms and conditions provided by Elsevier and Copyright Clearance Center.

License Number	4641811287737
License date	Aug 04, 2019
Licensed Content Publisher	Elsevier
Licensed Content Publication	Experimental Eye Research
Licensed Content Title	The functional morphology of the outflow systems of ocular and cerebrospinal fluids
Licensed Content Author	Ramesh C. Tripathi
Licensed Content Date	Jan 1, 1977
Licensed Content Volume	25
Licensed Content Issue	n/a
Licensed Content Pages	52
Start Page	65
End Page	116
Type of Use	reuse in a thesis/dissertation
Intended publisher of new work	other
Portion	figures/tables/illustrations
Number of figures/tables/illustrations	2
Format	both print and electronic
Are you the author of this Elsevier article?	No
Will you be translating?	No
Order reference number	Tripathi1977
Original figure numbers	Figures 13 and 17
Title of your thesis/dissertation	The mechanobiology of the inner wall endothelium of Schlemm's canal
Publisher of new work	Imperial College London
Expected completion date	Aug 2019
Estimated size (number of pages)	150
Requestor Location	Imperial College London Department of Bioengineering Royal School of Mines Prince Consort Road London, SW7 2BP United Kingdom Attn: Imperial College London
Publisher Tax ID	GB 494 6272 12
Total	0.00 USD

Association for Research in Vision and Ophthalmology LICENSE
TERMS AND CONDITIONS

Jan 03, 2020

This is a License Agreement between Imperial College London -- Alice Spenlehauer ("You") and Association for Research in Vision and Ophthalmology ("Association for Research in Vision and Ophthalmology") provided by Copyright Clearance Center ("CCC"). The license consists of your order details, the terms and conditions provided by Association for Research in Vision and Ophthalmology, and the payment terms and conditions.

All payments must be made in full to CCC. For payment instructions, please see information listed at the bottom of this form.

License Number	4642970790950
License date	Aug 03, 2019
Licensed content publisher	Association for Research in Vision and Ophthalmology
Licensed content title	Investigative ophthalmology
Licensed content date	Jan 1, 1977
Type of Use	Thesis/Dissertation
Requestor type	Academic institution
Format	Print, Electronic
Portion	chart/graph/table/figure
Number of charts/graphs/tables/figures	1
The requesting person/organization is:	Alice Spenlehauer, Imperial College London
Title or numeric reference	Figure 2

of the portion(s)	
Title of the article or chapter the portion is from	The Relationship Between Pore Density and Outflow Facility in Normal and Glaucomatous Human Eyes
Editor of portion(s)	N/A
Author of portion(s)	Allingham, R R DeKater, A W Ethier, C R Anderson, P J Hertzmark, E Epstein, D L
Volume of serial or monograph.	33
Issue, if republishing an article from a serial	5
Page range of the portion	1661-9
Publication date of portion	1992
Rights for	Main product
Duration of use	Life of current and all future editions
Creation of copies for the disabled	yes
With minor editing privileges	no
For distribution to	Worldwide
In the following language(s)	Original language of publication
With incidental promotional use	no
The lifetime unit quantity of new product	Up to 499
Title	The mechanobiology of the inner wall endothelium of Schlemm's canal

Institution name	Imperial College London
Expected presentation date	Aug 2019
Billing Type	Invoice
Billing Address	Imperial College London Department of Bioengineering Royal School of Mines Prince Consort Road London, United Kingdom SW7 2BP Attn: Imperial College London
Total (may include CCC user fee)	0.00 USD

Terms and Conditions

TERMS AND CONDITIONS

The following terms are individual to this publisher:

None

Other Terms and Conditions:

A reprint of this material must include a full article citation and acknowledge ARVO as the copyright holder.

STANDARD TERMS AND CONDITIONS

1. Description of Service; Defined Terms. This Republication License enables the User to obtain licenses for republication of one or more copyrighted works as described in detail on the relevant Order Confirmation (the "Work(s)"). Copyright Clearance Center, Inc. ("CCC") grants licenses through the Service on behalf of the rightsholder identified on the Order Confirmation (the "Rightsholder"). "Republication", as used herein, generally means the inclusion of a Work, in whole or in part, in a new work or works, also as described on the Order Confirmation. "User", as used herein, means the person or entity making such republication.

2. The terms set forth in the relevant Order Confirmation, and any terms set by the Rightsholder with respect to a particular Work, govern the terms of use of Works in connection with the Service. By using the Service, the person transacting for a republication license on behalf of the User represents and warrants that he/she/it (a) has been duly authorized by the User to accept, and hereby does accept, all such terms and conditions on behalf of User, and (b) shall inform User of all such terms and conditions. In the event such person is a "freelancer" or other third party independent of User and CCC, such party shall be deemed jointly a "User" for purposes of these terms and conditions. In any event, User shall be deemed to have accepted and agreed to all such terms and conditions if User republishes the Work in any fashion.

Association for Research in Vision and Ophthalmology LICENSE
TERMS AND CONDITIONS

Jan 03, 2020

This is a License Agreement between Imperial College London -- Alice Spenlehauer ("You") and Association for Research in Vision and Ophthalmology ("Association for Research in Vision and Ophthalmology") provided by Copyright Clearance Center ("CCC"). The license consists of your order details, the terms and conditions provided by Association for Research in Vision and Ophthalmology, and the payment terms and conditions.

All payments must be made in full to CCC. For payment instructions, please see information listed at the bottom of this form.

License Number	4642970949663
License date	Aug 03, 2019
Licensed content publisher	Association for Research in Vision and Ophthalmology
Licensed content title	Investigative ophthalmology
Licensed content date	Jan 1, 1977
Type of Use	Thesis/Dissertation
Requestor type	Academic institution
Format	Print, Electronic
Portion	chart/graph/table/figure
Number of charts/graphs/tables/figures	1
The requesting person/organization is:	Alice Spenlehauer, Imperial College London
Title or numeric reference of the	Figure 1

portion(s)

Title of the article or chapter the portion is from	Two pore types in the inner-wall endothelium of Schlemm's canal
Editor of portion(s)	N/A
Author of portion(s)	Ethier, C. Ross Coloma, Fides M. Sit, Arthur J. Johnson, Mark
Volume of serial or monograph.	39
Issue, if republishing an article from a serial	11
Page range of the portion	2041-2048
Publication date of portion	1998
Rights for	Main product
Duration of use	Life of current and all future editions
Creation of copies for the disabled	yes
With minor editing privileges	no
For distribution to	Worldwide
In the following language(s)	Original language of publication
With incidental promotional use	no
The lifetime unit quantity of new product	Up to 499
Title	The mechanobiology of the inner wall endothelium of Schlemm's canal
Institution name	Imperial College London

Expected presentation date	Aug 2019
Billing Type	Invoice
Billing Address	Imperial College London Department of Bioengineering Royal School of Mines Prince Consort Road London, United Kingdom SW7 2BP Attn: Imperial College London
Total (may include CCC user fee)	0.00 USD

Terms and Conditions

TERMS AND CONDITIONS

The following terms are individual to this publisher:

None

Other Terms and Conditions:

A reprint of this material must include a full article citation and acknowledge ARVO as the copyright holder.

STANDARD TERMS AND CONDITIONS

1. Description of Service; Defined Terms. This Republication License enables the User to obtain licenses for republication of one or more copyrighted works as described in detail on the relevant Order Confirmation (the "Work(s)"). Copyright Clearance Center, Inc. ("CCC") grants licenses through the Service on behalf of the rightsholder identified on the Order Confirmation (the "Rightsholder"). "Republication", as used herein, generally means the inclusion of a Work, in whole or in part, in a new work or works, also as described on the Order Confirmation. "User", as used herein, means the person or entity making such republication.

2. The terms set forth in the relevant Order Confirmation, and any terms set by the Rightsholder with respect to a particular Work, govern the terms of use of Works in connection with the Service. By using the Service, the person transacting for a republication license on behalf of the User represents and warrants that he/she/it (a) has been duly authorized by the User to accept, and hereby does accept, all such terms and conditions on behalf of User, and (b) shall inform User of all such terms and conditions. In the event such person is a "freelancer" or other third party independent of User and CCC, such party shall be deemed jointly a "User" for purposes of these terms and conditions. In any event, User shall be deemed to have accepted and agreed to all such terms and conditions if User republishes the Work in any fashion.

3. Scope of License; Limitations and Obligations.

3.1 All Works and all rights therein, including copyright rights, remain the sole and exclusive property of the Rightsholder. The license created by the exchange of an Order Confirmation (and/or any invoice) and payment by User of the full amount set forth on that document includes only those rights expressly set forth in the Order Confirmation and in

Association for Research in Vision and Ophthalmology LICENSE
TERMS AND CONDITIONS

Jan 03, 2020

This is a License Agreement between Imperial College London -- Alice Spenlehauer ("You") and Association for Research in Vision and Ophthalmology ("Association for Research in Vision and Ophthalmology") provided by Copyright Clearance Center ("CCC"). The license consists of your order details, the terms and conditions provided by Association for Research in Vision and Ophthalmology, and the payment terms and conditions.

All payments must be made in full to CCC. For payment instructions, please see information listed at the bottom of this form.

License Number	4642970639661
License date	Aug 03, 2019
Licensed content publisher	Association for Research in Vision and Ophthalmology
Licensed content title	Investigative ophthalmology
Licensed content date	Jan 1, 1977
Type of Use	Thesis/Dissertation
Requestor type	Academic institution
Format	Print, Electronic
Portion	chart/graph/table/figure
Number of charts/graphs/tables/figures	1
The requesting person/organization is:	Alice Spenlehauer, Imperial College London
Title or numeric reference of the	Figure 1

portion(s)	
Title of the article or chapter the portion is from	The Mechanism of Increasing Outflow Facility during Washout in the Bovine Eye
Editor of portion(s)	N/A
Author of portion(s)	Darryl Overby; Haiyan Gong; Guanting Qiu; Thomas F. Freddo; Mark Johnson
Volume of serial or monograph.	43
Issue, if republishing an article from a serial	N/A
Page range of the portion	3455-3464
Publication date of portion	November 2002
Rights for	Main product
Duration of use	Life of current and all future editions
Creation of copies for the disabled	yes
With minor editing privileges	no
For distribution to	Worldwide
In the following language(s)	Original language of publication
With incidental promotional use	no
The lifetime unit quantity of new product	Up to 499
Title	The mechanobiology of the inner wall endothelium of Schlemm's canal
Institution name	Imperial College London

Expected presentation date	Aug 2019
Billing Type	Invoice
Billing Address	Imperial College London Department of Bioengineering Royal School of Mines Prince Consort Road London, United Kingdom SW7 2BP Attn: Imperial College London
Total (may include CCC user fee)	0.00 USD

Terms and Conditions

TERMS AND CONDITIONS

The following terms are individual to this publisher:

None

Other Terms and Conditions:

A reprint of this material must include a full article citation and acknowledge ARVO as the copyright holder.

STANDARD TERMS AND CONDITIONS

1. Description of Service; Defined Terms. This Republication License enables the User to obtain licenses for republication of one or more copyrighted works as described in detail on the relevant Order Confirmation (the "Work(s)"). Copyright Clearance Center, Inc. ("CCC") grants licenses through the Service on behalf of the rightsholder identified on the Order Confirmation (the "Rightsholder"). "Republication", as used herein, generally means the inclusion of a Work, in whole or in part, in a new work or works, also as described on the Order Confirmation. "User", as used herein, means the person or entity making such republication.

2. The terms set forth in the relevant Order Confirmation, and any terms set by the Rightsholder with respect to a particular Work, govern the terms of use of Works in connection with the Service. By using the Service, the person transacting for a republication license on behalf of the User represents and warrants that he/she/it (a) has been duly authorized by the User to accept, and hereby does accept, all such terms and conditions on behalf of User, and (b) shall inform User of all such terms and conditions. In the event such person is a "freelancer" or other third party independent of User and CCC, such party shall be deemed jointly a "User" for purposes of these terms and conditions. In any event, User shall be deemed to have accepted and agreed to all such terms and conditions if User republishes the Work in any fashion.

3. Scope of License; Limitations and Obligations.

3.1 All Works and all rights therein, including copyright rights, remain the sole and exclusive property of the Rightsholder. The license created by the exchange of an Order

ELSEVIER LICENSE
TERMS AND CONDITIONS

Aug 04, 2019

This Agreement between Imperial College London -- Alice Spenlehauer ("You") and Elsevier ("Elsevier") consists of your license details and the terms and conditions provided by Elsevier and Copyright Clearance Center.

License Number	4641560338351
License date	Aug 03, 2019
Licensed Content Publisher	Elsevier
Licensed Content Publication	Experimental Eye Research
Licensed Content Title	The changing paradigm of outflow resistance generation: Towards synergistic models of the JCT and inner wall endothelium
Licensed Content Author	Darryl R. Overby,W. Daniel Stamer,Mark Johnson
Licensed Content Date	Apr 30, 2009
Licensed Content Volume	88
Licensed Content Issue	4
Licensed Content Pages	15
Start Page	656
End Page	670
Type of Use	reuse in a thesis/dissertation
Intended publisher of new work	other
Portion	figures/tables/illustrations
Number of figures/tables/illustrations	1
Format	both print and electronic
Are you the author of this Elsevier article?	No
Will you be translating?	No
Order reference number	Overby2009PoresImages
Original figure numbers	Figure 3
Title of your thesis/dissertation	The mechanobiology of the inner wall endothelium of Schlemm's canal
Publisher of new work	Imperial College London
Expected completion date	Aug 2019
Estimated size (number of pages)	150
Requestor Location	Imperial College London Department of Bioengineering Royal School of Mines Prince Consort Road London, SW7 2BP United Kingdom Attn: Imperial College London
Publisher Tax ID	GB 494 6272 12
Total	0.00 USD

ELSEVIER LICENSE
TERMS AND CONDITIONS

Aug 04, 2019

This Agreement between Imperial College London -- Alice Spenlehauer ("You") and Elsevier ("Elsevier") consists of your license details and the terms and conditions provided by Elsevier and Copyright Clearance Center.

License Number	4594830383272
License date	May 23, 2019
Licensed Content Publisher	Elsevier
Licensed Content Publication	Experimental Eye Research
Licensed Content Title	The trabecular meshwork outflow pathways: Structural and functional aspects
Licensed Content Author	Ernst R. Tamm
Licensed Content Date	Apr 30, 2009
Licensed Content Volume	88
Licensed Content Issue	4
Licensed Content Pages	8
Start Page	648
End Page	655
Type of Use	reuse in a thesis/dissertation
Portion	figures/tables/illustrations
Number of figures/tables/illustrations	4
Format	both print and electronic
Are you the author of this Elsevier article?	No
Will you be translating?	No
Original figure numbers	Fig. 1, Fig 2., Fig. 3 and Fig. 4
Title of your thesis/dissertation	The mechanobiology of the inner wall endothelium of Schlemm's canal
Expected completion date	Jun 2019
Estimated size (number of pages)	150
Requestor Location	Imperial College London Department of Bioengineering Royal School of Mines Prince Consort Road London, SW7 2BP United Kingdom Attn: Imperial College London
Publisher Tax ID	GB 494 6272 12
Total	0.00 USD
Terms and Conditions	

INTRODUCTION

1. The publisher for this copyrighted material is Elsevier. By clicking "accept" in connection with completing this licensing transaction, you agree that the following terms and conditions apply to this transaction (along with the Billing and Payment terms and conditions

ELSEVIER LICENSE
TERMS AND CONDITIONS

Aug 04, 2019

This Agreement between Imperial College London -- Alice Spenlehauer ("You") and Elsevier ("Elsevier") consists of your license details and the terms and conditions provided by Elsevier and Copyright Clearance Center.

License Number	4564700320439
License date	Apr 09, 2019
Licensed Content Publisher	Elsevier
Licensed Content Publication	Experimental Eye Research
Licensed Content Title	A model of giant vacuole dynamics in human Schlemm's canal endothelial cells
Licensed Content Author	Ryan M. Pedrigi,David Simon,Ashley Reed,W. Daniel Stamer,Darryl R. Overby
Licensed Content Date	Jan 1, 2011
Licensed Content Volume	92
Licensed Content Issue	1
Licensed Content Pages	10
Start Page	57
End Page	66
Type of Use	reuse in a thesis/dissertation
Intended publisher of new work	other
Portion	figures/tables/illustrations
Number of figures/tables/illustrations	3
Format	both print and electronic
Are you the author of this Elsevier article?	No
Will you be translating?	No
Original figure numbers	Fig. 1, 4 and 5
Title of your thesis/dissertation	The mechanobiology of the inner wall endothelium of Schlemm's canal
Expected completion date	Jun 2019
Estimated size (number of pages)	150
Requestor Location	Imperial College London Department of Bioengineering Royal School of Mines Prince Consort Road London, SW7 2BP United Kingdom Attn: Imperial College London
Publisher Tax ID	GB 494 6272 12
Total	0.00 GBP
Terms and Conditions	

INTRODUCTION

Bibliography

1. Hoagland E. Feeling my way into blindness. 2016.
2. Scott AW, Bressler NM, Ffolkes S, Wittenborn JS and Jorkasky J. Public Attitudes About Eye and Vision Health. JAMA Ophthalmology 2016;134:1111.
3. Flaxman SR, Bourne RRA, Resnikoff S et al. Global causes of blindness and distance vision impairment 1990-2020: a systematic review and meta-analysis. The Lancet. Global health 2017;5:e1221–e1234.
4. Tham YC, Li X, Wong TY, Quigley HA, Aung T and Cheng CY. Global prevalence of glaucoma and projections of glaucoma burden through 2040: a systematic review and meta-analysis. Ophthalmology 2014;121:2081–90.
5. Kass MA. The Ocular Hypertension Treatment Study. Archives of Ophthalmology 2002;120:701–13.
6. Leske MC, Heijl A, Hussein M, Bengtsson B, Hyman L and Komaroff E. Factors for glaucoma progression and the effect of treatment: the early manifest glaucoma trial. Archives of Ophthalmology 2003;121:48–56.
7. Collaborative Normal-Tension Glaucoma Study Group. The effectiveness of intraocular pressure reduction in the treatment of normal-tension glaucoma. American Journal of Ophthalmology 1998;126:498–505.
8. McEwen WK. Application of Poiseuille's law to aqueous outflow. A.M.A. archives of ophthalmology 1958;60:290–4.
9. Grant WM. Clinical measurements of aqueous outflow. A.M.A. archives of ophthalmology 1951;46:113–31.
10. Mäepea O and Bill A. Pressures in the juxtacanalicular tissue and Schlemm's canal in monkeys. Experimental eye research 1992;54:879–83.
11. Grant WM. Experimental aqueous perfusion in enucleated human eyes. Archives of Ophthalmology 1963;69:783–801.
12. Johnson M. What controls aqueous humour outflow resistance? Experimental Eye Research 2006;82:545–57.

13. Overby DR, Stamer WD and Johnson M. The changing paradigm of outflow resistance generation: Towards synergistic models of the JCT and inner wall endothelium. Experimental Eye Research 2009;88:656–70.

14. Allingham RR, Kater AW de, Ethier CR, Anderson PJ, Hertzmark E and Epstein DL. The relationship between pore density and outflow facility in human eyes. Investigative ophthalmology & visual science 1992;33:1661–9.

15. Johnson M, Chan D, Read AT, Christensen C, Sit A and Ethier CR. The pore density in the inner wall endothelium of Schlemm's canal of glaucomatous eyes. Investigative Ophthalmology and Visual Science 2002;43:2950–5.

16. Braakman ST. Biomechanical regulation of permeability in Schlemm's canal endothelium with respect to glaucoma. Doctoral dissertation. Imperial College London, 2014.

17. Overby DR, Zhou EH, Vargas-Pinto R et al. Altered mechanobiology of Schlemm's canal endothelial cells in glaucoma. Proceedings of the National Academy of Sciences of the United States of America 2014;111:13876–81.

18. Nilsson SFE. The uveoscleral outflow routes. Eye 1997;11:149–54.

19. Johnson M and Erickson K. Mechanisms and routes of aqueous humour drainage. Ed. by Saunders WB. 3rd ed. 2000:2577–95.

20. Bill A and Svedbergh B. Scanning electron microscopic studies of the trabecular meshwork and the canal of Schlemm□an attempt to localize the main resistance to outflow of aqueous humor in man. Acta ophthalmologica 1972;50:295–320.

21. Tamm ER. The trabecular meshwork outflow pathways: structural and functional aspects. Experimental Eye Research 2009;88:648–55.

22. Johnson DH. The effect of cytochalasin D on outflow facility and the trabecular meshwork of the human eye in perfusion organ culture. Investigative ophthalmology & visual science 1997;38:2790–9.

23. Bhatt K, Gong H and Freddo TF. Freeze-fracture studies of interendothelial junctions in the angle of the human eye. Investigative Ophthalmology & Visual Science 1995;36:1379–89.

24. Lutjen-Drecoll E and Rohen JW. [Endothelial studies of the Schlemm's canal using silver-impregnation technic]. Albrecht von Graefes Archiv fur klinische und experimentelle Ophthalmologie. 1970;180:249–66.

25. Ramos RF, Hoying JB, Witte MH and Daniel Stamer W. Schlemm;s Canal Endothelia, Lymphatic, or Blood Vasculature? Journal of Glaucoma 2007;16:391–405.

26. Heimark RL, Kaochar S and Stamer WD. Human Schlemm's canal cells express the endothelial adherens proteins, VE-cadherin and PECAM-1. Current eye research 2002;25:299–308.

27. Krohn J. Expression of factor VIII-related antigen in human aqueous drainage channels. Acta ophthalmologica Scandinavica 1999;77:9–12.

28. Garron LK, Feeney ML, Hogan MJ and McEwen WK. Electron microscopic studies of the human eye. I. Preliminary investigations of the trabeculas. American Journal of Ophthalmology 1958;46:27–35.

29. Tripathi RC. Ultrastructure of Schlemm's canal in relation to aqueous outflow. Experimental Eye Research 1968;7:335–41.

30. Inomata H, Bill A and Smelser GK. Aqueous humor pathways through the trabecular meshwork and into Schlemm's canal in the cynomolgus monkey (Macaca irus). An electron microscopic study. American Journal of Ophthalmology 1972;73:760–89.

31. Holmberg A. The Fine Structure of the Inner Wall of Schlemm's Canal. A.M.A. Archives of Ophthalmology 1959;62:956–8.

32. Braakman ST, Pedrigi RM, Read AT et al. Biomechanical strain as a trigger for pore formation in Schlemm's canal endothelial cells. Experimental Eye Research 2014;127:224–35.

33. Pedrigi RM, Simon D, Reed A, Stamer WD and Overby DR. A model of giant vacuole dynamics in human Schlemm's canal endothelial cells. Experimental Eye Research 2011;92:57–66.

34. Johnstone MA and Grant WM. Pressure-dependent changes in structures of the aqueous outflow system of human and monkey eyes. American Journal of Ophthalmology 1973;75:365–83.

35. Grierson I and Lee WR. The fine structure of the trabecular meshwork at graded levels of intraocular pressure. (1) Pressure effects within the near-physiological range (8-30 mmHg). Experimental eye research 1975;20:505–21.

36. Park DY, Lee J, Park I et al. Lymphatic regulator PROX1 determines Schlemm's canal integrity and identity. The Journal of clinical investigation 2014;124:3960–74.

37. Grierson I and Lee WR. Pressure effects on the distribution of extracellular materials in the rhesus monkey outflow apparatus. Albrecht von Graefes Archiv für Klinische und Experimentelle Ophthalmologie 1977;203:155–68.

38. Lai J, Su Y, Swain DL, Huang D, Getchevski D and Gong H. The Role of Schlemm's Canal Endothelium Cellular Connectivity in Giant Vacuole Formation: A 3D Electron Microscopy Study. Investigative ophthalmology & visual science 2019;60:1630–43.

39. Tripathi RC. The functional morphology of the outflow systems of ocular and cerebrospinal fluids. Experimental Eye Research 1977;25:65–116.

40. Grierson I and Lee WR. Pressure-induced changes in the ultrastructure of the endothelium lining Schlemm's canal. American journal of ophthalmology 1975;80:863–84.

41. Overby DR. The Mechanobiology of Aqueous Humor Transport across Schlemm's Canal Endothelium. In: *Mechanobiology Handbook*. Ed. by Nagatomi J. CRC Press Boca Raton, FL, 2011. Chap. 17:367–90.

42. Ethier CR, Coloma FM, Sit AJ and Johnson M. Two pore types in the inner-wall endothelium of Schlemm's canal. Investigative Ophthalmology and Visual Science 1998;39:2041–8.

43. Ethier CR, Read AT and Chan DW. Effects of Latrunculin-B on Outflow Facility and Trabecular Meshwork Structure in Human Eyes. Investigative Opthalmology & Visual Science 2006;47:1991.

44. Braakman ST, Read AT, Chan DWH, Ethier CR and Overby DR. Colocalization of outflow segmentation and pores along the inner wall of Schlemm's canal. Experimental Eye Research 2015;130:87–96.

45. Ethier CR, Read AT and Chan DWH. Effects of latrunculin-B on outflow facility and trabecular meshwork structure in human eyes. Investigative Ophthalmology & Visual Science 2006;47:1991–8.

46. Sit AJ, Coloma FM, Ethier CR and Johnson M. Factors affecting the pores of the inner wall endothelium of Schlemm's canal. Investigative ophthalmology & visual science 1997;38:1517–25.

47. Johnson M, Johnson DH, Kamm RD, DeKater AW and Epstein DL. The filtration characteristics of the aqueous outflow system. Experimental Eye Research 1990;50:407–18.

48. Raviola G and Raviola E. Paracellular route of aqueous outflow in the trabecular meshwork and canal of Schlemm. A freeze-fracture study of the endothelial junctions in the sclerocorneal angel of the macaque monkey eye. Investigative ophthalmology & visual science 1981;21:52–72.

49. Ye W, Gong H, Sit A, Johnson M and Freddo TF. Interendothelial junctions in normal human schlemm's canal respond to changes in pressure. Investigative Ophthalmology and Visual Science 1997;38:2460–8.

50. Holmberg Å. Schlemm's canal and the trabecular meshwork. An electron microscopic study of the normal structure in man and monkey (Cercopithecus ethiops). Documenta Ophthalmologica 1965;19:339–73.

51. Kayes J. Pore Structure of the Inner Wall of Schlemm's Canal. Investigative Ophthalmology & Visual Science 1967;6:381–94.

52. Grierson I, Lee WR, Abraham S and Howes RC. Associations between the cells of the walls of Schlemm's canal. Albrecht von Graefes Archiv fur Klinische und Experimentelle Ophthalmologie. 1978;208:33–47.

53. Tripathi RC. Mechanism of the aqueous outflow across the trabecular wall of Schlemm's canal. Experimental Eye Research 1971;11:116–21.

54. Grierson I and Lee WR. Pressure effects on flow channels in the lining endothelium of Schlemm's canal: A quantitative study by transmission electron microscopy. Acta Ophthalmologica 1978;56:935–52.

55. Grierson I, Lee WR, Moseley H and Abraham S. The trabecular wall of Schlemm's canal: a study of the effects of pilocarpine by scanning electron microscopy. The British journal of ophthalmology 1979;63:9–16.

56. Eriksson A and Svedbergh B. Transcellular aqueous humor outflow: a theoretical and experimental study. Albrecht von Graefes Archiv fur klinische und experimentelle Ophthalmologie. Albrecht von Graefe's archive for clinical and experimental ophthalmology 1980;212:187–97.

57. Moseley H, Grierson I and Lee WR. Mathematical modelling of aqueous humour outflow from the eye through the pores in the lining endothelium of Schlemm's canal. Clinical physics and physiological measurement : an official journal of the Hospital Physicists' Association, Deutsche Gesellschaft fur Medizinische Physik and the European Federation of Organisations for Medical Physics 1983;4:47–63.

58. Hamanaka T and Bill A. Morphological and functional effects of Na2EDTA on the outflow routes for aqueous humor in monkeys. Experimental eye research 1987;44:171–90.

59. Hamanaka T and Bill A. Effects of alpha-chymotrypsin on the outflow routes for aqueous humor. Experimental eye research 1988;46:323–41.

60. Peterson JA, Tian B, Bershadsky AD et al. Latrunculin-A increases outflow facility in the monkey. Investigative Ophthalmology and Visual Science 1999;40:931–41.

61. Johnson M, Shapiro A, Ethier CR and Kamm RD. Modulation of outflow resistance by the pores of the inner wall endothelium. Investigative Ophthalmology and Visual Science 1992;33:1670–5.

62. Overby D, Gong H, Qiu G, Freddo TF and Johnson M. The mechanism of increasing outflow facility during washout in the bovine eye. Investigative ophthalmology & visual science 2002;43:3455–64.

63. Sabanay I, Gabelt BT, Tian B, Kaufman PL and Geiger B. H-7 effects on the structure and fluid conductance of monkey trabecular meshwork. Archives of ophthalmology (Chicago, Ill. : 1960) 2000;118:955–62.

64. Ethier RC, Read TA and Chan D. Biomechanics of Schlemm's canal endothelial cells: influence on F-actin architecture. Biophysical Journal 2004;87:2828–37.

65. Balaban NQ, Schwarz US, Riveline D et al. Force and focal adhesion assembly: a close relationship studied using elastic micropatterned substrates. Nature cell biology 2001;3:466–72.

66. Tan JL, Tien J, Pirone DM, Gray DS, Bhadriraju K and Chen CS. Cells lying on a bed of microneedles: an approach to isolate mechanical force. Proceedings of the National Academy of Sciences of the United States of America 2003;100:1484–9.

67. Grierson I and Lee WR. Changes in the monkey outflow apparatus at graded levels of intraocular pressure: a qualitative analysis by light microscopy and scanning electron microscopy. Experimental eye research 1974;19:21–33.

68. Kayes J. Pressure gradient changes on the trabecular meshwork of monkeys. American journal of ophthalmology 1975;79:549–56.

69. Ethier RC. The inner wall of Schlemm's canal. Experimental Eye Research 2002;74:161–72.

70. Tschumperlin DJ, Oswari J and Margulies AS. Deformation-induced injury of alveolar epithelial cells. Effect of frequency, duration, and amplitude. American journal of respiratory and critical care medicine 2000;162:357–62.

71. Gipson IK and Anderson RA. Actin filaments in cells of human trabecular meshwork and Schlemm's canal. Investigative ophthalmology & visual science 1979;18:547–61.

72. Tian B, Geiger B, Epstein DL and Kaufman PL. Cytoskeletal involvement in the regulation of aqueous humor outflow. Investigative ophthalmology & visual science 2000;41:619–23.

73. Read TA, Chan WHD and Ethier RC. Actin structure in the outflow tract of normal and glaucomatous eyes. Experimental Eye Research 2007;84:214–26.

74. Hamanaka T, Thornell LE and Bill A. Cytoskeleton and tissue origin in the anterior cynomolgus monkey eye. Japanese journal of ophthalmology 1997;41:138–49.

75. Bahler CK, Hann CR, Fautsch MP and Johnson DH. Pharmacologic disruption of Schlemm's canal cells and outflow facility in anterior segments of human eyes. Investigative Ophthalmology and Visual Science 2004;45:2246–54.

76. Zhou EH, Krishnan R, Stamer WD et al. Mechanical responsiveness of the endothelial cell of Schlemm's canal: Scope, variability and its potential role in controlling aqueous humour outflow. Journal of the Royal Society Interface 2012;9:1144–55.

77. Lee WR and Grierson I. Pressure effects on the endothelium of the trabecular wall of Schlemm's canal: A study by scanning electron microscopy. Albrecht von Graefes Archiv für Klinische und Experimentelle Ophthalmologie 1975;196:255–65.

78. Brilakis HS and Johnson DH. Giant vacuole survival time and implications for aqueous humor outflow. Journal of Glaucoma 2001;10:277–83.

79. Stamer WD, Roberts BC, Howell DN and Epstein DL. Isolation, culture, and characterization of endothelial cells from Schlemm's canal. Investigative Ophthalmology & Visual Science 1998;39:1804–12.

80. Perkumas KM and Stamer WD. Protein markers and differentiation in culture for Schlemm's canal endothelial cells. Experimental Eye Research 2012;96:82–7.

81. Tanna AP and Johnson M. Rho Kinase Inhibitors as a Novel Treatment for Glaucoma and Ocular Hypertension. Ophthalmology 2018;125:1741–56.

82. Uehata M, Ishizaki T, Satoh H et al. Calcium sensitization of smooth muscle mediated by a Rho-associated protein kinase in hypertension. Nature 1997;389:990–4.

83. Ishizaki T, Uehata M, Tamechika I et al. Pharmacological properties of Y-27632, a specific inhibitor of rho-associated kinases. Molecular pharmacology 2000;57:976–83.

84. Narumiya S, Ishizaki T and Ufhata M. Use and properties of ROCK-specific inhibitor Y-27632. In: *Methods in Enzymology*. Ed. by Balch WE, Der CJ and Hall A. Vol. 325. Academic Press, 2000:273–84. DOI: https://doi.org/10.1016/S0076-6879(00)25449-9. URL: http://www.sciencedirect.com/science/article/pii/S0076687900254499.

85. Kaibuchi K, Kuroda S and Amano M. Regulation of the cytoskeleton and cell adhesion by the Rho family GTPases in mammalian cells. Annual review of biochemistry 1999;68:459–86.

86. Rao PV, Deng PF, Kumar J and Epstein DL. Modulation of aqueous humor outflow facility by the Rho kinase-specific inhibitor Y-27632. Investigative Ophthalmology & Visual Science 2001;42:1029–37.

87. Lu Z, Overby DR, Scott PA, Freddo TF and Gong H. The mechanism of increasing outflow facility by rho-kinase inhibition with Y-27632 in bovine eyes. Experimental Eye Research 2008;86:271–81.

88. Tian B and Kaufman PL. Effects of the Rho kinase inhibitor Y-27632 and the phosphatase inhibitor calyculin A on outflow facility in monkeys. Experimental eye research 2005;80:215–25.

89. Honjo M, Tanihara H, Inatani M et al. Effects of rho-associated protein kinase inhibitor Y-27632 on intraocular pressure and outflow facility. Investigative ophthalmology & visual science 2001;42:137–44.

90. Sherwood JM, Reina-Torres E, Bertrand JA, Rowe B and Overby DR. Measurement of outflow facility using iPerfusion. PLoS ONE 2016;11:e0150694.

91. De Chaumont F, Dallongeville S, Chenouard N et al. Icy: An open bioimage informatics platform for extended reproducible research. Nature Methods 2012;9:690–6.

92. Dufour A, Thibeaux R, Labruyère E, Guillén N and Olivo-Marin JC. 3-D active meshes: Fast discrete deformable models for cell tracking in 3-D time-lapse microscopy. IEEE Transactions on Image Processing 2011;20:1925–37.

93. Alvarado JA, Betanzos A, Franse-Carman L, Chen J and Gonzalez-Mariscal L. Endothelia of Schlemm's canal and trabecular meshwork: distinct molecular, functional, and anatomic features. American journal of physiology. Cell physiology 2004;286:C621–34.

94. Kimura K, Ito M, Amano M et al. Regulation of myosin phosphatase by Rho and Rho-associated kinase (Rho-kinase). Science (New York, N.Y.) 1996;273:245–8.

95. Chrzanowska-Wodnicka M and Burridge K. Rho-stimulated contractility drives the formation of stress fibers and focal adhesions. The Journal of cell biology 1996;133:1403–15.

96. Fletcher DA and Mullins RD. Cell mechanics and the cytoskeleton. Nature 2010;463:485–92.

97. Janmey PA, Euteneuer U, Traub P and Schliwa M. Viscoelastic properties of vimentin compared with other filamentous biopolymer networks. J Cell Biol 1991;113:155–60.

98. Blose SH and Meltzer DI. Visualization of the 10-NM filament vimentin rings in vascular endothelial cells in situ: close resemblance to vimentin cytoskeletons found in monolayers in vitro. Experimental cell research 1981;135:299–309.

99. Helmke BP, Goldman RD and Davies PF. Rapid displacement of vimentin intermediate filaments in living endothelial cells exposed to flow. Circulation Research 2000;86:745–52.

100. Amano M, Nakayama M and Kaibuchi K. Rho-kinase/ROCK: A key regulator of the cytoskeleton and cell polarity. Cytoskeleton (Hoboken, N.J.) 2010;67:545–54.

101. Tinevez JY, Schulze U, Salbreux G, Roensch J, Joanny JF and Paluch E. Role of cortical tension in bleb growth. Proceedings of the National Academy of Sciences of the United States of America 2009;106:18581–6.

102. Herrmann H, Bär H, Kreplak L, Strelkov SV and Aebi U. Intermediate filaments: from cell architecture to nanomechanics. Nature reviews. Molecular cell biology 2007;8:562–73.

103. Schwayer C, Sikora M, Slováková J, Kardos R and Heisenberg CP. Actin Rings of Power. Developmental Cell 2016;37:493–506.

104. Segal D, Zaritsky A, Schejter ED and Shilo BZ. Feedback inhibition of actin on Rho mediates content release from large secretory vesicles. Journal of Cell Biology 2018;217:1815–26.

105. Warboys CM, Eric Berson R, Mann GE, Pearson JD and Weinberg PD. Acute and chronic exposure to shear stress have opposite effects on endothelial permeability to macromolecules. American Journal of Physiology-Heart and Circulatory Physiology 2010;298:H1850–H1856.

106. Tarbell JM, Demaio L and Zaw MM. Effect of pressure on hydraulic conductivity of endothelial monolayers: role of endothelial cleft shear stress. Journal of Applied Physiology 1999;87:261–8.

107. Dull RO, Mecham I and McJames S. Heparan sulfates mediate pressure-induced increase in lung endothelial hydraulic conductivity via nitric oxide/reactive oxygen species. American Journal of Physiology-Lung Cellular and Molecular Physiology 2007;292:L1452–L1458.

108. Sill HW, Chang YS, Artman JR, Frangos JA, Hollis TM and Tarbell JM. Shear stress increases hydraulic conductivity of cultured endothelial monolayers. The American journal of physiology 1995;268:H535–43.

109. Underwood JL, Murphy CG, Chen J et al. Glucocorticoids regulate transendothelial fluid flow resistance and formation of intercellular junctions. American Journal of Physiology - Cell Physiology 1999;277:C330–42.

110. Gong H, Tripathi RC and Tripathi BJ. Morphology of the aqueous outflow pathway. Microscopy Research and Technique 1996;33:336–67.

111. Albelda SM, Sampson PM, Haselton FR et al. Permeability characteristics of cultured endothelial cell monolayers. Journal of Applied Physiology 1988;64:308–22.

112. Sill HW, Butler C, Hollis TM and Tarbell JM. Albumin permeability and electrical resistance as means of assessing endothelial monolayer integrity in vitro. Journal of Tissue Culture Methods 1992;14:253–7.

113. Michel CC and Curry FE. Microvascular permeability. Physiological Reviews 1999;79:703–61.

114. Tam LCS, Reina-Torres E, Sherwood JM et al. Enhancement of outflow facility in the murine eye by targeting selected tight-junctions of Schlemm's canal endothelia. Scientific reports 2017;7:40717.

115. Ethier CR, Coloma FM, Kater AW de and Allingham RR. Retroperfusion studies of the aqueous outflow system. Part 2: Studies in human eyes. Investigative ophthalmology & visual science 1995;36:2466–75.

116. Epstein DL, Rowlette LL and Roberts BC. Acto-myosin drug effects and aqueous outflow function. Investigative Ophthalmology and Visual Science 1999;40:74–81.

117. Dewey CFJ. Effects of fluid flow on living vascular cells. Journal of Biomechanical Engineering 1984;106:31–5.

118. Remuzzi A, Dewey CF, Davies PF and Gimbrone MA. Orientation of endothelial cells in shear fields in vitro. Biorheology 1984;21:617–30.

119. Ives CL, Eskin SG and McIntire LV. Mechanical effects on endothelial cell morphology: in vitro assessment. In Vitro Cellular & Developmental Biology : Journal of the Tissue Culture Association 1986;22:500–7.

120. Imberti B, Morigi M, Zoja C et al. Shear stress-induced cytoskeleton rearrangement mediates NF-kappaB-dependent endothelial expression of ICAM-1. Microvascular research 2000;60:182–8.

121. Garcia-Cardeña G, Comander J, Anderson KR, Blackman BR and Gimbrone MA. Biomechanical activation of vascular endothelium as a determinant of its functional phenotype. Proceedings of the National Academy of Sciences of the United States of America 2001;98:4478–85.

122. Galbraith CG, Skalak R and Chien S. Shear stress induces spatial reorganization of the endothelial cell cytoskeleton. Cell motility and the cytoskeleton 1998;40:317–30.

123. Tarbell JM. Shear stress and the endothelial transport barrier. Cardiovascular research 2010;87:320–30.

124. Colgan OC, Ferguson G, Collins NT et al. Regulation of bovine brain microvascular endothelial tight junction assembly and barrier function by laminar shear stress. American journal of physiology. Heart and circulatory physiology 2007;292:H3190–7.

125. Collins NT, Cummins PM, Colgan OC et al. Cyclic strain-mediated regulation of vascular endothelial occludin and ZO-1: influence on intercellular tight junction assembly and function. Arteriosclerosis, thrombosis, and vascular biology 2006;26:62–8.

126. Ethier CR, Kamm RD, Johnson M, Pavao AF and Anderson PJ. Further studies on the flow of aqueous humor through microporous filters. Investigative Ophthalmology and Visual Science 1989;30:739–46.

127. DeMaio L, Chang YS, Gardner TW, Tarbell JM and Antonetti DA. Shear stress regulates occludin content and phosphorylation. American Journal of Physiology-Heart and Circulatory Physiology 2001;281:H105–H113.

128. Ghim M, Alpresa P, Yang SW et al. Visualization of three pathways for macromolecule transport across cultured endothelium and their modification by flow. American journal of physiology - Heart and circulatory physiology 2017;313:H959–H973.

129. Garcia JG, Liu F, Verin AD et al. Sphingosine 1-phosphate promotes endothelial cell barrier integrity by Edg-dependent cytoskeletal rearrangement. The Journal of clinical investigation 2001;108:689–701.

130. Lee JF, Zeng Q, Ozaki H et al. Dual roles of tight junction-associated protein, zonula occludens-1, in sphingosine 1-phosphate-mediated endothelial chemotaxis and barrier integrity. The Journal of biological chemistry 2006;281:29190–200.

131. Singer KL, Stevenson BR, Woo PL and Firestone GL. Relationship of serine/threonine phosphorylation/dephosphorylation signaling to glucocorticoid regulation of tight junction permeability and ZO-1 distribution in nontransformed mammary epithelial cells. The Journal of biological chemistry 1994;269:16108–15.

132. Arthur FE, Shivers RR and Bowman PD. Astrocyte-mediated induction of tight junctions in brain capillary endothelium: an efficient in vitro model. Brain research 1987;433:155–9.

133. Stamer W, Szymanski D, Torrejon KY et al. A biomimetic Schlemm's canal inner wall: A model to study outflow physiology, glaucoma pathology and high-throughput drug screening. Biomaterials 2015;65:86–92.

134. Ashpole NE, Overby DR, Ethier CR and Stamer WD. Shear stress-triggered nitric oxide release from Schlemm's canal cells. Investigative Ophthalmology & Visual Science 2014;55:8067–76.

135. Junglas B, Kuespert S, Seleem AA et al. Connective tissue growth factor causes glaucoma by modifying the actin cytoskeleton of the trabecular meshwork. American Journal of Pathology 2012;180:2386–403.